The response of silicon PNCCD sensors with aluminum on-chip filter to visible light, UV- and X-ray radiation

DISSERTATION
zur Erlangung des Grades eines Doktors
der Naturwissenschaften

vorgelegt von
Dipl. Phys. Stefanie Granato, geb. Ebermayer

eingereicht bei der Naturwissenschaftlich-Technischen Fakultät
der Universität Siegen
Siegen 2012

Tag der mündlichen Prüfung: 18.10.2012

Erster Gutachter:	Prof. Dr. Lothar Strüder
Zweiter Gutachter:	Prof. Dr. Ullrich Pietsch

Abstract

There are various scientific applications, from astronomical observations to free electron lasers, that make use of X-ray semiconductor detectors like PNCCDs. The PNCCD is a pixelized semiconductor detector for simultaneous X-ray imaging and spectroscopy. For the seven PNCCD cameras of the eROSITA space telescope, a radiation entrance window including an on-chip optical blocking filter has been designed. The blocking filter is a necessity to minimize electron generation by visible light and UV radiation affecting X-ray spectroscopy. A PNCCD with such a blocking filter has not been used so far in astronomy. The following work deals with the analysis of the response of PNCCDs with on-chip filter. This includes the study of photon absorption and emission processes as well as the transport of electrons inside the detector entrance window. Furthermore it comprises the experimental characterization of the detector properties regarding the attenuation of light as well as their X-ray spectral redistribution function and quantum efficiency. With the ability to reveal the involved physical processes, the PNCCD is subject of analysis and measurement device at the same time.

In addition to the results of the measurements, simulations of the solid state physics inside the detector are presented. A Geant4 Monte-Carlo code is extended by the treatment of charge loss in the entrance window and is verified by comparison with experimental data. Reproducing the chain of processes from photon absorption to charge collection, this work provides a detailed understanding of the formation of PNCCD spectra. The spectral features observed in the measurements are attributed to their point of origin inside the detector volume and explained by the model. The findings of this work allow high precision analysis of spectra of silicon detectors, e.g. of the eROSITA data, based on the presented detailed spectral response model.

Zusammenfassung

Halbleiterdetektoren, wie z.B. PNCCDs, werden in den unterschiedlichsten wissenschaftlichen Feldern eingesetzt, von astronomischen Beobachtungen hin zu Experimenten an freien Elektronenlasern. Ein PNCCD ist ein pixelierter Halbleiterdetektor zur gleichzeitigen Abbildung und Spektroskopie von Röntgenstrahlung. Für die sieben PNCCD-Kameras des eROSITA Weltraumteleskops wurde ein Strahleneintrittsfenster mit einem auf dem Chip aufgebrachtem Lichtfilter entwickelt. Dieser Filter schwächt die Intensität von optischem Licht und UV-Strahlung ab. Der störende Einfluss der durch Licht generierten Elektronen im Silizium auf die Röntgenspektroskopie wird dadurch minimiert. Ein PNCCD mit einem solchen Lichtfilter wurde bisher noch nie für die Röntgenastronomie genutzt. In der folgenden Arbeit wird die Antwortfunktion von PNCCDs mit Filter untersucht. Diese Untersuchung beinhaltet die Analyse der Photonenabsorptions- und Emissionsprozesse sowie des Transports von Elektronen im Eintrittsfenster. Des Weiteren umfasst sie die experimentelle Charakterisierung der Detektoreigenschaften bezüglich der Lichtabschwächung sowie der spektralen Verteilungsfunktion und Quanteneffizienz für Röntgenstrahlung. Der PNCCD ist hierbei Gegenstand der Analyse und zugleich Messinstrument, da dieser hochsensitive Detektor es ermöglicht, die bei der Umwandlung von Photonen in Signalladung beteiligten physikalischen Prozesse zu untersuchen.

Die Messungen werden durch Simulationen der Festkörperphysik im Detektor ergänzt. Ein auf Geant4 basierendes Monte-Carlo Programm wird um die Ladungsverlustmechanismen im Eintrittsfenster erweitert und durch Vergleich mit experimentellen Daten verifiziert. Durch die Nachbildung der Ereigniskette zwischen der Absorption eines Photons und der Ladungssammlung gibt diese Arbeit ein detailliertes Verständnis der Bildung von Röntgenspektren mit PNCCDs. Die charakteristischen Strukturen in den gemessenen Spektren werden ihrem Entstehungsort im Detektorvolumen zugewiesen und durch das Modell erklärt. Auf Basis des vorgestellten Modells erlauben die Ergebnisse dieser Arbeit eine überaus genaue Analyse von Spektren wie sie in Zukunft mit eROSITA gemessen werden.

Contents

Glossary vi

Acronyms vii

1. Introduction 1
1.1. The eROSITA mission . . . 1
1.2. The eROSITA PNCCDs . . . 2
1.3. Motivation . . . 3

2. Interaction of radiation with matter 5
2.1. Atomic model and band structure in solids . . . 5
2.2. Interaction of visible and VUV radiation . . . 8
2.3. Optical properties of thin films . . . 13
2.4. Interaction of EUV and X-ray radiation . . . 16
2.5. Atomic relaxation . . . 19
2.6. Secondary electron interactions . . . 22

3. Radiation detection with PNCCDs 26
3.1. The pn junction . . . 26
3.2. PNCCD detector concept . . . 28
3.3. Readout electronics . . . 31
3.4. The detector entrance window . . . 32
3.5. The PNCCD spectrum . . . 34

4. Radiation sources 40
4.1. LEDs and laser diodes . . . 40
4.2. X-ray tubes . . . 41
4.3. Radioactive sources . . . 41
4.4. Synchrotron radiation . . . 42
4.5. Monochromators . . . 43

5. Experimental methods 45
5.1. CCD system setup . . . 46
5.2. Experimental facilities of BESSY II and MLS . . . 47
5.3. Measurement of optical attenuation using photodiodes . . . 49
5.4. PNCCD measurements in integrating mode . . . 52
5.5. QE measurements with a continuous synchrotron spectrum . . . 59
5.6. Measurement of the X-ray spectral redistribution function . . . 60

6. Data analysis methods 61
6.1. The PNCCD Standard Analysis Procedure . . . 61
6.2. Event filtering and recombination . . . 62

6.3. Energy calibration and gain linearity . . . 64
6.4. Evaluation of monochromatic spectra . . . 66
6.5. Evaluation of the QE measurement with continuous spectrum . . . 67
6.6. Determining an integrated signal with PNCCDs . . . 69

7. Attenuation of visible light and UV radiation by the on-chip filter 70
7.1. Measurement results . . . 70
7.2. The aluminum thin film structure . . . 72
7.3. An empiric description of the attenuation factor . . . 74

8. Analysis of X-ray quantum efficiency measurements 78
8.1. Absorption edge fine structure . . . 79
8.2. The quantum efficiency between 200 eV and 10 keV . . . 80
8.3. Homogeneity of the quantum efficiency . . . 84

9. Monte-Carlo simulation of the X-ray spectral redistribution 87
9.1. Motivation . . . 87
9.2. Simulation overview . . . 88
9.3. Photon and electron transport and interaction . . . 89
9.4. Detector specific model . . . 91

10. Analysis of the spectral redistribution function 95
10.1. Spectral features . . . 95
10.2. Spectra at the K-shell absorption edges . . . 97
10.3. Comparison between measurement and simulation . . . 99
10.4. Energy resolution . . . 102
10.5. Formation of the flat shelf . . . 105

11. Conclusions for eROSITA 108
11.1. Analytic description of the redistribution function . . . 108
11.2. The spectral response of eROSITA flight cameras . . . 114
11.3. Comparison of on-chip and external filter . . . 116

12. Summary 118

Bibliography 120

List of Figures 126

List of Tables 129

A. Absorption length in Al, Si, SiO_2 and Si_3N_4 130

B. Measurement data 132

C. Deriving the analytic expression for the peak shape 138

D. Comments on the Geant4 simulation 140

Acknowledgements 143

Glossary

α	absorption coefficient
γ	parameter of CCE model: maximum charge loss
ϵ	event energy in a spectrum
$\varepsilon_r(\omega)$	relative dielectric function
$\mathcal{E}$	electric field
κ	extinction coefficient
λ	wave length
μ	mass absorption coefficient
ν_{e}	rate of electron-hole pair generation
ν_{ph}	photon count rate
ρ	density
σ_a	interaction cross section
σ_{det}	detector readout noise
σ	standard deviation
τ_r	relaxation time
τ	parameter of CCE model: characteristic length
φ	photon flux
χ	attenuation factor
ω_p	plasma frequency
E_{bind}	electron binding energy
E_{ph}	photon energy
$f_{\sigma,1}$	event threshold for data analysis
$f_{\sigma,2}$	surrounding threshold for data analysis
$f_{\text{redist,E}}$	spectral redistribution function
I_{photo}	photocurrent
I_{ring}	synchrotron ring current
l_{abs}	absorption length
$\tilde{n}$	complex refraction index
n	real part of the refraction index
P	radiant power
QE	quantum efficiency
R	reflectivity at an interface
$R_{2\sigma}$	2σ-radius of charge cloud assuming Gaussian charge distribution
R_e	electron range in matter
R_{th}	radius of charge cloud after thermalization
SR	spectral responsivity
T	transmittance of a specimen
t_{cyc}	PNCCD cycle time
t_{read}	PNCCD readout time
t_{shift}	PNCCD shift time
w	mean energy to create an electron-hole pair

Acronyms

BESSY	Berliner Elektronenspeicherring-Gesellschaft für Synchrotronstrahlung
CAMEX	CMOS amplifier and multiplexer
CCE	charge collection efficiency
CTE	charge transfer efficiency
CTI	charge transfer inefficiency
ENC	equivalent noise charge
eROSITA	extended Roentgen survey with an imaging telescope array
EXAFS	extended X-ray absorption fine structure
FWHM	full width at half maximum
ICC	incomplete charge collection
MLS	Metrology Light Source
PNCCD	charge coupled device with pn-junction transfer gates
PTB	Physikalisch-Technische Bundesanstalt
QE	quantum efficiency
XANES	X-ray absorption near-edge structure

1. Introduction

1.1. The eROSITA mission

X-rays are an important probe for the study of the Universe for several reasons. Accreting black holes and other strong gravitational potentials heat up matter to temperatures sufficiently high for X-ray emission. A significant fraction of baryons in galaxy clusters are in the form of hot gas which can only be observed through X-rays. Furthermore, the K-shell transition lines of most elements occur the medium X-ray regime (Hasinger, 2006).

The main scientific goal of the eROSITA mission (**e**xtended **Ro**entgen **s**urvey with an **i**maging **t**elescope **a**rray) is the assessment of the origin, geometry, and dynamics of the Universe through the study of its large-scale structures, i.e. galaxy clusters. The mission includes the first imaging all-sky survey in the medium energy X-ray range up to 10 keV with an unprecedented spectral and angular resolution. In addition to the all-sky survey it is foreseen to observe the extragalactic sky with high sensitivity to detect 50 to 100 thousand clusters of galaxies. The eROSITA observations will allow to test cosmological models and investigate the nature of Dark Matter and Dark Energy (Predehl et al., 2010).

Figure 1.1.: The eROSITA instrument with seven Wolter-I mirror systems and cameras in their focal points. eROSITA will be the primary instrument on-board the Russian Spectrum-Roentgen-Gamma satellite. Picture by the Max-Planck-Institute for Extraterrestrial Physics (MPE).

eROSITA will be the primary instrument on-board of the Russian Spectrum-Roentgen-Gamma (SRG) satellite which will be launched from Baikonur in the near future and placed in an orbit

around the Lagrangian point L2 in a distance of around 1.5×10^6 km from earth. The telescope, shown in fig. 1.1, will consist of seven identical Wolter-I mirror modules, each having a camera with a PNCCD detector in its focus. It is a follow-up mission to ROSAT, a mission launched in 1990, whereas the higher quantum efficiency and energy resolution of eROSITA allows an extension to higher X-ray energies and high precision measurements even at low X-ray energies.

A typical X-ray spectrum of eROSITA will contain X-ray background radiation and a variety of emission lines. The X-ray background allows conclusions about the temperature of hot gases in the Universe. However, a detector typically shows an intrinsic instrumental background that has to be separated from the astronomical data. It therefore requires the characterization and understanding of even small features of the PNCCD response function to be able to interpret the measurement results.
The distance of an astronomical object can be determined from the redshift of a measured spectrum. Blue and red shifts due to the rotation of black holes for example lead to a further broadening of the observed X-ray emission lines. A high energy resolution and most precise knowledge of the PNCCD response function is crucial for such data analysis.

1.2. The eROSITA PNCCDs

The scientific goals of eROSITA put high demands on the performance of PNCCD detectors (Meidinger et al., 2006a), which are developed and manufactured at the MPI Semiconductor Laboratory (MPI HLL) in Munich. Each detector consists of an array of 384 × 384 imaging pixels and is read out with a frame rate of 20 Hz. The specification for the energy resolution defines an upper limit for the full width at half maximum of 138 eV for 5.9 keV-photons.

As astronomical objects not only emit X-rays, but also visible light and UV radiation, a blocking filter is crucial to enable high accuracy spectroscopic measurements. The XMM-Newton camera and most other astronomical X-ray telescopes are protected by optical blocking filters that are applied externally by a filter-wheel. The blocking filter for the described eROSITA detector is integrated directly on the chip. By the use of such an option, the risk of filter rupture during satellite launch is prevented.
On the side where radiation enters the detector, thin layers of silicon dioxide, silicon nitride and aluminum are deposited onto the silicon wafer. These layers have thicknesses of 30 nm, 40 nm and 200 nm respectively. Together with the first nanometers of the silicon volume, which are highly doped, they form the radiation entrance window. This part of the detector mainly influences the measured spectra at low X-ray energies, as the X-ray radiation absorbed in the entrance window may not or only partially be collected. Furthermore, secondary photons or electrons are generated in the entrance window, leading to specific features in PNCCD spectra.
In addition to those detectors with on-chip filter, a batch of conventional PNCCDs without aluminum filter was produced at the Semiconductor Laboratory. These detectors have to be equipped with external filters on a filter wheel. A combination of PNCCDs with and without on-chip filter can be chosen for the seven eROSITA cameras.
PNCCDs based on the same technology were successfully used for the XMM-Newton X-ray space telescope. In comparison to the XMM-Newton PNCCD (see Strüder et al., 2001), lower

noise and the ultra-thin rectifying p^+-doping profile at the entrance window of eROSITA PN-CCDs allow spectroscopy down to photon energies of 100 eV.

1.3. Motivation

The combination of spectral, spatial and time resolution of the eROSITA cameras is extraordinary compared to other semiconductor X-ray detectors. The on-chip optical blocking filter, allowing the observation of X-ray sources with high emission of visible light, has never been used before in an astronomical mission.
For calibration and data analysis of the camera as well as for future detector development, the spectral redistribution function and detection efficiency of the described PNCCDs need to be analyzed. Elsewise even marginal features in the detector response could lead to the misinterpretation of the measured X-ray spectra. A thorough understanding of the photon and electron interaction mechanisms inside the detector can be derived from the comparison of theoretical models and measurements of the spectral response function.

There have been studies on the response of silicon detectors in recent years, as for example by Lechner (1998). The low energy spectra at this time though were affected by a higher detector noise. A more recent work by Popp (2000) dealt with the analytic description of PNCCD specific effects on the detector response. With focus on the involved physical mechanisms, Eggert (2004) characterized the detector response of silicon drift detectors with an aluminum entrance window by measurements and semi-analytical, partially Monte-Carlo assisted calculations. Campbell et al. (2001) and Goto (1993) modeled the response of Si(Li) detectors by a combination of Monte-Carlo simulations of the photon and electron interactions at high energies, combined with analytical expressions for thermalization and incomplete charge collection.
The results of such calculations can not be translated directly to the response function of eROSITA PNCCDs. They depend on the purity of the silicon material and the material specific interface properties between sensitive and insensitive volume, including processing. Therefore, the simulation of the photon conversion and electron transport inside the PNCCD is performed in this work in order to reproduce and understand measurement results.
The novel type of PNCCD with on-chip optical blocking filter requires the analysis of its response to X-ray radiation, and furthermore to visible light and UV radiation. As known from thin film physics, the optical properties of thin films with a thickness of several tenths or hundreds of nanometers are not necessarily equal to bulk properties. Reasons for this can be imperfections in the layer structure as well as the modified solid state physics on small scales. The use of an on-chip filter requires hence the experimental characterization of the optical properties of the detector. Furthermore, an analysis investigating the origin of the observed properties admits improvements for future detector development.

Based on existing work and the considerations above this thesis sets focus on the following tasks:

- Experimental characterization of the X-ray quantum efficiency and spectral redistribution as well as the attenuation of visible light and UV radiation of the eROSITA PNCCDs with on-chip blocking filter
- Examination of the microstructural and optical properties of aluminum on-chip filters
- Investigation on the photon conversion and electron transport inside the entrance window by comparison of Monte-Carlo simulations and experiments
- Evaluation of analytical models for the quantum efficiency and spectral redistribution function

With measurements over an exceptionally wide range of photon energies from 1.9 eV up to 11 keV this work gives a full picture of the PNCCD detector efficiency. Two different experimental procedures for the quantum efficiency measurement are presented that lead to very detailed results. In addition, measured monochromatic spectra at energies from 100 eV to 11 keV are presented. With an optimized experimental setup and an intentionally limited set of data corrections, these spectra permit a detailed analysis of the PNCCD response.
In this work, the PNCCD is subject of analysis and measurement device at the same time. A simulation of the photon conversion and charge collection process inside the detector gives insight into the point of origin of certain features in PNCCD spectra. For this purpose, a Geant4 Monte-Carlo code is applied, extended by charge loss mechanisms in the entrance window. Furthermore, PNCCD specific effects are described as far as there is considerable impact on the evaluation of response data. The simulation includes all relevant statistical aspects of the formation of a spectrum and can thus explain the energy resolution in contrast to previous studies.

The outline of this work started with an introduction on the eROSITA project and detector as well as on the motivation of this work. In the second chapter a review of the fundamentals of photon and electron interaction in solids is given. In addition to the involved physical processes, their description by material parameters is introduced. The third chapter describes the basic properties of PNCCDs as used for the measurements in this work. The experimental facilities and methods are outlined in chapter 4 and 5, giving a general overview on radiation sources and, thereafter, more specific information on the measurement setup and experimental procedure. In chapter 6, the applied data analysis methods are detailed. The results on the attenuation of visible and UV light and on the X-ray quantum efficiency are presented in chapters 7 and 8. A description of the Monte-Carlo model of the photon conversion and electron transport process in chapter 9 is followed by results on the spectral redistribution function in chapter 10. Conclusions for the eROSITA detectors are given in the 11th chapter. The last chapter closes with a summary of the findings of this work.

2. Interaction of radiation with matter

As carriers of the electromagnetic force, photons interact with charged particles, like electrons and protons. This interaction of electromagnetic radiation and matter is described by various different models and equations depending on the photon energy and based on different fields of physics. Depending on the experimental purpose, one or another model may be applicable, but the suitability of a model mainly depends on the radiation energy range. Table 2.1 shows an overview of the common separation between bands of electromagnetic radiation. The phenomenological and mathematical description of photon interactions is mainly divided into two regions, which are separated at a photon energy of about 50 eV, at the border between the XUV and soft X-ray regime. To understand this separation and the basic aspects of the subsequent sections, a short introduction on atomic and solid structure is given in the next section.

The whole chapter is intended as a summary of those topics that are essentially necessary for the understanding of this work. They are discussed in detail in standard literature such as Kittel (1995) for solid state physics, Mayer-Kuckuk (1997) for atomic physics and Fox (2001) for optical properties of solids.

2.1. Atomic model and band structure in solids

The atomic model, reduced to those aspects relevant for the following discussion, consists of the protons and neutrons inside the core and electrons distributed to several electron shells. In case of silicon, the total number of 14 electrons is distributed over 3 main shells as shown in table 2.2. These shells are subdivided into several energy levels denoted by quantum numbers (see section 2.4). According to the Pauli principle, no quantum state can be occupied by

name	abbreviation	wavelength	energy
near infrared	NIR, IR-A	1400 - 780 nm	1.1 - 1.6 eV
visible light		780 - 380 nm	1.6 - 3.3 eV
near ultraviolet	UV-A	380 - 315 nm	3.3 - 3.9 eV
medium ultraviolet	UV-B	315 - 280 nm	3.9 - 4.4 eV
far ultraviolet	UV-C-FUV	280 - 200 nm	4.4 - 6.2 eV
vacuum ultraviolet	UV-V-VUV	200 - 100 nm	6.2 - 12 eV
extreme ultraviolet	EUV or XUV	100 - 1 nm	12 eV - 120 eV
soft X-ray		10 - 1 nm	120 eV - 1.2 keV
medium X-ray		1 - 0.1 nm	1.2 - 12 keV
hard X-ray		0.1 - 0.01 nm	12 - 120 keV

Table 2.1.: Separation of common names for different photon energy regimes. The separation between the regimes is not unambiguous and the notation varies between different fields of physics, so this table can only serve as a guideline (see for example Wikipedia (2011)).

main quantum number	number of electrons$^-$	occupation
n = 1 (K-shell)	2	$1s^2$
n = 2 (L-shell)	8	$2s^2 2p^6$
n = 3 (M-shell)	4	$3s^2 3p^2$

Table 2.2.: The main shells of a silicon atom and their occupation with electrons. For example, the 2s-orbital is occupied by two electrons, the 2p-orbital by 6 electrons.

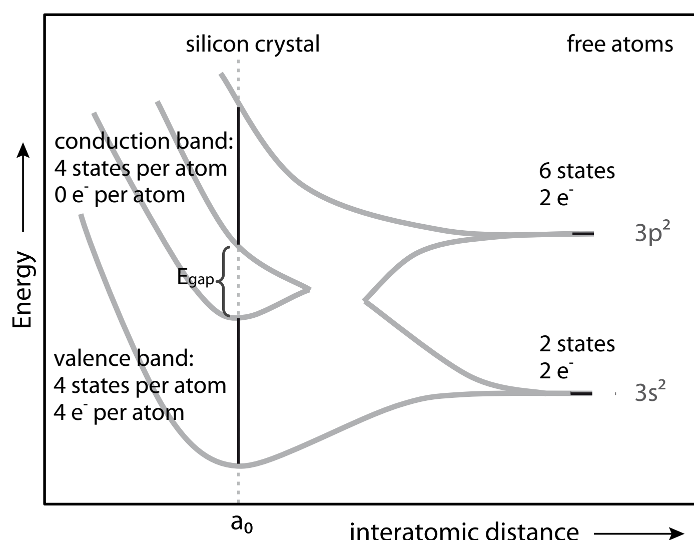

Figure 2.1.: Allowed electron energies for M-shell electrons in Si in condensed state (with interatomic distance a_0) and as free atom (right side) at absolute zero temperature: in free atoms, the electrons can only occupy the discrete states of the s- and p-orbitals. When bringing many atoms closely together, the outer orbitals overlap and form the valence band and the conduction band, separated by a band gap energy E_{gap}. Similar illustrations can be found in Fox (2001) and Ibach & Lüth (2003).

more than one electron, hence every electron is bound to the atom with a different, characteristic binding energy. Photon interaction with free atoms occurs with these bound electrons and therefore at discrete energy levels defined by the binding energies.
The outermost principal shell, the M-shell in the case of silicon, is called the valence orbital. When atoms condense to a solid, the outermost orbitals overlap. In the case of silicon, the 3s and 3p orbitals split up into two sp3-hybrid orbitals, each holding 4 free states per atoms. If a large number of atoms is involved, the huge number of overlapping orbitals with infinitesimally small energy steps form quasi-continuous energy bands, the valence and the conduction band. Inner shells, where the overlap is small, retain their atomic shell-like character. The formation of energy bands at the example of silicon is shown schematically in fig. 2.1.
For semiconductor materials and insulators, the valence and conduction band are separated by an energy region with no electron states, the band gap. At absolute zero temperature, all electrons are located in the valence band, as shown in fig. 2.2. However, under real conditions, electrons are distributed over both bands due to their thermal energy. In contrast to semiconductors, the band gap energy of insulators is so high, that even at room temperature the conduction band is almost empty. Semiconductors exhibit a smaller band gap and hence

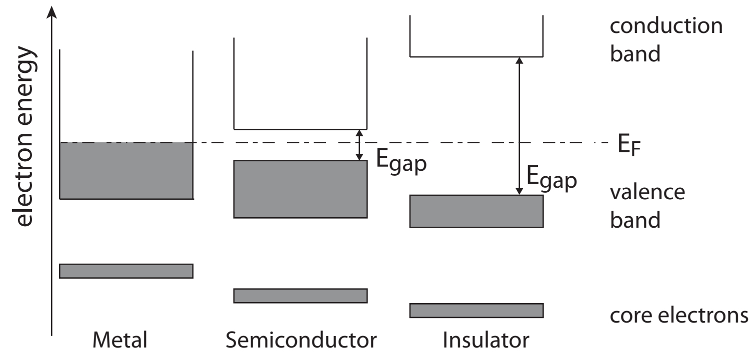

Figure 2.2.: Energy level diagrams for metals, semiconductors and insulators. Even at T = 0 K metals have a partly occupied band (shaded). Semiconductors and insulators have a filled valence band and empty conduction band, with the Fermi level inside the band gap. Illustration after Ibach & Lüth (2003).

a significant number of electrons in the conduction band at room temperature. In metals, valence and conduction band overlap and no band gap is formed (see fig. 2.2), leading to a high density of conduction electrons even at low temperature. The energy up to which the conduction band of metals is filled with electrons is called the Fermi energy E_F. This quantity is also applied to semiconductors, where it is usually called the Fermi level. Similar to the Fermi energy in metals, the Fermi level in semiconductors describes the degree to which the conduction band is filled. In semiconductors and insulators E_F is positioned inside the band gap.

In a perfect crystal, there are no available electrons states within the band gap. In real semiconductors, imperfections in the crystal structure form localized states that can have binding energies inside the band gap. These localized states, called traps, are capable of capturing and re-emitting charge carriers.

The introduction of energy bands in this chapter is a very simplified one. A detailed derivation and description of the band structure in solids would go beyond the scope of this work, but can be found for example in Kittel (1995) or Ibach & Lüth (2003). In the context of this work it is important to understand the connection between the band structure and the optical properties of a solid.

The band structure, or the electronic dispersion relation, describes the relation between electron energy states and their wave vector, respectively their momentum. In general, the wave vector $\vec{k}$ is used to describe a wave and can be written as

$$\vec{k} = k \cdot \vec{n}_k = \frac{2\pi}{\lambda} \cdot \vec{n}_k = \frac{\vec{p}}{\hbar}\,. \tag{2.1}$$

$\vec{k}$ points in the direction of wave propagation, here indicated by the normalized vector $\vec{n}_k$, and its absolute number k is reciprocal to the wavelength λ. Electrons can be described by a wave vector, as they exhibit both particle and wave properties. Their wave number is determined by the electron momentum $\vec{p}$ and the reduced Planck constant $\hbar$. Due to the periodicity of a crystal, the band structure can be displayed in a reduced zone scheme. In this

scheme, the wavenumber takes values within the first Brillouin zone, a representation of the crystal lattice in reciprocal space. The first Brillouin zone for silicon and aluminum is shown in fig. 2.3. The critical points or directions in the Brillouin zone, as for example Γ, Δ, Σ, are later used to describe the wave vector direction in the band structure diagrams.

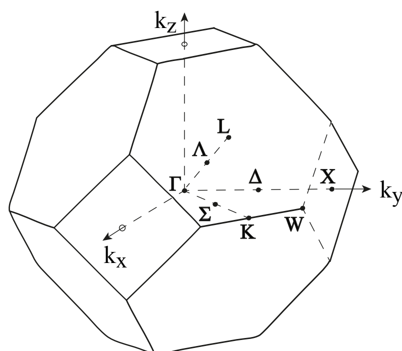

Figure 2.3.: First Brillouin zone of silicon and aluminum and its critical points. Illustration after Madelung (1996).

The band structure is closely connected to the physical properties of solids, including optical absorption. Band structures of silicon and aluminum are therefore shown later in fig. 2.4 in order to explain the optical properties of these materials.

At the beginning of this chapter it was stated that the phenomenological and mathematical description of photon interactions is mainly divided into two regions, separated at about 50 eV, the border between the XUV and soft X-ray regime. At lower photon energies, the absorption process involves electrons of the valence orbital, which forms the valence and conduction band in solids. These energy bands are characteristic for the condensed state of a system, e.g. the type of crystal lattice or the chemical composition of a solid. Due to the continuous structure of energy bands, the optical properties change continuously with energy. At higher energies, the condensed state of atoms can mostly be neglected, as the interaction of radiation takes place with bound electrons of inner shells of the atoms. The discrete nature of the atomic structure allows the interaction mechanisms to be described by discrete processes. Furthermore, the interaction probability can be derived from atomic data and the density of the material. Only to some extent the condensed state of elements influences the X-ray absorption properties, which is presented in section 2.4.

2.2. Interaction of visible and VUV radiation

The optical properties of solids are of interest in this work as the eROSITA PNCCD is equipped with an on-chip optical blocking filter, which consists of several thin layers. Thus, an overview on optical properties of solids is given in this section, and the characteristic features of thin films are presented thereafter.

One approach to understand the optical properties of a material is to analyze its band structure, shown for silicon and aluminum in fig. 2.4. Photon absorption through electronic transitions between different bands, the so-called **interband transitions**, occurs whenever it is allowed by the conservation laws. Thus, only if the total energy and momentum of the system is conserved, the absorption process is possible. Photons exhibit a very low momentum compared to their kinetic energy. Hence, the absorption of a photon without any tertiary particles involved causes a transition that can be depicted in the band structure as an almost vertical arrow, as shown in fig. 2.4. Transitions over a large k-range (with large momentum transfer)

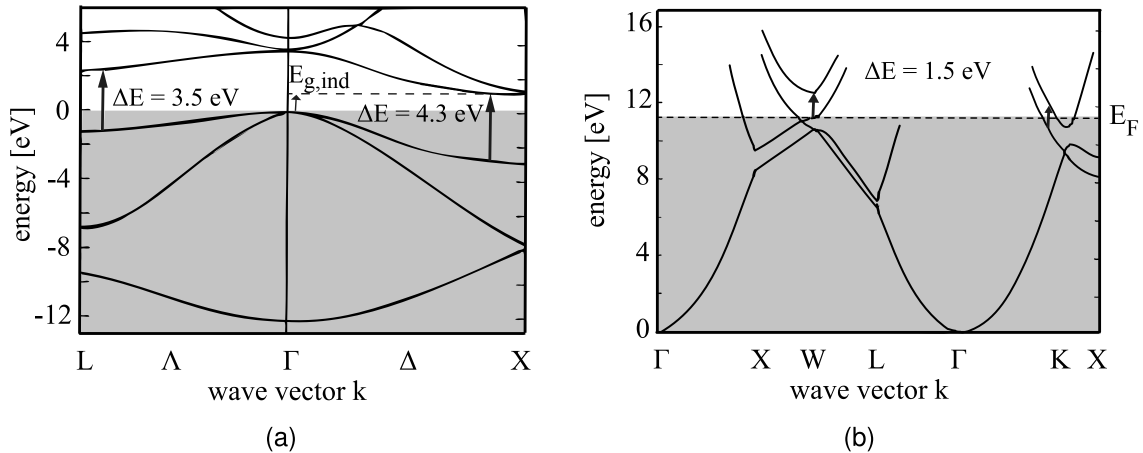

Figure 2.4.: Band structure of (a) silicon: the indirect band gap $E_{g,ind}$ and the two parallel-band positions with transition energies 3.5 eV *and* 4.3 eV *are marked with arrows. For photon energies below $E_{g,ind}$, silicon is transparent. (b) aluminum: the conduction band is half filled up to the Fermi level E_F at any temperature, hence aluminum does not exhibit a band gap. The parallel-band positions with a transition energy of* 1.5 eV *are marked by arrows. Hence, a rise in absorption for energies above* 1.5 eV *is observed, as shown later in fig. 2.5. Both figures are adapted from Fox (2001).*

require a third particle in order to fulfill both energy and momentum conservation. This can be achieved by the involvement of a phonon, the quasi-particle describing lattice vibrations in solids. Transitions with (almost) unchanging wave vector are called **direct transitions**, while those with significant momentum transfer are called **indirect transitions**. Likewise, the respective energy gap for such transitions is called indirect or direct band gap, the smallest of both is called the fundamental band gap. The transitions occur between occupied and free electron states, hence between parts of the band structure below and above the Fermi energy or Fermi level. In the infrared, visible or ultraviolet spectral region, insulators and semiconductors exhibit an absorption edge caused by the onset of transitions across the fundamental band gap. For silicon, the fundamental band gap amounts 1.1 eV and leads to the optical properties shown in fig. 2.5a. Although the involvement of one or more phonons in the absorption process allows almost any transition across the band structure, indirect transitions are significantly less probable than direct transitions. At higher photon energies, the absorption properties are therefore dominated by direct transitions. The absorption probability depends on the number of electrons for which a transition of the given energy is possible. Accordingly, absorption is especially probable for photons with energies equal to the energetic distance of parallel band sections. This phenomenon is called the **parallel-band effect**, and the respective sections in the band structure for silicon and aluminum are marked by arrows in fig. 2.4. In the case of metals, absorption is possible through **intraband transitions** of electrons within the conduction band. Here, an electron is lifted into an energetically higher state inside the same energy band. Due to the high number of conduction band electrons with an equally high number of available final states, metals are strong absorbers and have a high reflectivity in the visible. Furthermore, all metals share a sharp drop in reflectivity and absorption at a cut-off frequency in the ultraviolet, the plasma frequency ω_p, as discussed at the end of this section.

To this point, the mentioned physical models are based on electronic physics in solids. Beyond that, the classical theory of optical propagation provides another approach for the understanding of interaction of photons with matter. In this approach, light is treated as electromagnetic waves. A quantitative description of the interaction of electromagnetic waves with a continuous medium are provided by the Maxwell equations (see for example Fox, 2001). The continuous medium properties can then be quantified by macroscopic parameters, as the **dielectric constant** or the **refractive index**.

In a non-absorbing medium, the refractive index n is defined as the fraction of the velocity of light c in free space to the velocity of light v in the medium.

$$n = \frac{c}{v} = \frac{ck}{\omega} \tag{2.2}$$

The velocity v can also be expressed by the wave number k and frequency ω of the wave, as seen in the second part of the equation. This equation can be generalized to the case of an absorbing medium by allowing the refractive index and the wave number to be complex, here denoted by $\tilde{n}$ and $\tilde{k}$:

$$\tilde{n} = \frac{c\tilde{k}}{\omega} \tag{2.3}$$

The complex refractive index consists of a real part n, which is often just called the refractive index, and the imaginary part κ, the so-called **extinction coefficient**.

$$\tilde{n} = n + i\kappa \tag{2.4}$$

For a non-magnetic material, the connection between the **relative complex dielectric constant** ε_r and complex refractive index is given by

$$\tilde{n}^2 = \tilde{\varepsilon_r} \ . \tag{2.5}$$

It will become apparent in the following that both dielectric constant and refractive index are used to describe the optical properties of materials.

A plane wave, propagating in z direction with an electrical field amplitude $\mathcal{E}_0$, can be written as

$$\mathcal{E}(z,t) = \mathcal{E}_0 e^{i(kz-\omega t)} \ . \tag{2.6}$$

For propagation inside a medium with refractive index $\tilde{n}$, the wave number k is substituted with $\tilde{k}$. Accordingly, eq. 2.3 and eq. 2.4 inserted into eq. 2.6 lead to

$$\mathcal{E}(z,t) = \mathcal{E}_0 \cdot e^{i(\omega\tilde{n}z/c-\omega t)} = \mathcal{E}_0 \cdot e^{-\frac{\kappa\omega z}{c}} e^{i(\frac{\omega n z}{c}-\omega t)}. \tag{2.7}$$

The resulting expression in eq. 2.7 is a plane wave with modulated amplitude. The real part of the refractive index determines the phase velocity of the wave front, as in the definition of n in eq. 2.2. The extinction coefficient κ leads to an exponential decay of the wave amplitude with increasing depth z in the medium. This exponential decay of electromagnetic waves in media is known as **Lambert-Beer Law**,

$$I(z) = I_0 e^{-\alpha z} = I_0 e^{-\frac{z}{l_{abs}}} , \tag{2.8}$$

with the absorption coefficient α or the absorption length l_{abs} describing the slope of the decay. Hence, the radiation intensity after the transition through a material of thickness z is decreased from I_0 to $I(z)$. The parameters α, l_{abs} and κ are connected through

$$\alpha = \frac{1}{l_{abs}} = \frac{4\pi\kappa}{\lambda} . \tag{2.9}$$

At the interface of two dielectrics, the Maxwell equations and the application of boundary conditions lead to the **Fresnel equations** (see for example Bergmann & Schaefer, 2003). These equations describe the transmission and reflection of electromagnetic radiation at interfaces for arbitrary angles of incidence. In the special case of normal incidence, the quotient of reflected intensity to incident intensity is

$$R = \frac{(n_0 - n_1)^2 + (\kappa_0 - \kappa_1)^2}{(n_0 + n_1)^2 + (\kappa_0 + \kappa_1)^2} , \tag{2.10}$$

which is called the **reflectivity** R. The refractive indices are $\tilde{n}_1$ and $\tilde{n}_2$ respectively at both sides of the interface. The real and imaginary parts of $\tilde{n}$, as defined in eq. 2.4, are denoted with indices 0 and 1 for the two adjacent materials. For an interface of a solid with air or vacuum, this equation reduces to

$$R = \frac{(n - 1)^2 + (\kappa)^2}{(n + 1)^2 + (\kappa)^2} \tag{2.11}$$

with $n_{air} \approx 1$ and $\kappa_{air} \approx 0$. For non-absorbing materials, κ is zero and n is usually in the range between 1.3 to 5 in the visible range. This leads to a reflectivity of roughly $1\,\%$ to $40\,\%$. For metals, κ is much larger than n and therefore leads to a reflectivity of about $90\,\%$.

When light passes a slice of material with thickness d, as for example one layer of the PNCCD entrance window, a fraction of the light is reflected when entering the material according to eq. 2.10. After a thickness d, an additional fraction of light is absorbed according to eq. 2.8. The quotient of transmitted intensity to incident intensity is

$$T = (1 - R) \cdot e^{-\frac{d}{l_{\text{abs}}}} , \tag{2.12}$$

and is called the **transmittance** of the layer. In this definition, T includes the reflection at one interface and absorption inside the layer. The fraction of light transmitted through a layer stack can be calculated by multiplying the transmittances of all layers. This formula can also be applied to X-ray radiation, although the reflectivity R for X-rays at normal incidence is so small

that it can be neglected.

To this point, the refractive index and relative dielectric constant were treated as constant parameters. This is true for a given light frequency ω, respectively wavelength λ. When describing the full spectrum of light, it makes sense to speak of a relative dielectric function $\varepsilon_r(\omega)$. The relative dielectric function can be derived from classical theory of optical propagation, treating atoms or molecules as classical dipole oscillators.
The so-called **Lorentz-oscillator model** is based on the assumption that photon interaction can be regarded as the forced resonance of electromagnetic radiation with several oscillators inside a medium, each having its own resonance frequency. For example, at infrared frequencies, vibrational oscillations of oppositely charged ions in a solid contribute to the response of the material. In particular, the resonance of bound electron oscillations defines the properties of materials in the optical range. The dielectric function resulting from such calculations (see for example Kopitzki, 1986) even explains the specific properties of metals, insulators and semiconductors. For metals, the **Drude-Lorentz oscillator model** takes into account the interaction with the free electron plasma, a mechanism that is referred to as intraband absorption in electronic physics. The Drude-Lorentz oscillator model explains the characteristically high absorption and reflection values of metals and predicts the absorption cut-off at the plasma frequency. The relative dielectric function of a material is constituted of different oscillator components, in this case as an example for metal:

$$\varepsilon_r(\omega) = \varepsilon_{\text{intra}} + \varepsilon_{\text{Drude}} \tag{2.13}$$

ε_{intra} and ε_{Drude} are the intraband and the free electron (interband) component respectively. The latter results from the Drude model and can be written as

$$\varepsilon_{\text{Drude}}(\omega) = 1 - \frac{\omega_p^2}{\omega^2} \frac{1}{1 + i(\tau_r \omega)^{-1}} \,. \tag{2.14}$$

Accordingly, $\varepsilon_{\text{Drude}}$ depends on the plasma frequency ω_p and the electron relaxation time τ_r. The latter parameter quantifies the scattering rate of the free electrons and is inverse proportional to the electron mean free path. The plasma frequency is defined by

$$\omega_p = \frac{N_C e^2}{\varepsilon_0 \varepsilon_{el} m^*} \,. \tag{2.15}$$

N_C is the number of conduction band electrons per volume and m^* the reduced electron mass. ε_0 denotes the vacuum permittivity and ε_{el} the dielectric function resulting from bound electron vibration (interband transitions). The term for ε_{el} can be found in literature, as for example Kopitzki (1986) but can not be treated in detail in this context.

The previously discussed features in the dielectric function or respectively the optical constants of materials can be reproduced using the example of silicon and aluminum. Figure 2.5a shows n and κ for silicon in the range of 1 eV to 5 eV. It illustrates the onset of absorption at the indirect band gap energy E_g = 1.1 eV. At E_1 = 3.5 eV and E_2 = 4.3 eV, absorption is increased due to the parallel bands around the L and X points. The band gap and parallel band points for silicon were already displayed in the band structure in fig. 2.4a. Figure 2.5b shows n

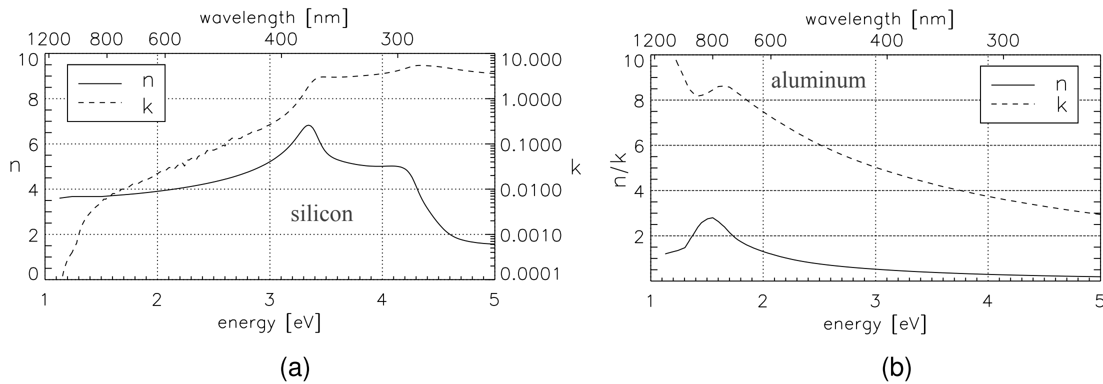

Figure 2.5.: Refractive index n and extinction coefficient κ (Palik, 1985). (a) For silicon: the onset of absorption at the band gap energy E_{gap} = 1.1 eV and a rise in absorption at the parallel-band transitions at 3.5 eV and 4.3 eV are clearly visible. (b) For aluminum: strong absorption throughout the optical regime is caused by free electron absorption (intraband transitions). Interband transitions at energies above 1.5 eV are extremely pronounced due to parallel-bands. Furthermore, aluminum exhibits a dip in reflection at this photon energy. See also fig. 2.4 with the band structure of silicon and aluminum.

and κ for aluminum, with an obvious increase of absorption around 1.5 eV due the the parallel band effect (see also the aluminum band structure in fig. 2.4b). The absorption lengths of all materials contained in the PNCCD entrance window are furthermore shown in appendix A, for the whole energy range from visible light to X-ray radiation. The drop in absorption, and therefore a rise in absorption length, of aluminum at the plasma edge can be seen in fig. A.1 at $\omega_p \approx 16$ eV.
The previous considerations on optical properties of solids are based on the assumption of infinitely large structures, neglecting any kind of surface or boundary effects. For small structures, as for example thin films, some of the described interaction mechanisms have to be reconsidered.

2.3. Optical properties of thin films

The PNCCD entrance window consists of several thin layers with thicknesses between 30 nm and 200 nm. These thicknesses are on the order of the wavelength of visible light and close to the scale of crystalline structures. In order to understand the light-blocking properties of the filter, the previous description of light interaction with solids has to be extended. A summary on the specific optical features of thin films is hence given in this section.

Interference effects on thin films As drawn out in section 2.2, the reflection and transmission of light at material interfaces can be derived from the Fresnel equations. This leads for example to the expression in eq. 2.10, the reflectance at an interface for normal incident light. However, when the film thickness d is on the order of the coherence length of the light, destructive and constructive interference between multiply reflected beams occur. Therefore, the reflection and transmission at thin film stacks has to be calculated by a matrix method

including the phase information and phase shift for the reflected and transmitted beams. This is for example described in MacDonald (1971).
Interference effects on the reflectance and transmittance of a layer stack are only significant if the material is highly transparent. For optical dense media, especially for metal layers, the transmittance is mainly determined by the amount of absorbed radiation. For the optical blocking properties of the on-chip filter, interference is therefore of minor importance. Absorption as well as reflection properties of thin metal layers are more important, and are severely influenced by microstructural effects.

The microstructure of thin films Only in rare cases does a film consist of a homogeneous parallel-sided layer. Thin films with thicknesses below a few µm usually exhibit characteristic structures, which directly affect their optical properties. The following considerations are restricted to thin metal layers, as the crucial aspect within the context of this work is the optical transmittance of the on-chip aluminum blocking filter. The most significant changes between bulk and thin film properties are observed for metal films compared to other materials.
Thin metal films are in most cases polycrystalline, with characteristic grain sizes equal to the film thickness. The grain size may depend on the material and the way of material deposition. Heating or cooling of a thin layer on the substrate can further alter the structure. The optical constants of such thin films can deviate from those of compact bulk material for two main reasons: First, the scale of thin film structures may be as large as several atomic layers, directly influencing the intrinsic dielectric function of an individual homogeneous region or grain. This is further denoted as the **intrinsic effect** on the dielectric function. Secondly, the macroscopic dielectric function of a heterogeneous material may be changed due to its composition and/or microstructure, although the intrinsic properties of each grain are unchanged. This type of impact is referred to as **structural effects**. The same classification is discussed in several publications on this topic, for example Fragstein & Römer (1958), Niklasson et al. (1986), Schopper (1954). In most cases, both effects influence the observable properties of thin metal layers.

Intrinsic effects: As presented in the last section, the dielectric function of metals is determined by two absorption mechanisms, the interband and intraband transitions. Intraband absorption, caused by transitions of free electrons within the conduction band, is for most metals dominant in the visible light regime. For shorter wavelengths, interband transitions from valence to conduction band predominantly influence the dielectric function. For aluminum in particular, interband absorption is pronounced for photon wavelengths near $\lambda = 830$ nm (photon energy 1.5 eV) due to the parallel-band effect.
Both interband and intraband absorption can be affected by the small structures in thin metal layers. The following considerations follow the studies of Fragstein & Römer (1958), Niklasson et al. (1986), Parmigiani et al. (1986).
Lattice contraction or expansion, for example caused by thermal expansion of substrate or thin film material, may change the density of free electrons in a metal, affecting the intraband component of the dielectric function. Furthermore, changes in the lattice structure may cause shifts in the valence electron binding energies, hence modifying the interband component. If the grain size is smaller than the electron mean free path, which is approximately 50 nm for metals at room temperature, the granular structure can cause variations in the dielectric function by a change of the electron relaxation time τ_r (see also eq. 2.14). For example Niklasson

et al. (1986) deduced a relation between relaxation times in bulk material $\tau_{r,b}$ and metal grains $\tau_{r,g}$ according to

$$\frac{1}{\tau_{r,g}} = \frac{1}{\tau_{r,b}} + \frac{3}{2}\frac{R}{1-R}\frac{v_F}{L} \,. \tag{2.16}$$

Here, R is the reflectivity at the grain boundaries and v_F is the Fermi velocity ($\approx 10^6$ m/s in silicon). L denotes the mean free path of electrons inside a grain and can be approximated by the mean radius of a grain. Equation 2.16 and eq. 2.14 show, that a sufficiently small grain radius may lead to shorter relaxation times in granular thin films, resulting in a higher absorption probability for optical radiation. Next to a decreased relaxation time for the free electrons, thin film grain size may furthermore cause the broadening of parallel-band features in the absorption spectrum. The decrease of the parallel-band peak in the aluminum dielectric function was observed and theoretically reproduced by Niklasson et al. (1986).
The analysis of intrinsic effects in non-bulk optical properties requires extensive calculations, which are not further presented but can be found in the given literature. However, the poor reproducibility of thin film composition and structure sets limits to the experimental prospects. Furthermore, structural effects dominate the properties of such thin metal films in most cases. This hinders the detailed description of intrinsic effects and rises interest in the examination of structural effects.

Structural effects: Structural effects in thin metal layers can cause drastic changes in the optical properties on the order of several magnitudes. They are closely connected to the method and conditions of layer deposition. For example, sputtered metal layers can form islands instead of a plane structure on the substrate. The size of such islands depends strongly on the deposition temperature (see for example Nguyen et al., 1993). Consequently, in such layers there may be voids between metal grains, leading to a reduced effective density of the thin film material compared to bulk material. In a first approach, this reduced density can be accounted for by a reduced effective layer thickness inserted into eq. 2.8. A more accurate and established method to describe the effective macroscopic dielectric function of an inhomogeneous thin film is the **effective medium theory** . This theory describes the macroscopic properties of an inhomogeneous medium based on the properties and the relative fractions of its constituents. It may not only be applied to a metal layer containing voids, but also to granular compositions of two different materials, e.g. aluminum layers deposited with a certain fraction of silicon as in the study of Niklasson et al. (1986). Effective medium theory includes several similar approaches, as for example the Maxwell-Garnett or the Bruggemann theory. The Maxwell-Garnett model is restricted to relatively low volume fractions of a material a which is completely surrounded by a material b. The Bruggemann theory can be applied to mixtures with comparable volume fractions with random-mixture microstructure. The derivation of effective medium equations and their application to thin film properties is described for example in Aspnes (1982). The Bruggemann relation for composite of material a and b with respective volume fractions f_a and f_b is

$$f_a \frac{\varepsilon_a - \varepsilon}{\varepsilon_a + 2\varepsilon} = f_b \frac{\varepsilon_b - \varepsilon}{\varepsilon_b + 2\varepsilon} \,, \tag{2.17}$$

with f_a + f_b = 1. ε is the dielectric function of the heterogeneous medium with dielectric functions ε_a and ε_b of the respective constituents.
This equation was successfully applied in order to explain the properties of aluminum-silicon

composed thin films by Niklasson et al. (1986).
In addition to the described microscopic structure of metal grains, pinholes can occur in thin metal films, dramatically increasing the amount of transmitted light.

2.4. Interaction of EUV and X-ray radiation

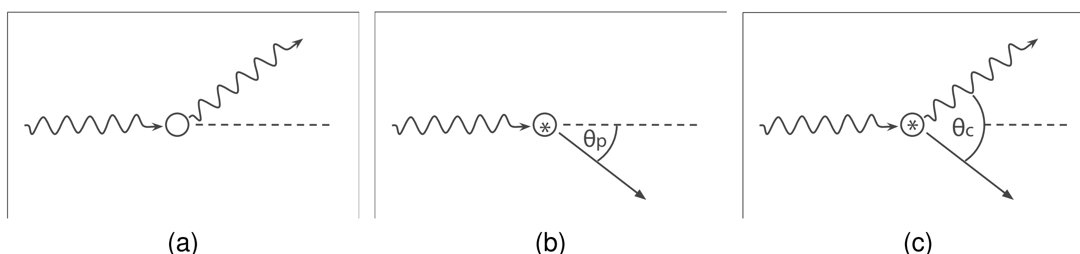

Figure 2.6.: Schematics of (a) Rayleigh scattering, (b) Photoabsorption and (c) Compton scattering of photons. The excited atom is marked by a star. Photons are illustrated by wave arrow, electrons by a straight arrow.

In contrary to the previously described mechanisms, interaction with photons of the XUV and X-ray regime takes places with inner-shell electrons instead of valence electrons. Due to the context of this work, the X-ray energy of interest is limited to photon energies up to 20 keV. In this regime, three basic interaction mechanisms can be distinguished, namely Rayleigh scattering, photoabsorption and Compton scattering (see fig. 2.6): (a) A photon can be scattered in a perfectly elastic collision with an electron, where the photon energy remains the same while the direction changes. This is called **coherent (Rayleigh) scattering or diffraction**. In solid state detectors, Rayleigh scattering has low impact on the detected signal, as it only deflects the path of a photon. (b) If the energy of the photon is equal to or greater than the binding energy of an electron, energy can be transferred to the electron, striking it out of the shell. This is called **photoelectric effect or photoabsorption** which is predominant for X-ray energies below 50 keV. The photon is absorbed completely, while the so-called photo electron is emitted with kinetic energy E_{kin} equal to the difference between the original photon energy E_{ph} and the binding energy of the electron's former atomic shell E_{bind}:

$$E_{\text{kin}} = E_{\text{ph}} - E_{\text{bind}} \tag{2.18}$$

With rising photon energy, it is possible to strike out electrons with increasing binding energy. Hence, the photoelectric cross section, elsewhere decreasing continuously with energy, shows sharp discontinuities (edges) at each characteristic binding energy of an atomic shell (see fig. 2.7). These absorption edges have an extended fine structure, which will be discussed at the end of this section. (c) For light elements and high photon energies, an inelastic collision between photon and inner-shell electrons can occur. As the phase relationship between incident and emitted photon is lost, this mechanism is called **incoherent scattering (Compton scattering)** . The photon energy after the scattering process depends on the emission angle θ_C (see for example Lifshin, 1999) according to

$$\Delta\lambda = \frac{h}{m_e \cdot c}\left(1 - cos(2\theta_C)\right) \ . \tag{2.19}$$

The term $\frac{h}{m_e \cdot c}$ is called the Compton wavelength and is equal to λ_c = 2.43 × 10^{-12} m. The maximum energy difference between incident and emitted photon occurs for an emission angle of 180° with a maximum wavelength shift of twice the Compton wavelength.
The maximum kinetic energy E_e of the recoil electron, at a scattering angle of 180°, is then

$$E_\mathrm{e} = \frac{2E_\mathrm{ph}^2}{m_e c^2 + 2E_\mathrm{ph}} \ , \tag{2.20}$$

where E_ph is the initial photon energy and $m_e c^2$ (≈ 511 keV) the rest mass energy of the electron. As shown later, Compton scattering causes the so-called Compton continuum in X-ray spectra. The high-energy cutoff of this continuum, the Compton edge, is equal to the maximum energy transferred to the electron, as given by eq. 2.20.

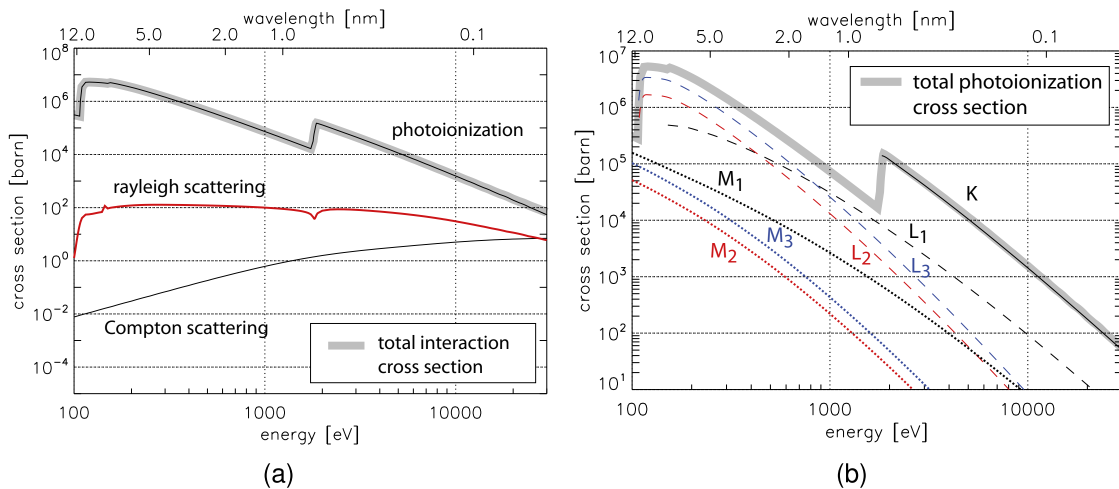

Figure 2.7.: Interaction cross sections for X-ray photons in silicon based on EPDL97 data (Cullen et al., 1997). (a) Photoabsorption, Rayleigh and Compton scattering. (b) Photoionization cross sections, depending on the original atomic shell of the emitted photoelectron. Only if the photon energy is higher than the respective binding energy, absorption in this shell is possible, leading to the so-called absorption edges.

The X-ray absorption properties of matter can be derived from the **atomic scattering factor** or **atomic form factor** f. This factor, multiplied with the amplitude scattered by a single free electron, gives the amplitude scattered by a particular atom (see Henke et al., 1993). The X-ray atomic scattering factor is calculated from the Fourier transform of the electron density distribution of an atom or ion, which can be derived from theoretical wave functions for free atoms (see for example Henke et al. (1982)). The atomic form factor f is a complex number,

$$f = f_1 + i f_2, \tag{2.21}$$

whose complex part defines the absorption properties of a material. The atomic absorption cross section σ_a, often expressed in barn (1 b = 10^{-28} m^2), can be derived from f_2 via (Gullikson, 2001a)

$$f_2 = \frac{\sigma_a}{2r_e\lambda} , \tag{2.22}$$

where r_e is the electronic radius and λ the radiation wave length. The atomic factors or cross sections for particular absorption processes are tabulated in literature (e.g. Perkins et al., 1991b) and, for silicon, shown in fig. 2.7. Similar to the description for optical light, the attenuation of X-ray radiation in matter can be calculated from the Lambert-Beer Law. In eq. 2.8, this relation is parameterized by the absorption coefficient α, whereas for X-ray radiation it is commonly expressed by the mass absorption coefficient μ and density ρ of a material:

$$I(z) = I_0 \cdot e^{-\mu\rho z} . \tag{2.23}$$

$I(z)/I_0$ is the relative fraction of photons transmitted through a material of thickness z. According to Gullikson (2001b), μ is connected to σ_a via

$$\mu = \frac{N_A}{M_A}\sigma_a. \tag{2.24}$$

Here, N_A is the Avogadro constant and M_A is the molar mass of the atoms. For material compounds containing x_i atoms of type i, the mass absorption coefficient can be derived from the constituents' atomic cross sections $\sigma_{a,i}$ through

$$\mu = \frac{N_A}{M}\sum_i x_i\sigma_{a,i} , \tag{2.25}$$

where the molar mass M of the compound is derived from the molar masses $M_{A,i}$ of the constituents' atoms according to $M = \sum_i x_i M_{A,i}$. Values for the atomic scattering factors of elements have been tabulated by Henke et al. (1993). This description is an approximation that neglects the interaction of atoms and is applicable for photon energies above 30 eV and far away from the absorption edges.

Around the absorption edges two basic features can be observed in photoabsorption cross sections of condensed matter:

1. **Absorption edge shift:** For free atoms, the binding energy refers to the energy necessary to release an electron to vacuum. Hence, it is given with reference to the vacuum energy level E_{vac}. In solids, an electron can be removed out of an inner shell as soon as it is lifted to the conduction band which exhibits free electron states. In the conduction band, it can take continuous values of kinetic energy and move quasi-free through the solid. Hence, the zero level for the binding energy in this context refers to the lower edge of the conduction band. This reduces the binding energy by some eV and furthermore depends on the chemical compound in which an element is found, leading to different properties depending on the solid being a semiconductor, metal or insulator. According to Sevier (1979), the physical state (e.g. gaseous or solid state), leads to a shift in electron binding energy of several eV. Whether a solid is in its elemental form or

	Silicon		Aluminum		Oxide	Nitride
	binding energies [eV]					
shell	atomic	condensed	atomic	condensed	molecular	molecular
K	1846	1839 ± 2	1567	1558	543	410
L_I	156	149 ± 2	126	118	32	25
L_{II}	107	100 ± 2	81	73	17	15
L_{III}	106	99	80	73	17	15
M_I	15.2		11			
M_{II}	8.2		6.0			

Table 2.3.: Binding energies for elemental silicon and aluminum in their atomic and condensed state as well as for oxide and nitride in molecular (gaseous) state (Sevier, 1979). The binding energies are given depending on the electron shell. The main shells L and M are split into subshells, depending on their quantum numbers (see also fig. 2.9).

chemically bound to other elements (e.g. oxidized state) is referred to as chemical state with energy shifts of up to 10 eV. In gaseous state, the chemical shift is only as large as ~ 2 eV. Table 2.3 contains the binding energies of silicon and aluminum in their atomic and condensed state as well as for oxide and nitride in atomic state taken from Sevier (1979). The specific K-shell binding energy of oxygen and nitrogen in silicon compounds can be determined from the measurement results shown in section 8.1.

2. **Absorption fine structure:** Measured absorption cross sections of solids exhibit an oscillatory fine structure around the absorption edges. The oscillations that extend in a region of about 30 eV to 40 eV beyond the absorption edge are called **X-Ray Absorption Near-Edge Structure (XANES)**. They are caused by multiple scattering of the excited photoelectrons. Beyond the XANES region, another oscillation structure extends for up to more than 100 eV above the edge, which is called **Extended X-Ray Absorption Fine Structure (EXAFS)**. A photoelectron emerges from its atom in the solid as a spherical wave. It is reflected by the atoms surrounding the ionized atom, which leads to a self-interference of the electron wave reflected back onto itself (Lifshin, 1999). The radial distribution function, a one dimensional projection of all of the bond distances in a crystal, can be obtained by the Fourier transformation of the EXAFS signal. Hence, EXAFS analysis is a powerful tool to analyze the structure of solids. As the oscillations are observed in the absorption coefficient of materials, they affect the quantum efficiency curves of solid state detectors (see section 8.1).

In addition to the interaction mechanisms of X-ray photons in matter, secondary particles and processes have to be taken into account. The relaxation of atoms is discussed in the next section, followed by the interaction process of electrons thereafter.

2.5. Atomic relaxation

An atom, excited by the photoelectric effect or Compton scattering process, exhibits at first a vacant electron state in one of the inner shells. The atom relaxes from this excited state as an electron from an outer shell fills the vacant electron position. The released energy can be emitted in two ways, by the emission of a fluorescence photon or an Auger electron.

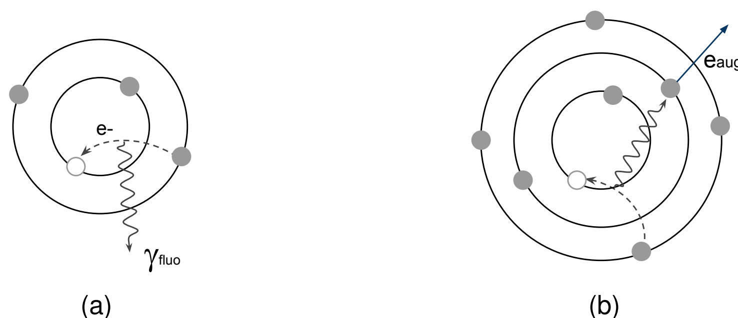

Figure 2.8.: Schematics of atomic relaxation processes, caused by a hole in one of the inner atomic shells: (a) fluorescence photon emission (b) Auger electron emission

The energy E_{fl} of a **fluorescence photon** is defined by the difference of the binding energies of the vacant electron state, $E_{bind,0}$, and the initial state, $E_{bind,1}$, of the electron that fills the vacancy:

$$E_{\mathrm{fl}} = E_{\mathrm{bind,0}} - E_{\mathrm{bind,1}} \tag{2.26}$$

Each material exhibits characteristic fluorescence energies, also called fluorescence lines. All fluorescence lines that are emitted by the filling of a K-shell vacancy are called K-lines. The according nomenclature applies for the other shells. Additionally, the fluorescence lines are denoted with sequential Greek letters depending on the initial shell of the electron transition (see fig. 2.9). For example, the transition of an electron from the L- to the K-shell causes the emission of a K_α-photon. The intensity of α-lines is higher than for the others, as the transitions between adjacent shells is most probable. The fine structure due to the splitting of the main shells into subshells is indicated by additional roman number indices in ascending order of the fluorescence photon energy, also shown in fig. 2.9. The ratio ω of the number of fluorescence photons produced to the number of vacancies created is called **fluorescence yield**. It denotes the probability of a radiative transition for a given atomic vacancy. Values for ω can be found in the Evaluated Atomic Data Library (EADL) by Perkins et al. (1991b), here listed in table 2.4a for the materials contained in the eROSITA entrance window. The fluorescence energies given in table 2.4a are calculated from the respective difference in binding energies of Sevier (1979) (as listed in table 2.3).

If the fluorescence photon is reabsorbed before leaving the atom, it causes the emission of an electron, the so-called **Auger electron**. Such a non-radiative transition, the Auger transition, leaves behind a doubly charged ion. For an Auger transition caused by a vacancy with binding energy $E_{\mathrm{bind,0}}$ the kinetic energy of the Auger electron E_{Auger} is determined by

$$E_{\mathrm{Auger}} = E_{\mathrm{bind,0}} - E_{\mathrm{bind,1}} - E_{\mathrm{bind,2}}. \tag{2.27}$$

Here, $E_{bind,1}$ is the initial binding energy of the cascading electron, which fills the vacancy with binding energy $E_{\mathrm{bind,0}}$ (see fig. 2.8b). The cascading electron transfers its energy to the Auger electron, which leaves its bound state of energy $E_{\mathrm{bind,2}}$. If a vacancy is filled by an electron of the same shell, the transition is called **Coster-Kronig transition**. The nomenclature for

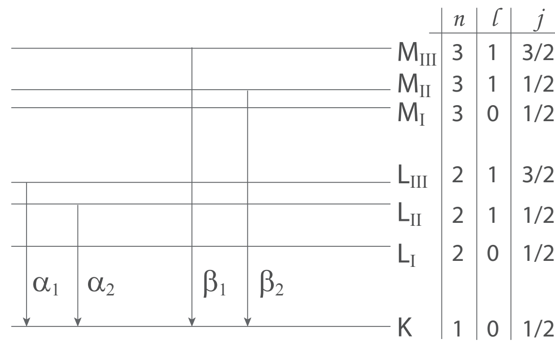

Figure 2.9.: Notation for X-ray fluorescence lines at the example of the K-lines. Greek letters denote the initial shell of the electron transition that causes the emission of a fluorescence photon. The fine structure between these lines is denoted by numbers in ascending order of the transition energy. The schematic shows only those transitions that are allowed by the selection rules (see for example Lifshin, 1999).

Radiative transitions		
transition	ω_X	E_{fluo} [eV]
K-shell vacancy		
N: $KL_{II,III}$	0.006	395
O: $KL_{II,III}$	0.003	526
Al: $KL_{II,III}$	0.0371	1485
Si: $KL_{II,III}$	0.0485	1739
L_I-shell vacancy		
Si: $L_IL_{II,III}$	4×10^{-4}	49
$L_{II,III}$-shell vacancy		
Si: $L_{II,III}M$	5×10^{-5}	100

(a)

Nonradiative transitions (only in silicon)		
transition	p_X(Y,Z)	E_{Auger} [keV]
K-shell vacancy		
KL_IL_I	0.07	1.54
$KL_IL_{II,III}$	0.24	1.59
$KL_{II,III}L_{II,III}$	0.57	1.64
$KL_{II,III}M$	0.05	1.74
L_I-shell vacancy		
$L_IL_{II,III}M_{I,II}$	0.97	0.05
$L_{II,III}$-shell vacancy		
$L_{II,III}MM$	1.00	0.1

(b)

Table 2.4.: The given probabilities p_X in both tables describe the transition probabilities in the case of an existing vacancy in a shell X. Only the most probable transitions are listed. (a) Radiative transitions: fluorescence probabilities and photon energies for the elements contained in the entrance window. (b) Nonradiative transitions: transition probabilities and kinetic energy of Auger electrons, limited to the most probable transitions.
Transition probabilities are taken from Perkins et al. (1991b) and transition energies calculated from the binding energies listed in table 2.3.

Auger electrons contains the denominator of the initial vacancy, followed by the denominators of the final two vacancies in order of decreasing binding energy. Auger electrons, similar to fluorescence photons, are observed at material specific energies. Silicon K-shell vacancies predominantly relax through non-radiative transitions with a probability of more than 95 %. The transition rates for the most probable Auger transitions and their respective electron energies in silicon are shown in table 2.4b. The given rates apply for the case of a vacancy in the respective shell.

2.6. Secondary electron interactions

The photon absorption and atomic relaxation process described up to now leads to secondary electron production inside the absorbing material. These electrons with kinetic energies up to several keV are strongly interacting with the solid. Starting with electrons of high energies (~ 0.1 keV to ~ 10 keV), three basic processes are dominant: scattering with atoms, scattering with electrons and the emission of Bremsstrahlung.
(a) When electrons scatter at atoms, the kinetic energy of the electron is practically unchanged due to the large mass difference between the electron and the atom, while the trajectory of the electron changes its direction. This process is therefore often called **electron backscattering** or **elastic scattering**. (b) In contrast to that, interaction with the inner shell electrons of the atoms is an inelastic process. It causes the **excitation** of an atom, or even its **ionization**, if the initial electron energy is high enough. The difference to photon absorption is that the scattering electron is usually not completely absorbed but looses a part of its energy. (c) The third of the above mentioned mechanisms is the emission of the so-called **Bremsstrahlung**. As every charged particle emits electromagnetic radiation during acceleration or deceleration, the deflection of electrons in the field of orbital electrons causes this kind of radiation. The cross section for the emission of Bremsstrahlung is much lower than for inelastic scattering, whereas the mean free path of the generated photons is much longer than for electrons in the keV energy regime. Interaction cross sections for the respective electron interaction mechanisms are shown in fig. 2.10a.

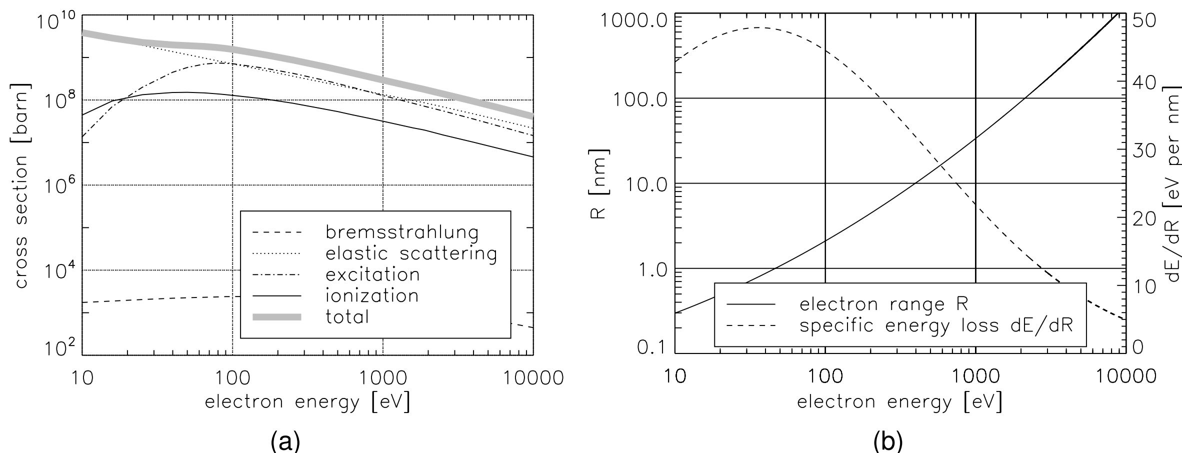

Figure 2.10.: (a) Interaction cross sections for electrons in silicon based on data from Perkins et al. (1991a); (b) Range and specific energy loss of electrons in silicon according to eq. 2.29 and eq. 2.30.

Electrons exhibit a distinctively larger probability for inelastic scattering in matter than photons of the same energy regime. The energy loss of electrons however is rather small for a single collision, whereas photons are completely absorbed in the photoelectric process. Thus, inelastic scattering of electrons is usually modeled by a continuous energy loss along the path, also called the **specific energy loss** or **linear stopping power** S:

$$S = -\frac{dE}{dx} \tag{2.28}$$

It is important to notice that the stopping power increases strongly with decreasing electron energy. Hence, electrons loose almost all of their kinetic energy in a very short path at the end of the stopping process.
The classical expression that describes the energy loss of charged particles in matter is the Bethe formula, which can be found for example in Knoll (1989). Based on this equation, several approximations describing the range and specific energy loss of electrons in matter can be found in literature. An approximation that is widely used is the formula by Iskef et al. (1983),

$$R_e = \frac{10 \cdot A}{Z \cdot \rho} \exp\left(a_0 + a_1 ln(E) + a_2 (ln(E))^2\right), \tag{2.29}$$

giving the range R_e of an electron of energy E. Iskef fitted the parameters a_0, a_1 and a_2 to extrapolated experimental data, resulting in $a_0 = -4.5467$, $a_1 = 0.311\,04$ and $a_2 = 0.077\,73$. R_e is given in nm, with A and Z as the mass and charge number of the material of density ρ in g/cm^2. The indicated standard error of this estimation is 25 %. The derivative of this equation results in the specific energy loss

$$\frac{dE}{dR_e} = \frac{E}{R_e\,(2a_2 \cdot ln(E) + a_1)}\,. \tag{2.30}$$

The resulting electron range and specific energy loss in silicon is shown in fig. 2.10b.

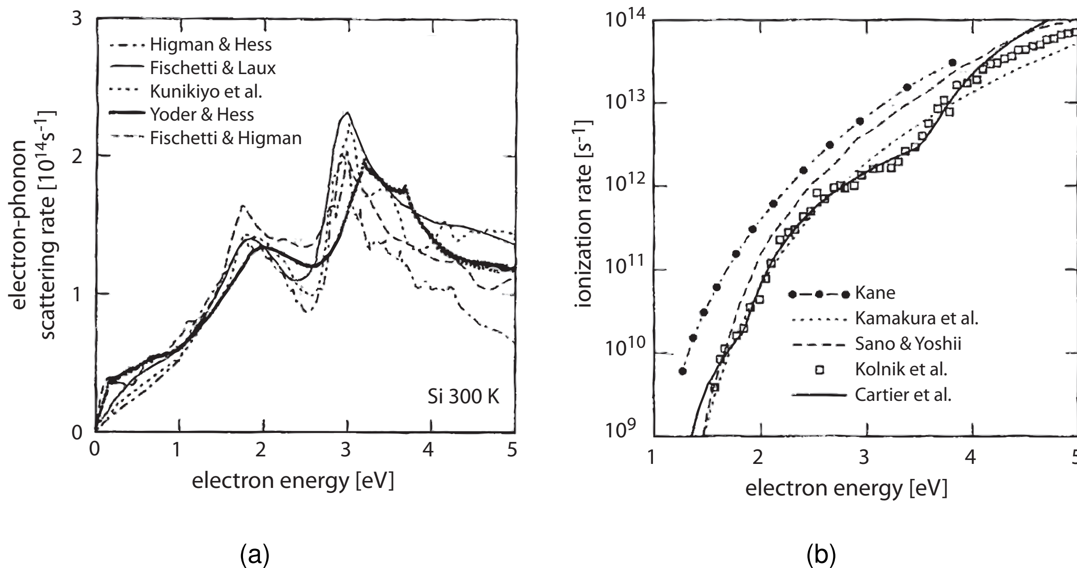

Figure 2.11.: Scattering rates (a) for electron - phonon scattering and (b) electron - electron (ionization) scattering. Figures are adapted from Fischetti et al. (1995). The different lines show different calculation methods. For all energies between 1.5 eV *and* 5 eV*, phonon scattering is more probable than ionization. This leads to short path lengths and to a mean electron-hole pair creation energy of more than the band gap energy.*

During their path through material, electrons loose their energy as described above until they reach an energy regime of ~ 10 eV to ~ 100 eV. The interactions of such low energy electrons

are especially important for semiconductor detectors. In this energy regime, the interaction probability increases strongly and leads to very short ranges. With regard to the eROSITA-PNCCD, electrons of such low energies released in outer layers of the blocking filter can not reach the sensitive volume and therefore the following considerations can be limited to silicon. In semiconductors, electrons with an energy greater than the band gap and up to ~ 10 eV are called hot electrons. At these energies, they are not only subject to **ionization scattering**, but also **phonon scattering**. The latter denotes the transfer of an electrons' kinetic energy to lattice vibrations, which are described by quasi-particles, called phonons. The scattering rates for phonon scattering and ionization are shown in fig. 2.11 (taken from Fischetti et al. (1995), see also Jungemann et al. (1996)).

As stated before, ionization scattering means the energy transfer to electrons in the valence band which are thereby lifted into the conduction band. For each of these transitions, a corresponding hole is created in the valence band. If the external electrical field is strong enough to separate the charge carriers in sufficiently short time, they are detected as charge signal in the CCD later. A photon entering the detector material produces electron-hole pairs until its initial kinetic energy has relaxed. The mean number $\bar{n}$ of generated electron-hole pairs during this so-called **thermalization** process is proportional to the initial photon energy E_{ph} and defined by the electron-hole **mean pair creation energy** w.

$$\bar{n} = \frac{E_{\text{ph}}}{w} \tag{2.31}$$

As the electrons are subject to phonon scattering, transferring a part of their energy to lattice vibrations, and hence to heat, the mean pair creation energy is significantly larger than the band gap energy. Furthermore, the thermalization process is of statistical nature and thus exhibits a variance in the number of created electron-hole pairs. This is of particular interest for spectroscopic semiconductor detectors, as this variance is directly connected to the energy resolution of the detector. If the creation of charge carriers strictly followed a Poisson process, the variance would be equal to the mean number of produced electron-hole pairs. In fact it is lower than that by a factor F, the **Fano factor** (Knoll, 1989).

$$F = \frac{\text{observed statistical variance}}{\text{Poisson variance}} = \frac{\text{observed statistical variance}}{E_{\text{ph}}/w} \tag{2.32}$$

The mean pair creation energy w and the Fano factor F, especially for silicon, was subject to various experimental and theoretical studies in the recent years. For photon energies from 50 eV to 1500 eV Scholze et al. (2000) listed a value of w = 3.66 $\pm$ 0.03 eV at room temperature. The temperature dependency according to Fraser et al. (1994) is

$$\frac{dw}{dT} = \frac{-0.01\%}{K} \; . \tag{2.33}$$

The PNCCD temperature during measurements is in the range between $-70\,°$C and $-80\,°$C. The corresponding value for the mean pair creation energy, w = 3.69 eV, is further used for calculations. The same value is used for EUV radiation, as there are no accurate values available in this energy regime. The mean pair creation energy for UV radiation below 6 eV and for visible light is derived from the number of created electrons per photon measured by

Hartmann et al. (2000).
The thermalization process occurs in a timescale of several picoseconds according to Klein (1968). The radius of the resulting Gaussian-distributed **charge cloud** is determined by the mean free path of low energy electrons. Lechner (1998) derived a formula of the energy dependent charge cloud radius after thermalization, assuming a spherical charge cloud with homogeneous charge distribution. The radius R_{th} after thermalization is

$$R_{\text{th}}(E) = R_0 + \beta \cdot E, \tag{2.34}$$

with an initial radius R_0 = 125 nm to 170 nm and a parameter β describing the increase of radius with energy. β is in the range of 0.023 nm /eV to 0.027 nm /eV. For the application of PNCCDs it is important to notice that the given charge cloud radius applies immediately after the thermalization process. Due to diffusion and electrostatic repulsion, the charge cloud expands strongly while drifting to the collection depth. After the drift, the 2σ-radius of the Gaussian charge distribution is approximately $R_{2\sigma}$ = 16 µm, containing 95 % of the charge (Kimmel, 2008).
After thermalization, the electrons of the electron-hole pairs that are formed in the silicon are transferred and read-out by the PNCCD electronics. Depending on the absorption depth, photon or electron loss can occur, leading to specific features in the resulting PNCCD spectra. The PNCCD detector concept as well as the properties of X-ray spectra obtained with this device are presented in the following chapter.

3. Radiation detection with PNCCDs

PNCCDs (charge-coupled devices) are used in various scientific fields, ranging from astronomical observations to experiments at synchrotrons and free electron lasers. Their properties regarding time-, energy- and spatial resolution make PNCCDs valuable measurement devices. PNCCDs were developed at the MPI Semiconductor Laboratory and are designed and manufactured there since the 1990ies (Meidinger et al., 2006b).
In this chapter, an overview on the basic working principle and the performance of a PNCCD is given. Special focus is drawn on those elements that have major influence on the spectral response of the detector. A short introduction on PNCCD spectra and the definition of various terms describing the detector performance with respect to the spectral response is presented thereafter.

3.1. The pn junction

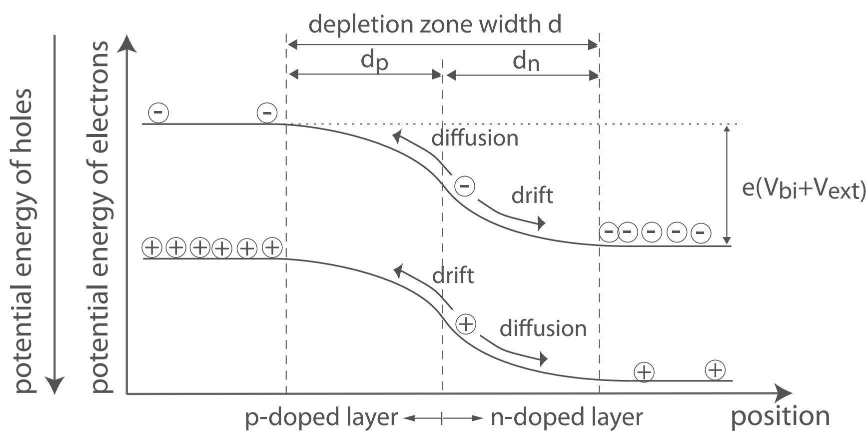

Figure 3.1.: Schematic of a semiconductor pn-junction. At thermal equilibrium, drift and diffusion currents over the junction result in a region depleted of charge carriers. In this depletion region, an electric field is formed by the remaining ionized donors and acceptors, leading to a potential barrier of V_{bi}, which can be enhanced or reduced by an externally applied voltage V_{ext}.

In a pure semiconductor, the number of charge carriers in the conduction band is defined by the intrinsic charge carrier density n_i. As every electron in the conduction band leaves a hole in the valence band, the intrinsic charge carrier densities of electrons and holes are equal. This balance can be changed by n- or p-doping, creating a majority of electrons or holes respectively in the material. Doping in silicon is often performed by the insertion of Phosphorus or Boron atoms, which have 5 and 3 valence electrons respectively, compared to 4 valence

electrons per silicon atom. When silicon is doped with Phosphorus, only four of the Phosphorus valence electrons contribute to the covalent bonds of the crystal, so one electron per dopant atom acts as majority charge carrier in the semiconductor (n-doping). Analogously, Boron doping causes holes as majority carriers in the material (p-doping).
One of the most common structures in semiconductor electronic devices is the pn-junction, extensively treated in literature on semiconductor physics, for example in the book of Sze (1981). It is formed by bringing a p-doped layer in direct contact with an n-doped layer. Electrons, the majority charge carriers in the n-doped region, diffuse into the p region and leave positively charged donor ions behind. Similarly, holes near the p-n interface diffuse into the n-type region leaving fixed acceptor ions with negative charge. An electric field counteracting the diffusion process forms around these ionized atoms. The resulting **space charge region**, also called **depletion zone**, is free of charge carriers, except for a small number that is continuously thermally generated. The electric field inside the depletion zone leads to a difference of potential between both parts of the pn-junction, the **built-in potential** V_{bi}. In equilibrium state V_{bi} can be expressed by

$$V_{bi} = \frac{k_B T}{e} \ln \left(\frac{N_D N_A}{n_i^2} \right), \tag{3.1}$$

assuming a donor concentration of N_D and an acceptor concentration of N_A in the n-doped, respectively the p-doped region. e is the electron charge, k_B the Boltzmann constant, T the temperature in Kelvin and n_i the intrinsic carrier density. The potential difference V_{bi} leads to band bending as shown in fig. 3.1, which can be enhanced or reduced by an externally applied voltage V_{ext}.
A pn-junction inside a circuit operates as a diode, allowing current to flow in one direction and blocking it in the other. For an unbiased diode, the diffusion current is compensated by the drift current in the electric field region, leading to an equilibrium state with zero net current flow. If an external voltage $V_{ext} < 0$ is applied, a more negative voltage at the n-contact with respect to the p-contact, majority carriers are swept into the depletion zone from both sides. Thus its width is reduced and the potential barrier is lowered. Only those carriers that are thermally generated inside the depletion region or the minority carriers in a distance of a diffusion length around it can contribute to the drift current. Hence the diffusion current increases, while the reversely directed drift current through the depletion region is limited by the number of minority carriers. Accordingly, the diffusion current dominates the net carrier flow and leads to a significant current flow in direction of the forward bias. When applying a reverse voltage $V_{ext} > 0$, the majority carriers are pulled away from the junction, enlarging the space-charge region and the voltage drop at the junction. The diffusion current is reduced and the drift current is still limited by the number of available minority charge carriers. Hence, the reverse current increases only slowly with the size of the depleted volume, and therefore the number of therein generated charge carriers. The reverse current of a pn-junction diode is much lower than the forward current, in most cases negligible, up to field strengths where the diode breaks down.
For PNCCD applications, the pn-junction is operated with reverse bias. The width d of the depletion layer, depending on the doping concentrations and an external reverse voltage $V_{ext} \geq 0$ is

$$d = \sqrt{\frac{2\varepsilon}{e} \left(\frac{N_A + N_D}{N_A \cdot N_D} \right) \cdot (V_{bi} + V_{ext})}, \tag{3.2}$$

with ε being the permittivity of the semiconductor. The width d of the depletion zone comprises of the widths d_n and d_p of the n- and p-doped region. These widths are connected through

$$N_A \cdot d_n = N_D \cdot d_p \,. \tag{3.3}$$

A pn-junction of strongly p-doped material (often called p$^+$-doped) and weakly n-doped material is hence enlarged in the n-region and only narrow in the p-region.

A pn-junction can be used as photodetector. The absorption of photons causes the creation of electron-hole pairs in silicon. Each electron-hole pair that is generated in the depleted region of a pn-junction is separated by the electric field and the electrons, respectively the holes, drift to the n- or p-contact. The photocurrent between n- and p-contact is a measure for the absorbed energy. Based on the concept of a pn-junction, the PNCCD designed to measure precisely the energy of X-ray photons.

3.2. PNCCD detector concept

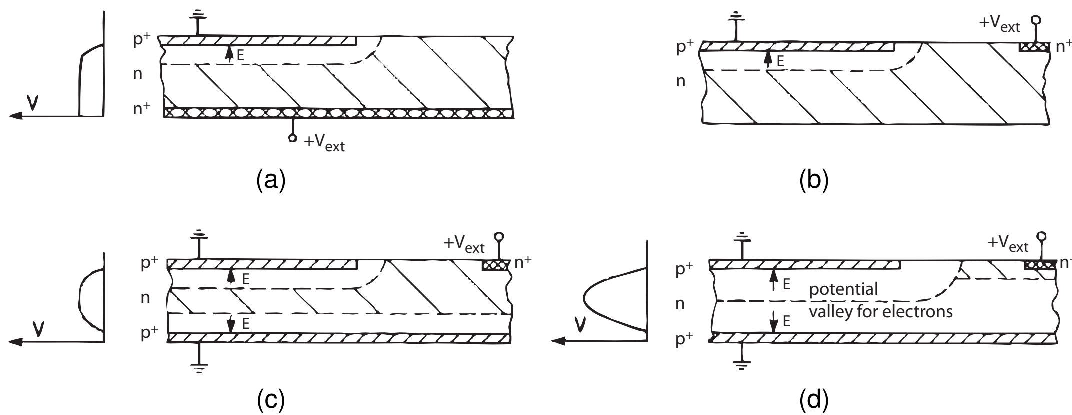

Figure 3.2.: Basic structures leading to sidewards depletion (taken from Lutz (1999)). (a) partially depleted diode ; (b) diode with depletion from the side; (c) double diode partially depleted; (d) double diode completely depleted

PNCCDs are used to detect X-ray photons and resolve their energy by the amount of created charge in a depleted silicon volume. In contrast to the simple pn-structure discussed up to now, PNCCDs use the principle of **sidewards depletion** in order to fully deplete the detector and hence to maximize the sensitive volume. A schematic of this method is shown in fig. 3.2. Starting from a typical pn-structure (a), the n$^+$-contact is situated at the side of the detector (b). At the front and back side of an n-doped wafer are p-doped layers, from where two depletion regions extend into the bulk (c). Finally, for high enough reverse bias, both regions join, so that the whole volume is depleted (d). Inside this bulk, a potential minimum for electrons forms. Here the generated electrons accumulate while the holes drift to the p-contacts. In the following discussion, the back side of a PNCCD denotes the side where the photons enter the silicon. By applying a more negative voltage U_{dep} between the back side and n-contact than between the front side and n-contact, the potential minimum is shifted to the front side. For

standard operating voltages of the eROSITA PNCCD it is formed at $\approx 7\,\mu m$ from the front side, fixed by an additional high energy phosphorus implant in this depth.

In addition to the described pn-structure, a PNCCD exhibits a pixel structure. A simplified schematic of the doping profiles inside one pixel is displayed in fig. 3.3. The front side contact is structured into stripes, forming the so-called register p^+-implants. The registers are used to separate and shift the collected charge to the readout anode by applying a sequence of external voltages. In transfer direction, perpendicular to the register structures, the so-called channel guides and channel stops are integrated inside the silicon bulk. These n- and p-doped regions form potential wells and barriers for the collected electrons. Hence, an electron is confined inside a pixel by the external register voltages and the potential well of the channel guides. A PNCCD with a pixel size of $75\,\mu m$ allows a spatial resolution of down to $\approx 2\,\mu m$ by means of an elaborate data analysis (Kimmel, 2008). By periodically altering the register voltages ϕ_1, ϕ_2 and ϕ_3, the charge packages inside the pixels can be simultaneously transferred along a channel without being mixed. At the end of each channel, the charge is shifted to a **readout anode**. It is connected to the gate of a monolithically integrated JFET (junction gate field-effect transistor) acting as first amplification stage, the so-called **'first FET'**. This structure, together with further signal processing, is described in detail in the next section.

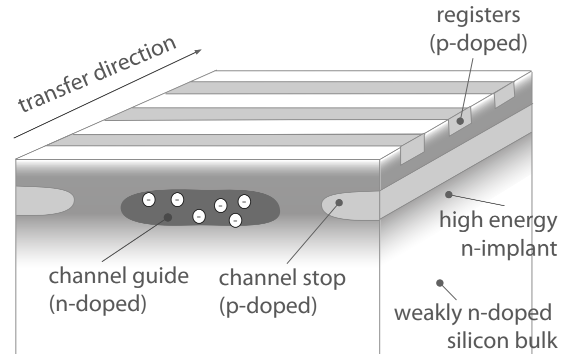

Figure 3.3.: Cross section of one pixel in the silicon bulk. The channel stops confine the charge inside one channel. At the registers a sequence of voltage pulses is applied to confine and shift the charge along a channel.

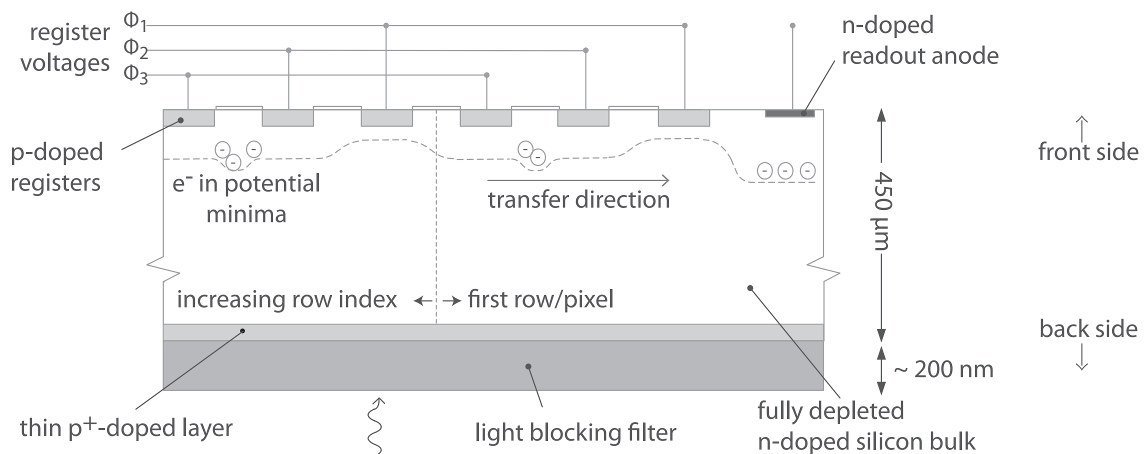

Figure 3.4.: Schematic of a PNCCD, displayed as a cross section alongside of one channel. By sequentially changing the electric potential of the register contacts, the charge of each pixel is shifted separately to the readout anode. Schematic is not true to scale.

The charge transfer process is illustrated in fig. 3.4, a schematic cross section along one PNCCD channel. Two register contacts of each pixel are biased with a less negative voltage,

forming the potential minimum. One register contact per pixel is biased with a more negative voltage, forming the potential barrier that separates two pixels of one channel. Sequentially, the potential of the registers is changed so that the charge carriers are transferred to the readout structure. The p-doped layer on the detector back side is only tens of nanometers thick and covered with nonsensitive layers to accomplish a light blocking filter. This part on the back side of the detector is called the entrance window, further described in section 3.4.
During the charge shift along a channel, impurities in the silicon can lead to trapping of charge carriers. Although the PNCCD is built from ultra-pure silicon, a small amount of charge loss can not be avoided. A parameter that quantifies the relative charge loss per pixel transfer is the **charge transfer inefficiency (CTI)**, with typical values in the range of CTI = 10^{-5} to 10^{-7}. A detailed description of the PNCCD pixel structure and the electric fields inside the PNCCD bulk can be found in the dissertation of Kimmel (2008).

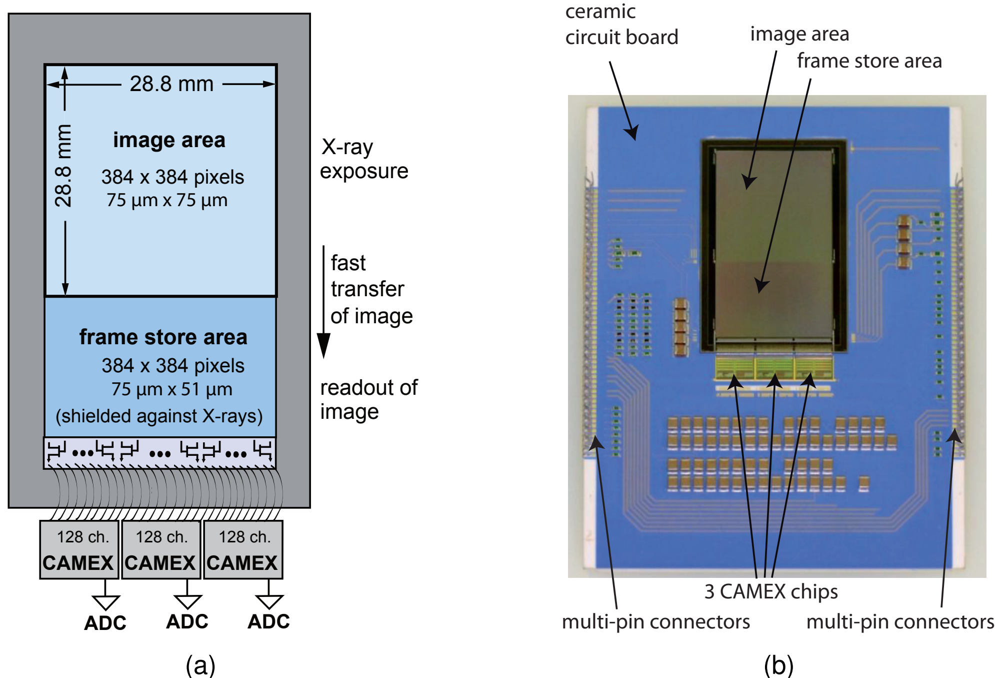

Figure 3.5.: Schematic from Meidinger et al. (2011) (left side) and photograph (right side) of an eROSITA PNCCD mounted on a ceramic board as used in the laboratory. The PNCCD is separated into image and frame store area. At the end of each channel, a bond wire connects the source of the first FET to the respective channel of a CAMEX chip.

Figure 3.5 shows a schematic and a photographic image of an eROSITA PNCCD on a ceramic circuit board, with charge transfer direction pointing downwards. It is a frame store (frame transfer) PNCCD, divided into an image- and a frame store area. The frame store CCD was developed to reduce the disturbing effect of photon counts during the readout phase. If a photon enters the detector during the shift of the charge to the readout structure, it is assigned to the wrong row coordinate, forming a so-called **out-of-time event**. As the charge shift itself can be performed much faster than the readout, the concept of the frame-store PNCCD was introduced. For each frame cycle, the charge is quickly shifted from the image to the frame store area and then slowly shifted to the readout anodes. Out-of-time events during the slow shift are prevented by a shielding of the frame store area against X-rays. Both areas exhibit

separate register contacts, so that charge shift can be performed in one or the other area independently. The time consumed for the complete shift and readout of one frame is further denoted the **shift time** t_{shift} and **readout time** t_{read} respectively. The **cycle time** t_{cyc} defines the period between two complete readout processes. It can be chosen arbitrarily but not shorter than the readout and shift time. An image recorded with the PNCCD in one cycle time is called a **frame**.

The pixels in the image and frame store area of eROSITA PNCCDs are $75\,\mu\text{m} \times 75\,\mu\text{m}$ and $51\,\mu\text{m} \times 75\,\mu\text{m}$ large. Each area comprises 384×384 pixels. In frame store mode, the time for the shift of one row for eROSITA PNCCDs amounts to 300 ns, leading to $t_{\text{shift}} \approx 0.1\,\text{ms}$. The readout of one row takes approximately $23\,\mu\text{s}$, hence $t_{\text{read}} \approx 9\,\text{ms}$. Using these standard timing settings, the minimum cycle time for an eROSITA PNCCD is therefore 9 ms.

The PNCCD in fig. 3.5 is mounted on a ceramic circuit board, together with 3 readout chips called **CAMEX (CMOS Amplifier and MultiplEXer)** ASICs (application-specific integrated circuit), each capable to read out 128 channels in parallel.

3.3. Readout electronics

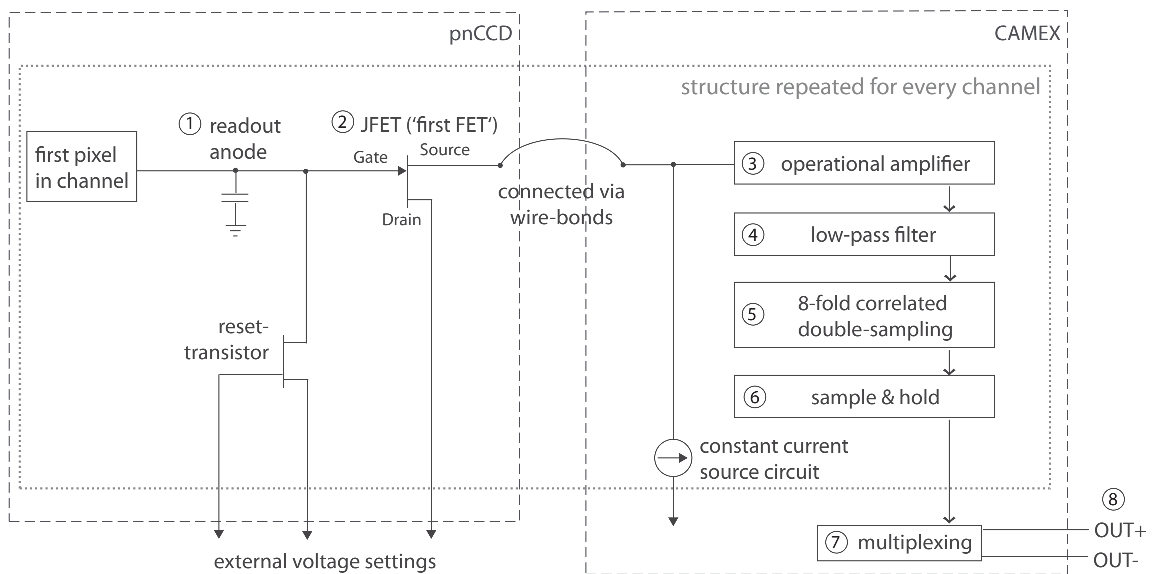

Figure 3.6.: Schematic of the readout structure of a PNCCD. The picture shows the amplification at the first FET and the amplification and filtering of the CAMEX as described in the text.

In the last section, fig. 3.4 illustrated the shift of charges to the readout anode, realized by an n-implant at the end of each PNCCD channel. Connected to the readout anode and monolithically integrated on the PNCCD is a JFET, the first-FET. Those two devices are indicated by the numbers **(1)** and **(2)** in fig. 3.6, which illustrates the readout and amplification process for eROSITA PNCCDs. Integrating the first FET on the PNCCD reduces the effective capacitance of the structure formed by readout anode and first-FET gate, indicated by the equivalent capacitance in the schematic. With lower anode capacitance, a given charge on the anode translates into a higher voltage step of the first-FET gate and hence to a better signal-to-noise ratio. As the first FET is directly adjacent to the anode, this capacitance is kept small and leads

to a high voltage signal even for low charge amounts. The first-FET is operated in source follower mode (see for example Horowitz & Hill, 1989), and serves as impedance converter for later amplification. For this purpose, a constant source-drain current through the first FET is driven by a circuit integrated in the CAMEX. All PNCCD and CAMEX structures surrounded by the dotted box in the schematic are implemented 128-fold (one for each channel). The first-FET source voltage is further processed by the CAMEX. The difference in voltage amplitude with and without signal is amplified by an operating amplifier **(3)** and delivered to a passive low-pass filter **(4)**. The resulting voltage is applied to 8 capacitances **(5)**, of which each is sampled successively. This so-called 8-fold correlated double sampling reduces readout noise by sampling the same signal 8 times. The sampled signal is again amplified using an operational amplifier. Three switchable capacitances are part of the amplifier circuit. Hence the amplification factor, also called gain, can be chosen and adapted during operation through programmable registers of the CAMEX ASIC. Employing a sample and hold stage **(6)** after the 8-fold correlated double sampling circuit, the readout of the subsequent row can already be performed, while the multiplexer **(7)** processes the current row. The multiplexer forwards the signals of all 128 channels sequentially onto a differential output buffer **(8)**. This output is connected to the ADCs, which convert the analog to digital signals (see for example Herrmann et al., 2008).
One commonly used value to express the performance of a system is the so-called Equivalent Noise Charge (ENC). It transforms the noise signal into a corresponding number of signal electrons. The PNCCD and CAMEX system exhibits an electronic noise level of 2.5 electrons rms (root mean square). The noise level, also called read noise, can be determined during a measurement with zero illumination. It is for example caused by thermally generated electrons in the silicon bulk or voltage and current noise in the electronic circuits of the CAMEX.
In the case of very high radiation intensities, high amounts of charge are shifted onto the readout anode. To avoid a potential shift and nonlinear amplification of the analog signal, the so-called reset transistor is connected to the anode (see fig. 3.6). By applying a voltage pulse to the reset gate contact a conductive channel is created and the anode can be discharged. If the reset pulse is applied after the complete readout of each frame, it is further called **frame-wise reset**. If the reset pulse is applied after the readout of each row, this operation mode is referred to as **row-wise reset**. Naturally, during the row-wise reset it is possible to measure even higher amounts of charge than in the frame-wise reset mode. However, the readout noise is increased by pulsing the reset gate. The reset current, located close to the silicon surface, presumably leads to the caption of electrons in interface traps. These trapped electrons are released from the interface traps and cause an additional, statistically fluctuating, signal during the readout. In row-wise reset mode, the mean noise is about 5.5 electrons rms (ENC).

3.4. The detector entrance window

As presented in section 1.2, the eROSITA PNCCDs are equipped with an on-chip optical blocking filter, consisting of several thin layers of material on the detector back side. Together with the first few hundreds of nanometers of the silicon volume, which exhibit specific properties regarding the charge collection, they form the detector **entrance window**. The composition of the entrance window is a trade-off between X-ray quantum efficiency, blocking properties and technological feasibility.
The composition of the eROSITA entrance window including the on-chip filter is illustrated in fig. 3.7. Directly on the silicon, a 30 nm layer of amorphous SiO_2 is grown thermally by heating

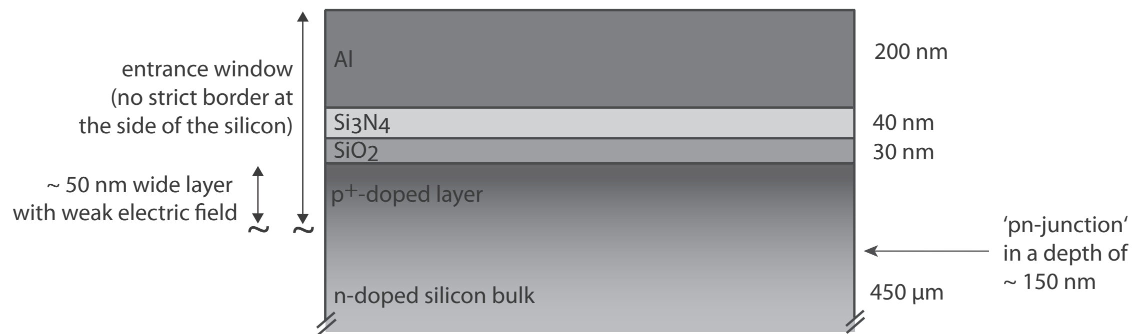

Figure 3.7.: The eROSITA entrance window consists of Al, SiO_2 and Si_3N_4 layers on top of the p^+-doped region on the back side of the PNCCD. The first few hundreds of nanometers of the silicon are affected by incomplete charge collection.

the wafer in an oxygen atmosphere. A 40 nm layer of Si_3N_4 is deposited on top of the silicon dioxide. Then, 200 nm of aluminum are sputtered onto the silicon nitride. The adhesion of the aluminum layer is improved by adding a fraction of approximately 1% of silicon into the aluminum sputtering target.

The properties of the **silicon-SiO_2 interface** have major impact on the X-ray response of PNCCDs. Here, so-called trivalent silicon centers (P_b centers) with an open (dangling) bond form at the interface. Such trivalent centers cause traps inside the band gap of silicon (Poindexter & Caplan, 1983), leading to an increased recombination rate of electrons and holes. Furthermore, trivalent silicon centers cause fixed oxide charges at the interface. The number of dangling bonds depends on the crystal orientation of silicon with respect to the silicon-SiO_2 surface. For example the surface of a <111> silicon wafer exhibits a higher number of open bonds than <100> silicon. In order to reduce partial charge loss through recombination at the Si-SiO_2 interface, the eROSITA PNCCDs are fabricated on silicon wafers with <100> crystal orientation (see also Lutz, 1999).
Besides the silicon material, the doping profile of the **p$+$ layer** has impact on the amount of partial charge loss. The depletion zone does not end abruptly, but ends in a region with weak electric field. A weak electric field leads to a slower charge collection process, so that a part of the charge carriers recombine prior to their separation. The size of this region with reduced electric field can be reduced by an optimized doping profile, but cannot be fully avoided. eROSITA PNCCDs are manufactured with an ultra-thin p^+-layer at the entrance window side. Through the optimized doping profile, the depletion zone reaches the detector back side up to a distance of only ~ 50 nm, as shown in fig. 3.7.
The quality of the entrance window is especially important for the spectral response at low X-ray energies, as photons with low energies (below ≈ 500 eV) are mainly absorbed in the first few hundred nanometers of silicon.

Charge loss due to the described mechanisms can be described by a **charge collection efficiency (CCE)**, a parameterized function specific for the entrance window of a detector. The layer where the CCE is smaller than unity is called **ICC layer** (incomplete charge collection). For absorption far away from the entrance window (several hundreds of nm), the CCE approaches 1.

Partial charge loss, the transport of electrons and the generation of photons in the vicinity of the entrance window cause characteristic features in PNCCD spectra. These features and the general properties of a PNCCD spectrum are described in the following section.

3.5. The PNCCD spectrum

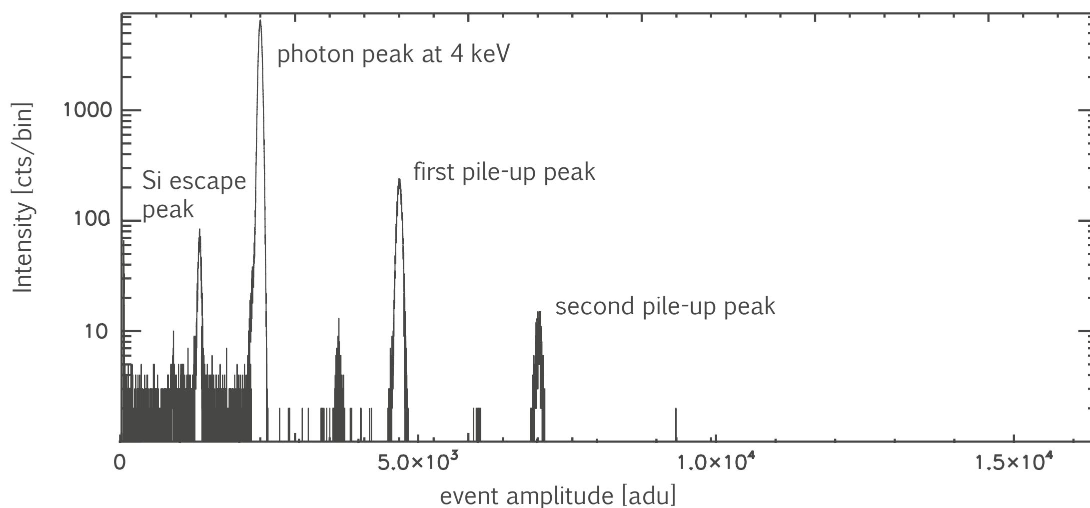

Figure 3.8.: Example for a spectrum taken with a PNCCD at a photon energy of 4 keV*. It shows the distribution of detector counts sorted by their energy, measured in arbitrary digital units.*

A PNCCD X-ray spectrum, as shown in fig. 3.8, is a histogram of photon counts versus photon energy. In order to get such a spectrum, the data measured with X-ray PNCCDs have to be processed. Pixel signals that are above a lower threshold are extracted, thus noise excesses are discarded. In order to account correctly for photon events that have spread over a cluster of pixels, neighboring pixels above the threshold are summed up to one event cluster, further called **event**. After this procedure and several corrections, described in chapter 6, all events are sorted into bins according to their signal amplitude. If enough data is accumulated, a spectrum as shown in fig. 3.8 is formed. The event amplitudes, further denoted by ϵ, are given in arbitrary digital units (adu) or in energy units after calibration with the photon energy. A monochromatic spectrum exhibits a Gaussian peak at the photon energy and **pile-up peaks** at multiples of this energy, caused by several photons hitting the same event cluster within one frame. Furthermore, the so-called silicon escape peak is visible in fig. 3.8. Its origin can be explained by the absorption and charge conversion process inside the detector, as described in the following section.

3.5.1. Features in PNCCD spectra

A closer look to the PNCCD spectrum shows that the shape of a photon peak deviates from a pure Gaussian shape. Figure 3.9 shows a calibrated, normalized spectrum recorded with 3 keV photons. At this level of detail, several features in the X-ray spectrum become apparent.

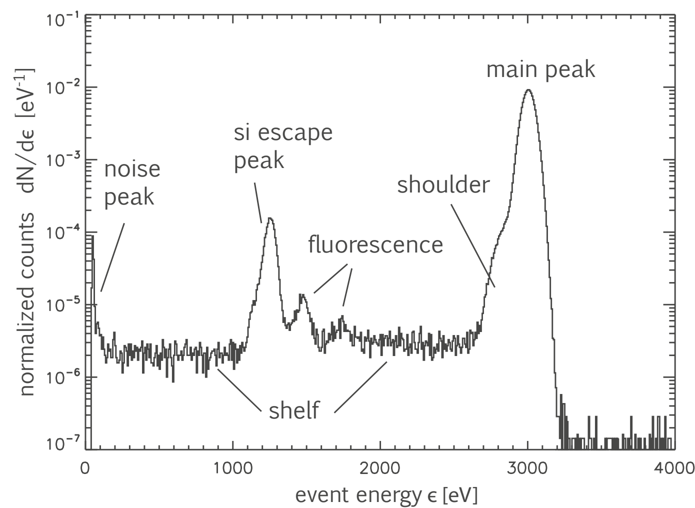

Figure 3.9.: Calibrated and normalized spectrum recorded with 3 keV photons. A typical X-ray spectrum shows the main peak and additional off-peak features, as fluorescence peaks and the flat shelf. The main peak exhibits a low energy shoulder caused by charge loss in the entrance window. As the peak-to-valley ratio is as high as 5000, the off-peak features are emphasized by the logarithmic scale for better visibility.

For the analysis of an X-ray spectrum it is important to understand and quantify the distribution of these features. Starting at high energies, the observed features in such a spectrum are the following:

- **Main peak:** Most photons absorbed in the detector cause entries in the main peak of the spectrum. The following properties of the main peak are important:
  - The peak position, ideally centered at the photon energy
  - The peak width, which is mainly a function of readout and Fano noise
  - The peak shape, which is approximately Gaussian with a more or less distinct shoulder at the low-energy side of the main peak

  Partial charge loss in the first hundred nanometers of the silicon, where the charge collection efficiency is smaller than 1, can cause a shift and distortion of the main peak. As described later, further influence on the main peak is for example possible by nonlinear amplification, charge transfer loss and event detection by data analysis.

- **Shelf:** Between zero and the photon energy, a flat shelf extends over the spectrum. It is usually by orders of magnitudes lower than the main peak. The flat shelf is caused by electron transport into or out of the sensitive volume, leading to an energy deposit inside the sensitive volume of less than the photon energy. Electron transport causes entries in the spectrum in a continuous energy range between zero and the main peak, as electron energy loss in matter is a continuous process. A step-like structure in the shelf may be observed at some photon energies, caused by photo- and Auger electrons, which have distinct energies, escaping the sensitive volume.

- **Fluorescence peaks:** Fluorescence photons that are generated outside the sensitive volume, may traverse the distance into the sensitive volume and be detected as an event in the spectrum. They cause the so-called fluorescence peaks. In the case of eROSITA, aluminum and silicon fluorescence is observed, caused in the outer layers of the entrance window.
- **Escape peak:** Fluorescence photons generated inside the silicon may traverse the distance out of the sensitive volume, leading to events with an energy reduced by the fluorescence photon energy. These events form the escape peak, which is often one of the most prominent off-peak features in semiconductor detectors.
- **Compton edge:** At X-ray energies above several keV, Compton scattering of photons leads to the Compton spectrum superimposed on the flat shelf (not visible for a photon energy as low as 3 keV). Photons that are backscattered at atomic electrons loose a part of their energy to the respective electron. If this process occurs close to the entrance window, the photon can leave the sensitive volume, causing an event in the spectrum that matches the amount of energy transferred to the electron.
- **Noise peak:** As the readout signal of a detector is affected by noise, some pixel signals can be significantly above zero without being generated by an X-ray photon. If such noise fluctuations are above the event detection threshold, they are displayed in the resulting spectrum. The noise peak forms at zero energy, but is cut by the event detection threshold.

The spectrum entries that are outside the main peak are called **off-peak events**. They are unwanted features in PNCCD data, as the assignment of these events to their origin is often difficult. A thorough characterization of the detector enables a more accurate analysis and interpretation of the astronomical data taken with the detector. This characterization comprises several detector properties that are summarized in the next section.

3.5.2. The instrumental response function

The instrumental response function, also called response or spectral response function, relates the incident spectral flux to the observed spectrum of an X-ray detector. This parameter includes two properties that will be discussed separately in this work, the spectral redistribution function and the detection efficiency.

The **spectral redistribution function** describes the distribution of events in a monochromatic photon spectrum, such as shown in the last section. The spectral redistribution function $f_{\text{redist,E}}(\epsilon)$ gives the number of counts dN per event energy bin $d\epsilon$ in a spectrum caused by photons with energy E:

$$f_{\text{redist,E}}(\epsilon) = \frac{dN}{d\epsilon} \tag{3.4}$$

For better comparability, $f_{\text{redist,E}}(\epsilon)$ between zero and an energy ϵ_0 above the main peak is often normalized to unity:

$$\int_0^{\epsilon_0} f_{\text{redist,E}}(\epsilon)\ d\epsilon = 1 \tag{3.5}$$

The discussion of the spectral features in the last section shows that the spectral redistribution function cannot be described by a simple analytic expression. However, it can be approximated by analytical models or simulations.

The **detection efficiency** of radiation detectors, denoting the fraction of detected to incident photons, is quantified in various ways, depending on the measurement device and the photon energy range. In this work, the parameter quantum efficiency (for PNCCD X-ray properties), attenuation factor (for optical and UV properties) and responsivity (for diodes and PNCCDs as integrating device) are used.
The **quantum efficiency** denotes the quotient of the photon count rate ν_{ph} and the incident photon flux φ according to

$$QE = \frac{\nu_{\text{ph}}}{\varphi}\ . \tag{3.6}$$

Here, both φ and ν_{ph} are in units of [s^{-1}], describing a number of photons per second. In order to avoid confusion, in this work the term quantum efficiency will only be applied to X-ray photon energies, where single photon resolution is possible.

The term **spectral responsivity** SR, also called **photoyield** or **responsivity**, is a measure for the electrical output per optical input of photodiodes. It is defined by the ratio of the generated photocurrent I_{photo} to the incident radiant power P_{in},

$$SR = \frac{I_{\text{photo}}}{P_{\text{in}}}\ , \tag{3.7}$$

and usually given in [$\text{A}\,\text{W}^{-1}$] or [$\text{C}\,\text{J}^{-1}$]. When applying the term of responsivity to PNCCDs, the photocurrent can be expressed by the number of created electron-hole pairs ν_{e} and the elementary charge e. A responsivity for PNCCDs can hence be given by

$$SR = \frac{\nu_{\text{e}} \cdot e}{P_{\text{in}}}\ . \tag{3.8}$$

Especially for low photon energies below 50 eV, where single photon counting is not possible with a PNCCD, it is appropriate to use SR instead of the QE to describe the detection efficiency. For X-ray photons, the quantum efficiency can be derived from responsivity measurements as shown in section 5.4.

The **attenuation factor** χ characterizes the properties of the PNCCD regarding visible and UV light. χ is the quotient of incident photons to detected photons and is in fact the inverse of the quantum efficiency. As it is only used in the low photon energy regime, it is derived from the responsivity SR:

$$\chi = \frac{e}{SR \cdot w} \tag{3.9}$$

In many scientific contributions, the characteristic parameter to describe a light blocking filter is its transmittance. In the case of eROSITA PNCCDs, filter and detector are in one piece. Hence the filter transmittance and detector quantum efficiency are subsumed in one parameter, the attenuation factor.

3.5.3. Photon counting statistics

PNCCD spectra are formed by counting and sorting signals according to their event amplitude. In order to evaluate such data, statistical methods are useful. The most important relations are summarized in the following.
The main peak of a monochromatic spectrum, located at the photon energy E_{ph}, is of nearly Gaussian shape. The width, or standard deviation, σ of the Gaussian is determined by several, independent noise contributions on the signal. It can hence be approximated by the square-root sum of the standard deviations of all contributions (Knoll, 1989) according to

$$\sigma^2 = \frac{1}{N} \sum_{i=1}^{N} \sigma_i^2 \tag{3.10}$$

In the case of semiconductor X-ray detectors, the main impact on peak width is given by Fano noise and readout noise. Derived from the definition of the Fano factor in eq. 2.32, the Fano noise σ_{Fano} in eV at a given photon energy E_{ph} is

$$\sigma_{\mathrm{Fano}} = \sqrt{w \cdot F \cdot E_{\mathrm{ph}}}\,. \tag{3.11}$$

The readout noise of PNCCDs is approximately 2 to 3 electrons rms (ENC), depending on the amplification factor. The resulting peak width is usually expressed by the **full width at half maximum value (FWHM)**, describing the corresponding peak width at 50 % peak height.

The quality of an X-ray spectrum depends also on the number of photon counts. With increasing number of photons in an energy bin, the deviation from the expected mean value decreases. This deviation can be derived from Poisson statistic (Knoll, 1989). For a given mean number of photons in an energy interval in the measurement time, the standard deviation σ of the detected number of photons is

$$\sigma = \sqrt{n}\,. \tag{3.12}$$

The relative deviation σ_{rel} of the number of entries in a bin from the expected value is hence

$$\sigma_{\mathrm{rel}} = \frac{\sqrt{n}}{n} = \frac{1}{\sqrt{n}}\,. \tag{3.13}$$

An upper limit for the photon rate is given by the rising number of pile-up events. If pile-up occurs due to two or more photons hitting the same pixel during one cycle time, it is called **event pile-up**. The probability $P(n > 1)$ for event pile-up of the order n or larger for a photon count rate per pixel $\nu_{\mathrm{ph,\,pix}}$ and a cycle time t_{cyc} is

$$P(n > 1) = 1 - e^{-\nu_{\text{ph, pix}} t_{\text{cyc}}} \,, \tag{3.14}$$

as for example given in Knoll (1989). **Pattern pile-up** occurs if two or more adjacent photon events are combined to one event cluster by the event recombination algorithm. The probability for pattern pile-up is higher than given in eq. 3.14 and can be estimated by simulations.
For low X-ray photon energies, pile-up peaks merge with the main peak, leading to a distortion of the spectrum. At high X-ray photon energies, where the pile-up peaks are clearly separated, pattern pile-up still leads to a reduction of the count rate. A trade-off between high photon count rate and low pile-up rate is desirable, often limited by constraints of the experimental setup.

4. Radiation sources

In order to determine the PNCCD detector response, various measurements were performed. Different kinds of radiation sources were used for this purpose, depending on the particular demands of each experiment. While the optical measurements required a high flux in order to overcome the high attenuation of the on-chip filter, the photon flux of X-ray measurements had to be low in order to resolve single photons on the PNCCD. The applied radiation sources for the analysis of the eROSITA entrance window at the MPI Semiconductor laboratory were light emitting diodes and laser diodes for visible light, and an X-ray tube and a radioactive fluorescence source for X-ray radiation. A great part of the measurements has been conducted at the synchrotrons BESSY II (Berliner Elektronenspeicherring-Gesellschaft für Synchrotronstrahlung) and MLS (Metrology Light Source) in Berlin. These synchrotrons provide radiation in the range from near ultraviolet to hard X-ray radiation. All these types of radiation sources are introduced in this chapter in order to give a basic knowledge on their working principle.

4.1. LEDs and laser diodes

LEDs (light emitting diodes) are semiconductor light sources which emit radiation in the ultraviolet, visible or infrared range. They work on the principle of luminescence, that is the emission of optical radiation caused by electronic excitation of a material (Sze, 1981). LEDs are made of a semiconductor pn-junction, operated in forward bias direction. A large number of electrons and holes can pass the junction, as the barrier height is reduced by the bias voltage. Here they recombine, meaning that electrons transit from the conduction to the valence band. The hereby released energy can be emitted through radiative or non-radiative processes, hence by photons or phonons and electrons respectively. Only those materials where radiative processes are dominant are suitable for the application of LEDs. Therefore, these devices are made of direct band gap materials, most commonly III-V semiconductors. The exact choice of semiconductor determines the peak wavelength of the emitted spectrum. The purity of the spectrum is characterized by the full width at half maximum, also called spectral half-width. For LEDs used in this work, the spectral half width is roughly 20 nm to 40 nm. LEDs are very cheap and uncomplicated light sources. The intensity can be adjusted by modulating the forward current, following an almost linear slope.
Laser diodes are a specialized form of LED. The active part of a laser diode is very narrow (about 1 µm), and in one direction confined by reflecting passive material which forms an optical resonator. The forward current level is increased to a point where charge carrier population inversion occurs. Stimulated emission as the dominant process has the active layer leads to laser light emission. The emitted light is highly coherent and has a wavelength bandwidth of a few nanometers. Laser diodes are operated with higher current than LEDs and hence have to be cooled to prevent damage through heating. Laser diodes can be focused by optics to a spot size of only a few micrometers. This is very difficult with LEDs, as their active area is larger.

4.2. X-ray tubes

An X-ray tube is a conventional method of producing X-rays in a laboratory. Usually, such a tube contains a tungsten cathode filament and an anode target. When driving current through the filament, electrons are emitted from the cathode and are accelerated by the applied high voltage between cathode and anode. These electrons hit the target and ionize atoms, causing the emission of fluorescence photons. Hence, the spectrum of an X-ray tube contains fluorescence emission lines characteristic for the respective target material. In order to increase the number of available emission lines, the anode can be implemented as a target wheel containing several materials. In addition to the emission lines, the spectrum of an X-ray tube contains a continuum caused by bremsstrahlung of the electrons decelerated by the target. To minimize this background radiation, thin filters are used. By choosing a proper filter material, the bremsstrahlung continuum or some of the emission lines in a spectrum can be attenuated. X-ray tubes as radiation source are quite flexible, as the X-ray energy and flux can be adapted. Still, the bremsstrahlung continuum is too high to allow for measurements that require highly monochromatic radiation. Furthermore, X-ray tubes have to be cooled and are quite large and expensive experimental facilities. An easier way to create X-ray photons of defined energy are radioactive fluorescence sources.

4.3. Radioactive sources

If stable irradiation with X-ray photons of defined energy is required, for example for calibration measurements of X-ray detectors, radioactive sources may be used. A commonly used γ-ray source is Fe^{55} which decays by electron capture to Mn^{55}. The vacant place of the electron is filled by an electron of a higher shell, releasing the difference in energy by a photon.

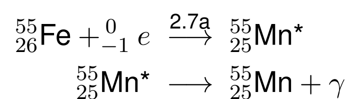

$$
\begin{aligned}
{}^{55}_{26}\text{Fe} + {}^{0}_{-1}e &\overset{2.7a}{\longrightarrow} {}^{55}_{25}\text{Mn*} \\
{}^{55}_{25}\text{Mn*} &\longrightarrow {}^{55}_{25}\text{Mn} + \gamma
\end{aligned}
$$

The energy of the photon depends on the binding energies of the original and final electron shell, in this case the K- and L-shell. A Fe^{55} source hence emits radiation of an energy $E_{K\alpha}$ = 5.89 keV and, with significantly lower intensity, of energy $E_{K\beta}$ = 6.49 keV (Schötzig, 2000). The radioactive half-life is 2.7 years and hence high enough to guarantee a quasi-constant level of photon emission over several weeks.
The number of γ-ray sources in the medium X-ray range that have an adequate half-life and emission energy is limited. As stated above, radioactive sources can also be used to stimulate fluorescence in target materials. This kind of X-ray source was used for example for the calibration of the AXAF (Advanced X-ray Astrophysics Facility) CCD imaging spectrometer at energies where the efficiency of the X-ray tube was too low (Jones et al., 1996).

4.4. Synchrotron radiation

If a well-defined spectrum of photon energies is needed for a measurement, synchrotron radiation is an excellent radiation source. A synchrotron is a storage ring for electrons, which are accelerated and simultaneously forced on a circular trajectory by magnetic fields. The electrons are constantly deflected transversely to their direction of motion and therefore emit electromagnetic radiation (see for example Wiedemann, 2003). The energy loss to this kind of radiation is so large that it can cause technical and economic limits for synchrotron operation. On the other hand, the emitted radiation intensities exceed those of other sources, especially in the vacuum ultraviolet and X-ray region, providing great opportunities for research on electromagnetic radiation. The spectrum of this so-called bending magnet radiation reaches from microwaves up to the critical photon energy defined by

$$E_c = \frac{3\hbar c}{2(m_e c^2)^3} \frac{E_e^3}{\rho} , \tag{4.1}$$

where E_e is the electron energy and ρ the bending radius of the storage ring.
For an observer at a certain position outside the synchrotron, the radiation is emitted in pulses. Every time an electron, or electron bunch, passes the observer, radiation is emitted in his direction. The characteristic time of these pulses is on the order of pico- or nanoseconds and therefore appears as continuous radiation for PNCCD detectors with readout times of several milliseconds.
In many cases it is desirable to create X-ray radiation harder than the critical energy without increasing the electron energy. Then additional dipole magnets, the so-called wavelength shifter, are used to deflect the electrons and cause the emission of radiation with lower wavelength than the critical cutoff. The electrons are deflected up and down or left and right, but in such a way that the net deflection is zero in order to preserve the storage ring geometry. A series of such magnets used to increase the photon flux is called wiggler. By operating the magnets at a strongly reduced field strength, the electron can be brought into a sinusoidal transverse oscillation, causing it to emit radiation of a limited bandwidth. This is called a undulator, which is used to create radiation only in the vicinity of a desired wavelength with increased brightness.
The spatial and spectral distribution of synchrotron radiation can be determined by the Schwinger equation (Schwinger, 1949). This complex equation describes the emitted spectrum depending on storage ring parameters, as for example the synchrotron ring current I_{ring}, the electron energy and magnetic induction at the source point as well as additional geometrical parameters (Klein & Ulm, 2005). The number of electrons circulating in the storage ring decreases with time due to collisions between circulating electrons. The ring current is therefore a particularly important measurand, as it is used to monitor and normalize the emitted photon flux during a measurement. At the synchrotron BESSY II, the ring current is continuously measured and provided to the experimental stations through an internal information system.
The emitted photon distribution of a continuous synchrotron spectrum is homogeneous along the horizontal plane, but is a function of the vertical distance from the orbital plane of the circulating electrons. The spectrum at the BESSY II synchrotron for different distances z from the orbital plane is shown in fig. 4.1.

The fact that the photon flux can be calculated precisely is a major advantage of synchrotron radiation as photon source. It enables to use the synchrotron as **primary radiation standard**

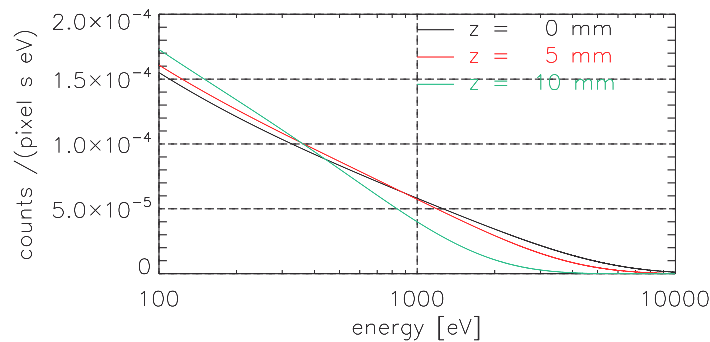

Figure 4.1.: Calculated photon flux for the experiments at BESSY II (data provided by the Physikalisch-Technische Bundesanstalt). The spectrum changes with vertical distance z, perpendicular to the orbital plane of the circulating electrons.

and hence to do measurements that need absolute calibration without the need of a calibrated reference detector.
It is also possible to use synchrotron radiation as input for wavelength dispersive devices like monochromators. In this case the information about the photon flux is lost and has to be determined by reference detectors.

4.5. Monochromators

If the photon energy for a measurement has to be defined within a small bandwidth, monochromators may be used. **Grating monochromators** are based on the principle of diffraction at multiple slits, leading to constructive and destructive interference depending on the entrance and exit angle and the wavelength of electromagnetic radiation. For a fixed entrance angle, a certain wavelength can be selected by confining the exit angle by slits. The diffraction pattern behind a grating shows main maxima according to the **Bragg condition** of constructive interference (see for example Bergmann & Schaefer, 2003)

$$\frac{n \cdot \lambda}{d} = sin(\phi), \tag{4.2}$$

where λ is the wavelength, n is the order of the maximum, d is the distance between the grating lines and ϕ the angle between the normal and the exit ray (see fig. 4.2a). The main maxima themselves are modulated by an oscillating structure as shown in fig. 4.2b. The higher the number of lines in a grating, the more distinct are the main maxima, while the modulating structure vanishes. The position of the main maxima does not depend on the number of lines of a grating, but only on the grating constant. It can be derived from eq. 4.2 that not only the first maximum, but higher order maxima of photons with multiple wavelengths appear at the same angle. For example, at a fixed angle, there can be the first order maximum of wavelength λ_1 as well as the second order maximum of wavelength 0.5 $\cdot\lambda_1$. If the grating constant is in a rational ratio with respect to the width of the slits, certain orders of maxima can vanish (Bergmann & Schaefer, 2003). Furthermore, the number of higher orders is limited through the condition that $sin(\phi) \leq 1$.

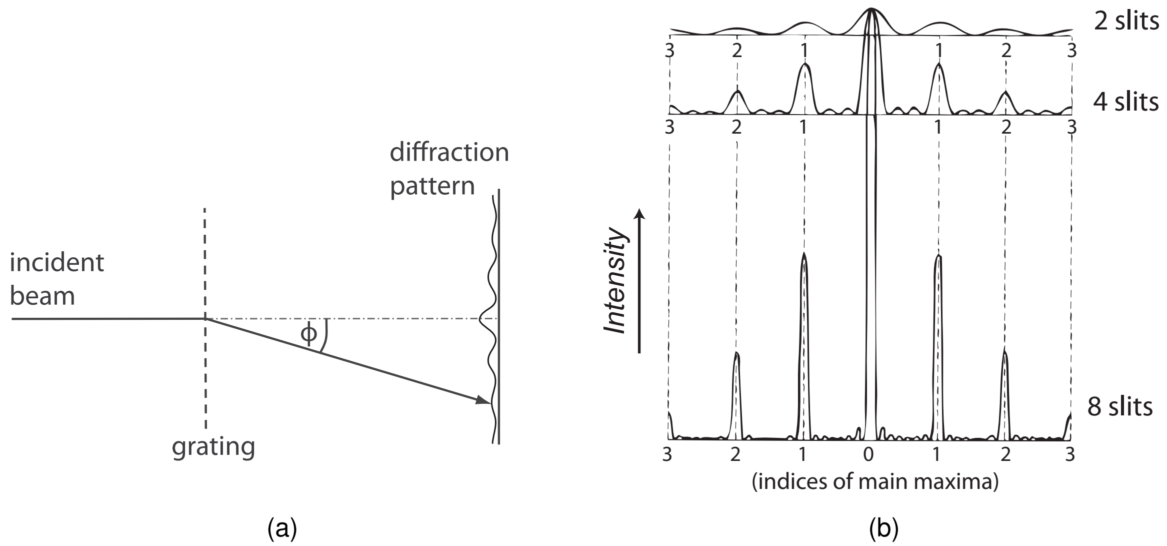

Figure 4.2.: Diffraction behind gratings and multiple slits. The left side shows a schematic of a beam diffracted by a grating. The right side shows a qualitative intensity distribution for diffraction at 2, 4 or 8 slits. The abscissa is divided into units of λ/d, with d the distance between slits. Note that $d >> b$, where b is the size of the slit. The main maxima at multiples of λ/d are modulated with an oscillating structure that vanishes with increasing grating constant. Schematic adapted from Bergmann & Schaefer (2003).

As mentioned above, the diffraction pattern behind a grating gets more distinct with increasing number of lines. This is quantified by the **spectral resolution** or **resolving power** RP, defined by

$$RP = \frac{\lambda}{\Delta\lambda} = \frac{n}{N}, \tag{4.3}$$

where $\Delta\lambda$ is the smallest wavelength difference that can be resolved in the vicinity of a wavelength λ. N is the number of lines in the grating and n is the order of the maximum. For higher orders, the diffraction spectrum is wider and hence the spectral resolution is higher.
The considerations above included the normal incidence of radiation and the diffraction of the transmitted beam. However, grating monochromators can also be designed as reflecting gratings, leading to a modulation of radiation intensity of the reflected beam. For very short wavelengths of single nanometers or Ångstrom, the fabrication of gratings reaches a natural limit. Here, the crystal lattice structure of solids is used as diffraction grating, the **crystal monochromator** . For the measurements in this work, grating and crystal monochromators in the laboratories of the Physikalisch-Technische Bundesanstalt (PTB) at the electron storage ring BESSY II in Berlin were used. These and other measurements are described in the next chapter.

5. Experimental methods

In order to gain experimental knowledge about the spectral response of PNCCDs with aluminum blocking filter, various measurements regarding the redistribution function, attenuation and quantum efficiency were conducted. To some extent the optical properties of eROSITA detectors were characterized using diodes with the same entrance window as the eROSITA PNCCDs. Additionally, optical measurements and preparatory X-ray experiments with PNCCDs were performed at the MPI Semiconductor Laboratory. Further experiments were conducted at the experimental stations of the PTB (Physikalisch-Technische Bundesanstalt) in Berlin. Here it is possible to make use of two synchrotron storage rings as radiation sources, namely BESSY II and MLS. At MLS and BESSY II the attenuation and quantum efficiency was measured and monochromatic X-ray spectra were recorded. QE measurements were performed at the PTB monochromator beamlines in integrating mode, where the integrated charge generated in the detector is used as a measure for the number of detected photons. In addition to the monochromator setup, a quantum efficiency measurement was performed at a beamline with continuous synchrotron spectrum. There, a low photon flux for the operation of the PNCCD in single photon counting mode is possible. The measurement at this beamline permits the verification of the QE derived from monochromator measurements and furthermore the evaluation of its spatial homogeneity.
The PNCCD measurement setup and the PTB facilities are introduced in section 5.1 and 5.2 respectively. Descriptions of the conducted experiments are given in sections 5.3 to 5.6. Table 5.1 shows a summary of the different experiment types, including the used detector, photon energy range and the experimental facility.

detector	measurement type	photon energy	light source/facility	see sect.
photodiode	attenuation	1.9 eV (λ = 660 nm)	laserdiode setup at the Semiconductor Laboratory	5.3
PNCCD	attenuation	visible light	LED illumination at the RÖSTI facility (Semiconductor Laboratory)	5.4.1
PNCCD	attenuation	UV and VUV	monochromator at MLS storage ring	5.4.2
PNCCD / photodiode	QE (integrating mode)	X-ray regime	PTB monochromators at BESSY II storage ring	5.4.2
PNCCD	QE (single photon counting mode)	X-ray regime	PTB beamline with continuous synchrotron spectrum at BESSY II storage ring	5.5
PNCCD	monochromatic spectra	X-ray regime	PTB monochromators at BESSY II storage ring	5.6

Table 5.1.: Overview on the conducted measurements, the detector type, the respective photon energy range and the used light source and facility.

5.1. CCD system setup

All PNCCD measurements in this work were performed with eROSITA type PNCCDs. The employed detectors only vary in the number of pixels and, for optical measurements, in aluminum layer thickness of the entrance window. Hence, the general properties of PNCCD and electronic system are the same for all experiments. While the PNCCD and its entrance window are outlined in chapter 3, the general test setup is described in this section. It includes a cooling system, CCD controller and data acquisition.

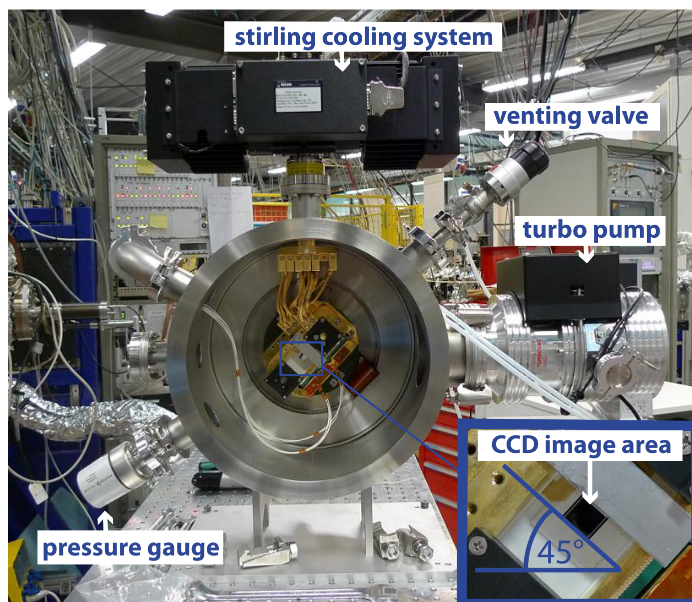

Figure 5.1.: The RÖSTImobil vacuum chamber is used for measurements at the synchrotrons. The enlarged detail shows the PNCCD image area, which is tilted by 45° versus the horizontal plane.

At the MPI Semiconductor Laboratory, X-ray measurements with eROSITA PNCCDs are conducted at the RÖSTI facility, which is an X-ray tube and vacuum chamber equipped with a complete electronic, mechanical and thermal system for PNCCD characterization. Very similar to this setup but without an X-ray tube is the mobile vacuum chamber RÖSTImobil, used for experiments outside the Semiconductor Laboratory. The chamber can be flanged to any other radiation source, as for example the synchrotron beamlines of the PTB laboratories. The RÖSTImobil vacuum chamber, shown in fig. 5.1, is equipped with a turbopump and a Stirling cooling system. The setup permits a stable CCD temperature in the regime of the operating temperatures in space, e.g. $-80\,^\circ$C, and a pressure of less than 10^{-6} mbar. A built-in rotatable manipulator with a mounted photodiode allows to switch between CCD and diode measurements. The photodiode can be cooled by a Peltier element, reaching a minimum temperature of about $-10\,^\circ$C. The detector inside the chamber is tilted to an angle of 45° relative to the horizontal plane to avoid high intensities in single rows or single columns of the detector, as explained in section 5.4.2. In front of the detector frame store area, an aluminum plate is installed to block the frame store region from photons. This cover plate is required for the measurement with continuous synchrotron spectrum, where the radiation is not limited to a single spot.

The electronic system comprises a set of power supplies for the PNCCD and CAMEX. A compactPCI (cPCI) Rack contains the ADC (analog to digital converter) cards which digitize the output signal of the CAMEX. The external sequencer, which generates the digital signals to synchronize the CCD, CAMEX, and ADC, is as well realized as a cPCI card. The cPCI Bus is coupled via an optical interface to a PC running Linux (for details see Elbs et al., 2010). For an immediate performance check including count rates, the data can be analyzed with an online analysis tool. The detailed analysis of the measurement is done after storage of the raw data on hard disk.

5.2. Experimental facilities of BESSY II and MLS

The mobile vacuum chamber RÖSTImobil was taken to the experimental facilities of the PTB laboratory in Berlin, whose synchrotron beamlines provide excellent conditions for detector characterization. At the synchrotron storage ring BESSY II with a maximum electron energy of 1.7 GeV, three beamlines operated by the PTB were used. Among these were two monochromator stations, namely SX700 (see Scholze et al., 2003b) and KMC (see Krumrey & Ulm, 2001), and the beamline with continuous synchrotron spectrum (see Thornagel et al., 2001). The PTB operates an own storage ring, the MLS (see Brandt et al., 2007), in direct vicinity of BESSY II. The MLS runs with a rather low electron energy of 105 MeV up to 630 MeV and is dedicated to radiometry and technological development in the UV, VUV and EUV spectral range. At this storage ring, one monochromator beamline for UV and VUV radiation, further called MLS-UV (see Brandt et al., 2007), was used for the characterization of attenuation of the PNCCD.

Monochromators allow to filter spectral lines out of the continuous spectrum of a synchrotron (explained in section 4.4 and section 4.5). If the desired photon energy ranges between visible light and soft X-ray radiation, the monochromator is usually realized by a grating. For higher photon energies, crystals are used as diffracting medium.
The normal incidence grating monochromator at the MLS beamline **MLS-UV** was used for attenuation measurements with radiation energies from 2.8 eV to 35 eV. A strong reduction of photon flux was necessary in order to ensure that the measured PNCCD signal was within the dynamic range. Therefore the MLS storage ring current, and thus the photon flux, was adjusted until the experimental constraints were met.
The experiments at higher photon energies, from 40 eV to 1700 eV, were conducted at the plane grating monochromator beamline of **SX700** type at BESSY II. The SX700 is a grazing incidence monochromator. In contrast to a normal incidence monochromator, it utilizes the beam reflected from the grating instead of the transmitted beam. As shown in fig. 5.2, the reflected beam is lead through mirrors and slits onto the detector. At both the SX700 and MLS-UV monochromators higher order radiation is reduced by edge filters. This reduces the fractional amount of higher order radiation to less than 0.15 % at the MLS-UV (private communication, A. Gottwald). A limit of 1 % is accomplished at the SX700 (Scholze et al., 2003a) for most slit and aperture configurations. However, for high photon energies near 1 keV and low flux, higher order radiation and diffuse stray light was observed with a relative intensity of up to about 30 %. The straylight is caused for example by diffuse scattered background radiation at the grating monochromator, or by radiation diffracted at the apertures.

The measurements at energies from 1800 eV to 11 keV were performed at the four-crystal-monochromator (**KMC**) at BESSY II. Depending on the photon energy range, a Si or a InSb crystal serves as diffraction medium. The Si crystal is used for energies down to 2.1 keV. Due to the Si-K absorption edge at 1.84 keV, the InSb crystal has to be used for energies lower than 2.1 keV. For reasons related to crystal symmetry, second order radiation is strongly suppressed for InSb and is forbidden for Si crystals (Krumrey & Ulm, 2001). At the KMC beamline, the spectral resolving power (see section 4.5) ranges between 4000 and 12 000, the higher order contribution decreases from 10^{-3} to 10^{-8} with increasing photon energy. A schematic of the four-crystal monochromator is shown in fig. 5.3. At both BESSY II monochromators, SX700 and KMC, low intensity was achieved by running the experiment during a time when the synchrotron was operated with reduced ring current (low-alpha multibunch mode, see Wustefeld et al. (2004)) and by using slits to lower the photon flux.
All three PTB experimental stations are equipped with calibrated photodiodes, which can be brought into and removed from the beam position to measure the photon flux.

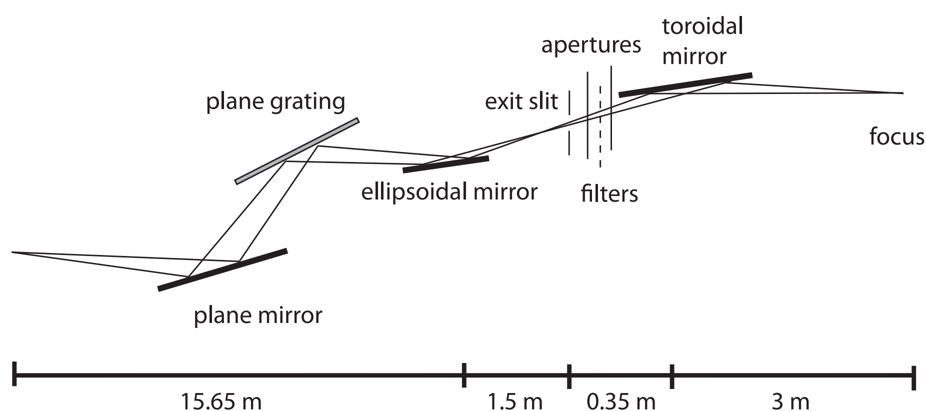

Figure 5.2.: SX700 (grazing incidence monochromator) setup at BESSY II (picture adapted from Scholze & Ulm (1994)).

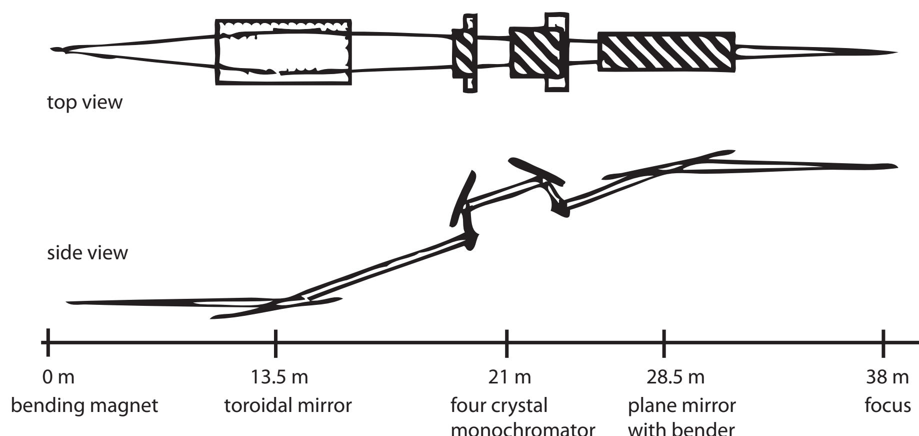

Figure 5.3.: KMC (four crystal monochromator) setup at BESSY II (picture adapted from Krumrey (1998)).

The PTB beamline for **continuous synchrotron radiation** of a bending magnet is not equipped with a monochromator. The emitted spectral radiant intensity of this beamline can be calculated from the Schwinger equation, as explained in section 4.4. It can therefore be used as calibrated X-ray source without the need of a reference detector. The radiant power is a function of parameters like the wavelength, electron energy, angle relative to the orbital plane and the ring current. To adjust the flux, the number of circulating electrons in the storage ring can be adjusted down to only one electron.
The measurements at all PTB beamlines were scheduled several months in advance and were limited to a few days per beamline. Therefore only essential measurements with one PNCCD detector were performed there.
Additional measurements, for example parameter studies about the influence of aluminum layer thickness on the optical attenuation, were conducted at the MPI Semiconductor Laboratory.

5.3. Measurement of optical attenuation using photodiodes

In contrast to PNCCDs, photodiodes are simple devices and can be fabricated, mounted and measured in a considerably shorter time. It is convenient to use these easy-to-handle structures for the comparison of the attenuation properties of various aluminum layer thicknesses. The attenuation properties are quantified by the attenuation factor, the quotient of incident photons to detected photons, as defined in eq. 3.9.
In the course of this work, attenuation measurements were commissioned at the certified calibration laboratory of Gigahertz GmbH[1]. This laboratory performs calibration measurements in the wavelength range from 250 nm up to 1160 nm in steps of 5 nm. However, the available photon flux and the specific diode geometry only allows to characterize devices with attenuation factors up to 10^4 in the optical regime. In order to determine the attenuation of diodes with relatively thick aluminum filter, an **attenuation measurement setup** at the MPI Semiconductor laboratory was designed and configured.
The **photodiodes** used for attenuation measurements are fabricated on the same wafers with the eROSITA PNCCDs. The diode front side is unstructured, and the back side exhibits a similar entrance window as shown in fig. 3.7. Only the aluminum blocking layer thickness of the tested diodes varies between 30 nm and up to 200 nm. The p-implanted diode back side is divided into an active diode area in the center, surrounded by the so-called guard ring (see fig. 5.4a). A guard ring is a structure fabricated on semiconductor detectors, acting as an isolation ring around the active area. It is biased similar to the active photodiode area, thereby collecting the leakage surface currents generated in the surrounding of the active area. Both photocurrents generated in the active area and guard ring are measured, as outlined in fig. 5.4b. In order to be able to measure currents in the range of picoamperes, the setup is optimized by collectively shielded cables, to avoid electromagnetic disturbances and leakage currents.

Figure 5.4a displays a top view of the diode structure, showing a small gap between the active diode region and the guard ring, which is not covered with aluminum. Straylight entering this non-shielded area leads to a parasitic photocurrent. The amount of straylight, and thus the parasitic photocurrent, can be derived from the photocurrent through the guard ring contact.

[1] Gigahertz GmbH, 82299 Türkenfeld (Germany) is a certified calibration laboratory for optical radiometry

Measurements showed that about half of the charge produced in the uncovered area drains off the guard ring contact, the other half via the p-contact of the active area as a parasitic photocurrent. Without a thorough straylight shielding, the parasitic current even exceeds the photocurrent generated in the active area for diodes with thick aluminum blocking filter. For this reason, the housing of the diodes is optimized to reduce the amount of straylight hitting the non-shielded area between diode and guard ring.

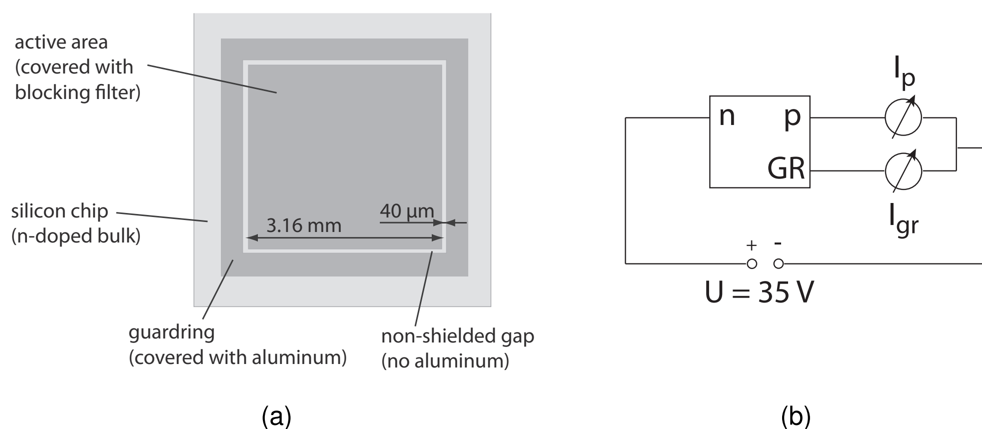

Figure 5.4.: The photocurrent of diodes with aluminum on-chip filter was measured to determine the attenuation of the filter. (a) Schematic of the diode back side, which is divided into active area and guard ring. Only a small area between the sensitive region and the guard ring is free of aluminum. (b) Circuit for photocurrent measurement with photodiodes. A positive voltage of 35 V is applied between the n-doped silicon bulk (n-contact) and the p-doped active area (p-contact) and the guard ring (gr-contact). The photocurrent generated in the active area of the diode is measured at the p-contact and serves as measure for the amount of light transmitted through the entrance window. The guard ring (GR) is biased with the same voltage as the active area. The current through this contact allows to estimate the amount of parasitic photocurrent caused by stray light.

On every diode, a thin, blackened aluminum plate is mounted in a short distance of about 200 µm above the entrance window (see fig. 5.5). A hole of 1 mm diameter in the aperture plate allows for illumination with a collimated laser beam. Diffusely reflected light outside and inside the housing can only reach the non-shielded area after several reflections and is thereby strongly attenuated. A corner of the covering plate is clipped in order to allow the wire bonding of the p-, n- and guard ring - contacts to the pins of the diode mount (see fig. 5.6a). At this corner, the non-shielded area between diode and guard ring is not covered by the blackened plate. Therefore, a cap is put on top of the aperture to minimize straylight entering laterally or at the open corner. With the described **housing**, the straylight fraction is low enough to determine attenuation factors of up to 10^7, which is sufficiently high for the studied devices. The monitoring of the guard ring current during illumination indicates if the straylight fraction is low enough. In any case, a measurement with such devices gives a lower limit for the attenuation factor, even at high guard ring currents.

The measurement setup, shown in fig. 5.6, consists of a light-tight aluminum box and a therein mounted laser with λ = 660 nm. The laser beam is collimated to a spot diameter of approximately 100 µm and the laser is movable in two directions by a manual positioning system. Its beam intensity is proportional to an externally applied voltage, allowing to adjust the photon

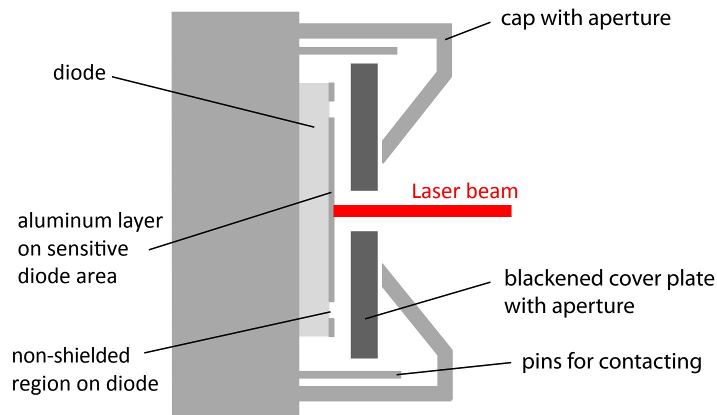

Figure 5.5.: Cross section of a mounted photodiode. To reduce straylight on the non-shielded area, the diode is covered with an aperture plate very close to the entrance window and an additional cap with aperture. The diode is illuminated with a focused laser beam.

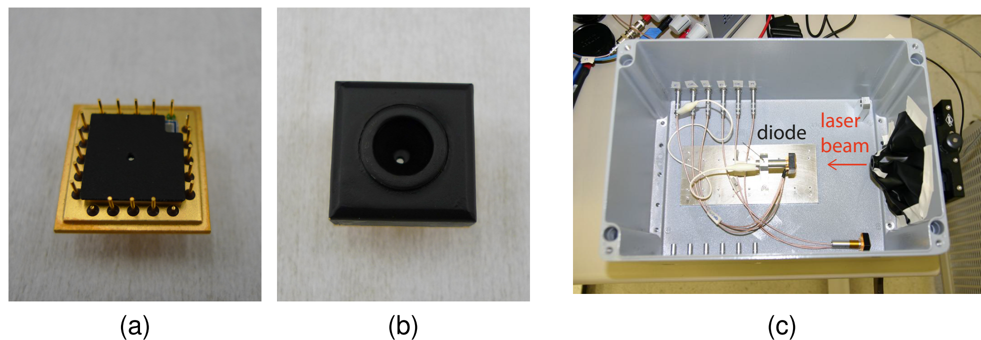

(a) (b) (c)

Figure 5.6.: The photodiodes for attenuation measurements are covered with (a) a blackened aperture plate and (b) an additional cap with aperture. By illumination with a focused laser inside a light-tight box, as shown in (c), the impact of straylight on the measurement result could be minimized.

flux. Inside the box, two diodes can be mounted using light-tight feed-throughs for the p-, n- and guard ring contacts.
During a measurement, the diode area illuminated through the aperture is scanned with the laser beam using the positioning system. Over the aperture area with 1 mm diameter, the variation in photocurrent and the mean value is determined. This variation is, as described later, due to the inhomogeneous structure of the aluminum layer. The laser beam size can resolve variations over a distance on the order of 100 µm, which is comparable to the PNCCD pixel size.
The **attenuation factor** χ, the quotient of incident photons to detected photons, is determined from the ratio of photocurrents measured with the reference diode and the diode under test. The responsivity of the reference diode, which exhibits the eROSITA entrance window with no aluminum on top, is SR_{ref} = 0.52 A/W at 660 nm. For diodes of this type the quantum efficiency and hence the responsivity can be calculated with high accuracy (Hartmann et al., 2000). This was confirmed by calibration measurements performed by the calibration laboratory at Giga-

hertz GmbH.
For constant photon flux on the laser, the ratio of photocurrents equals the respective ratio of responsivities according to

$$\frac{SR}{SR_{\text{ref}}} = \frac{I_{\text{photo}}}{I_{\text{photo, ref}}} \,. \tag{5.1}$$

Here, SR and I_{photo} refer to the diode under test, while the respective values for the reference diode are denoted with SR_{ref} and $I_{\text{photo, ref}}$. Substituting SR into eq. 3.9 leads to

$$\chi = \frac{I_{\text{photo, ref}} \cdot e}{I_{\text{photo}} \cdot SR_{\text{ref}} \cdot w} \,. \tag{5.2}$$

At λ = 660 nm each photon absorbed in the silicon creates one electron, so the mean energy w required for the generation of an electron-hole pair is equal to the photon energy E_{ph}.
The photocurrent at the reference diode compared to that at the diode with blocking filter is larger by a factor of approximately χ. Hence, when measuring a photocurrent of 10 pA with the diode including blocking filter, the reference photocurrent would amount up to $\approx$ 10 mA. However, the maximum photocurrent which allows for linear signal-to-input behavior is about 20 µA. This value was determined from sweeps of the diode current over the laser intensity for several diodes with different attenuation factors. In order to keep the photocurrent below this limit, diodes with intermediate attenuation factors were used as reference diodes for those diodes with $\chi > 10^6$. Nonlinear response of photodiodes at high photocurrents can be explained for example by the break-down of depletion in a region of strong absorption.
The measurement accuracy of the described setup is limited by the precision of the photon flux, which is controlled via an external voltage at the laser and by the signal-to-noise ratio at low photocurrent level. However, the measured attenuation factors were found to be dominated by the variation in attenuation over the aperture area, caused by the aluminum film structure.
The measurement with photodiodes is suitable to compare the attenuation factors of different entrance window types. However, a photodiode measurement can not replace the full characterization of the PNCCD optical properties. Attenuation measurements with a PNCCD were therefore performed in a much wider energy regime, as presented in the following section.

5.4. PNCCD measurements in integrating mode

PNCCDs are usually applied for the precise measurement of the energy of X-ray photons. This is only possible for low photon rates, applying event recognition and recombination algorithms to separate each photon signal charge. If pixel signal values of the PNCCD are summed up over the whole area of interest and a number of frames, this is further referred to as **integrating mode**. In integrating mode, no event recognition or recombination is performed and hence even a high amount of pile-up does not impact the results.

The measurement of optical and UV attenuation factors requires the measurement in integrating mode. The charge signal of single photons below 30 eV is less than 10 electrons and

therefore too close to the readout noise of about 3 electrons ENC of a PNCCD, so single photon counting is not possible. In contrast to that, the quantum efficiency in the X-ray regime can in principle be determined from experiments counting single photons. However, the experimental setup at the BESSY II monochromators SX700 and KMC in combination with a PNCCD detector is not suited for this purpose. As the photon flux at this setup is determined with calibrated reference diodes, the photon flux has to be chosen in a way that both PNCCD and reference diode give accurate results. A minimum photocurrent at the calibrated reference diodes requires a flux that causes high pile-up rates on the PNCCD, which inhibits the counting of single X-ray events with adequate accuracy. This can for example be avoided by attenuating the photon flux on the PNCCD by a defined factor using a mechanical shutter. Such an approach was chosen by Hartmann et al. (1999), who measured the X-ray quantum efficiency of PNCCDs for the XMM-Newton mission in single photon counting mode at the BESSY II monochromators. However, a mechanical shutter is limited to low frame rates and therefore not used in this work.
A measurement in integrating mode offers the advantage of relatively short measurement time. Within a few thousand frames, a high number of 10^5 to 10^6 photons can be accumulated within 2 minutes, leading to a statistical variation of only a few ‰ (see eq. 3.13). Accumulating the same number of photons in single photon counting mode would require a measurement with strongly reduced photon flux, and therefore a measurement time longer by a factor of 5 to 50, depending on the beam spot geometry. In addition, the required measurands for a quantum efficiency measurement in integrating mode, the reference current and PNCCD signal, can be determined with high accuracy and stability.
A measurement in integrating mode allows the determination of the detector responsivity from the number of created electron hole pairs, as given in eq. 3.8. The photon count rate ν_{ph} is determined from the number of generated electron-hole pairs ν_{e} through the mean energy w required for the generation of an electron-hole pair and the photon energy E_{ph}:

$$\nu_{\text{ph}} \approx \frac{\nu_{\text{e}} w}{E_{\text{ph}}} \,. \tag{5.3}$$

A change in the mean number of electron hole pairs per photon due to partial charge loss in the entrance window is neglected. This is a rather conservative approximation, as it can only lead to a slight underestimation of the quantum efficiency but not to an overestimation. The **quantum efficiency** given in eq. 3.6 and responsivity from eq. 3.8 are then connected by

$$QE \approx \frac{SR \cdot w}{e} \,. \tag{5.4}$$

Combining equations 3.8 and 5.4, the quantum efficiency is determined from the incident radiant power and the mean number of electron-hole pairs generated in the detector through

$$QE \approx \frac{\nu_{\text{e}} \cdot w}{P_{in}} \,. \tag{5.5}$$

The incident radiant power P_{in} and hence the photon flux on the detector can be determined with a calibrated reference diode. ν_{e} is determined from the averaged signal of the PNCCD. Details on the evaluation method are given in chapter 6, where data analysis methods applied in this work are presented.

In the following section, attenuation measurements at the Semiconductor Laboratory are presented. Subsequent, the experiments at the MLS and BESSY II storage rings are described.

5.4.1. Measurement of optical attenuation at the RÖSTI X-ray facility

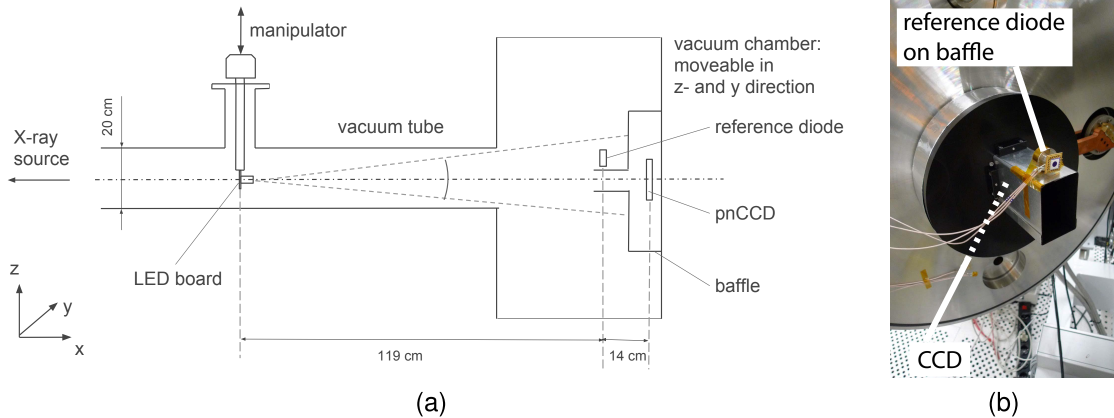

Figure 5.7.: (a) Schematic drawing of the RÖSTI X-ray facility. Positions of the CCD, LEDs, reference diodes and X-ray source are marked.(b) Baffle used to block straylight from the PNCCD front side during attenuation measurements.

Attenuation measurements on PNCCDs were conducted at the MPI Semiconductor Laboratory in order to confirm the diode test results and to resolve the spatial characteristics of attenuation all over the detector area. The attenuation properties are quantified by the attenuation factor, the quotient of incident photons to detected photons, as defined in eq. 3.9. An **attenuation measurement setup** was arranged inside a vacuum chamber, where PNCCDs can be mounted and cooled.

RÖSTI, the X-ray test facility for eROSITA PNCCDs at the MPI Semiconductor Laboratory, consists of an X-ray tube connected to a vacuum test chamber with a distance between the X-ray target and the detector of approximately 4 m. In order to perform attenuation measurements with PNCCDs, LEDs are mounted as optical light source inside the vacuum tube, as shown in fig. 5.7. The LED measurement setup meets two main requirements. First, the illumination pattern is homogeneous to a large extent, so that inhomogeneities in the attenuation characteristics caused by the aluminum thin film structure can be identified. Secondly, straylight on the front side of the PNCCD is reduced to a minimum. This is necessary as there is no light blocking filter on the detector front side (see fig. 3.3). At the same time, it is possible to perform X-ray measurements using the X-ray tube without venting the chamber to remove the LEDs from the X-ray beam. A manipulator with two LEDs wavelengths, $\lambda = 470$ nm and $\lambda = 530$ nm, is installed in the vacuum tube to illuminate the CCD from

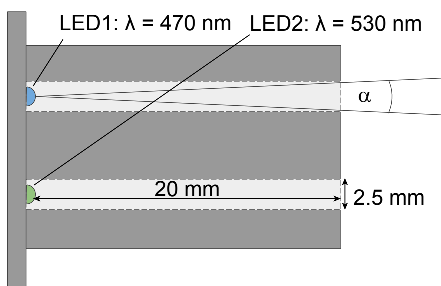

Figure 5.8.: LED board with two different LEDs and a cylindrical aperture. A length of 20 mm and diameter of ∅ 2.5 mm leads to an illumination angle of about 7°.

a distance of $1.2\,\mathrm{m}$. A cylindrical aluminum aperture in front of the LEDs, shown in fig. 5.8, leads to a small illumination angle of 7°. Narrowing the beam opening angle suppresses reflections inside the chamber, as the direct beam does not hit the lateral chamber walls. This decreases the amount of straylight and also leads to a uniform illumination of the PNCCD area, as reflections from chamber edges may cause bright spots on the PNCCD entrance window. The PNCCD itself is shielded with a blackened baffle (see fig. 5.7b) with interchangeable top pieces in order to adapt the aperture to various PNCCD sizes.
The reference measurements in this setup are performed with a reference diode of the same type as used in the laser setup described in section 5.3. It is mounted on top of the PNCCD baffle, so that it can be brought into and removed from the beam spot by moving the chamber in vertical direction. It was ensured by measurements with several reference diodes at different positions that moving the chamber has no impact on the LED beam pattern.
Similar to the measurements at the laser test setup, the **attenuation factor** χ is determined through a responsivity measurement, in this case using a PNCCD instead of a diode. In contrast to the laser test setup, the illuminated area and distance to the source are different between PNCCD and reference diode. As the photon flux decreases quadratically with the distance and is proportional to the sensitive, illuminated area of each detector, a geometrical correction factor α is introduced in order to transform the radiant power determined with the reference diode, P_{ref}, to the incident radiant power P_{in} on the PNCCD:

$$P_{\text{in}} = \frac{1}{\alpha} \cdot P_{\text{ref}} \tag{5.6}$$

α can be calculated from the pixel and diode area and the distance of the respective detectors to the light source according to

$$\alpha = \frac{{d_{\text{CCD}}}^2 \cdot a_{\text{ref}}}{{d_{\text{ref}}}^2 \cdot a_{\text{pixel}}} = 2.22 \cdot 10^3. \tag{5.7}$$

P_{ref} is derived from the reference diode photo current and responsivity according to eq. 3.7. P_{in} is substituted into eq. 5.5, where the mean number of created electron-hole pairs, ν_{e}, is evaluated as a mean value per pixel.

Attenuation factors for PNCCDs with different types of aluminum layer were determined with this setup, as well as maps of pixel-wise attenuation factors. Furthermore, the results derived with this setup were necessary input to estimate the optimum measurement conditions for the subsequent measurements at BESSY II and MLS.

5.4.2. Measurement of attenuation and QE at PTB synchrotron beamlines (MLS and BESSY II)

In order to extend the measurement results gained from the laser and RÖSTI test setup, and to determine the X-ray quantum efficiency, measurements were performed using synchrotron radiation. This was done at the MLS and BESSY II storage rings using the experimental stations of the Physikalisch-Technische Bundesanstalt.
Deliberately, a chip smaller than the eROSITA PNCCDs was chosen for these measurements, namely a **1/9-eROSITA PNCCD** with only 128 rows and 128 channels in the image area

(eROSITA chips have 384 × 384 pixels). This enabled the operation of the PNCCD with a minimum cycle time of less than 5 ms compared to 9 ms for large eROSITA chips.

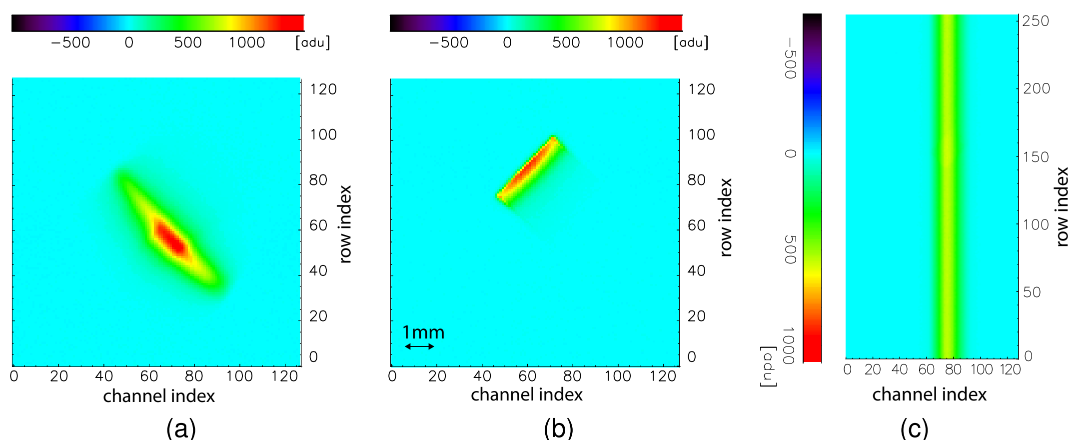

Figure 5.9.: Example of the image recorded during QE measurements with a photon energy of (a) 34.5 eV *at the MLS monochromator, (b)* 480 eV *at the SX700 monochromator and (c)* 1.88 keV *at the crystal monochromator. In order to avoid large amounts of charge in single rows or columns, the CCD is tilted by* 45° *versus the horizontal plane, leading to a tilted spot on the PNCCD image. At high photon energies, the PNCCD is operated in full frame mode with a very short cycle time in order to smear the image over the complete channel (as shown in (c)).*

At the MLS and BESSY II monochromators the attenuation factor and quantum efficiency is determined in a similar way to the measurements at RÖSTI. However, the illumination is not uniform, as the slits and apertures for beam adjustment create an inhomogeneous **beam spot** on the detector. The spot size is about 2 mm × 5 mm at UV and VUV energies and rather 1 mm × 2 mm at X-ray energies, with varying shape because of slit and aperture adjustment for each energy. An exemplary image of beam spots at 34.5 eV and 480 eV is shown in fig. 5.9a and 5.9b. The beam spot may exhibit a relatively large flux along a narrow stripe on the detector. To avoid the accumulation of a large amount of photons in only few channels or rows of the detector, the mounting of the CCD inside the RÖSTImobil vacuum chamber is tilted by 45° in the vertical plane. At high photon energies, the PNCCD is operated in full frame mode with short cycle time. Through the high amount of out-of-time events, the beamspot is smeared over the complete channel (see fig. 5.9c), avoiding too large photon signals in single pixels, which could exceed the dynamic range.
For each energy, the intensity is adjusted in a way that the generated charge per CCD pixel and channel does not exceed the dynamic range and that the **reference diode current** is above a minimum value. This minimum reference current, 1 pA at the SX700 and 50 pA at the KMC, guarantees a measurement accuracy of the reference current of ≈ 1 %. At the MLS monochromator, the attenuation factor of the PNCCD is such high that the required photon flux leads to reference photocurrents in the range of µA. In order to achieve high accuracy of the quantum efficiency in the X-ray regime, a current measurement is repeated 10-20 times at the SX700 beamline to decrease the impact of statistical fluctuations (see eq. B.1). At the KMC, each diode measurement is performed 3 to 10 times and the deviation between the single current values is compared. As the dark current of the reference diode at the KMC is slightly unstable, the whole measurement is repeated if the deviation between these values is larger than 1 %.

After the reference measurement, the reference diode is removed from the beam to illuminate the **PNCCD** for about one minute. The high amplification of the PNCCD for X-ray radiation leads to relatively high PNCCD signal and low signal at the reference diode. Therefore, the PNCCD was operated using the row-wise reset mode, as described in section 3.3. The reset ensures a stable potential of the readout anode and hence a stable amplification factor even at high photon flux. Hence for photon energies above 2.5 keV, the PNCCD is operated in full frame mode with a short cycle time. This leads to a smearing of the beam spot along the whole channel, avoiding to exceed the range of the 14-bit ADC. A tabulated overview on the reference current and PNCCD signal of different QE datasets is given in appendix B.1.1.
The **quantum efficiency** is determined from the PNCCD signal and the photocurrent of a reference diode with given responsivity, as described in eq. 5.5. In contrast to the ROESTI measurements, the beam spot is fully comprised in the reference diode area as well as the PNCCD area. The rate of detected electrons ν_{e} is hence summed up over the illuminated region on the PNCCD and a geometrical conversion of the incident radiant power is not necessary. However, a synchrotron as radiation source requires to account for the decrease in photon flux with decreasing ring current (see section 4.4). The storage ring current is therefore used as normalization factor for both PNCCD and reference diode measurements. The radiant power P_{in} is derived from the radiant power P_{ref} determined by the reference diode current according to

$$P_{\text{in}} = P_{\text{ref}} \cdot \frac{I_{\text{ring, PNCCD}}}{I_{\text{ring, ref}}} \,. \tag{5.8}$$

$I_{\text{ring, PNCCD}}$ is the ring current measured during the PNCCD dataset, while $I_{\text{ring, ref}}$ refers to the ring current during the reference diode measurement.

In addition to PNCCD measurements, the responsivity of a **photodiode** of eROSITA material and entrance window (further called eROSITA-diode) is measured at energies between 35 eV and 1800 eV. The current at the PTB reference diode for this measurement is on the order of µA which leads to a higher accuracy of the reference current measurement. The reverse bias voltage applied at the eROSITA-diode is 30 V which is significantly lower than the depletion voltage of the PNCCD. However, the size of the depletion region only affects photon absorption at high penetration depths for energies above 4 keV while the eROSITA-diode is only used for measurements up to 1.8 keV. The QE of the eROSITA-diode is determined by substituting ν_{e} by the measured photocurrent I_{photo} in eq. 5.5.

In the **UV energy regime**, the attenuation factor varies severely, between $10 < \chi < 10^9$. It describes the quotient of incident photons to detected photons, as defined in eq. 3.9. Hence, measurement conditions have to be adapted so that the CCD signal remains within the dynamic range for all measurements. This adaption is achieved by a combination of changing the storage ring current, the aperture at the monochromator and the cycle time of the detector. As presented in chapter 7, aluminum gets almost transparent to radiation for photon energies above the aluminum plasma frequency $\omega_p \approx 15$ eV, . Hence the UV attenuation of the eROSITA detector decreases abruptly. This slope in the attenuation function inherently enhances second order monochromator radiation whenever the nominal photon energy is below the plasma frequency, while the second order is above this energy limit. For some photon energies, the difference in attenuation between the first and second diffraction order exceeds the fractional

amount of second order radiation of 1 %. Hence, the measurement signal is completely dominated by the second diffraction order, while the reference diode current represents a measure for the flux of photons with nominal energy. The attenuation factor measured under such circumstances is effected with a high inaccuracy and represents only a lower limit for the actual attenuation factor.
With increasing photon energy at the SX700, the fraction of higher order light rises, which was revealed in the measured spectra above 600 eV. This leads to false QE readings, if the quantum efficiency at the higher order photon energy differs from the QE at the nominal photon energy. At 800 eV, the fraction of higher order light can be estimated from the monochromatic spectrum and amounts about 20 %. The QE data is therefore evaluated including the estimated second order radiation, using QE values at double energy from measurements at the KMC station.
The **measurement accuracy** of the monochromator measurements is mainly limited by the impact of higher order radiation, the calibration accuracy of the reference diodes and the detector gain as described in detail in appendix B.1.2.

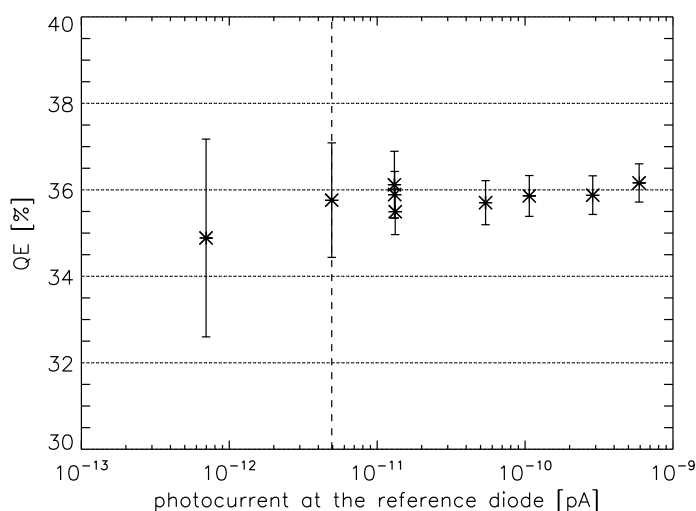

Figure 5.10.: Quantum efficiency measurements with a PNCCD in integrating mode at a photon energy of 380 eV*, with varying photon flux. In integrating mode, the pixel signal values of the PNCCD are summed up over the whole area of interest and a number of frames. No systematic impact of the photon flux, proportional to the photocurrent, on the measurement result is visible. Only the QE value measured at a photocurrent of about* 0.7 pA *shows a deviation from the other values. This deviation is not significant with regard to the measurement accuracy indicated by error bars. The estimated error of the diode measurement decreases with increasing photocurrent.*

As single photon counting is not possible during the measurement, it is important to prove that the measured signal caused by photons is proportional to their energy. For example trapping of charge carriers can lead to a reduction of the mean charge per photon at very low photon flux. At a large enough photon flux it is expected that such traps are saturated and do not influence the measurement. Furthermore, it has to be verified that even a strong variation in photon flux does not lead to variations in the electronic amplification, the gain. A measurement with varying photon flux, shown in fig. 5.10, confirms the stability of the QE measurement. It shows several evaluated quantum efficiency datasets at a photon energy of 380 eV, measured with varying photon flux. Over a range of three orders of magnitude, the photon flux leads to

no significant systematic influence on the measurement result. The application of the row-wise reset mode allows for such stable operation. Only the measurement with lowest photocurrent in fig. 5.10 deviates from measurements with higher photon flux. A systematic trend can not be derived from this value, as the estimated uncertainty of the reference photocurrent increases with decreasing photocurrent (see also appendix B.1.2). As a result, a reference photocurrent of at least $10\,\mathrm{pA}$ was aimed as long as the PNCCD operation remained within the dynamic range. This trade-off guaranteed a high measurement accuracy at both PNCCD and reference diode.

5.5. QE measurements with a continuous synchrotron spectrum

A quantum efficiency measurement with a continuous synchrotron spectrum was performed in order to verify and extend the results from monochromatic measurements. It serves as additional validation of the quantum efficiency measurements in integrating mode.
In contrast to the monochromator experiments, the PNCCD is operated in **single photon counting mode** during illumination with a continuous synchrotron spectrum. The emitted photon spectrum can be calculated from storage ring and geometrical parameters, as described in section 4.4. Hence it is not necessary to perform reference measurements with calibrated diodes. The photon distribution is homogeneous along the horizontal plane, but is a function of the vertical distance from the orbital plane of the circulating electrons. An example for the emitted spectrum is shown in fig. 4.1.

A measurement of a continuous photon spectrum as shown in fig. 4.1 subsumes photon counts at all energies in one dataset. Pile-up counts can not be identified from the resulting spectrum and falsify the QE measurement result. Hence, the fractional amount of pile-up has to be reduced during this kind of measurement. A sufficiently low photon flux can be achieved by reducing the ring current of the BESSY II storage ring.
The **measurement accuracy** is defined by the pile-up fraction and the statistical fluctuation in photon counts. An estimation about these uncertainties was performed previous to the measurements in order to assure the proper adjustment of photon rate and measurement time. Pile-up was estimated following the analytic expression in eq. 3.14, assisted by a Monte-Carlo code simulating pattern pile-up. In order to reach a pile-up fraction of $1\,\%$ at maximum, the photon count rate was fixed to a maximum limit of 7×10^{-4} counts per pixel and frame. The number of photons per energy bin was fixed to a minimum of 10^4 in order to limit the statistical error to $1\,\%$ (see eq. 3.12). By increasing the energy bin size at large photon energies the statistical error could be reduced without elongating the measurement time. According to these considerations, the lowest possible photon flux at BESSY II with only one electron in the storage ring was chosen.
Quantum efficiency measurements with a continuous X-ray spectrum have been done for several astronomical detectors before, as for example by Bautz et al. (1998), Krumrey et al. (1989). For evaluation, a model of the detector response is folded with the incident photon spectrum and then compared to the measurement data. Details on the evaluation of this measurement are given in section 6.5.

5.6. Measurement of the X-ray spectral redistribution function

The spectral redistribution function of the eROSITA PNCCDs, measured with monochromatic radiation at the BESSY II storage ring, is a necessary input for the detector characterization. **Monochromatic spectra** were therefore recorded at about 20 different photon energies between 70 eV and 11 keV. Through a real-time analysis of the QE measurements, the energies directly below and above the absorption edges could be determined. Spectra at these energies were recorded as they give insight into the origin of features in the spectrum.
The data sets from 100 eV up to 1800 eV were taken at the SX700 monochromator, those from 1800 eV up to 11 keV at the KMC experimental station. Data was taken with photon rates of about 5 to 20 photons per frame within an area of about 30 to 200 pixels. This leads to a pile-up fraction lower than a few percent for most measurements. Due to the strongly inhomogeneous illumination spot at the monochromators, higher pile-up intensities at some photon energies could not be avoided. A minimum number of 100 000 photons per measurement was accumulated. Due to the measurement time of about 20 minutes for one spectrum, higher statistics were sacrificed to be able to measure the most important photon energies during the limited time at the synchrotron. Measurement parameters, as for example temperature, voltage settings at the CAMEX and PNCCD and the mean photon flux were held constant for all photon energies to allow best comparability. The PNCCD was operated with frame-wise reset instead of row-wise reset in order to reduce the mean dark noise.
Crucial for spectral measurements however is not only the experimental setup but also the data analysis method with all necessary corrections, described in the following chapter.

6. Data analysis methods

6.1. The PNCCD Standard Analysis Procedure

For all previously described measurements with PNCCDs, the data is written to files without preprocessing. This means, raw data containing frames with pixel-wise values in adu (arbitrary digital units) is stored and later evaluated with the 'Offline Analysis Tool' (for example described in Andritschke et al., 2008). The main steps performed by this evaluation tool, which is the standard software for eROSITA data analysis at the MPI Semiconductor Laboratory, are shortly described in the following. In the further sections, particular analysis methods applied in this work are presented.

The first analysis step of the Offline Analysis Software is the generation of the **offset map** using the dark frames. In contrast to signal frames, dark frames are recorded while the PNCCD is not illuminated with photons. The offset map is established by averaging the pixel-wise adu signals of all dark frames. The offset map is subtracted from all signal frames, resulting in offset corrected frames.
As a next step, a **common mode correction** is performed. The common mode is a time dependent bias common to all pixels in a row. It can be caused by an external electromagnetic disturbances, present during the readout of the respective row. As long as the number of photons per row is much smaller than the number of pixels per row, it is corrected by subtracting the median of each row in each frame.
Using the common-mode corrected dark frames, the standard deviation is determined and stored pixel wise, forming the **noise map**. By averaging over all values in the noise map, the readout noise level of the PNCCD is calculated. Even if no radiation source is present, there is always a low background rate of MIPs (minimum ionizing particles[1], mainly cosmic muons). To minimize the influence of MIPs on the determined noise value, the n highest noise values for each pixel within the dark frames are discarded. To avoid a systematic modification to lower noise values, also the n lowest values are discarded. The number n, typically 5, depends on the number of frames and the cycle time. The noise level influences the minimum photon energy that can be separated from the dark noise, and leads to peak broadening.
The extraction of photon data from the PNCCD signal frames is performed in two steps, data reduction and event recombination. **Data reduction** includes the identification and separation of all pixels containing signal charge caused by photon interaction. In order to distinguish photon signals from noise fluctuations, all pixel values above a previously defined threshold are selected from the offset- and common-mode corrected signal frames. This threshold is set to a multiple of the mean readout noise σ_{det} of each pixel.

[1] Charged particles loose energy in ionizing collisions with the atoms when passing through matter. If their kinetic energy is such, that the mean energy loss rate derived from the Bethe-Bloch equation is close to the minimum, they are called minimum ionizing particles.

All selected pixels containing significant signal charge are then processed by the second analysis step, **event recombination**. Signal pixels that are in direct vicinity of each other are clustered in order to recombine the signal charge of a photon that was distributed over several pixels. According to the number of clustered pixels, the recombined events are categorized as singles, doubles, triples or quadruples. Noise excesses, MIPs and pile-up events are undesired events in a spectrum. Hence, the clustered events are subject to a plausibility check after recombination. All recombined patterns are classified as valid or invalid according to the distribution of signal amplitude and position inside a pixel cluster. With a pixel size of $75\,\mu m \times 75\,\mu m$, a charge cloud can not spread over more than two pixels in one direction, e.g. clusters of three alongside signal pixels are discarded.
During the charge shift along a channel, electrons can be trapped by impurities in the silicon, leading to the so-called charge transfer loss. With increasing row index, the peak position is shifted to lower values as the amount of charge loss increases. The **charge-transfer efficiency (CTE)** is determined from row-wise fits of the spectrum peak position by the Offline Analysis Software, using only single pixel events. Thereafter, a charge loss correction is performed, by adding the projected charge loss as a function of CTE and row index to the total adu signal of each event.
Finally, all valid events are added to a spectrum and their adu amplitudes are converted into energy values by a conversion factor that is determined in a calibration measurement.

For the evaluation of the spectra shown in chapter 10, analysis parameters are chosen in a way that the results are best comparable, both between different photon energies as well as with the simulation results. Hence, some further available correction methods are not applied in order to keep the results as clear as possible. Sections 6.2 to 6.4 describe the most important details on the applied evaluation techniques for spectrum analysis. Section 6.5 focuses on the evaluation of the quantum efficiency measurement with continuous X-ray spectrum. Section 6.6 presents the method applied for the determination of integrated adu signals for quantum efficiency measurements with monochromatic radiation.

6.2. Event filtering and recombination

The data analysis process, especially event processing, affects the resulting spectrum of an X-ray measurement with PNCCDs. Two important parameters for event processing are the **primary threshold** $f_{\sigma,1}$ and the optional **secondary threshold** $f_{\sigma,2}$. Those parameters, also called event and surrounding threshold, take effect whenever charge splitting and accordingly event reconstruction occur. The primary threshold sets the limit to detect pixels containing a relevant amount of signal charge. Noise excesses above this threshold are interpreted as events and form the so-called noise peak, which is cut at by the primary threshold. Even additional noise peaks from double, triple or quadruple noise events can occur as shown in fig. 6.1. The secondary threshold is applied to all pixels around the pixel that exceeded $f_{\sigma,1}$. It is always equal or lower than $f_{\sigma,1}$ and affects the multiplicity (single, double etc.) and the total signal of an event. A high secondary threshold leads to the neglect of pixels with a small fraction of charge, while a small secondary threshold can lead to an increasing number of noise excesses that are added to the photon events and form invalid patterns. In short, the position and shape of the photon peak in an X-ray spectrum is affected by the secondary threshold, while the separation from the noise peak is influenced by the primary threshold. By choosing

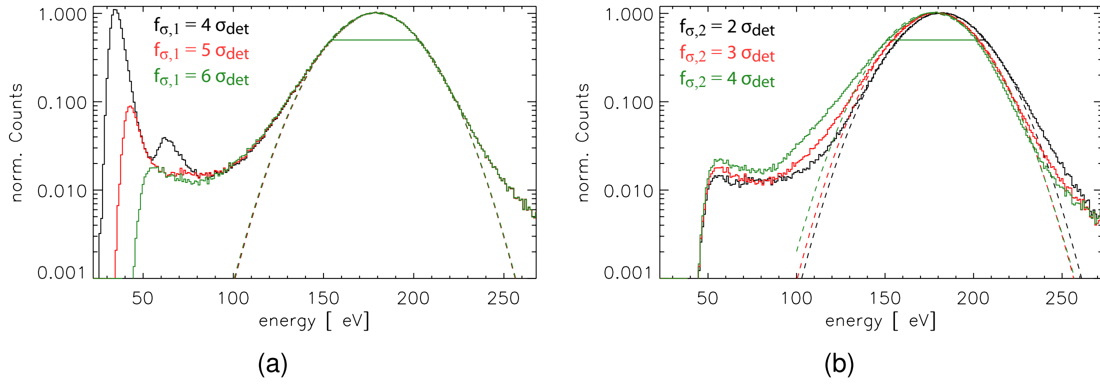

Figure 6.1.: The impact of a variation of primary and secondary threshold is shown for a measured spectrum at E_{ph} = 200 eV (readout noise $\sigma_{\rm det}$ = 2.6 electrons rms). (a) The noise peak, caused by noise excesses, is cut by the primary threshold $f_{\sigma,1}$ ($f_{\sigma,2}$ is held constant at 3 $\sigma_{\rm det}$). For $f_{\sigma,1}$ = 4 · $\sigma_{\rm det}$ a second peak is visible. It is caused by noise excess events where two neighbouring pixels are both above the threshold, forming a double event. (b) The secondary threshold $f_{\sigma,2}$ influences the peak position and shape ($f_{\sigma,1}$ is held constant at 6 $\sigma_{\rm det}$).

a high primary threshold, the number of noise excesses can be drastically reduced. By choosing a lower secondary threshold, the distortion of peak position and shape can be reduced to a minimum. Figure 6.1 shows the described effects on the example of a measurement at a photon energy of $E_{\rm ph}$ = 200 eV. For the evaluation of spectra in the following chapters, a primary threshold of 6 σ_{det} is chosen so that the main peak of spectra down to 200 eV is not cut by the threshold and the noise peak is reduced to a minimum. Furthermore, a surrounding threshold of 3 σ_{det} is chosen such that the peak distortion is weak.

To be able to analyze charge loss effects in the entrance window, the influence of spectrum distortion by event processing has to be quantified and separated from other effects. For this purpose, a Monte-Carlo Simulation was performed, creating frames files with Gaussian signal charges of known peak position and width. The simulation generates signals with Gaussian energy distribution, with a standard deviation equal to the Fano noise. Additionally, a Gaussian noise distribution is added in order to simulate readout noise. Each photon signal has a lateral Gaussian distribution, a charge cloud. The photon events are uniformly distributed over the area of one pixel, causing charge splitting to the surrounding pixels. Values for the charge cloud size are taken from Kimmel (2008), with a 2σ-radius of the charge cloud of approximately $R_{2\sigma}$ = 15 µm to 17 µm, increasing with photon energy. In the described simulation, the peak center position of the simulated signal is set to a photon energy $E_{\rm ph}$. Charge splitting, event detection and recombination cause the shift and broadening of the final event distribution in the spectrum. The peak center position E_{peak} is determined by a Gaussian fit on the spectrum. It is shifted with respect to the initial photon energy $E_{\rm ph}$ by a value $\Delta_{\rm E,split}$

$$E_{peak} = E_{\rm ph} - \Delta_{\rm E,split}\ . \tag{6.1}$$

Without any charge splitting and recombination, the width of the peak can be calculated from Fano and readout noise according to eq. 3.10. Charge splitting and recombination lead to

$f_{\sigma,1}$ / $f_{\sigma,2}$	6 σ_{det}/ 3σ_{det}			6 σ_{det}/ 4σ_{det}		
E_{ph} [eV]	*200*	*600*	*3000*	*200*	*600*	*3000*
$\text{FWHM}_{\text{nosplit}}$ [eV]	32	45	88	32	45	88
$\text{FWHM}_{\text{split}}$ [eV]	40	52	94	41	54	95
σ_{split} [electrons rms]	2.8	3.2	3.5	3.0	3.5	4.2
$\Delta_{\text{E,split}}$ [eV]	5	5	5	5	6	8

Table 6.1.: Overview on simulated peak shift and peak broadening by event splitting and recombination, as defined in eq. 6.1 and eq. 6.2. The values for the peak shift $\Delta_{E,split}$ and noise contribution σ_{split} are determined by comparing the peak width of simulations with and without event splitting ($FWHM_{split}$ and $FWHM_{nosplit}$). The simulated readout noise is 2.6 electrons rms*, matched to a gain of* 2.23 adu/eV.

an additional noise contribution σ_{split}. The resulting peak width of the simulated photon peak σ_{peak} can be determined by a Gaussian fit, leading to

$$\sigma_{\text{peak}} = \sqrt{\sigma_{\text{det}}^2 + \sigma_{\text{Fano}}^2 + \sigma_{\text{split}}^2}\,. \tag{6.2}$$

Values for peak shift and broadening are listed in table 6.1. The peak is shifted by approximately 5 eV at a threshold setting of 6 σ_{det}/ 3σ_{det} and broadened by a noise component as large as 2.8 eV to 3.5 eV. At a photon energy of 600 eV, this results in an effective increase of the FWHM by 7 eV. As expected, with higher secondary threshold the impact is increased.

6.3. Energy calibration and gain linearity

In order to draw conclusions about the detector response regarding signal linearity, a precise energy calibration is needed. Hence, the electronic amplification function of the signal charge has to be known to high accuracy. As described in section 3.2 the CAMEX amplifies signal charge by generating an output voltage proportional to the number of signal electrons on the readout anode. This output voltage is digitized by the ADC into arbitrary digital units (adu). The conversion from electrons to adu is a quasi linear function that can be described by a conversion factor. This conversion factor g is called gain and is usually expressed in adu per eV, assuming a known mean electron-hole pair creation energy w. The digitized output signal S in adu as a function of energy E in eV is then

$$S(E) \approx g \cdot E \tag{6.3}$$

The CAMEX allows to program different amplification factors, each resulting in a different value for g. It can be calibrated by determining the peak position in adu of a spectrum recorded with monochromatic photons of known energy. However, the conversion function $S(E)$ of a real circuit is never perfectly linear over the full range of signal amplitudes. For the CAMEX IJD chips used for eROSITA-CCDs the deviation of amplification from a linear slope can be approximated by a quadratic term. In order to improve the accuracy of the spectral data evaluated in the course of this work, the conversion function $S(E)$ was determined and linearized as described below.

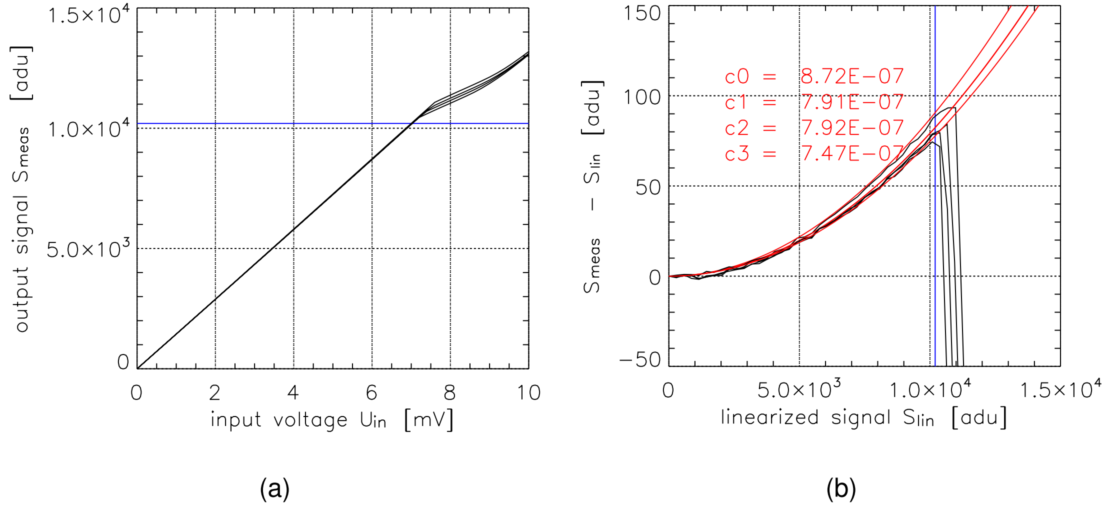

Figure 6.2.: The digitized output signal S_{meas} measured for a linear ascending input voltage U_{in} at the CAMEX. Both pictures show data for four exemplary channels of the CCD. (a) Saturation occurs above 10 200 adu *(blue line). The very small, quadratic nonlinearity of the digitized output signal is only visible in (b): Here, the deviation between measured and linearized signal is shown. The red lines represent the quadratic fit of the deviations as described in equation eq. 6.6 and their fit parameters c.*

Gain linearity measurements were performed in the semiconductor laboratory with the same detector board, and hence CAMEX chip, that was used for the experiments at BESSY II and MLS. Voltage pulses with linearly ascending amplitude U_{in} were applied to the input of the CAMEX amplification stage. Up to a saturation limit of about 10 200 adu, the output signal is highly linear, as shown in fig. 6.2a. The CAMEX output signal below this limit can be described by a quadratic function with a very small quadratic term:

$$S_{meas}(U_{in}) = a \cdot U_{in} + b \cdot U_{in}^2 \tag{6.4}$$

A quadratic fit was performed on the offset corrected (zero-based) input and output values of the voltage pulse measurement for each CCD channel in the range between 0 and 10 000 adu. Parameter *a* defines the linear part S_{lin} of the output function, therefore

$$S_{\text{lin}} = a \cdot U_{in}. \tag{6.5}$$

It is the purpose of the voltage pulse measurements to separate linear and quadratic terms of the output function to be able to linearize CAMEX output data in future photon measurements. For estimations of the difference between measured and linearized signal, the relationship resulting from eq. 6.4 and eq. 6.5 can be written as

$$S_{\text{lin}} = S_{\text{meas}} - c \cdot S_{\text{lin}}^2 \overset{*}{\approx} S_{\text{meas}} - c \cdot S_{\text{meas}}^2. \tag{6.6}$$

The coefficient *c* in the quadratic term of eq. 6.6 is in the range of 7×10^{-7} to 9×10^{-7}. The approximation (*) is gained from evaluating S_{lin}^2, neglecting all terms smaller than $\mathcal{O}(cS)^2$ as $cS \ll 1$. Figure 6.2b shows the deviation between measured and linearized adu signals as well as the values for *c* for four different CCD channels.
Voltage pulse measurements were performed with each channel of the CAMEX chip, resulting in a table mapping linear with non-linear output signals. This table is applied to each future PNCCD dataset, converting nonlinear to linear signal values. After this correction, the data analysis process as further described in this chapter is carried out. By using the linearized signal S_{lin} instead of S_{meas} the gain g can be easily calibrated by determining the peak position at a known photon energy, while providing high calibration accuracy. The gain in adu per eV is fixed by one calibration measurement per gain value. For the higher gain this is done at a photon energy E_{ph} = 3 keV. The fitted peak position in adu is calibrated to 2994 eV (value determined by the simulation described in chapter 9), resulting in a mean gain for all channels of g = 2.229 adu/eV. For the lower gain, a calibration at E_{ph} = 11 keV with an estimated peak position of 10 994 eV results in a gain of 0.580 adu/eV. The deviation between peak position and photon energy at these calibration energies is mainly due to the event threshold. All spectral measurements are evaluated with these gain values.
In the case of no linearity correction, the error due to nonlinear amplification of the CAMEX would be about 14 adu for offset-corrected signal amplitudes of 3000 adu, decreasing for higher and lower signals. This example includes a calibration at about 6500 adu, as the deviation between linearized and non-linearized data depends on the signal amplitude used for calibration. The amplification of the CAMEX was found to be highly linear and the impact of the nonlinearity correction rather small. Nevertheless, the described procedure was performed in order to allow for the analysis of peak shifts and peak widths with high accuracy.

6.4. Evaluation of monochromatic spectra

For the analysis and comparison of the spectral redistribution function at different photon energies and different total photon counts, the monochromatic spectra were normalized to unity. The lower limit of the energy interval for this normalization is defined by the primary event threshold $f_{\sigma,1}$ = $6\sigma_{det}$, depending on the mean readout noise and hence the gain (see table 6.2). The usage of a sufficiently high primary threshold, as described in section 6.2, ensures that the influence of the noise peak to the normalization is negligible. The upper limit of the normalization energy interval is chosen between the main peak and the first pile-up peak. Hence, pile-up events are not included in the normalized spectrum.

gain [adu/eV]	readout noise [e^-ENC]	lower event threshold [eV]
0.149	4.9	110
0.580	2.9	65
2.229	2.4	53

Table 6.2.: Overview on the mean readout noise during spectral measurements for given gain settings and during frame-wise reset mode. Out of all possible gain values, only the above listed were used. The lower event threshold is fixed to $6\sigma_{det}$ and here given in eV.

As the peaks in X-ray spectra derive from perfect Gaussian shape, a Gaussian fit is only a first approximation for the peak shape. A fit of the full peak shape requires specific models,

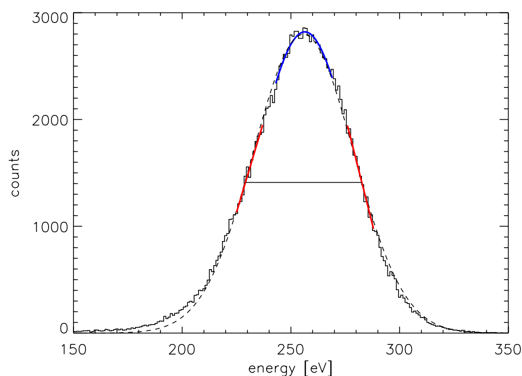

Figure 6.3.: A Gaussian fit (dashed black line) over the full photon peak deviates from the measured peak shape (solid black line). Therefore, the peak maximum and width are gained from a Gaussian fit over a small range (blue line) and linear fits of the peak flanks (red lines).

as described in section 11.1. For the evaluation of the energy resolution and signal linearity, the peak width and peak maximum can be determined by a more simple approach. The peak position, that is the peak maximum, in a spectrum are therefore determined by a least-squares fit of a Gaussian of the form

$$f(\epsilon) = a_0 \cdot exp\left(-\frac{z^2}{2}\right) \quad with \;\; z = \frac{\epsilon - a_1}{a_2}\,, \tag{6.7}$$

with peak position, or centroid, a_1, peak width a_2 and the height of the Gaussian a_0. The fit range around the peak is chosen to be as small as $\pm$ 1/4 · FWHM, so that the distortion from a Gaussian distribution is negligible. An exemplary spectrum with Gaussian fit is shown in fig. 6.3.
The peak width, or FWHM, is gained by a linear fit of the peak flanks, shown as red lines in fig. 6.3. This method leads to stable and comparable results at all photon energies.

6.5. Evaluation of the QE measurement with continuous spectrum

The synchrotron spectrum is a continuous photon spectrum over the full X-ray regime. It was used to perform a quantum efficiency measurement in single photon counting mode. The resulting datasets were evaluated by the standard analysis software, in the same manner as monochromatic spectra. A CTI correction was not performed, as the CTI varies with photon flux and photon energy, so that a correction based on calibration measurement data would not lead to an improvement of the data accuracy.

In order to evaluate a QE measurement, the spectral count rate determined with the PNCCD is compared to the theoretically predicted count rate. This predicted spectral count rate is calculated by folding the input spectrum with the detector response. The resulting count rate dN per energy bin $d\epsilon$ at a given position ϵ in the spectrum is then

$$\frac{dN}{d\epsilon}(\epsilon) = \int \frac{d\varphi(E)}{dE} \cdot QE(E) \cdot f_{\text{redist,E}}(\epsilon)\, dE\,. \tag{6.8}$$

$f_{\text{redist,E}}(\epsilon)$ denotes the spectral redistribution function for a photon energy E, evaluated at an event energy ϵ. $\varphi(E)$ is the photon flux depending on the photon energy. The integral is carried out over all energies in the synchrotron spectrum. The total sum of all events in $f_{\text{redist,E}}(\epsilon)$ for a given photon energy is 1 by definition. Therefore, the convolution of the synchrotron photon spectrum with f_redist,E leads to a redistribution of events in the spectrum, but keeps the total number of counts in the whole spectrum unchanged. In order to gain results with a high accuracy regarding the QE, the spectral redistribution function used for evaluation is modeled by interpolation of results from monochromatic measurements. For this purpose, the spectrum is divided into its components, namely flat shelf, fluorescence peaks and main peak. For the evaluation of a continuous spectrum it is important to account for the shift of the peak centroid rather than the peak shape. Therefore, the fluorescence peaks and the main peak are described by Gaussian distributions and the low energy shoulder is neglected. The flat shelf is modeled by a constant count rate between zero energy and the main peak. The Compton spectrum can be neglected as the photon flux for high photon energies is low. The parameters for peak positions, widths and the flat shelf count rate were determined from measured spectra and are listed in appendix B.2.

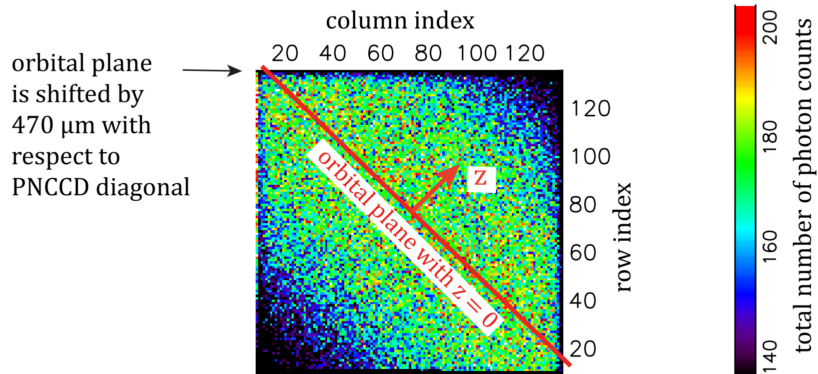

Figure 6.4.: Spatial distribution of the number of photon counts between 1.65 keV *and* 3 keV *for illumination with the continuous synchrotron spectrum. The count rate reaches a maximum in the (horizontal) orbital plane. Due to the* 45° *tilt of the detector, this is in diagonal direction on the PNCCD image. Due to limited accuracy during the detector adjustment, the orbital plane is shifted by* 470 µm *with respect to the detector diagonal.*

The measurement with continuous synchrotron spectrum can as well be used to determine the relative quantum efficiency variation over the detector area. The photon flux is a function of photon energy and the distance from the orbital plane, as illustrated in fig. 4.1. Figure 6.4 shows the count rate of photons with energies between 1.65 keV and 3 keV. The photon flux reaches a maximum in the (horizontal) orbital plane. Due to the 45° tilt of the detector, this is in diagonal direction on the PNCCD image. Due to limited accuracy during the detector adjustment, the detector diagonal is shifted with respect to the orbital plane. A shift of 470 µm from the orbital plane was determined from the photon flux distribution.

For the calculation of the relative QE variation, the measured count rate is normalized by the spectral flux of the synchrotron spectrum.

6.6. Determining an integrated signal with PNCCDs

As described in section 5.4, single event detection and recombination is not performed in integrating mode. The detector gain is determined in a separate calibration measurement and applied for the conversion of adu into energy, including a linearity correction as presented in section 6.3.
The mean signal measured with a PNCCD can be determined by subtracting the mean signal s_d of the dark frames from the mean signal s_{ph} of the signal frames. Both s_d and s_{ph} are determined by integrating all mean pixel values within a rectangular area on the CCD, closely surrounding the beam spot. In cases where the QE or attenuation factor are determined in a full frame measurement, the beam spot is smeared over the whole channel (see fig. 5.9c). In full frame mode, s_d and s_{ph} are determined by integrating only over all pixels in the illuminated channels. Integrating over the illuminated pixels instead of the whole PNCCD minimizes deviations caused by common mode fluctuations or straylight and background light at the beamline. A common mode correction is not performed, as the estimated impact is below few ‰. The mean rate ν_{e} of charge created in the detector is then

$$\nu_{\mathrm{e}} = \frac{s_{\mathrm{ph}} - s_d}{g \cdot w \cdot t_{\mathrm{cyc}}} \,. \tag{6.9}$$

g is the detector gain, w is the mean pair creation energy and t_{cyc} the cycle time. Statistical deviations, caused by fluctuations in the number of photons detected per pixel, are negligible for this kind of measurement due to the high number of detected photons.

7. Attenuation of visible light and UV radiation by the on-chip filter

7.1. Measurement results

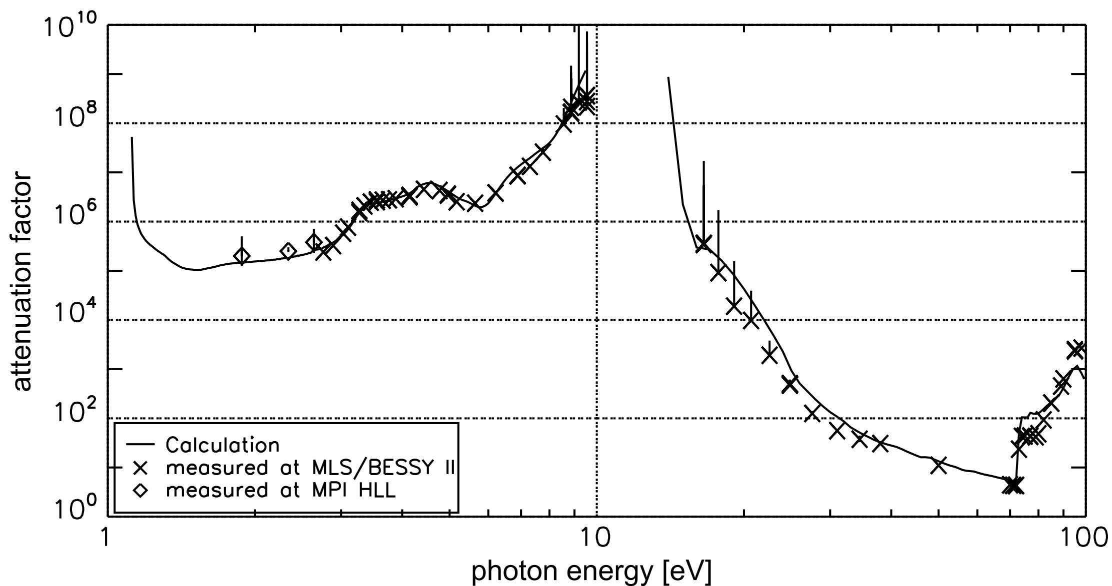

Figure 7.1.: Attenuation factor of the eROSITA entrance window with on-chip filter in the optical and UV energy regime. The line represents a calculation including photon absorption in all layers and taking into account the thin film structure of the aluminum layer. Measurements at MLS/BESSY II and at the Semiconductor Laboratory (MPI HLL) are displayed.

The attenuation of optical and UV radiation by an eROSITA PNCCD with on-chip filter was mainly measured at the monochromators at BESSY II and MLS (see section 5.4.2). Although single photon counting with eROSITA PNCCDs is possible down to 70 eV, the measurement of UV and optical attenuation requires the operation of the PNCCD in integrating mode. This means that the total integral of photons over an area of several pixels is determined and compared to a reference diode signal. Additional measurements with LEDs and laser light using CCDs or photodiodes were conducted to prepare and complete the synchrotron measurements (see section 5.3 and section 5.4.1). Figure 7.1 shows the results of attenuation measurements at BESSY II and MLS as well as those determined with LED and laser illumination at three different wavelengths at the MPI Semiconductor laboratory (see also table 5.1). Tabulated values and a discussion of the measurement uncertainty can be found in appendix B.1. As shown in fig. 7.1, the filter attenuates visible light by a factor of more than 10^5. Above 3 eV, up to 10 eV, the attenuation rises due to strong absorption of all filter materials, namely aluminum, SiO_2 and Si_3N_4. As presented in section 2.2, the aluminum absorption coefficient

decreases abruptly at the plasma frequency of 15.8 eV. The attenuation factor in the range between 15 eV and 73 eV decreases, reaching values of less than 10. At 73 eV, the aluminum-L absorption edge leads to an abrupt increase of absorption and hence attenuation by the blocking filter. It is further increased at the silicon-L absorption edge at 100 eV, due to absorption in the SiO_2 and Si_3N_4 layers.
The solid line in fig. 7.1 shows an empiric calculation that takes into account the non-bulklike properties of the aluminum layer. A detailed analysis of the morphology of the aluminum film and a description of the calculation method is described in the following sections.

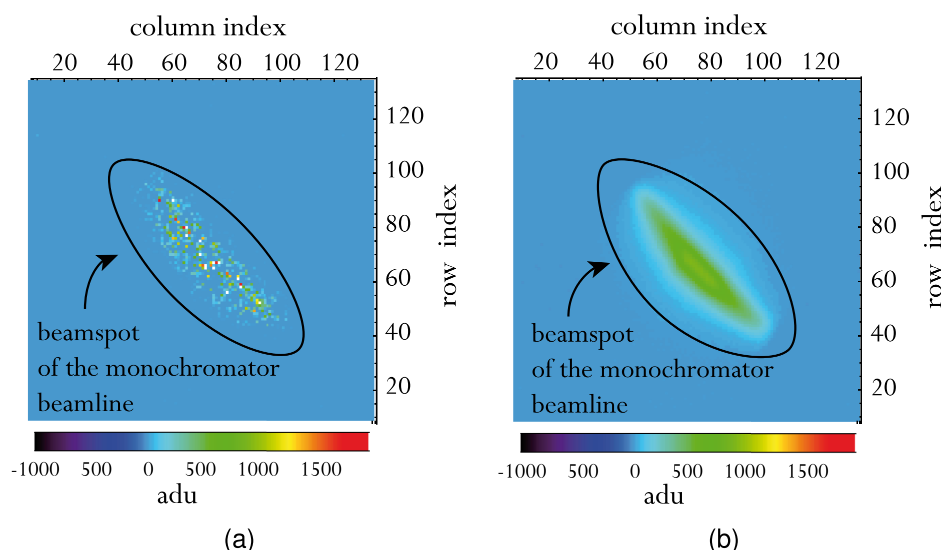

Figure 7.2.: Measured photon intensity for illumination with monochromatic photons at the MLS. (a) E = 3.45 eV: The high absorption coefficient of aluminum in the visible light reveals pixel-wise inhomogeneities in the attenuation factor. These variations are not caused by photon statistics but are fixed in position on the PNCCD. The attenuation factor of the brightest pixels is still above 2×10^5. (b) E = 24.8 eV: The aluminum is almost transparent at this photon energy and no inhomogeneities are visible.
In order to examine the pixel wise attenuation factors, a measurement with homogeneous illumination was performed at the Semiconductor Laboratory, as shown later in fig. 7.6.

The attenuation factor as shown in fig. 7.1 represents a mean value determined over an area of about 2 $\times$ 4 mm. The illuminated area during the measurement at the MLS storage ring, the beam spot, was adjusted by slits and apertures at the monochromator. This beam spot is shown in fig. 7.2 at photon energies of 3.45 eV and 24.8 eV. It comprises in both cases approximately 20 $\times$ 50 pixels. The PNCCD image in fig. 7.2a exhibits pixel-wise variations of the measured photon flux, in contrast to the image at 24.8 eV in fig. 7.2b. These variations are due to the aluminum microstructure and only visible at photon energies where aluminum is strongly absorbing (see also aluminum absorption data in appendix A). The observed pixel variations showed to be fixed in position even when moving the beam spot. Statistical variations in the measured photon number are negligibly small compared to the observed variations.
It is clear that a thin film showing such variations in attenuation does not exhibit bulk-like properties. The microstructure of the aluminum film and its impact on both optical and UV attenuation thus has to be analyzed.

7.2. The aluminum thin film structure

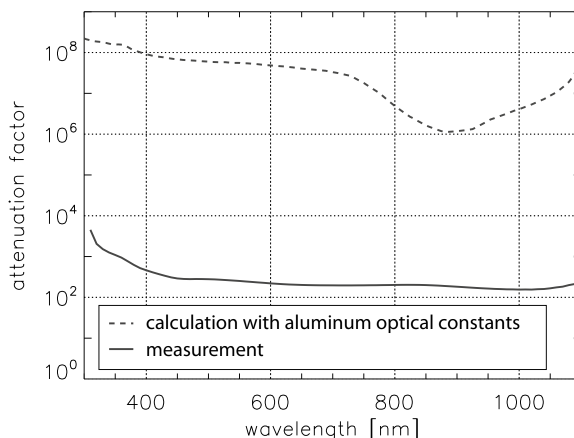

Figure 7.3.: The calculated attenuation of 100 nm *aluminum using bulk optical constants compared with measurement results for an on-chip filter with* 100 nm *aluminum layer. The strong deviation shows that the optical properties of the aluminum layer can not be described with bulk optical constants.*

In order to understand the blocking properties of the on-chip filter for eROSITA, measurements with PNCCDs and photodiodes with different on-chip filter types were performed. As explained in section 2.3, the optical properties of thin metal layers are different from those of bulk aluminum. Two types of effects may cause a change in the observed optical properties of thin films. First, intrinsic effects, such as a change in the band structure, can alter the dielectric function of a thin film material. Second, so-called structural effects such as voids and surface roughness lead to a deviation of the properties with respect to bulk values.

The extent of the observed differences between thin film and bulk aluminum optical properties are illustrated in fig. 7.3. It shows the attenuation factor in dependence of the wavelength for an on-chip filter with 100 nm aluminum on top of the Si_3N_4 and SiO_2 layers. The attenuation factor is predominantly defined by the absorption in the aluminum layer. Absorption and reflection in oxide and nitride layers causes an attenuation by a factor of 1.7 at maximum in the optical regime and is therefore neglected in the following considerations. The dashed line shows a calculation including reflection and absorption on the basis of bulk aluminum optical constants. The measured attenuation for an entrance window with 100 nm aluminum is displayed by a solid line. This measurement was commissioned at the calibration laboratory Gigahertz GmbH (see section 5.3). Both curves differ by four to five orders of magnitude. Furthermore, the calculation shows a distinct structure around 900 nm. This structure is formed by the parallel-band effect in aluminum, where the photon energy is equal to the energetic distance of parallel band sections in the band structure (see fig. 2.4b). This leads to an increase of the absorption coefficient and hence the attenuation factor between 900 nm and 750 nm (see fig. 2.5b). The measured curve exhibits no such parallel-band feature.

Intrinsic and structural effects in the thin film can lead to a quantitative and qualitative change of the attenuation curve. A reduced electron mean free path, caused by the granular structure of the thin film, leads in general to a blurring of the parallel band feature (Niklasson et al., 1986). However, a reduced electron mean free path also causes an increase instead of a reduction of the absorption coefficient. This and other intrinsic effects discussed in section 2.3,

as for example a change of the lattice structure, can not solely explain the large absolute deviation of more than four orders of magnitude observed between calculation and measurement. The microstructure of the thin film was therefore subject to further investigations.
The aluminum film on the eROSITA entrance window is deposited by sputtering. A sputtered metal film forms grains on the substrate, whereas the size of such grains depends on several processing parameters (see for example Nguyen et al., 1993). Conclusively, there can be voids in between the metal grains of a layer.
The observed inhomogeneities in light attenuation on the scale of micrometers in fig. 7.2 suggest the presence of such microstructural voids inside the material. This would explain a decreased mean attenuation and a variation over detector area. In the course of detector development at the Semiconductor Laboratory, the aluminum layer of the on-chip filter was deposited in two layers instead of one layer. As long as the growth of grains and voids does not propagate into the next layer, highly transmitting microstructural voids in one layer are covered by the other layer. A component with such a two-layer aluminum blocking filter was analyzed by transmission electron microscopy (TEM), by cutting a thin lamella into the material. Figure 7.4 shows the TEM image of a lamella in cross sectional direction through the entrance window. The contrast in this image is formed by the amount of transmitted electrons. It shows, however with partially weak contrast, the granular structure of polycrystalline material.

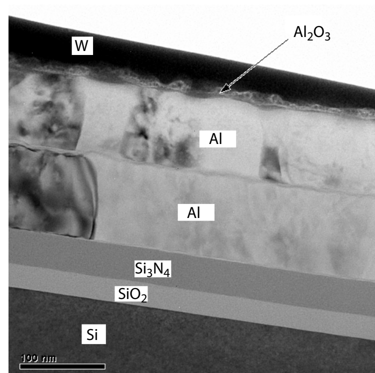

Figure 7.4.: TEM image of the blocking filter, consisting of SiO_2, Si_3N_4 and two layers of aluminum. In this picture, areas with different lattice orientation appear in different brightness. The granular structure of the aluminum film is visible. The grain size is in the order of the layer thickness and many grains extend throughout one aluminum layer, but do not propagate into the second aluminum layer. No voids are visible in the picture and silicon grains can not be distinguished from aluminum grains due to lacking contrast. The TEM image was commissioned at Infineon Technologies AG.

Figure 7.4 shows that the grain size in the aluminum is in the order of the layer thickness. Small voids between these grains can lead to the observed increase in transmission. These voids do not necessarily appear at all grain boundaries and are not visible in the TEM image. However, it can be seen that the grains in one layer do not propagate into the second aluminum layer. Therefore, light transmitted through voids between grains can only pass one layer and are blocked by the other.
The aluminum of the on-chip filter is sputtered together with a fractional amount of $1\,\%$ of silicon to increase the adhesion on the substrate. As described in Niklasson et al. (1986), the solubility of silicon in aluminum is practically zero, which causes both materials to separate while cooling down and forming grains of crystalline aluminum and probably amorphous

particles of silicon. The resulting grain size decreases with increasing silicon fraction. The existence of silicon grains in the aluminum can not be resolved by the image shown in fig. 7.4. However, optical inspection of aluminum on-chip filters during the production process at the MPI Semiconductor Laboratory showed silicon grains on the scale of µm in the aluminum layer.

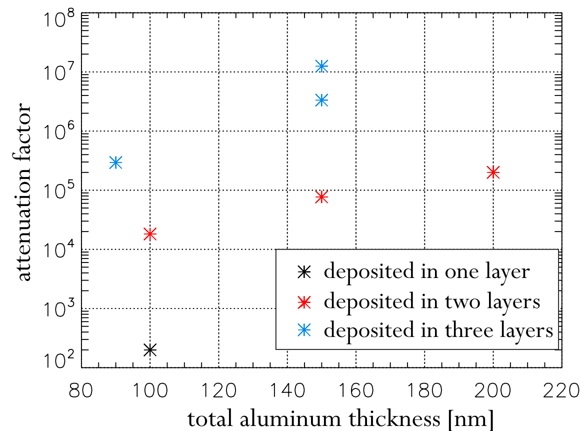

Figure 7.5.: Attenuation factor versus thickness of on-chip aluminum layer of photodiodes. The measurements were performed using a laser diode with λ = 660 nm, *as described in section 5.3. In order to achieve better attenuation values, aluminum layers were deposited in several separate steps in the course of technology development at the MPI Semiconductor Laboratory. The measured attenuation depends less on the total aluminum thickness, but strongly on the number of layer deposition steps.*

Attenuation measurements with photodiodes of different number of layers and thicknesses were performed. For this purpose, the laser setup as described in section 5.3 was used. The results for different total aluminum thicknesses, deposited in one, two or three layers, are shown in fig. 7.5. The total aluminum thickness of all deposited layers is given on the x-axis, ranging between 90 nm and 200 nm. The measurement results reveal that by depositing an aluminum layer in two or three steps, a significant increase in attenuation can be achieved at the same total aluminum thickness. In contrast to that, an increase in layer thickness has only small effect. Conclusively, a large amount of light is transmitted through voids and silicon grains in the aluminum layer. This can be mitigated by depositing an additional aluminum layer on top.
On basis of the presented findings, the properties of the on-chip filter can be explained by microstructural voids and silicon grains inside the aluminum layer. Both silicon grains and voids can extend through the full single aluminum layer. Only in this case, a deviation from bulk optical constants as strong as the observed one can be explained.

7.3. An empiric description of the attenuation factor

The attenuation of the eROSITA blocking filter, dominated by the non-bulklike properties of the aluminum layer, can only be described by an empiric model. Such a calculation includes the quantum efficiency of a detector without aluminum filter and the absorption in an aluminum

layer with voids and silicon grains.
First of all, the quantum efficiency of a PNCCD with an SiO_2 and Si_3N_4 entrance window can be determined to high accuracy with a calculation accounting for multiple reflections and interference (Hartmann et al., 2006), shortly described in section 2.3.
The attenuation factor is calculated from the inverse of the quantum efficiency $QE_{\text{nit,ox}}$ (see notes to eq. 3.9) of a PNCCD without aluminum and the transmittance T_{Al} of the aluminum layer according to

$$\chi = (T_{\text{Al}} \cdot QE_{\text{nit,ox}})^{-1} \ . \tag{7.1}$$

To estimate the aluminum transmittance, an area fraction f_{voids} of completely transparent voids and f_{Si} of silicon grains are introduced, both extending throughout one aluminum layer. These area fractions are free parameters of the model and are adapted to the measurement results later. A filter can be composed of several aluminum layers, with mutual independent distributions of voids or silicon grains. Based on eq. 2.12, the transmittance of the aluminum filter T_{Al}, consisting of n layers, is estimated by

$$T_{\text{Al}} = (1 - R_{\text{Al}}) \left(f_{\text{Al}} \cdot exp(\frac{-4 \cdot \pi \kappa_{Al} d}{\lambda}) + f_{Si} \cdot exp(\frac{-4 \cdot \pi \kappa_{\text{Si}} d}{\lambda}) + f_{\text{voids}} \right)^n \ . \tag{7.2}$$

As f_{voids} and f_{Si} are very small, it can be assumed that the area covered with aluminum, f_{Al}, is approximately unity. The idea of eq. 7.2 is to assess the influence of voids and silicon grains on the attenuation throughout the optical and UV energy regime. This model is able to explain a drastic deviation from an ideal aluminum layer regarding the amount of absorbed light in the optical regime. It also includes the strong absorption of silicon in the UV regime. Reflection compared to absorption is only of secondary importance. In this simplified model, only the reflection at the boundary between air/vacuum and the aluminum entrance window is taken into account by R_{Al}. Any reflection between aluminum layers and the Si_3N_4 is not explicitly calculated, but subsumed in the parameters of the model. With increasing photon energies in the UV reflection gets negligibly small, it is already less than 1 % at 30 eV. Absorption in all layers is taken into account by the exponent n in eq. 7.2.

The values $f_{\text{voids}} = 4 \times 10^{-3}$ and $f_{\text{Si}} = 5 \times 10^{-3}$ are used for the calculation shown as a solid line in fig. 7.1 and reproduce well the measured attenuation factor. The overall decrease in attenuation compared to ideal aluminum can be explained by voids with an area fraction of 4‰. At the low energy limit of the visible spectrum in fig. 7.1, for photon energies below 1.2 eV, the decreasing amount of absorption in the detector silicon bulk leads to an effective increase of the attenuation.
It is important to notice that the agreement throughout the photon energy range from visible light to UV radiation can only be achieved by taking into account not only voids but also silicon grains in the aluminum layer. Compared to aluminum, silicon is quite transparent to optical light, as can be seen from their absorption length in appendix A. However, silicon is strongly absorbing in the vicinity of the parallel-band points at 3.5 eV and 4.3 eV (see fig. 2.5). The rise of the attenuation curve in fig. 7.1 at the parallel-band points of silicon can not solely be explained by absorption in the SiO_2 and Si_3N_4, but only by additional silicon grains in the aluminum.

Equation 7.2 is not only valid for the optical and UV energy regime, but can also be evaluated in the X-ray regime. However, the amount of X-ray radiation transmitted through aluminum is high and therefore voids and silicon grains with an area fraction of only a few ‰ have no measurable influence on the attenuation factor, i.e. the quantum efficiency.

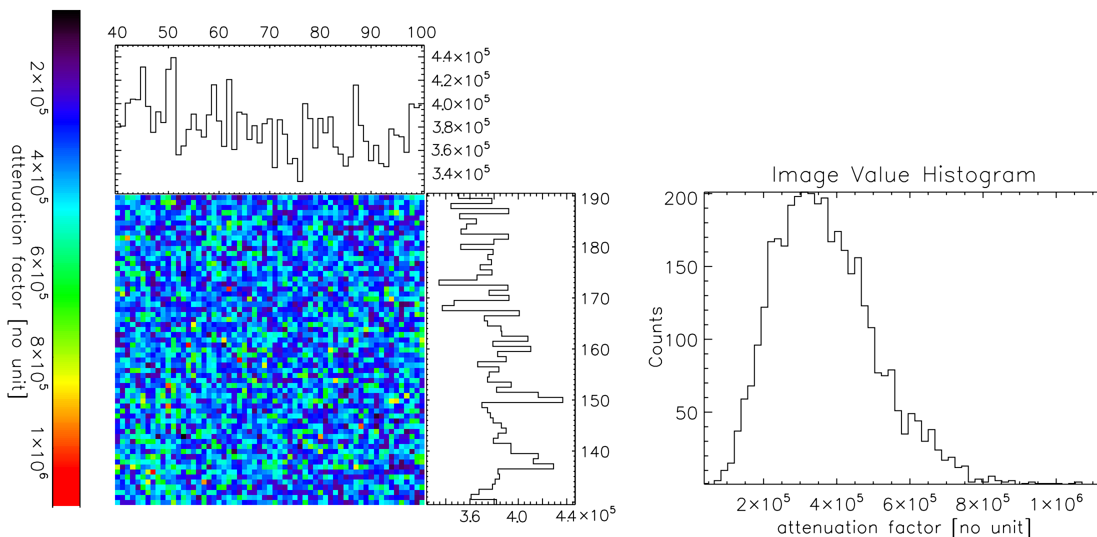

Figure 7.6.: Attenuation measurement with an eROSITA PNCCD with an aluminum layer thickness of 200 nm*, deposited in two steps. The detector is homogeneously illuminated with an LED* (λ = 470 nm)*. The pixel map (left hand side) shows the obtained values of the attenuation* χ *for each pixel, restricted to an area on the PNCCD where homogeneous illumination was achieved. The histogram (right hand side) shows the distribution of the attenuation values from the pixel map. The mean attenuation factor is* $A = 3.8 \times 10^5$*. The reason for the observed fluctuations in attenuation values lies in the aluminum microstructure.*

The described model, assuming area fractions of voids and holes in the aluminum, gives no further information about the mean size of single voids and silicon grains. The size of these structures can be estimated from the spatial homogeneity of the attenuation factor on the PNCCD. As the beam spot at the MLS storage ring is of arbitrary shape, it is not suitable to quantify pixel wise variations of the attenuation factor. Therefore, a setup at the Semiconductor Laboratory was optimized for homogeneous illumination with LEDs (see section 5.4.1).
Figure 7.6 shows the pixel-wise attenuation factors at a wavelength of 470 nm, measured with LED light at the RÖSTI facility. Around a mean of $\chi = 3.8 \times 10^5$, the attenuation takes values with a mean deviation of $-29\,\%$ and $+76\,\%$. The asymmetry of the pixel distribution shown on the right side of fig. 7.6 can be explained by the 2-layer structure of the aluminum film. The overlay of two holes, independently distributed in each layer, leads to very low attenuation factors, however observed with very low probability.
The measurement results displayed in fig. 7.6 show that the mean number of voids per pixel of an aluminum layer is significantly larger than one, elsewise the pixel-to-pixel variation of the attenuation factor would vary by several orders of magnitude between pixels with no voids or at least one void. To estimate the distribution of holes, eq. 7.2 is evaluated at a photon energy of 470 nm for 2 layers with each 100 nm thickness:

$$\chi = 14.2 \cdot \left(f_{\mathrm{Al}} \cdot 2.3 \cdot 10^{-7} + f_{Si} \cdot 0.72 + f_{\mathrm{voids}}\right)^{-2} \propto f^{-2} \,. \tag{7.3}$$

The light transmitted through aluminum at this photon energy can be neglected, and both voids and silicon grains contribute almost equally to the resulting photon intensity. Both parts can be subsumed to an effective area fraction of structural defects of $f = f_{Si} \cdot 0.72 + f_{\mathrm{voids}}$. The attenuation is therefore proportional to f^{-2} and f has a mean value of 0.008.
Assuming a diameter of about 1.5 µm for circular defects leads to a mean number of defects of about $n = 25$ per pixel for a pixel size of $75 \times 75\,\mu m^2$. According to the Poisson distribution, the mean deviation in the number of defects per pixel is then $\Delta n = 5$ (see eq. 3.12). According to eq. 7.3 a variation of the defect area fraction f by a factor of $\frac{\Delta n}{n}$ leads to a spread of the attenuation factor between $-31\,\%$ and $56\,\%$ with respect to the mean value. Comparing this with the measured spread, between $-29\,\%$ and $+76\,\%$, shows a good agreement. It seems likely that the voids and silicon grains inside the aluminum layer have a size on the order of a single µm and the number is on the order of 25 per pixel. Naturally, the real morphology of the aluminum structure will be more complex, with voids and silicon grains of different size.

The previous considerations show that the attenuation factor of eROSITA PNCCDs, caused by the aluminum on-chip filter, can be explained by the microstructure of the aluminum thin film. Due to the low absorption in the X-ray regime, the structure of the aluminum layer does not alter the X-ray quantum efficiency of the detector compared to bulk aluminum.

8. Analysis of X-ray quantum efficiency measurements

The eROSITA X-ray quantum efficiency was measured in the course of this work employing two different synchrotron beamlines. One of these beamlines provided monochromatic radiation, while the other delivered radiation of a continuous spectrum. Through the different experimental methodology and data evaluation techniques these two measurement types complement each other and serve as cross check.
The quantum efficiency of eROSITA PNCCDs, the ratio of detected to incident photons, is derived from the product of the transmittances of all insensitive entrance window layers (see eq. 2.12) and the amount of absorbed radiation in the silicon bulk (see eq. 2.23). This results in:

$$QE = (1 - \exp(-\mu_{Si}\rho_{Si}d_{Si})) \cdot \prod_{i=1}^{3} \exp(-\mu_i \rho_i d_i) \ , \tag{8.1}$$

with indexes Si for silicon and i for the nonsensitive entrance window layers SiO_2, Si_3N_4 and aluminum. The amount of absorbed radiation depends on the density ρ, mass absorption coefficient μ and the thickness d of the layer.
The calculation above assumes that every absorbed photon causes a count in the measured spectrum. This approach gives a good estimate for the total quantum efficiency, which includes by definition all photon counts in the spectrum. Silicon escape events and flat shelf events generated in the silicon are therefore comprised in this definition of the quantum efficiency. Aluminum fluorescence photons generated in the entrance window are not part of the calculation, but can be neglected, as they amount only up to 3 ‰ of the total number of events. Additional flat shelf events caused by photo- and Auger electrons from the insensitive entrance window layers are also not included, but contribute only with about 1 % (see section 11.1). Only directly above the silicon K-edge and for photon energies below 400 eV, the fraction of shelf events in the spectrum increases to up to 4 %. However, this is on the same order as the accuracy of absorption data, as shown in the following section.
Mass absorption coefficients or interaction cross sections against photon energy are published in literature. In order to achieve the best description of the quantum efficiency, a mixture of different data sources is used for the presented calculations. For almost all photon energies, interaction cross sections by Cullen et al. (1997) were used, applying the preprocessing tool by Cullen (2010). These data refer to elements in atomic state, not reflecting the specific properties of crystals or chemical compounds. Coefficients for Si, SiO_2 and Si_3N_4 including the absorption edge fine structure around the silicon K-edge are taken from Owens et al. (2002). Empiric values for the absorption coefficient of SiO_2 for X-ray energies below 155 eV are furthermore taken from Palik (1985).
The measurement results presented in the following section deliver findings on the near-edge structure of the eROSITA quantum efficiency. In section 8.2, a comparison and evaluation

of QE measurements and calculations is given. An evaluation on the homogeneity of the quantum efficiency over the detector area is presented in section 8.3.

8.1. Absorption edge fine structure

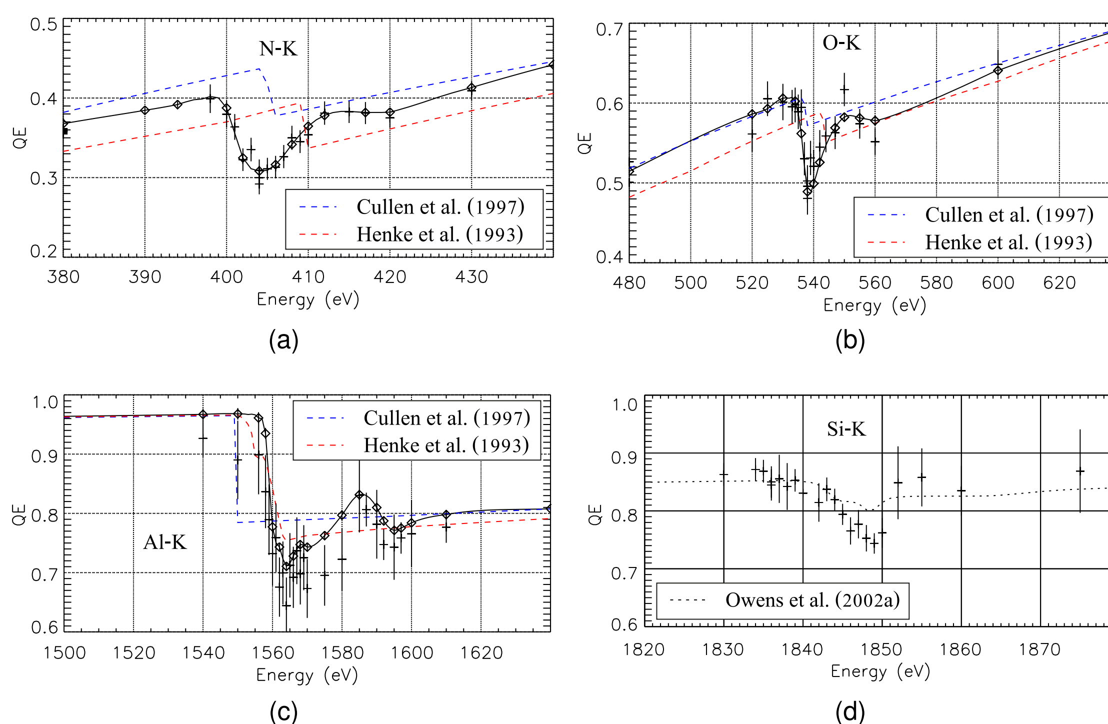

Figure 8.1.: Quantum efficiency around the K-shell absorption edges of O, N, Al and Si for a PNCCD with eROSITA entrance window including on-chip filter. Crosses mark PNCCD measurement data, diamonds represent data derived from photodiode measurements. The solid line connects the diode values as a guide to the eye. The dashed lines show QE calculations using literature data from different sources. Cullen et al. (1997) and Henke et al. (1993) sources are based on atomic material properties and do not take into account fine-structure or edge-shift in chemical compounds.

As mentioned in section 2.4, edges in the photon absorption cross sections of elements appear at energies equal to the specific electron binding energies. These absorption edges are therefore visible in the quantum efficiency curve of PNCCDs. The electron binding energies of condensed matter or compounds compared to free atoms may be shifted by several eV, leading to a shift of the absorption edges. Furthermore, an oscillatory structure exceeding several tens to hundreds of eV above the edges is present in the absorption cross sections of condensed matter. This modulation of the absorption probability is referred to as XANES and EXAFS. As described in section 2.4, its oscillatory structure is characteristic for the condensed state of a material, e.g. the lattice constant.
In order to gain a full picture of the eROSITA quantum efficiency, measurements with high energy resolution were performed around the absorption edges. For this purpose, monochromatic radiation was used, operating the PNCCD in integrating mode. A description of the

applied data analysis method is given in section 6.6. In addition, photocurrent measurements with a diode of the same entrance window were performed. Figure 8.1 shows the quantum efficiency measured with the PNCCD and photodiode. The data points measured with the photodiode are connected by a solid line in fig. 8.1, showing clearly the oscillating structure behind the absorption edges. Due to the high photocurrent and therefore low statistical error, the diode instead of the PNCDD was used to scan the absorption edge structure in steps of 1 eV.
Figure 8.1a to 8.1d show a strong decrease in quantum efficiency directly above the edges followed by an oscillating structure. The **nitrogen-K** absorption edge in Si_3N_4, shown in fig. 8.1a, is located at 401 eV. Its position is shifted to lower energy compared to the atomic value of 410 eV (see also table 2.3). The **oxygen-K** edge in SiO_2 is found at 537 eV in fig. 8.1b, instead of 543 eV for atomic oxygen. These results match the findings of Prigozhin et al. (1998), who also determined the QE of X-ray detectors containing Si_3N_4 and SiO_2. The **aluminum-K** edge in fig. 8.1c is located at 1559 eV, which is very similar to the tabulated value of 1558 eV for aluminum in condensed state. According to Prigozhin et al. (1998), the **silicon K-edge** of the eROSITA QE is expected to split into two parts, at an energy of 1847 eV and 1845 eV, due to absorption in the SiO_2 and Si_3N_4 respectively. The QE determined from photodiode measurements is missing in fig. 8.1d, as it is corrupted by a drift in the reference dark current and hence not further evaluated. The quantum efficiency directly above the silicon-K edge has already been measured by Hartmann et al. (1999) with an XMM PNCCD.
The red and blue dashed lines in fig. 8.1a to fig. 8.1c show the calculated quantum efficiency according to eq. 8.1 with two different data sources. As expected, calculations based on such atomic absorption coefficients do not fully agree with the measured quantum efficiency around the absorption edges. The black dotted line in fig. 8.1d is based on data published by Owens et al. (2002), who determined the absorption coefficients for SiO_2 and Si_3N_4 around the Si-K edge from total photocurrent measurements. However, even this calculation deviates from the measurement results at energies close to the silicon K-edge. The absorption coefficients by Owens et al. (2002) were determined from photocurrent measurements, assuming the proportionality between the absorption coefficient and the created photocurrent. This assumption includes an electron yield close to unity and neglects the effect of silicon escape events. The comparability of Owens et al. (2002) data with the measurement results is therefore still limited.
A calculation of absorption coefficients from the photocurrent data was not performed. It is argued if the observed fine structure in photocurrent measurements is only part of the absorption cross section, or if it occurs through indirect processes such as reabsorption of Auger electrons and fluorescence radiation (see also Cho et al. (1988), Owens et al. (1997)). Therefore, the calculation based on atomic data is also performed in all following quantum efficiency curves.

8.2. The quantum efficiency between 200 eV and 10 keV

Quantum efficiency measurements were performed throughout the energy range of interest for eROSITA. The measurements with monochromatic radiation were conducted in **integrating mode** with a PNCCD and a photodiode with eROSITA entrance window. They are shown in fig. 8.2 as crosses and diamonds respectively. The measurement uncertainty is indicated by vertical bars through the data points. Tabulated values and a discussion of the measurement

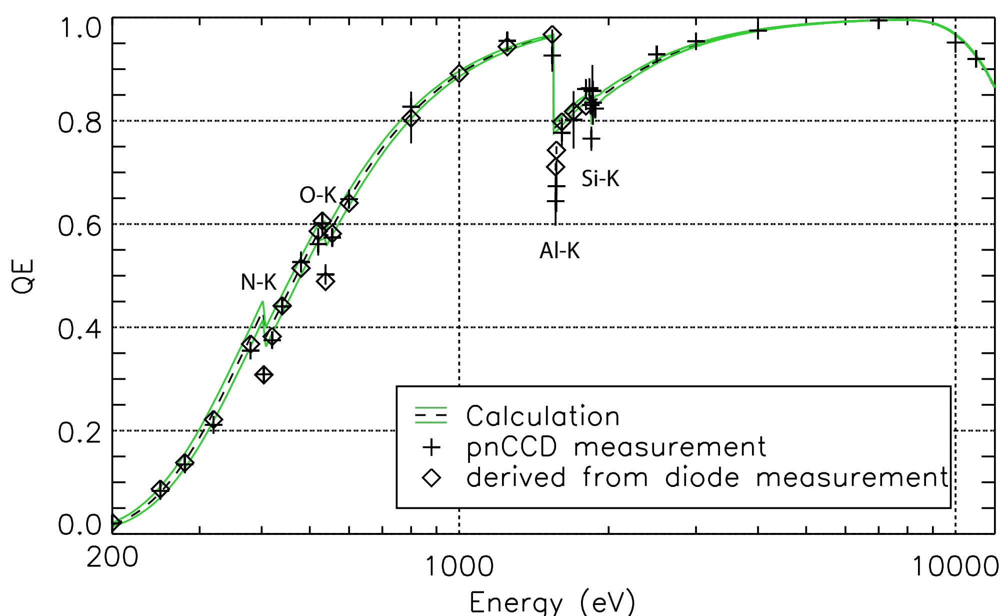

Figure 8.2.: Measured and calculated QE of detectors with eROSITA entrance window including aluminum on-chip filter. The dashed line shows the calculation according to eq. 8.1. The maximum variation of this calculation due to the uncertainty of layer thicknesses is shown by green solid lines. The shown measurement data points are gained from monochromator measurements with a PNCCD and a photodiode of the same entrance window. Apart from the absorption edges, already shown in fig. 8.1, measurement and calculation show high agreement.

uncertainty can be found in appendix B.1. The calculation based on eq. 8.1 is displayed as a dashed black line. The uncertainty in layer thickness due to processing of the entrance window is on the order of $\pm$ 5 %. A thereby caused variation of the quantum efficiency is indicated by green solid lines.

The quantum efficiency is above 85 % for photon energies between 2 keV and 11 keV, and above 50 % in the range between 500 eV and 1 keV. For lower photon energies, absorption mainly in the aluminum, but also in the silicon dioxide and silicon nitride layers leads to a drop of the quantum efficiency. It furthermore causes four absorption edges at the binding energies of the oxygen-K, nitrogen-K, aluminum-K and silicon-K shell. The fine structure around the absorption edges was already discussed in section 8.1.
At X-ray energies above 8 keV, an increasing fraction of photons traverse the silicon bulk without being absorbed, leading to a decrease of the quantum efficiency. Except for the absorption edges, where a deviation between measurement and calculation is expected, both curves show very good agreement.
At energies around 800 eV, the photon spectrum at the SX700 monochromator is significantly polluted by higher order radiation (also observed in quantum efficiency measurements by Prigozhin et al. (1998)). An adapted evaluation including the estimated straylight fraction, as mentioned in section 5.4.2, was applied for the data point shown at 800 eV in fig. 8.2.

For the evaluation of quantum efficiency measurements in integrating mode, eq. 5.3 was used, where the mean number of generated electrons is determined directly from the photon energy

E_{ph} (in contrast to the previous method described in Ebermayer et al. (2010)). By this approach, the reduced energy deposit of off-peak events, such as flat shelf, shoulder and silicon escape events, is not taken into account and the quantum efficiency is slightly underestimated. Electron loss by flat shelf events can be neglected, as the charge loss of those electrons leaving the silicon is compensated by those entering from the silicon oxide layer. Although partial charge loss in the ICC-layer is observed as a low energy shoulder in the spectra shown later in chapter 10, the total collected charge in integrating mode is presumably recovered by the saturation of traps or reemission of charge carriers. To avoid overcorrection of the data, a reduced energy deposit by partial charge loss in the ICC layer is thus also not taken into account. The charge loss by silicon escape events is neglected due to the low accuracy of absorption data at energies closely above the Si-K edge, as mentioned in section 8.1, inhibiting the precise validation of the results. In order to verify the chosen evaluation method, the results of the measurement in integrating mode are compared with those of a measurement in single photon counting mode.

All quantum efficiency results shown to this point were performed at the monochromator beamlines of BESSY II, operating the PNCCD in integrating mode (see section 6.6). An additional quantum efficiency measurement was performed using an **continuous synchrotron spectrum** instead of monochromatic radiation. As described in section 4.4, the spectral flux of a synchrotron spectrum can be calculated and serves as primary radiation source, without the need of a calibrated reference detector. The photon rate during this experiment was adjusted through the storage ring current in order to allow for **single photon counting**.
As discussed in section 3.5.1, X-ray photons create off-peak spectrum entries, causing for example the flat shelf, the escape peak and fluorescence peaks. In a measurement with a continuous synchrotron spectrum, the off-peak events caused by photons of higher energies accumulate at lower event energies in the spectrum. Conclusively, it is not possible to assign each event in the resulting spectrum to its original photon energy. Due to the described ambiguity, the quantum efficiency is not directly determined from such a measurement. Instead, a comparison between measurement and a data driven prediction of the spectrum allows to assess an existing quantum efficiency calculation. In order to create such a prediction for the measured spectrum, the incident spectrum is convoluted with a data driven model of the spectral response of the detector. The incident synchrotron spectrum during the measurement is calculated and provided by the Physikalisch-Technische Bundesanstalt (PTB). The response model contains the quantum efficiency calculation and a parameterized description of the spectral redistribution function, as presented in section 6.5. The impact of pile-up was estimated prior to the measurements to be less than approximately $1\,\%$. The measurement result shows a fraction of invalid patterns of $0.96\,\%$. These invalid events are presumably caused by pile-up and excluded from the spectrum. As the original photon energies of such events can not be identified, a fraction of $1\,\%$ is added to the overall error estimation.

The continuous spectrum measured at BESSY II is shown as a black line in the upper panel of fig. 8.3. The incident synchrotron spectrum during the measurement, calculated and provided by the Physikalisch-Technische Bundesanstalt (PTB), is indicated as blue line. The data driven prediction for the measured spectrum according to eq. 6.8 is illustrated by a dashed red line.
The lower panel of fig. 8.3 displays the relative deviation between measured and predicted spectrum. It shows very good agreement throughout the analyzed photon energy range. De-

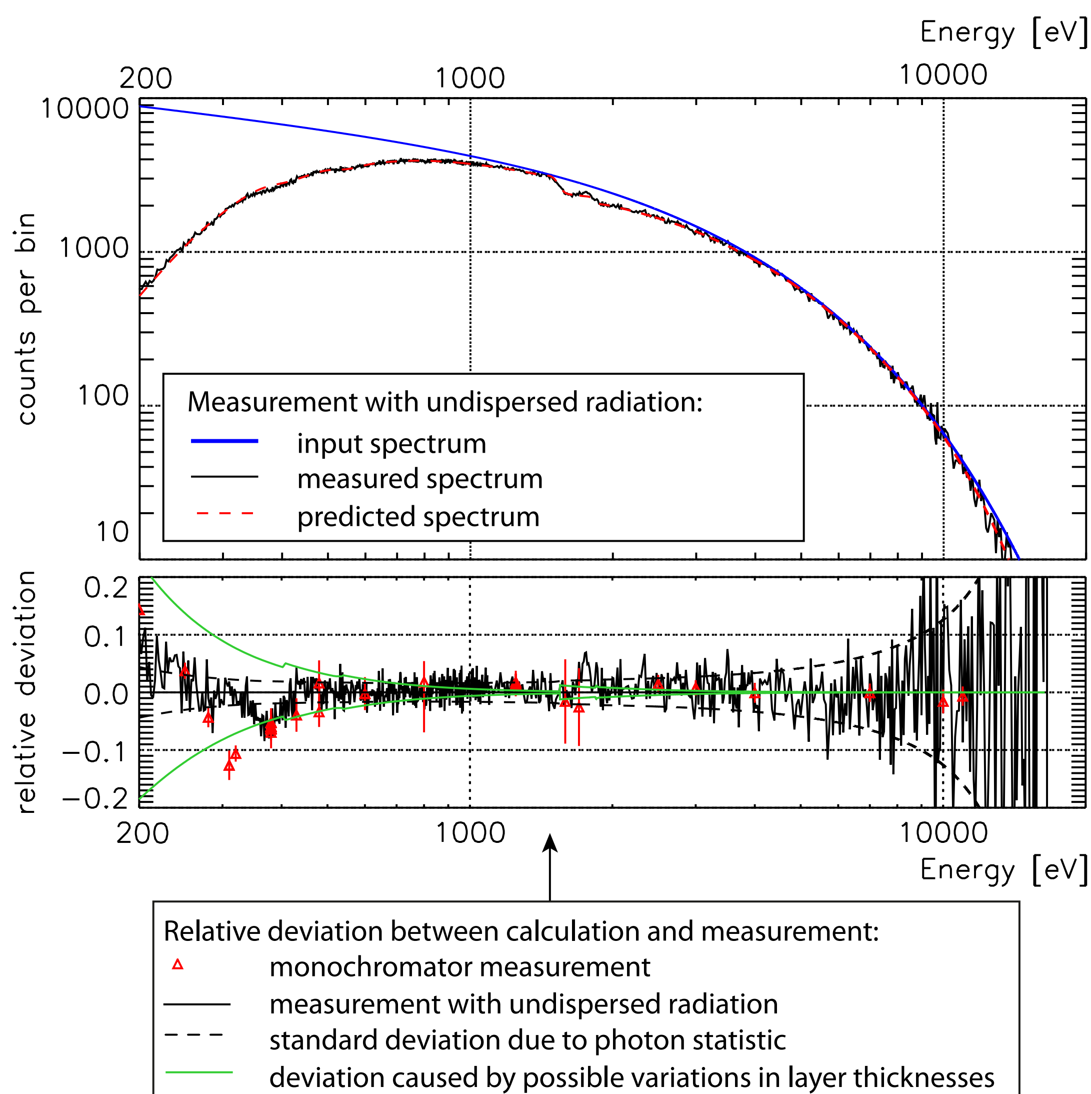

Figure 8.3.: Results from the measurement with a continuous synchrotron spectrum. The upper panel shows the comparison of incident synchrotron spectrum (blue), theoretically predicted CCD spectrum (dashed red) and measured CCD spectrum (black). The lower panel displays the deviation between measured and predicted spectrum as well as the deviation caused by photon statistics and possible thickness variations of the entrance window layers. Additionally, the red triangles show the deviation between measured and calculated QE values from the monochromator setup (restricted to values far away from absorption edges).

viations are observed around the nitrogen-K absorption edge. A possible explanation is the use of atomic absorption data for the calculation of the data driven calculation. The deviation between those data and the actual absorption edge fine structure is especially large at the nitrogen-K edge (see fig. 8.1a).
The expected standard deviation due to photon statistics, based on eq. 3.13, is shown as dashed black line. At high photon energies, the measurement error rises due to the low number of detected photons. This is countervailed by using a dynamic bin size for the shown histogram, increasing with event energy. At low photon energies, the influence of the spectral

redistribution model on the spectrum increases. For example, the predicted count rate in this energy regime is sensitive to peak shifts due to the rising slope of the measured spectrum. Furthermore, flat shelf counts caused by higher X-ray energies accumulate at low event energies.
In order to compare both applied measurement methods, the relative deviations between QE calculation and monochromator measurement results (as presented in fig. 8.2) are shown as red triangles. The accuracy of the monochromator measurements can be estimated as described in appendix B.1.2 and is indicated by error bars. Both experiments were conducted at different beamlines, applying different types of PNCCD operating mode. Despite independent systematic error contributions, their results show high agreement. This suggests a high measurement precision at those energies were the QE results are in agreement.
A deviation of the calculated quantum efficiency due to variations in the entrance window layer thicknesses between different wafers is possible and indicated by green lines in the lower panel of fig. 8.3. This leads to a spread in the low energy regime of up to $\pm 20\,\%$. The variation of layer thicknesses over the detector area is much smaller, as further analyzed in section 8.3.

8.3. Homogeneity of the quantum efficiency

As discussed in chapter 7, microstructural voids in the aluminum layer cause variations on pixel scale of the entrance window transmittance in the optical and UV regime. In the X-ray regime, the amount of radiation transmitted through these voids is small compared to the total transmitted radiation and can therefore be neglected. Relative X-ray quantum efficiency variations over the detector area can however be caused by a deviation of entrance window layer thicknesses on the order of few nanometers.
The homogeneity of the quantum efficiency over the detector area can be analyzed from the measurement with continuous synchrotron spectrum. In contrast to the monochromator measurement, the photon flux over the detector area is well defined for this input spectrum. While the flux is constant in horizontal direction, it varies with distance z to the orbital plane (see fig. 4.1). The variation of the spectral flux over the detector area can be calculated and was provided by the PTB. This allowed the measurement of a relative quantum efficiency variation over the detector area.
The relative quantum efficiency variation for photons with energies between 0.3 keV and 0.6 keV is shown in fig. 8.4 a, for photons between 0.6 keV and 1.4 keV in fig. 8.4 b and between 1.65 keV and 3 keV in fig. 8.4 c. With this separation it is possible to distinguish between photon energies below and above the aluminum K-edge at 1.56 keV, in case there is a significant influence of the aluminum layer thickness on the relative QE. The summation of photons of a large range of energies is necessary to achieve a sufficiently small statistical fluctuation. For the same reason, the relative quantum efficiency is determined in clusters of 16×16 pixels, leaving out the border pixels.

The measurement is evaluated similar to the results shown in fig. 8.3. Based on the data driven prediction of the measured spectrum, the expected number of photon events per cluster is calculated. The relative QE is determined by dividing the number N of photon counts in each cluster by the number of expected photon counts in the same cluster. Then the mean value of all clusters in a map is normalized to unity in order to gain a measure for the relative quantum efficiency variation over the detector area. The number of detected photons in each cluster

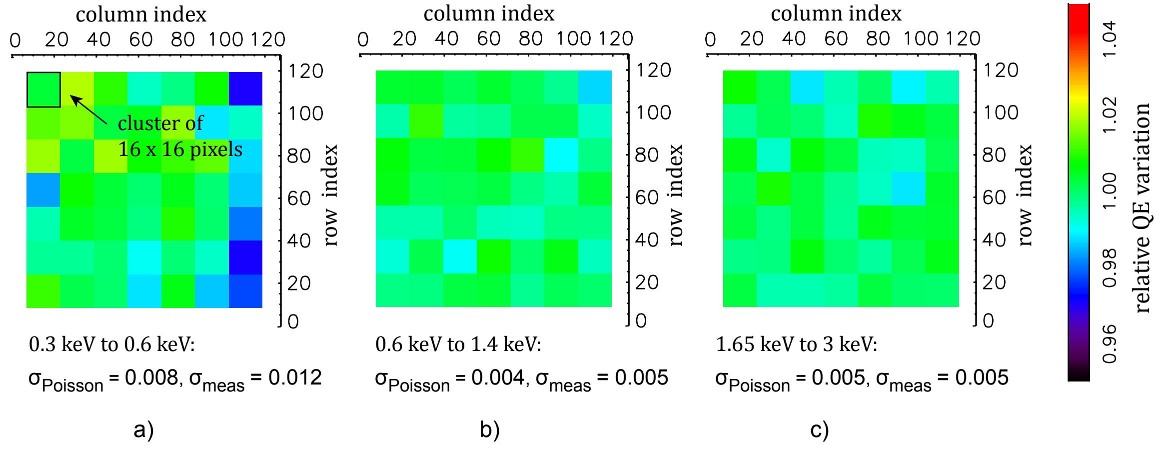

Figure 8.4.: Pixel maps showing the relative quantum efficiency variation over the detector area. These maps show measurement results for photons between (a) 0.3 keV *and* 0.6 keV*, (b)* 0.6 keV *and* 1.4 keV *and (c)* 1.65 keV *and* 3.0 keV*. The relative QE is determined in clusters of 16* $\times$ *16 pixels, leaving out the border pixels. The mean deviation between the clusters is given by* σ_{meas}*. The expected standard deviation due to Poisson statistics is denoted by* $\sigma_{Poisson}$*. The statistical variation sets the lower limit for a measurable quantum efficiency variation.*

can vary due to statistical fluctuations. The expected relative variation σ_{Poisson} in the number of photon counts N due to Poisson statistics is determined according to eq. 3.12:

$$\sigma_{Poisson} = \frac{1}{\sqrt{N}} \,. \tag{8.2}$$

The values for σ_{Poisson} given in fig. 8.4 represent the mean value for all clusters in a map. The mean deviation σ_{meas} of the measured values for the relative quantum efficiency,

$$\sigma_{meas} = \frac{1}{n_{\text{clusters}}} \sum_i (QE_{\text{rel},i} - 1)^2 \,, \tag{8.3}$$

is determined from the relative quantum efficiency values $QE_{\text{rel},i}$ for each cluster i. The number of clusters is n_{clusters} and the mean value for the relative QE is unity.

The statistical variation sets the lower limit for a measurable quantum efficiency variation. Therefore, both values for σ_{Poisson} and σ_{meas} are given in fig. 8.4. For photon energies above 1.65 keV, there is no significant variation of the quantum efficiency apart from statistical fluctuations. For photon energies below 600 eV, the variation in the quantum efficiency amounts to approximately 2 % between low and high column indexes of the PNCCD. Such a spread in the quantum efficiency can be explained by a thickness variation of aluminum. This variation is small compared to the possible spread of layer thicknesses between different silicon wafers, as shown by the green lines in fig. 8.3.

A measurement of the quantum efficiency variation over the detector area can as well be performed using an X-ray tube with large distance to the PNCCD. In this case, even lower statistical errors can be achieved by a larger measurement time. This is for example useful for the calibration of eROSITA flight cameras.

As stated in section 3.5.2, the response of a PNCCD comprises the quantum efficiency as well as the spectral redistribution function. The quantum efficiency was measured by two independent methods, with a more detailed analysis of the absorption edges and the homogeneity over the detector area. It was reproduced by a calculation including the absorption coefficients of the entrance window materials. In contrast to that, the spectral redistribution function of eROSITA PNCCDs can not be described by an analytic expression but requires a simulation model, presented in the following section.

9. Monte-Carlo simulation of the X-ray spectral redistribution

Numerical analysis techniques that use random numbers to establish the solution of a physical or mathematical problem are assigned to the group of Monte-Carlo methods. These methods are often applied for highly complex problems, where solving the equations of motion for each particle in the defined geometry is not practically feasible. A result for such a problem is gained by assigning probabilities to each physical mechanism and executing the simulation algorithm for a sufficiently large number of single experiments. In the 1940s, a Monte-Carlo approach was first applied for the calculation of neutron diffusion and multiplication in nuclear weapons. Ideas about this technique, whose name is derived from the Monte-Carlo casino in Monaco, already existed before, but the development of the electronic computer finally turned it into a practical tool.
A crucial task of a Monte-Carlo code is the generation of uniformly distributed random numbers and the sampling of random numbers with non-uniform distribution. Furthermore, the quality of the data sources, e.g. interaction cross sections, defines the accuracy of the simulation result.

9.1. Motivation

There have been various attempts to describe the spectral redistribution function of silicon detectors in the past. Many of these models are based on analytical methods, describing the spectral redistribution by parameterized functions, as for example in Lowe (2000), Popp (2000), Scholze & Ulm (1994). A very accurate quantification of the redistribution function is in most cases possible through the use of free parameters. In this case, a model function can be fitted to the spectral redistribution function from experimental results.
The aim of this work is a detailed characterization of the eROSITA response as well as the understanding of the involved processes that form the detector response properties. For this purpose, a Monte-Carlo approach was chosen. A Monte-Carlo simulation allows to reproduce complex sequences that cannot be described by analytical models. The comparison between measurement and simulation leads to a better understanding of the formation of a PNCCD energy spectrum. To a large extent, the redistribution function can be modeled by photon and electron interactions, described by universally valid material properties. Only the characteristics of the silicon-SiO_2 interface at the entrance window depend strongly on the detector material and processing parameters. In order to describe the charge collection efficiency in this regime, parameterized functions can be used. A combination of Monte-Carlo simulation and parameterized analytical model may be applied to fully reproduce the spectral redistribution function, as done for example by Campbell et al. (2001).
A similar approach is chosen to simulate the spectral redistribution function of the eROSITA

PNCCDs with on-chip filter. This approach enables the most precise understanding of the entrance window influence on the formation of a PNCCD spectrum. In addition, the simulation includes the full charge collection and readout process up to the creation of frame-wise detector data. A simulation of charge transfer loss is intentionally left out, as this is an effect that can vary with each device, and furthermore depends on temperature and the readout timing. The resulting data can be analyzed with the standard PNCCD analysis software. This allows to compare measurement results with the simulation and to separate data analysis artifacts from general physical processes caused inside the detector.

9.2. Simulation overview

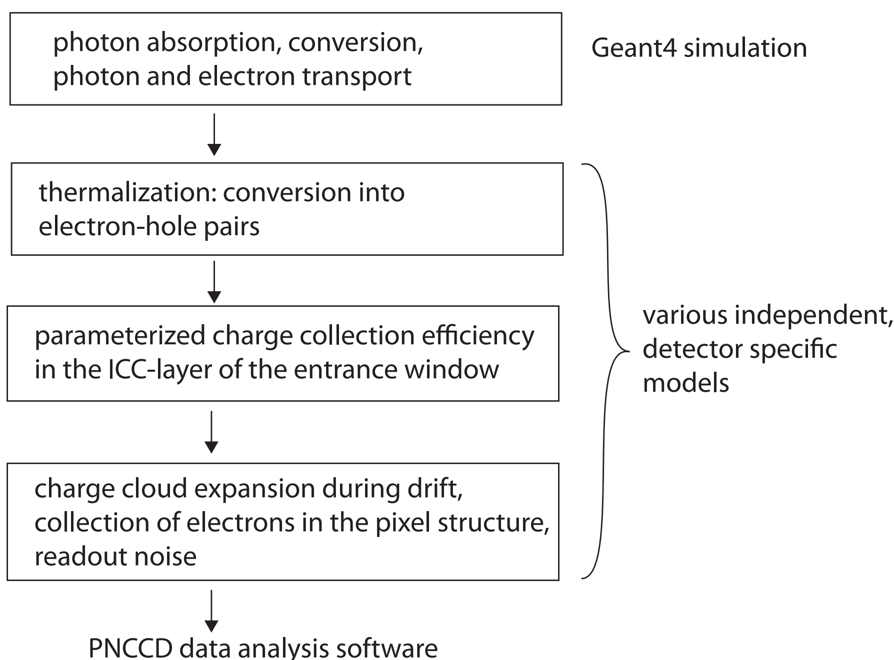

Figure 9.1.: Schematic of the simulation concept. The high energy interactions of photons and electrons in matter are covered by the Geant4 Monte-Carlo simulation. All energy deposits stored by the simulation are further processed using several independent models for thermalization, charge loss in the ICC-layer (incomplete charge collection), charge drift and collection. Charge transfer loss is not included in the simulation.

The basic structure of the presented simulations is shown in fig. 9.1. It consists of mainly two parts, the simulation of high energy electron and photon interactions using a Monte-Carlo code and several independent models treating the charge collection efficiency and detector specific behavior.
For the Monte-Carlo simulation of photon and electron interactions in the detector, the Geant4 toolkit (Agostinelli et al., 2003, Allison et al., 2006), version 4-9-2, is used. Geant4 is a C++ based software toolkit for Monte-Carlo simulations of particle interaction in matter. It is widely used in nuclear and accelerator physics as well as medical and space science. As a framework for Geant4, the MEGAlib package is used (Zoglauer et al., 2006). It comprises a hierarchy of C++-classes for geometry and simulation definition and the simulation tool Cosima

(Zoglauer et al., 2009). The simulation of photon and electron interactions with Geant4/Cosima is presented in section 9.3.

The simulation geometry comprises a silicon bulk of 450 µm thickness. The pixel structure as well as any other doping of the silicon can be neglected for the Geant4 simulation and is introduced later in the simulation (128 × 128 pixels with side length 75 µm). At the entrance window side, thin layers of SiO_2, Si_3N_4 and aluminum are located as shown in fig. 9.2. Outside the detector volume, on the side of the entrance window, a circular, homogeneous photon source of 3 mm diameter emits X-ray radiation perpendicular to the surface. The size of the beam and the photon flux are matched to similar values than those used for spectral measurements. Hence, the proportion of empty pixels to signal pixels and the relative fraction of pile-up are similar between simulated and measured spectra.

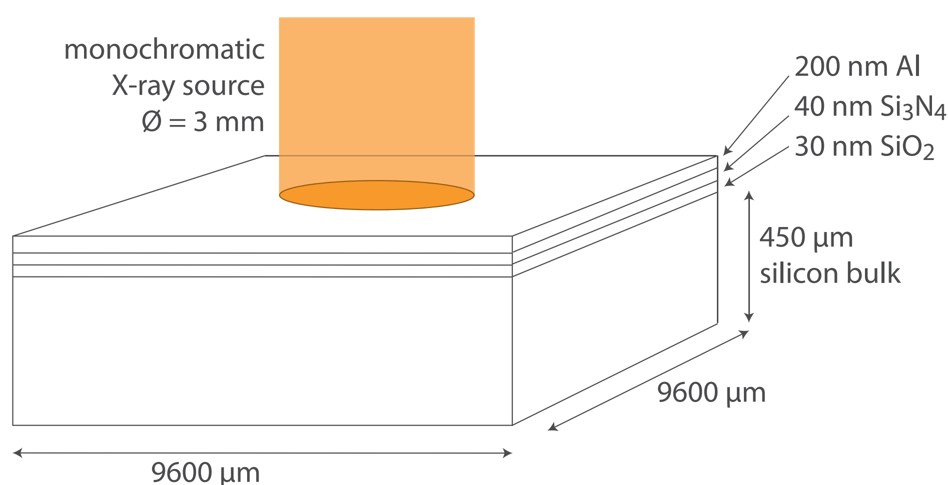

Figure 9.2.: Geometry for the Geant4 simulation, matching the entrance window of the PNCCD used for the experiments. The doping of the silicon is neglected and the pixel structure is introduced later in the simulation. A beam of monochromatic X-rays enters the detector through the entrance window side.

Geant4 is not suitable for the simulation of electrons with energies of a few eV and less. The thermalization process and all following mechanisms, as charge drift and diffusion and the separation of charge to pixels are treated by specific models. These models are included in the HLLDetSim package (Weidenspointner et al., 2011), presented in section 9.4. In the course of this work, the HLLDetSim package was extended in order to account for incomplete charge collection in the entrance window.

9.3. Photon and electron transport and interaction

Photons and electrons are both treated as particles in a Geant4 simulation. Each particle interaction is determined from tabulated cross section data, comprised in the Geant4 distribution. There are several data models available, each of which is suited for certain energy or

interaction regimes. The eROSITA response simulations are performed with the 'Low Energy Electromagnetic Processes' models for photons and electrons of energies down to 250 eV (Apostolakis et al., 1999). The interaction cross sections are taken from the Livermore Evaluated Libraries for electrons (Perkins et al., 1991a), photons (Cullen et al., 1989) and atomic relaxation (Perkins et al., 1991b). Further references about data sources, for example for binding energies or electron stopping powers, can be found in the 'Geant4 Physics Reference Manual' (GEANT4 collaboration, 2008).

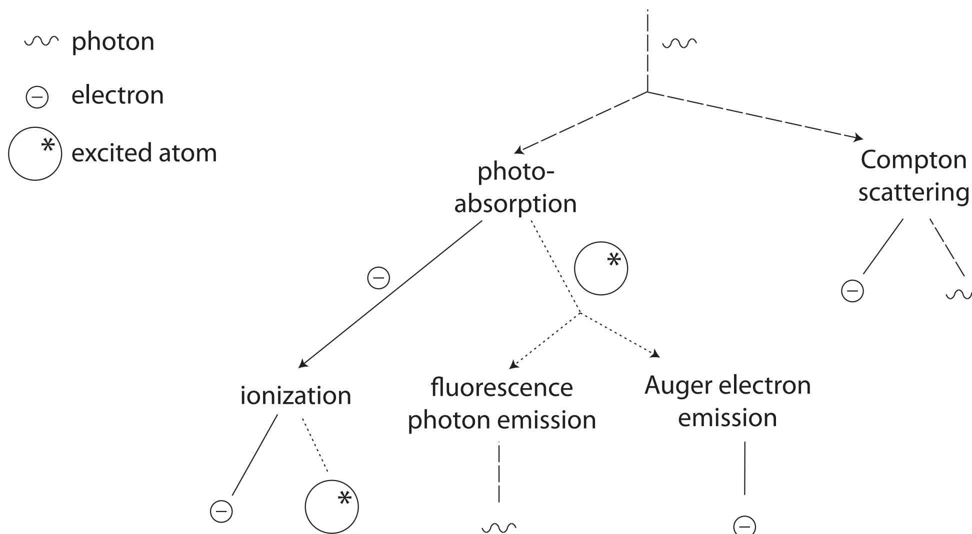

Figure 9.3.: Schematic of the interaction processes of photons and electrons in the detector. If an electron or photon escapes or enters the sensitive volume during the interaction process, a fraction of the energy is not deposited in the detector and appears as off-peak event in the spectrum later. The interaction cascade finally leads to a large number of low-energy electrons. Elastic scattering processes are left out as they only alter the direction of a photon or electron.

Figure 9.3 shows a schematic of all possible inelastic processes in the simulation. Each absorbed photon may cause a cascade of secondary particles. The cascade ends in the generation of low energy electrons and excited atoms (holes) inside the sensitive silicon volume. If an electron or photon escapes or enters the sensitive volume during the interaction process, a part of the energy is not deposited in the detector and shows as off-peak event in the spectrum later.

For all processes, the probability of an interaction is determined by interpolation of the tabulated interaction cross sections. For compounds, the interaction cross sections are determined from elemental data, taking into account the chemical multiplicity of each element in a compound and the overall density, as described for the mass absorption coefficient in eq. 2.25.
The relevant interaction mechanisms for **photons** in the energy range of interest comprise Rayleigh scattering, photoelectric effect and Compton scattering. For both Rayleigh and Compton scattering, a form factor is used to correctly describe the angular distribution of scattered photons (see also GEANT4 collaboration, 2008). The form factor leads to an almost isotropic angular distribution for the scattering of low energy photons, while at high photon

energies the emission distribution is forward-peaked. In a Compton scattering process, the photon energy is changed as given by eq. 2.19. Additionally, an electron is emitted, leaving an excited atom behind. The photoelectric effect leads to the absorption of a photon, the emission of an electron with energy given by eq. 2.18 and the excitation of an atom. The emission angle of the photoelectron is determined from the Sauter-Gavrila distribution, as further described in the Geant4 physics reference manual.

Electron interactions treated by the simulation include elastic scattering, excitation, ionization and the emission of Bremsstrahlung. In order to achieve realistic calculation times, interactions of charged particles in matter can be modeled by so-called condensed algorithms. These algorithms do not simulate each single scattering process. Instead, the net angular and spatial displacement and energy loss of electrons as a result of multiple scattering processes are determined. The Geant4 model functions have been chosen in such a way as to give the same moments of angular and spatial distribution as the Lewis theory (see GEANT4 collaboration, 2008). Electron interactions are modeled by a continuous energy loss per path length. The discrete nature of ionization processes is modeled by secondary electron emission. The emission of secondary electrons is limited by a user-defined secondary production threshold, which is set to 50 eV for the eROSITA response simulation. This value is chosen as low as possible in order to correctly reproduce low-energy electron interactions. A discussion of the impact of this threshold can be found in appendix D. The atomic shell of which the secondary electron is emitted is randomly selected and the energy of the secondary electron is sampled. Finally the angle of emission of the scattered and secondary electron is determined by energy-momentum conservation. After the ionization process, both scattered (primary) electron and secondary electron leave the atom. The interaction cross section for Bremsstrahlung in the simulated energy range is so low that it has practically no impact on the result.

Atomic relaxation is triggered by all processes resulting in an ionized atom, which are ionization collisions and the photoelectric effect. For the emission of a fluorescence photon, an outer transition shell is randomly selected based on tabulated transition probabilities. For an Auger emission process, two outer shells are selected. Fluorescence photons and Auger electrons are emitted in random direction, with an energy given by eq. 2.26 and eq. 2.27 respectively. For atomic relaxation processes, it is assumed that the binding energies of ionized atoms are equal to those of free, neutral atoms.

9.4. Detector specific model

As described in section 2.6, the interaction cascade of photons, electrons and excited atoms in the silicon leads to low-energy electron hole pairs. This cascade is simulated by Geant4 down to energies on the order of 10 eV to 100 eV, resulting in point-like energy deposits in the silicon bulk. The electron mean free path in matter at such kinetic energies is shorter than 2 nm, which is small compared to the size of a charge cloud after thermalization of approximately 0.2 µm (see eq. 2.34). Therefore, instead of simulating the trajectory of each electron hole pair, the subsequent thermalization process can be described by a statistical model comprised in the HLLDetSim package.

Thermalization: The relaxation of energy deposits, the thermalization process, is modeled by converting energy deposits into electron-hole pairs with a distribution according to the Fano theory. The mean number of electron hole pairs created by an energy deposit is defined by the mean pair creation energy w, with a statistical fluctuation defined by the Fano factor F. The used values of F = 0.118 and w = 3.69 eV are matched to the detector temperature of $-70\,°$C to $-80\,°$C during the measurements. The spatial distribution of electrons after thermalization, further called the initial charge cloud, is not explicitly modeled. This distribution is inherently comprised in the charge collection efficiency model.

Charge collection efficiency: As described in section 3.4, the first hundred nanometers of silicon exhibit properties different from the silicon bulk. Dangling bonds at the silicon-SiO_2 interface lead to trapping and recombination. Furthermore, a thin layer in the p^+-doped region exhibits a weaker electrical field compared to the bulk. The loss of electrons and holes in this ICC layer leads to a reduced number of signal charge that can be collected in the pixel structure at the detector front side. Therefore, a charge collection efficiency (CCE) is introduced, which is equal to unity inside the silicon bulk and smaller than unity close to the silicon-SiO_2 interface.

The properties of the very thin region around the silicon-SiO_2 interface can not be determined exactly, and vary with the given silicon material and wafer processing. Therefore, it is common to describe the charge collection efficiency by a parameterized function. A well-proven phenomenological approach is to use an exponential CCE function, with a minimum relative amount of collected charge of approximately 0.4 to 0.95 (Campbell et al., 2001, Lechner, 1998, Scholze & Ulm, 1994). One explication for such an approach is given by Goto (1993), who derives the exponential form of the CCE from charge carrier recombination, leading to the expression

$$CCE(z) = 1 - (1 - R) \cdot exp\Big(-\frac{v_s \cdot z}{D}\Big) \ . \tag{9.1}$$

Here, v_S is the electron saturation velocity and D the diffusion constant. A reflection coefficient R is introduced to the model in order to account for a finite recombination velocity. At 77 K, the characteristic length $\frac{D}{v_s}$ of the exponential function is ≈ 0.1 µm.

Following the same phenomenological approach, a parameterized exponential CCE function,

$$CCE(z) = 1 - \gamma \cdot exp\Big(-\frac{z}{\tau}\Big) \ , \tag{9.2}$$

is chosen in this work. It describes the probability of charge loss in a depth z in the silicon, as illustrated in fig. 9.4. The parameter γ denotes the maximum fractional amount of charge loss at a depth z = 0. Due to recombination at the silicon interface and the weak electric field, the largest charge loss occurs at this position. With increasing distance from the interface, the partial charge loss decreases and the charge collection efficiency approaches unity.

The charge collection efficiency model is directly applied to each (point-like) energy deposit. The damping coefficient τ of the CCE function therefore comprises the spatial distribution of traps as well as the initial charge cloud size, which is approximately 150 nm to 400 nm wide for photon energies between 0.1 keV and 10 keV (see eq. 2.34). The convolution of a Gaussian charge distribution onto an exponential charge collection efficiency results again in an

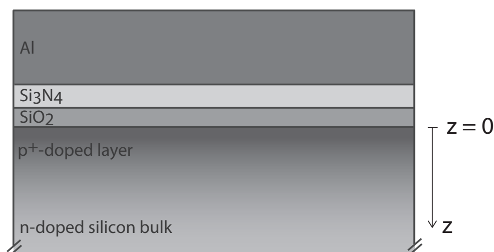

Figure 9.4.: The charge collection efficiency for charge carriers in the silicon bulk depends on their distance from the silicon-SiO_2 interface. It reaches its minimum at z = 0 and approaches unity in a relevant distance from the interface.

exponential charge collection efficiency with slightly different parameters. Therefore, it is more efficient to apply the CCE function directly on point-like energy deposits.
In the described model, the expansion of a charge cloud into the SiO_2 for photons absorbed in the silicon is not possible. This is an important aspect, as such an expansion would cause charge loss of up to almost 50 % for absorption processes close to the Si-SiO_2 interface. During the thermalization process the phonon interaction cross section decreases sharply (see fig. 2.11), so that the electron mean free path increases sharply from few nanometers to values on the order of the charge cloud size (Scholze & Ulm, 1994). At the point in time where the charge cloud develops to its full size, the electron energy is too low to overcome the potential barrier at the Si-SiO_2 interface.

In order to account for the statistical character of trapping and recombination charge loss, the CCE function can be regarded as a probability distribution. After the number of electron-hole pairs generated by an energy deposit is calculated, each electron is collected with a probability given by $CCE(z)$. At high photon energies, above 1 keV, the noise contribution by partial charge loss in the ICC layer is small compared to the Fano noise. Therefore, at high photon energies the CCE function is directly applied to calculate the fraction of collected charge without statistical component.

The CCE parameter values for eROSITA PNCCDs, as determined from measured spectra, are γ = 0.09 and τ = 0.1 µm (see chapter 10).

Charge drift and diffusion: During the charge drift to the pixel structure, the size of the charge cloud increases to several µm. In contrast to the initial charge cloud directly after thermalization, this spatial distribution is modeled in order to correctly account for split events in the PNCCD. When applying an event detection threshold during data analysis, split events lead to a shift and distortion of peaks in PNCCD spectra (see section 6.2). In order to reproduce this effect it is desirable to use the correct charge cloud size in the simulation.
In the HLLDetSim package, the electric potential in the silicon bulk is determined from the Poisson equation, neglecting the pixel structure and assuming full depletion. This potential leads to a drift of the charge to the detector front side. During the drift time of the charge, diffusion leads to a broadening of the charge cloud. Electromagnetic repulsion of the electrons

inside the charge cloud is not explicitly part of the model. The charge is separated into pixels in a depth on the order of the register structure size (Kimmel, 2008) from the detector front side, the so-called charge separation depth. The charge separation depth in the simulation is set to a value of 17 µm. This value was adapted in order to reproduce charge cloud sizes of $R_{2\sigma}$ = 14 µm to 16 µm measured by Kimmel (2008).

Readout and storage: The readout noise was introduced in the simulation by a Gaussian distribution around zero. Its standard deviation is chosen equal to the readout noise determined from dark frame measurements and given in table 6.2. The simulated noise and signal data for each pixel is written to files of the same format as the measurement data. It can hence be analyzed with the same software used for PNCCD data evaluation (Andritschke et al., 2008).

With the described simulation model, X-ray spectra were simulated to allow for comparison between measurement and model. The results of such measurements, the comparison with simulations as well as further conclusions drawn from the simulation are presented in the following chapter.

10. Analysis of the spectral redistribution function

The analysis of spectra accumulated during illumination with monochromatic radiation is crucial to quantify features in a spectrum and understand their formation. Section 10.1 gives an overview on the monochromatic spectra measured with an eROSITA PNCCD with on-chip filter. The origin of some spectral features can be assigned to the insensitive layers of the entrance window by a comparison of spectra directly below and above the absorption edges, as presented in section 10.2. In addition to the presented measurements, simulations of the spectral redistribution function were performed. In section 10.3, the degree of correlation between measurement and simulation is therefore examined. The energy resolution of the PNCCD, depending on the photon energy, is discussed in section 10.4. Furthermore, the analysis of the simulation provides insight into the point of origin of spectral features, as presented in section 10.5.

10.1. Spectral features

This section presents an overview on the evolution of the spectral redistribution function with photon energy. Compared to PNCCDs of past technology generations, as for example the EPIC PNCCD of the XMM mission, the spectral response for low energy photons has significantly improved. The eROSITA entrance window is optimized in order to achieve an almost Gaussian X-ray main peak in the spectrum. The relative intensity of off-peak features is close to the minimum. Such off-peak features are the flat shelf, fluorescence peaks and the Compton spectrum.
Measured spectra in the energy range between 100 eV and 11 keV are shown in fig. 10.1. Starting at low photon energies, the spectrum consists of the flat shelf and a main peak (fig. 10.1a, 10.1b and 10.1c). The **flat shelf** is caused by electrons traversing the interface between sensitive and insensitive material. The continuous energy loss along the electron trajectory leads to entries in the spectrum between zero and the photon energy. As mentioned in previous chapters, the **main peak** is affected by partial charge loss in the first hundred nanometers of silicon, the ICC layer (incomplete charge collection). For low energy X-rays, a large fraction of photons are absorbed in the ICC layer, leading to a shift and distortion of the main peak. In contrast to older PNCCD generations, this distortion is low enough so that even at 100 eV the photon peak can be separated from the noise peak. With increasing photon energy, less photons are absorbed in the ICC layer, and the peak shape approaches a Gaussian. For comparison, a Gaussian fit is displayed with each spectrum in fig. 10.1.
At photon energies in the medium X-ray regime, partial charge loss in the ICC layer forms a low energy **shoulder** adjacent to the main peak. This shoulder is especially pronounced at a photon energy of 1848 eV (fig. 10.1e), directly above the K-shell absorption edge of silicon.

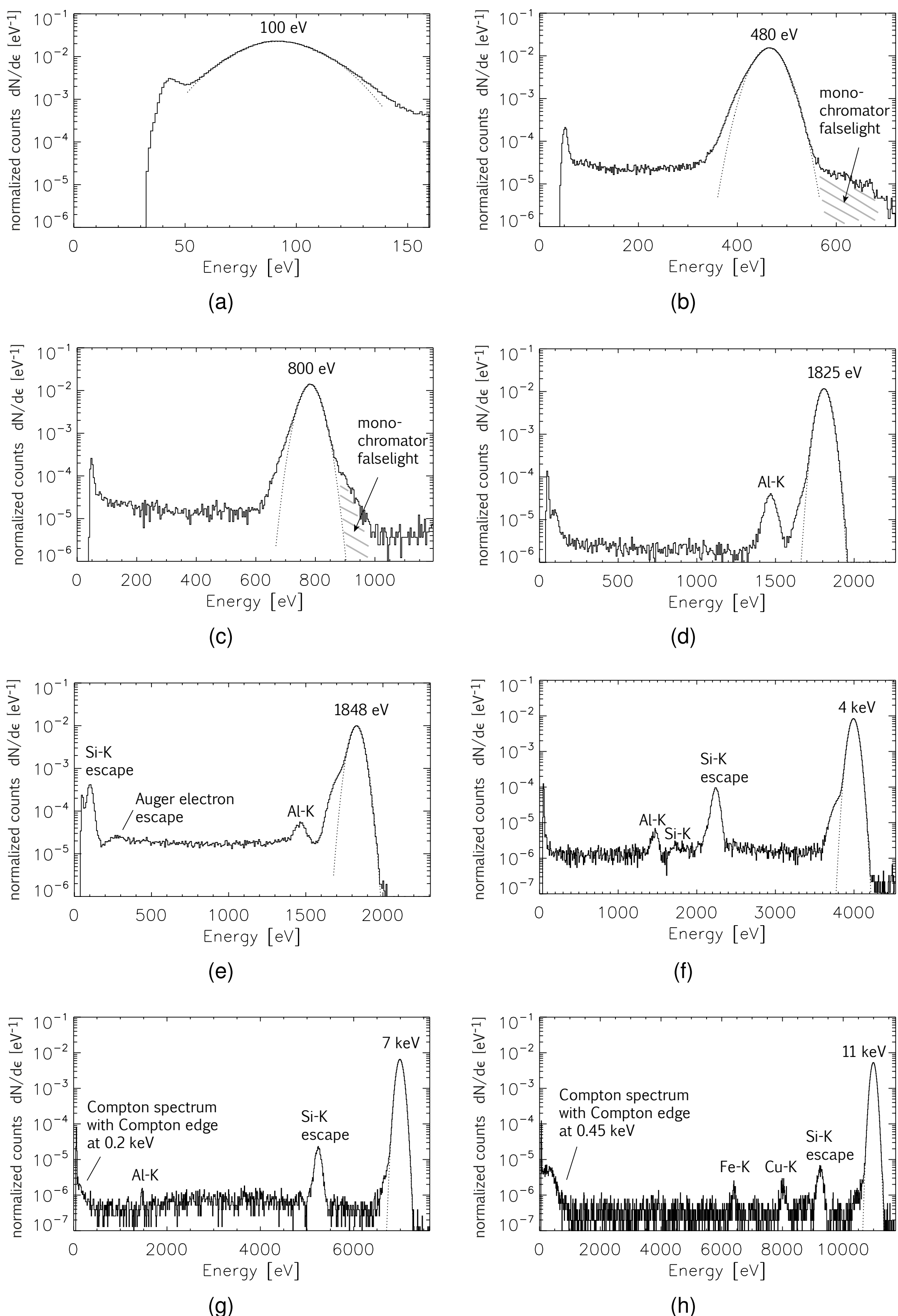

Figure 10.1.: Spectra measured with a PNCCD. The main peak approaches a Gaussian (dotted lines) with increasing photon energy. The peak-to-valley ratio ranges from 10 to more than 10000, and is limited by the flat shelf. The Al-K fluorescence peak and silicon escape peak are visible for photon energies above the respective K-shell absorption edge. At high photon energies, the Compton spectrum is superimposed on the flat shelf. In the 11 keV *spectrum, Fe-K and Cu-K fluorescence is caused by the detector surroundings.*

With increasing photon energy, and therefore increasing absorption length of photons in silicon, the relative intensity of the low energy shoulder declines. A similar situation prevails with the relative fraction of flat shelf events, which is directly connected to the amount of radiation absorbed in the vicinity of the silicon-SiO_2 interface. This can be analyzed by comparing spectra around the absorption edges, as discussed in section 10.2.
The **silicon escape** peak as well as the **aluminum fluorescence** peak are present in spectra with photon energies above the silicon and aluminum K-edge respectively. The energy of fluorescence photons is determined by the electron binding energies in a material as given in eq. 2.26, and the most probable transitions are listed in table 2.4. The aluminum-K fluorescence peak is found at an energy of 1.5 keV. The silicon escape peak is shifted by 1.74 keV with respect to the incident photon energy, due to the escape of a silicon-K fluorescence photon. In fig. 10.1h, additional Fe-K and Cu-K fluorescence is visible, caused by X-rays hitting the detector surroundings.
At high X-ray photon energies, the **Compton spectrum** is superimposed on the flat shelf (see fig. 10.1g and 10.1h). In a Compton scattering process, a fraction of the photon energy is transferred to an electron, while the photon is deflected. If such photons are backscattered and escape the sensitive volume, events with reduced energy are detected, forming the Compton spectrum. The maximum energy of the recoil electron occurs at a photon scattering angle of 180°, as given by eq. 2.20. This forms a high-energy cutoff of the Compton spectrum, the Compton edge. In the shown spectra of 7 keV and 11 keV photons, the Compton edge energy equals 0.20 keV and 0.45 keV respectively.
The **flat shelf** in the displayed X-ray spectra is almost unstructured, due to the continuous energy loss of electrons along their path. The flat shelf determines the peak-to-valley ratio, which ranges between 10 and more than 10 000 in the displayed X-ray energy regime. The origin of the flat shelf and its evolution with photon energy is discussed in the following sections. The low-energy cutoff of the flat shelf at 250 eV in fig. 10.1e is caused by Auger electron escape, explained in detail in section 10.5.
In the spectrum of 1825 eV photons in fig. 10.1d, a peak at about 100 eV is superimposed on the flat shelf and noise peak. Its origin is further discussed in section 10.3.

As stated in section 5.2, the amount of false light at the SX700 monochromator rises with energy, resulting in tails at both sides of the peak and a high-energy shoulder, visible in fig. 10.1b and fig. 10.1c. Spectra at energies between 800 eV and 1800 eV exhibit strong false light features and are therefore not further discussed. Spectra with photon energies above 1800 eV are measured at the KMC monochromator and do not exhibit false light contributions.
The shown measurement results give an overview on the spectral redistribution function of eROSITA PNCCDs. Further understanding can be derived from the comparison of spectra at energies below and above the absorption edges, as described in the following section.

10.2. Spectra at the K-shell absorption edges

The measurement of monochromatic spectra close to the absorption edges is especially interesting, as it allows to assign parts of a spectrum to each of the entrance window materials. In general, the physical interaction mechanisms forming the spectral redistribution function do not change in a photon energy range as small as a few eV. However, the absorption probability in only one material changes abruptly at the absorption edge energy, corresponding to the

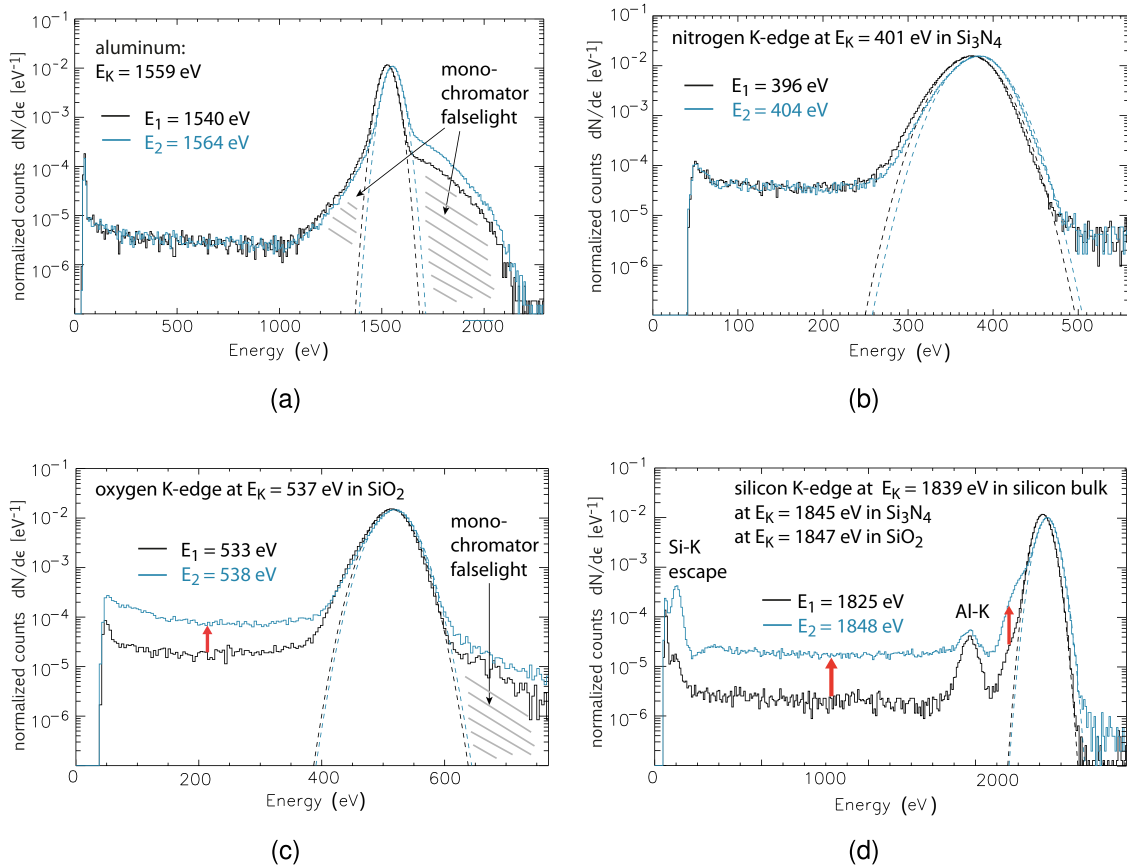

Figure 10.2.: Comparison of spectra below and above the K-shell absorption edges of aluminum, nitrogen, oxygen and silicon. The photon energies are indicated by E_1 and E_2, the absorption edge energy is given by E_K.
Around the aluminum and nitrogen K-edges, in (a) and (b), the spectral redistribution function does not change. An increase of the flat shelf count rate is observed above the oxygen and silicon K-edge, in (c) and (d). Furthermore, the shape of the main peak is altered when exceeding the silicon K-edge. The mentioned changes are indicated by red arrows.

electron binding energy in an atomic shell. If such a change in absorption probability leads to changes in the spectrum, the origin of the affected spectral feature can be assigned to the respective material.
The measured spectra around the K-shell binding energies of aluminum, nitrogen, oxygen and silicon are shown in fig. 10.2a to 10.2d. The energies of the absorption edges are derived from QE measurements and are in good agreement with values tabulated in literature (see table 2.3). In each plot in fig. 10.2, two spectra at photon energies E_1 and E_2 below and above each absorption edge are displayed.
Around the Al-K edge at 1559 eV and the N-K edge at 401 eV, in fig. 10.2a and fig. 10.2b, no significant change in the spectral redistribution is observed. This implies that photons absorbed in the outer layers of the filter, i.e. aluminum and Si_3N_4, do not contribute to the spectrum. These layers only lower the quantum efficiency of the detector. In contrast to that, the spectra around the O-K absorption edge at 537 eV in fig. 10.2c indicate that a high absorption probability in SiO_2 leads to a high flat shelf count rate. Conclusively, a significant fraction

of flat shelf counts is caused by Photo- and Auger electrons generated in the SiO_2 layer. This layer is directly adjacent to the sensitive silicon volume, and therefore the electrons exhibit enough kinetic energy to enter the silicon.
A similar conclusion can be drawn from the analysis of the spectra around the silicon edge in fig. 10.2d. The K-shell binding energy in crystalline silicon is 1839 eV, while it is shifted to 1845 eV and 1847 eV for silicon atoms in Si_3N_4 and SiO_2 respectively (Prigozhin et al., 1998). These three edges cannot be resolved individually. The observed changes in the spectral redistribution function below and above the edge may be caused inside any of these three materials. However, the measurement around the nitrogen K-edge suggests that the impact of photons absorbed in the silicon nitride is negligible. It is important to notice that with increasing photon energy the range of photoelectrons also increases, which may lead to an flat shelf contribution by electrons generated in the aluminum and Si_3N_4 at higher photon energies than the K-shell edge energy. However, an analysis of simulation results in the following sections confirms that the flat shelf is dominated by electrons from the silicon and SiO_2.
The main peak of the displayed spectra is only affected by the jump in absorption probability at the Si-K absorption edge (see fig. 10.2d). This confirms that with an increased absorption probability in the ICC layer, the number of counts inside the low-energy shoulder rises.
The described measurement results around the absorption edges verify the simulation model setup described in chapter 9. The direct comparison of modeled and simulated spectra allows to complete the analysis of the origin of spectral features.

10.3. Comparison between measurement and simulation

As described in chapter 9, the simulation model includes the Geant4 simulation of electron and photon interactions with matter, combined with models for the charge collection efficiency (CCE), statistics of the signal charges and distribution of the charge cloud onto pixels. If not mentioned otherwise, the CCE parameters γ = 0.09 and τ = 100 nm are used for the simulation. A further adaption of these parameters at low photon energies is discussed at the end of this section. The maximum fraction of charge loss γ = 0.09 describes the width of the low-energy shoulder of 0.09 E_{ph}. The characteristic thickness of the CCE layer of τ = 100 nm has impact on the number of events inside the shoulder and therefore on its height.
Figures 10.3a to 10.3d show very good agreement between simulation and measurement. While the flat shelf, the fluorescence and escape peaks and the Compton spectrum are inherently part of the Geant4 simulation, the parameterized CCE model reproduces well the low-energy shoulder next to the main peak.
The small deviation between measured and simulated peak positions of the aluminum fluorescence peaks and silicon escape peak can be explained by inaccuracies in the Geant4 binding energy data. Details on the deviations and possible improvements are given in Granato et al. (2011) and appendix D.
At event energies close to zero and to the peak, the number of simulated counts in the flat shelf is underestimated compared to the measurement results. This part of the spectrum, marked by dotted circles in fig. 10.3a and 10.3b, was seen to be created by electrons with a kinetic energy of a few hundred eV traversing the Si-SiO_2 interface. Such electrons are generated within a distance of about 10 nm around the interface. An underestimation of the electron range or the early termination of the electron trajectory simulation can have caused the observed underestimation (see also appendix D).

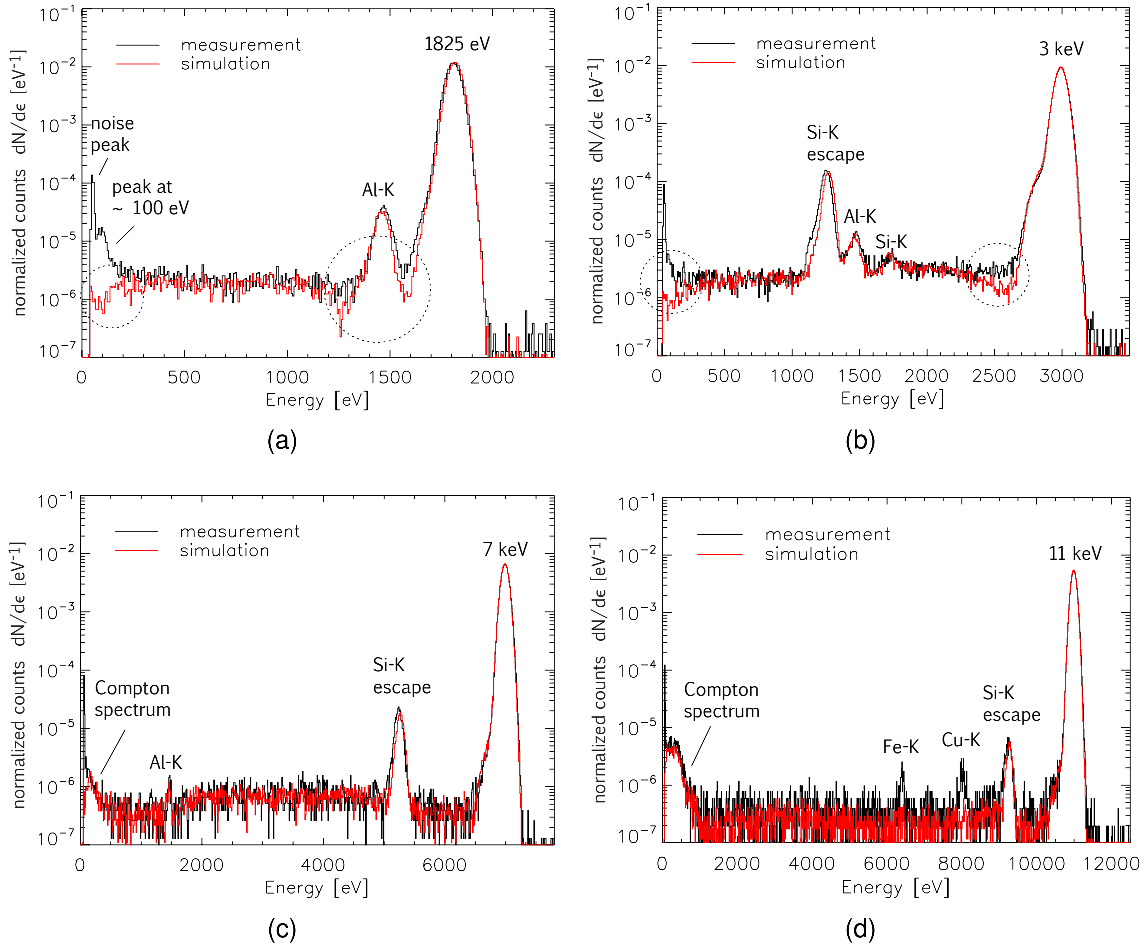

Figure 10.3.: Spectra measured with eROSITA PNCCDs compared to Geant4 simulations described in chapter 9. The flat shelf and peaks from aluminum fluorescence and silicon escape are well described by the simulation. The shape of the main peak is reproduced with a model for partial charge loss in the ICC-layer. The simulation is also able to describe the Compton spectrum, which is only present in spectra with rather high photon energies. Fluorescence from Copper (Cu - K at 8048 eV*) and Iron (Fe - K at* 6404 eV*) are not part of the simulation as they are caused by the detector surroundings.*

In the spectrum of 1825 eV photons, in fig. 10.3a, a peak at about 0.1 keV is visible. An obvious explanation would be Si-L fluorescence caused inside the SiO_2 and Si_3N_4 layers with an energy of 0.1 keV (see table 2.4). The absence of this peak in the simulation can not be attributed to a shortcoming of the Geant4 code. A simple estimation of the relative fraction of Si-L fluorescence photons can be performed from the amount of absorbed photons in the SiO_2 and Si_3N_4 and the Si-L fluorescence yield. This results in a value of 5×10^{-7}, much lower than the observed value in the spectrum. The estimation includes 1 % absorption in the SiO_2 and Si_3N_4 (see e.g. appendix A) and a fluorescence yield of 5×10^{-5}, as listed in table 2.4a. Another possible origin of the 0.1 keV peak in the 1825 eV spectrum is the collection of charge created in the insensitive SiO_2 layer. Thermalized electrons generated in an insensitive oxide layer can cause a weak second peak in silicon detectors (Bautz et al., 1999, Prigozhin et al., 2000). However, it seems remarkable that a relatively sharp peak and not a plateau is visible

in the spectrum.
Finally, it is possible that the 0.1 keV peak is caused by silicon $L_{II,III}$MM-Auger electrons created in the SiO_2, with an energy of 0.1 keV. Such Auger electrons entering the sensitive volume would define a high-energy cutoff of the shelf, forming a step similar to the one discussed in section 10.5. It is not possible to confirm this by comparison with the simulation, due to its uncertainty at such low electron energies.

With increasing photon energy, the agreement between simulated and measured shelf count rate throughout the spectrum becomes even more accurate. Figure 10.3c shows that the Monte-Carlo simulation of the full cascade after photon absorption is able to exactly reproduce the shape of the flat shelf. A more detailed analysis of the formation of the flat shelf is therefore discussed in section 10.5. The Compton spectrum, superimposed on the flat shelf, is as well given correctly by the simulation. The main peak, including the shoulder due to incomplete charge collection in the ICC-layer, can be reproduced with the same parameters for all photon energies displayed in fig. 10.3.

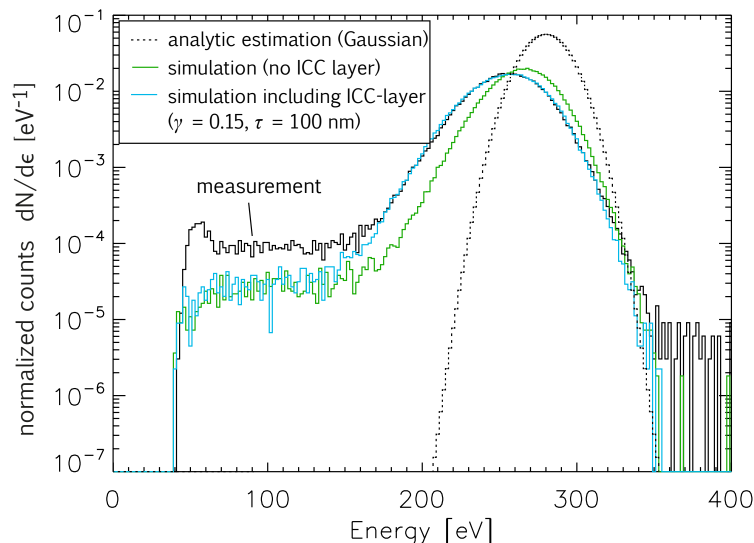

Figure 10.4.: 280 eV spectrum measured with eROSITA PNCCDs. A Gaussian peak with a width defined by Fano and readout noise can only poorly reproduce the peak shape. Geant4 simulations, as described in chapter 9, show much better agreement. For comparison, simulations with and without an ICC layer are shown. The flat shelf is underestimated due to inaccuracies in the simulation of low energy electrons in Geant4.

An increased influence of absorption inside the ICC-layer on the spectral redistribution function is given at low photon energies. Figure 10.4 shows a measured 280 eV spectrum as black line. A Gaussian peak with a width defined by Fano and readout noise according to eq. 3.10 only leads to a poor estimation of the measured spectrum. The Geant4 simulation, including electron transport and charge splitting (green line), can already give a better agreement. By additionally including the ICC layer to the simulation (blue line), with γ = 0.15 and τ = 0.1 µm, the peak shape can be well reproduced. Whereas high energy spectra can be reproduced with a constant value of γ = 0.09, an adaption of this parameter at low photon energies is necessary. The difference of the maximum charge loss parameter γ between high and low

photon energies can be explained by the saturation of traps. With decreasing photon energy, less traps are saturated, leading to a higher amount of charge loss (Popp, 2000). Other effects, as for example charge transfer loss that is not perfectly corrected for, can partly cause the additional peak distortion.
The deviation of flat shelf count rates between measurement and simulation in fig. 10.4 can be explained by the limited data accuracy for low energy electrons. The estimated error for the used ionization cross sections decreases with energy and is smaller than 30 % to 40 % in the energy range of interest. The stopping power data is divided into collisional, ionizing and excitation stopping powers with a respective accuracy of 2 % to 3 %, 10 % to 20 % and 20 % to 50 % (Perkins et al., 1991a).

The comparison of simulations with measurements in the full energy range of eROSITA shows high agreement, even for almost constant CCE parameters γ and τ in eq. 9.2. At photon energies below 500 eV, γ is varied from 0.09 to 0.15 in order to reproduce the measurement results. The parameter τ is constant at all photon energies. It is defined by the characteristic thickness of the ICC layer and the primary charge cloud radius. A fit of parameters to measured spectra at all photon energies can be performed with an analytical representation of the model (see also section 11.1). In contrast to that, the Monte-Carlo simulation calculates the full chain of events for every photon hitting the detector. It is thus able to follow all relevant statistical processes and to reproduce the energy resolution of the detector.

10.4. Energy resolution

The energy resolution of a PNCCD is given by the width of the main peak and is an important characteristic of an X-ray spectrum. In a first approach, the peak width can be estimated by accounting for the most prominent noise contributions in the spectrum, Fano- and readout noise. While the Fano noise is proportional to the square root of the photon energy (see eq. 3.11), the readout of the detector adds an additional constant noise contribution of about 2.5 electrons rms. The resulting peak width can be estimated from the square root sum of both contributions, as in eq. 3.10. Such an estimation is shown as dotted line in fig. 10.5. The peak widths of measured and simulated spectra in the same energy regime are displayed as crosses. These peak widths, also listed in table 10.1, were determined as described in section 6.4.

Energy [eV]	200	280	380	480	600	800	1848	3000	7000	11000
from measured spectra:										
FWHM [eV]	47	53	57	58	59	61	83	97	142	175
from simulated spectra:										
FWHM [eV]	43 (44)	48 (51)	53 (57)	55	56	59	81	95	140	171

Table 10.1.: Peak width given as FWHM in eV, from measured and simulated spectra with photon energies between 200 eV and 11 keV. The simulations were performed with the CCE parameters γ = 0.09 and τ = 100 nm. For low photon energies, additional simulation results with γ = 0.12 are given in brackets.

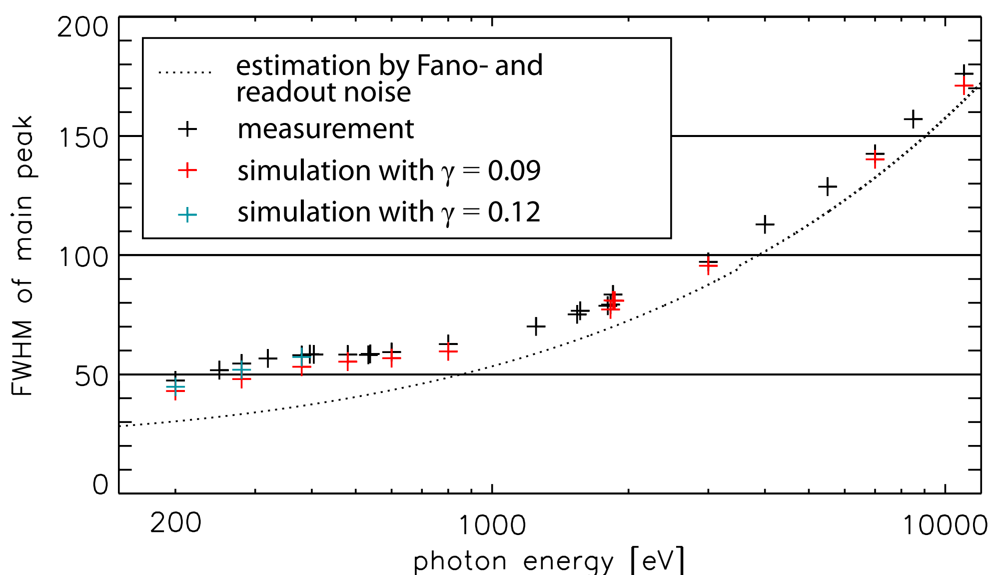

Figure 10.5.: FWHM of main peak in measured and simulated spectra of recombined events (singles to quadruples). The dotted line indicates the theoretical FWHM calculated from Fano noise (with a Fano factor of 0.118*) and readout noise according to eq. 3.10. The increased peak width compared to this calculation is mainly due to incomplete charge collection and event splitting and recombination. These aspects are included in the simulation (red), with further adaption of the CCE parameters at low energies (blue).*

It can be seen from fig. 10.5 that the simple estimation using Fano- and readout noise (dotted line) cannot fully reproduce the peak width of a PNCCD X-ray spectrum. A comparison with the simulation, giving a significantly better estimate, leads to a better understanding of the noise contributions.

At low photon energies, charge loss in the ICC layer leads to a significant broadening of the peak. The statistical fluctuation of such charge loss leads to a further peak broadening and is accounted for by a CCE probability function in the simulation. The simulation results, using the same CCE parameters $\gamma = 0.09$ and $\tau = 100\,\mathrm{nm}$ at all photon energies, are shown as red crosses. They give a good estimation of the measured peak width. As stated in the last section, the parameter γ of the CCE-model increases for low photon energies. Additional simulation results with $\gamma = 0.12$ are therefore shown in blue.

As seen from table 6.1 and eq. 6.2, event reconstruction due to split events causes a noise contribution of approximately $\sigma_{\mathrm{split}} = 3$ electrons rms. This noise contribution is a function of the pixel size, the charge cloud size, the readout noise and event detection threshold. In the spectrum it adds approximately $6\,\mathrm{eV}$ to $8\,\mathrm{eV}$ to the FWHM of the main peak, as listed in table 6.1. In the simulation, this effect is accounted for by including the whole charge collection and data reconstruction process. Furthermore, a variation of charge cloud size according to the absorption depth is inherently taken into account.

Not included in the simulation are charge transfer inefficiency (CTI) losses. For the spectral measurements, the lower part of the PNCCD was illuminated. The number of illuminated rows was intentionally held small, in the range of 20 to 40, in order to minimize the number of transfers and hence the impact of CTI losses. These CTI losses are corrected during data analysis of the measurement data. While a systematic charge loss with increasing number of

row shifts can be corrected, a statistical fluctuation of the CTI losses remains. This can explain an underestimation of peak widths at some photon energies in fig. 10.5 and table 10.1. At high energies, slight variations in the amplification factor of less than $1\,‰$ may also lead to additional noise contribution.

The dominant noise contributions of the eROSITA detector system are Fano noise, readout noise, charge splitting and recombination as well as charge loss in the entrance window. For eROSITA detectors, with larger number of rows compared to the PNCCD used for the measurements, a moderate increase of CTI induced noise is expected.

10.5. Formation of the flat shelf

Measurements around the absorption edges, as presented in section 10.2, show that the flat shelf is caused by electrons emitted in the silicon and SiO_2. Electrons emitted in the Si_3N_4 and aluminum are stopped in the insensitive material. The described measurements were performed at the absorption edges with photon energies below 2 keV. At higher photon energies, these measurement results can be complemented by the analysis of simulated spectra. As shown in section 10.3, the flat shelf in the spectra of medium X-ray photon energies is reproduced by the Geant4 simulation. In contrast to measurement data, the simulation data allow to assign each event in the spectrum to its point of origin in the detector and to reconstruct the chain of processes leading to the observed event energy. The point of origin denotes the depth of the first photoabsorption process of the primary photon, which can be in insensitive layers of the entrance window as well as in the silicon.

A simulation of the of photon and electron interactions as described in section 9.3 leads to the spectra shown in fig. 10.6a to 10.6d. For better visibility, these spectra are free of noise by omitting the detector specific models described in section 9.4. In Figure 10.6, the black line shows the simulated spectrum in total, while the colored lines display only those events with point of origin in certain parts of the entrance window. The location of the first photoabsorption process can be inside the aluminum (light blue), silicon nitride (dark blue), silicon dioxide (green) or silicon (red). All events absorbed in the first 30 nm of silicon are additionally displayed in orange.
Fluorescence photons, emitted in SiO_2, Si_3N_4 and aluminum, cause lines in the simulated spectra. In the 3 keV spectrum, aluminum fluorescence caused by silicon escape photons leads to an additional line at 2.75 keV. Such a rather weak fluorescence line, as well as the Si-K line in the 7 keV spectrum, is smeared by the Fano and readout noise later and therefore not visible in the spectra shown in fig. 10.3.
In the 1.85 keV and 3 keV spectra, shown in fig. 10.6a and fig. 10.6b, the flat shelf is formed by electrons emitted in the SiO_2 and the first 30 nm of silicon. In contrast to that, the shelf at higher photon energies is mainly caused by electrons with origin in aluminum and deeper in the silicon (see fig. 10.6c and fig. 10.6d). Evidently, the flat shelf is caused deeper inside the silicon bulk with increasing photon energy, and therefore increasing electron range. A minimum contribution to the flat shelf, generated by electron escape from the silicon, can therefore not be avoided even with an ultra-thin entrance window. Furthermore, the on-chip aluminum layer does not significantly increase the intensity of the flat shelf, and hence the signal-to-background ratio of the detector.

In all spectra in fig. 10.6 steps in the flat shelf are visible. In the spectrum of 1848 eV photons in fig. 10.6a, directly above the silicon K-shell absorption edge, a step at ≈ 0.25 keV is especially pronounced (see also fig. 10.1e). Photons with 1848 eV predominantly cause photoabsorption in the K-shell (see fig. 2.7), with the emission of a photoelectron with only a few eV of kinetic energy. The most important relaxation process for K-shell vacancies is the emission of a KLL - Auger electron with an energy of 1.6 keV (see table 2.4). Therefore, the flat shelf in fig. 10.6a is almost purely generated from KLL Auger electrons escaping the silicon. If such an Auger electron is emitted very close to the silicon interface, it can fully escape the sensitive volume. If it is generated deeper inside the silicon, a great part of its kinetic energy is deposited before the electron escapes. This creates event energies between 1.85 keV - 1.6 keV = 0.25 keV and 1.85 keV. The flat shelf caused by these Auger escape events therefore extends down to

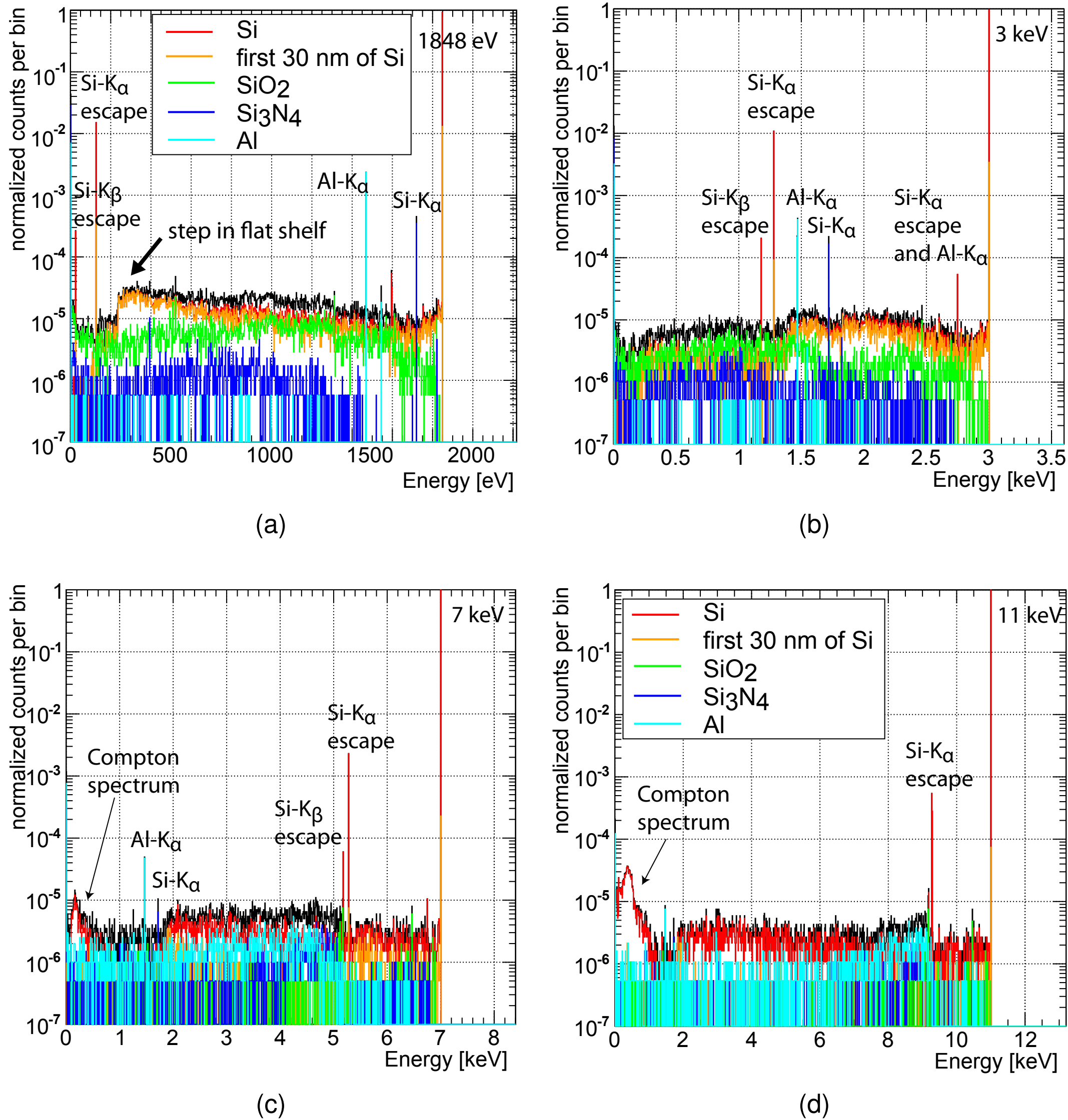

Figure 10.6.: Simulated spectra without Fano or readout noise. The color of each entry indicates the z-position of the photon absorption process (photoeffect). The origin of events inside the low energy shelf can thus be derived. Weak fluorescence peaks, here visible at distinct energies, are later smeared by the Fano and readout noise and merge with the shelf in the resulting spectrum.

0.25 keV, leading to the observed step. In the spectrum of 3 keV photons in fig. 10.6b, this step is found at 3 keV - 1.6 keV = 1.4 keV.

A similar conclusion can be drawn for electrons emitted in the insensitive entrance window layers, entering the silicon. For example aluminum K-shell photoelectrons possess an energy of E_{ph} - 1.6 keV, where E_{ph} is the photon energy (see table 2.3). In the spectrum of 11 keV photons in fig. 10.6d, these photoelectrons cause a flat shelf which extends up to a maximum energy of 9.4 keV.

The correct reconstruction of the flat shelf structure by simulations, as already shown in fig. 10.3, proves that the presented simulation model matches well the experimental findings. The simulation analysis shows that the fraction of flat shelf events in an X-ray spectrum is

defined by the type of electron emitted in the dominant relaxation process in silicon. This can be an Auger- or photoelectron, depending on the photon energy. This allows to perform an estimation of the number of flat events in a spectrum, as discussed in the next section.

11. Conclusions for eROSITA

11.1. Analytic description of the redistribution function

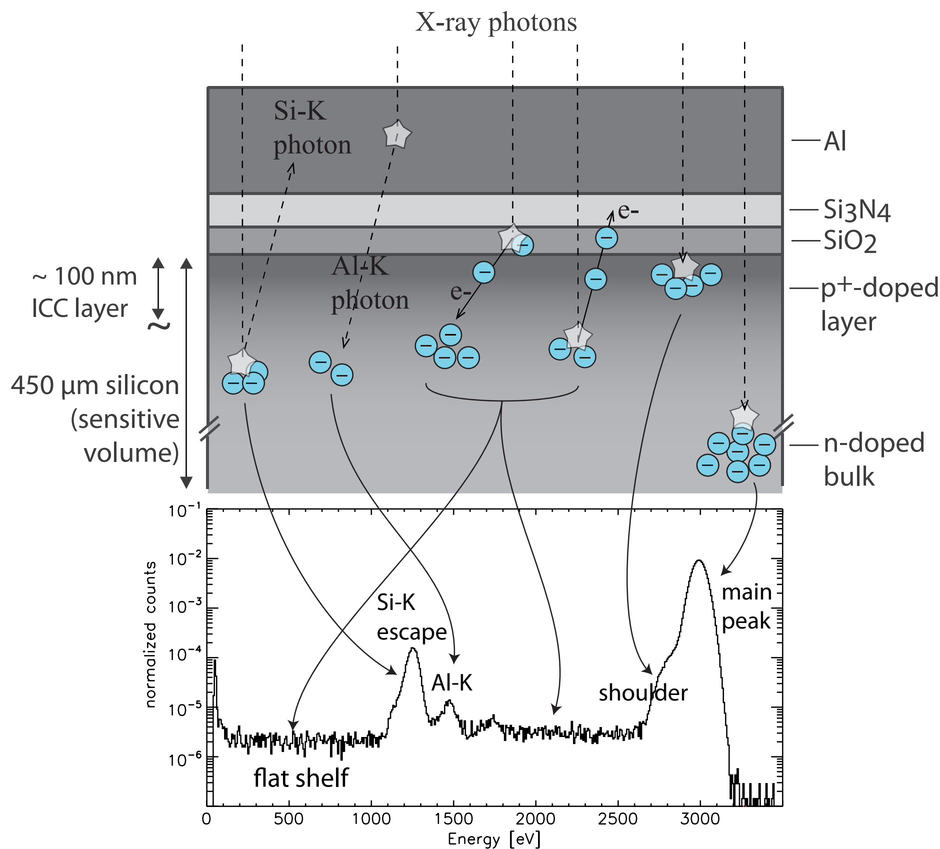

Figure 11.1.: Schematic of the origin of the most important spectral features in the eROSITA energy range of interest. The absorption of photons is marked by a star. In most cases, photons are absorbed in the silicon bulk (sensitive volume). The number of collected electrons is proportional to the photon energy, forming the main peak. In case of absorption in the ICC-layer, partial charge loss leads to spectrum entries in the low energy shoulder. The transition of electrons across the interface between silicon and SiO_2 causes flat shelf events, as these electrons deposit energy in the insensitive layers, mainly the SiO_2. Al-K fluorescence photons entering the silicon, as well as Si-K photons leaving the silicon cause additional peaks in the spectrum.

For the evaluation of eROSITA mission data it is necessary to formulate a detector response matrix that can be fitted to measured spectra. Naturally, to achieve efficient data analysis it is not possible to simulate the trajectory of each photon and electron in the detector. A

simplified analytic description of the detector response function is needed for this purpose. The response model used for the PNCCD cameras on XMM-Newton was described by Popp (2000). For eROSITA, the modified entrance window properties require a new model. The quality of such a description is evaluated based on the detailed experimental and simulation results of the previous chapters.

In fig. 11.1 the relevant constituents of the analytical detector redistribution function, that is the main peak, flat shelf, aluminum fluorescence and silicon escape peak, are displayed at a glance. A detailed discussion of the physical processes leading to these features has already been given in chapter 10. Simplified, analytic descriptions for these features are presented in the following. The Compton spectrum is not part of this simplified model, as its relative intensity is rather low for photon energies below 10 keV.

Flat shelf: The comparison of spectra around the absorption edges in section 10.2 as well as simulation results in section 10.5 give a picture of the origin of electrons contributing to the flat shelf in eROSITA spectra. Based on these findings, the relative amount of flat shelf events in a spectrum depending on the incident photon energy is estimated in the following, neglecting the structure within the flat shelf.
Electrons traversing the Si-SiO_2 interface deposit only part of their energy in the sensitive volume. It was seen in chapter 10 that the relative intensity of flat shelf events in a spectrum decreases with increasing photon energy, i.e. with the number of photons absorbed close to the silicon-SiO_2 interface. In the following model it is assumed that every absorption process in the silicon or SiO_2 can contribute to the shelf, as long as the electron range is large enough to reach the interface. Within this region, isotropic electron emission causes only half of the generated electrons to move in direction of the interface, adding a factor of 0.5 to the estimation. Summing up the contributions in the silicon and in the SiO_2, the number of flat shelf counts N_{shelf} in the spectrum of photons with energy E_{ph} is then

$$N_{\text{shelf}} = 0.5 N_0 \left(1 - e^{-\alpha_{\text{Si}} R_{\text{max,Si}}}\right) + 0.5 N_0 \left(1 - e^{-\alpha_{\text{SiO2}} R_{\text{max,SiO2}}}\right) \; . \tag{11.1}$$

The number of absorption processes is estimated from eq. 2.8 using the absorption coefficient α and the maximum electron range R_{max} in the respective material. N_0 is the number of photons incident on the Si-SiO_2 interface. The number of electrons generated in the Si_3N_4 and aluminum is small enough to be neglected in the estimation.
The range of electrons in matter increases with their kinetic energy, as shown in fig. 2.10 and given in eq. 2.29. With larger electron range, more absorption processes cause flat shelf entries in the spectrum. However, the absorption of monochromatic photons results in the generation of electrons with different kinetic energies and ranges, i.e. Auger- or photoelectrons from different shells. For an estimation it is sufficient to take into account only those electrons of the most probable transitions. By restricting oneself to those electrons with highest kinetic energy, the estimation is further simplified. In the SiO_2 layer, only the range of electrons from oxygen transitions are considered, which is larger than that of electrons from silicon transitions.

The maximum electron range in dependence of the incident photon energy was determined for silicon as well as for SiO_2 and is illustrated in fig. 11.2. The range of electrons emitted from silicon is displayed in black, for those emitted from oxygen in SiO_2 in red. As discussed in

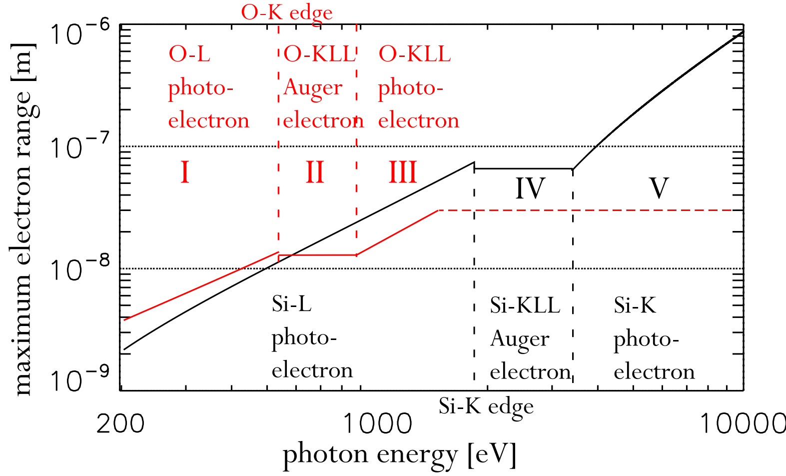

Figure 11.2.: Maximum range of electrons generated in a photon absorption process in silicon and SiO_2. The range of electrons emitted by silicon atoms is displayed in black, of those emitted by oxygen atoms in SiO_2 in red. The maximum range is used to define the thickness of the CED layer around the silicon-SiO_2, where flat shelf events are generated.

section 2.4, the energy of an emitted photoelectron rises with photon energy (see eq. 2.18), whereas the energy of an Auger electron is fixed, characteristic for the absorbing element (see eq. 2.27). In the energy regime I, the dominant part of shelf events with origin in the SiO_2 is caused by O-L photoelectrons. Above the O-K edge, absorption occurs almost completely in the O-K shell (O-K). In energy regime II, the range of O-KLL Auger electrons is larger than of O-K photoelectrons. Above 1 keV, the energy O-K photoelectrons exceeds the Auger electron energy (regime III). A range of 30 nm at maximum is taken into account for these electrons, limited by the SiO_2 thickness.
On the side of the silicon, the maximum range at low photon energies is given by Si-L photoelectrons in regimes I, II and III. Above the Si-K edge, Si-KLL Auger electrons (regime IV) and Si-K photoelectrons (regime V) add the main contribution to the flat shelf in the spectrum. At a photon energy of 10 keV, the electron range rises to up to 1 µm. It is obvious that the flat shelf is primarily caused by silicon bulk electrons at this photon energy, whereas the number of electrons emitted from the insensitive layers is limited by the material thickness of 270 nm.

The maximum electron ranges shown in fig. 11.2 are inserted into eq. 11.1 for the estimation of the number of flat shelf events. A photon absorption process in SiO_2 at a distance of R_{max} from the interface contributes with zero energy, as the electron deposits all its kinetic energy along its path through insensitive volume. An electron emitted in SiO_2, but directly at the silicon interface, contributes with the full energy. A corresponding consideration applies to silicon electrons. In first approximation, all flat shelf events determined by eq. 11.1 are evenly spread in the spectrum over event energies from zero to E_{ph}, resulting in a mean number of events per energy $< \frac{dN}{d\epsilon} >_{\text{shelf}}$ in a normalized spectrum of:

$$< \frac{dN}{d\epsilon} >_{\text{shelf}} = \frac{N_{\text{shelf}}}{E_{\text{ph}} N_{\text{tot}}} \,. \tag{11.2}$$

The total number of events in the spectrum, N_{tot}, is approximately equal to the number of photons absorbed in the silicon bulk. The estimated values from eq. 11.2 are shown as a

solid line in fig. 11.3, together with values derived from the measured spectra displayed as crosses. With increasing photon energy, the number of absorption processes near the silicon-SiO_2 interface and hence $< \frac{dN}{d\epsilon} >_{\text{shelf}}$ decreases. The O-K and Si-K edges in the absorption coefficient are as well visible. As the used absorption data for oxygen is based on atomic cross sections, a deviation from the measured values occurs due to absorption edge fine structure (see section 8.1). To accurately reproduce the amount of flat shelf events over such a large energy range, the varying electron range shown in fig. 11.2 is necessary. This is for example visible in energy regime V in fig. 11.3, where the increasing electron range of photoelectrons leads to a flattening of the slope of $< \frac{dN}{d\epsilon} >_{\text{shelf}}$ compared to the constant Auger electron range in regime IV.

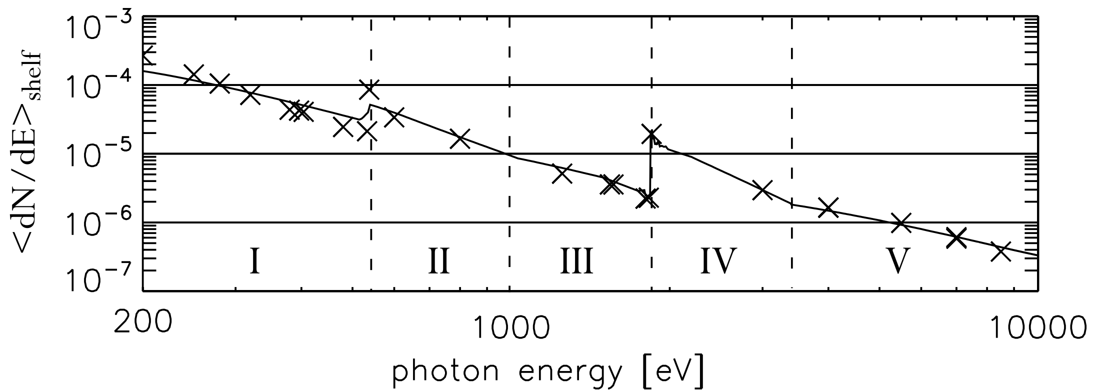

Figure 11.3.: The mean number of flat shelf events per energy determined from normalized measured spectra is shown by crosses (also listed in appendix B.2). Its overall decrease with photon energy is due to decreasing absorption near the Si-SiO_2 interface. The estimation of the flat shelf intensity based on eq. 11.1 and eq. 11.2 is shown as a solid line. The estimation takes into account the maximum electron range in fig. 11.2, defining the maximum distance from the Si-SiO_2 interface where shelf events can be generated.

In an earlier estimation by Popp (2000), the flat shelf description was connected to the parameter γ of the CCE-function, as the flat shelf electrons are mainly collected in the ICC layer and are therefore subject to partial charge loss. For eROSITA PNCCDs the maximum charge loss in the ICC layer, γ=0.1, is smaller and its impact on the flat shelf is weak. It is not included in the above described estimation of the flat shelf in order to avoid a misleading interdependency between the shape of the main peak and the flat shelf. More important for the estimation are the maximum electron ranges depending on the most probable electron transitions to allow the description of the flat shelf over a wide range of photon energies.

Silicon escape peak: If a silicon fluorescence photon escapes the sensitive volume, it causes an entry in the spectrum with an event energy reduced by the energy of the fluorescence photon. The probability of such events is given by the probability p_K of absorption in the K-shell, the probability of a radiative transition and the escape probability. An estimation of the escape probability P_{esc} was performed by Reed & Ware (1972) for silicon detectors. Using this estimation, the relative fraction of silicon escape events $k_{\text{Si, esc}}$ compared to the total number of events in a monochromatic spectrum can be determined according to

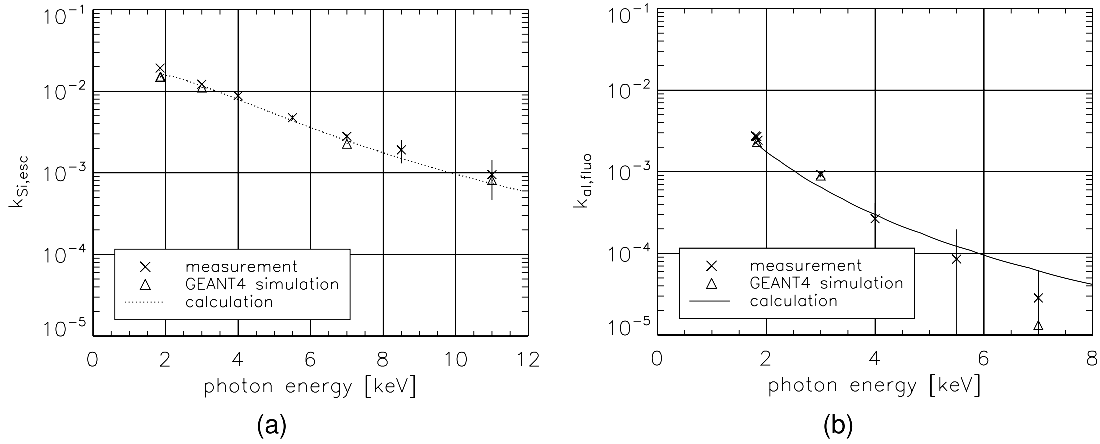

Figure 11.4.: Fraction of (a) silicon escape and (b) aluminum fluorescence events compared to the total number of events in eROSITA spectra as a function of the incident photon energy. The calculation as presented in eq. 11.3 and eq. 11.4 can reproduce well the measured values (also listed in appendix B.2). Furthermore, the results of Geant4 simulations are displayed. Some of these measured and simulated spectra are shown in fig. 10.1 and fig. 10.3.

$$k_{\text{Si, esc}} = p_K \cdot \omega_K \cdot P_{\text{esc}} \approx p_K \cdot \omega_K \cdot \frac{1}{2}\left(1 - \frac{\mu(1739\,\text{eV})}{\mu(E_{\text{ph}})} \ln\left(1 + \frac{\mu(E_{\text{ph}})}{\mu(1739\,\text{eV})}\right)\right) . \tag{11.3}$$

The probability of K-shell absorption relative to other shells, p_K, varies between 0.92 and 0.97 for photon energies between 1.85 keV and 10 keV (see also fig. 2.7b). It can be approximated by a constant value p_K = 0.95. The mass absorption coefficients μ at the photon energy and the energy of a silicon fluorescence photon can be found in Henke et al. (1993). The K-shell fluorescence yield is $\omega_{K,Si}$ = 0.0485, as listed in table 2.4.
Values calculated according to eq. 11.3, compared to those determined from measured and simulated spectra, are shown in fig. 11.4a. Closely above the Si-K edge, a high amount of silicon escape events of up two 2 % occurs. With rising photon energy, absorption occurs deeper inside the silicon bulk, leading to a lower fraction of silicon escape events. The calculation according to eq. 11.3 underestimates the measured values by about 10 % at lower and 20 % at higher photon energies. One reason for this is the limited accuracy of the fluorescence yield, as values for $\omega_{K,Si}$ found in literature spread by up to 20 %. The value for the fluorescence yield in the Geant4 data package, used for the simulation, is 0.0477. The decreasing number of silicon escape events with photon energy leads to an increasing uncertainty for the $k_{\text{Si, esc}}$ values determined from measured and simulated spectra.

Aluminum fluorescence peak: Aluminum fluorescence photons, generated in the aluminum layer of the on-chip filter, can enter the silicon and lead to an additional peak in the spectrum. By calculating the amount of generated fluorescence in the aluminum layer, reducing it by those photons reabsorbed in SiO_2 and Si_3N_4, the intensity of this peak is estimated. The fraction of aluminum fluorescence events $k_{\text{Al, fluo}}$ compared to the total number of events in the spectrum is determined by

$$k_{\text{Al, fluo}} = P_{\text{Al}} \cdot p_K \cdot \omega_{K,Al} \cdot 0.5 \cdot \prod_i T_i \ . \tag{11.4}$$

This calculation includes the absorption probability P_{Al} and the fluorescence yield $\omega_{K,Al}$ = 0.0371 of Aluminum (see table 2.4). The probability for K-shell absorption relative to other shells in aluminum for photon energies between 1.8 keV and 8 keV is p_K = 0.93 . The transmission of aluminum fluorescence photons through all layers between aluminum and silicon, in this case the SiO_2 and Si_3N_4, is taken into account by the product of transmittances T_i of each layer, calculated with eq. 2.12. To include only fluorescence photons emitted in direction of the silicon, a factor of 0.5 is added to eq. 11.4.
This calculation is shown as a solid line in fig. 11.4b, compared to the values determined from measured and simulated spectra (with $\omega_{K,Al}$ = 0.0369 in the Geant4 simulation). The aluminum fluorescence peak is only weakly pronounced in comparison to the silicon escape peak at all photon energies. For high photon energies, it is almost covered by the flat shelf and therefore the uncertainty for the determination of $k_{\text{Al, fluo}}$ from spectra rises.

Main peak: When using an analytic model to describe the main peak, all contributions that lead to the distortion or shift are subsumed in such a model. This includes not only partial charge loss in the ICC layer, but also the effect of event thresholds for recombination. For data evaluation of PNCCD data of the EPIC camera on XMM-Newton, the model by Popp (2000) was used. It exhibits four free parameters, of which the parameter S is equal to 1 - γ and τ is the same as used in this work. Due to the optimized entrance window, the two parameters γ and τ are sufficient to describe well the shape of the main peak for eROSITA spectra. With a charge collection efficiency identical to the one given in eq. 9.2, the total redistribution function without the influence of noise is given by

$$\frac{dN}{d\varepsilon}_{\sigma=0} = \begin{cases} < \frac{dN}{d\epsilon} >_{\text{shelf}} & : 0 \leq \varepsilon \leq E_{\text{ph}} \\ k_{\text{Al,fluo}} & : \varepsilon = 1485 eV \\ k_{\text{Si,esc}} & : \varepsilon = E_{\text{ph}} - 1739 eV \\ \frac{\tau\alpha}{(E_{\text{ph}} - \varepsilon)} \left[\frac{1}{\gamma} (1 - \frac{\varepsilon}{E_{\text{ph}}}) \right]^{\tau\alpha} & : (1-\gamma) \cdot E_{\text{ph}} < \varepsilon < E_{\text{ph}} \end{cases} . \tag{11.5}$$

Of course, the aluminum and silicon escape peaks are only added for photon energies above the respective K-shell energy. The last term, describing the main peak, is derived from the absorption function with absorption coefficient α and from the charge collection efficiency as described in appendix C.
In contrast to the presented simulations, statistical fluctuations can not be accounted for by such an analytical model. To include such statistical fluctuations, it is folded with a Gaussian distribution, adapting the width σ to the measured spectrum. Finally, the resulting function writes

$$\frac{dN}{d\varepsilon}_{\sigma}(\varepsilon) = \int_{-\infty}^{\infty} \frac{dN}{d\varepsilon}(\varepsilon + \tilde{\varepsilon}) \cdot \frac{1}{\sqrt{2\pi}\sigma} \exp\left(-\frac{1}{2} \frac{\tilde{\varepsilon}^2}{\sigma} \right) d\tilde{\varepsilon} \ . \tag{11.6}$$

The parameters γ and τ can be different to the ones shown in this work, as they will also include charge loss due to event splitting and recombination, especially for low energy photons. Figure 11.5 shows an exemplary spectrum of 3 keV photons with the estimation given by

eq. 11.6. The parameters for this spectrum are γ = 0.08 and τ = 95 nm. The used value for σ is equal to the sum of Fano noise σ_{Fano} (see eq. 3.11) and an additional noise contribution of 4.9 electrons (ENC).
Any structure within the flat shelf can not be reproduced with this simplified model. The silicon fluorescence peak, only weakly pronounced in the spectrum, is also not included in the model as it is covered by the flat shelf at almost all photon energies. A even better description could be achieved by applying the last term of eq. 11.5 not only to the main peak, but also to the silicon escape and aluminum fluorescence peaks in order to reproduce their shape. Such effects are inherently included in the Geant4 simulations, shown in fig. 10.3b for 3 keV photons. However, the trade-off between computing time and accuracy has to be decided upon with respect to the specific data analysis problem.

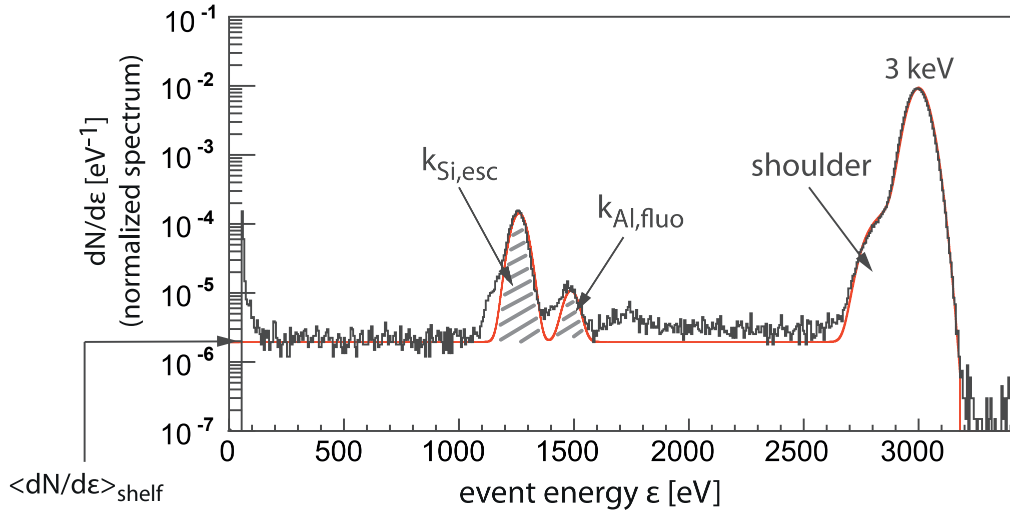

Figure 11.5.: Measured spectrum (black) at 3 keV *with analytic model for the redistribution function (red) as described in eq. 11.6. Compared to simulations (see chapter 9), this model gives a more simplified result for the spectral redistribution function, but needs less computing time. Any structure in the flat shelf is neglected in the analytic model. The parameters of the ICC-layer (γ = 0.08 and τ =* 105 nm*) and the total noise σ, describing the main peak shape, are adapted to the measurement. Not only partial charge loss in the entrance window, but also charge loss through event detection thresholds and its statistical fluctuations is subsumed in these parameters.*

11.2. The spectral response of eROSITA flight cameras

In chapter 10, the spectral response of detectors *with* on-chip filter is extensively analyzed by measurements and simulations. The eROSITA instrument contains seven PNCCD cameras, equipped with a choice of seven PNCCDs with and *without* on-chip filter. As presented in section 8.2 and section 10.3, a thorough understanding of the quantum efficiency and the spectral redistribution function was achieved. On the basis of these findings, conclusions on the expected response function of both types of flight CCDs can be drawn.

For calibration of the eROSITA instrument, the quantum efficiency in the energy range of inter-

est has to be known for each PNCCD detector. The results of this work show that calculations can well reproduce the quantum efficiency except for the fine structure around the absorption edges. For the calculation, the thickness of all entrance window layers has to be known. At low photon energies, even nanometers of material absorb a relevant fraction of radiation and change the quantum efficiency. This can occur through a contamination of the detector entrance window, for example caused by outgasing of materials in the detector surroundings of test facilities or in orbit. Therefore, a measurement of the quantum efficiency of flight detectors at few photon energies can assure that the detector is free of contamination, allowing to calculate the quantum efficiency in the full energy range.

The chip-to-chip variation of thickness of the aluminum layer is at maximum ± 10 nm, larger than that of SiO_2 and Si_3N_4 (about 2 nm). The relative variation in quantum efficiency between several detectors is mainly caused by variations in the aluminum layer thickness. As the absorption in aluminum is especially high at energies closely above the Al-K edge, it can best be determined by measuring the quantum efficiency in this energy regime. Alternatively, the comparison of the normalized number of aluminum fluorescence events in the spectrum can be used to determine the variation in aluminum thickness. An absolute determination of the aluminum layer thickness is only possible with a precision of several percent with these methods, limited by the precision of tabulated absorption coefficients close to the Al K-edge as well as the fluorescence yield.

Without aluminum on-chip filter, variations in the PNCCD quantum efficiency are expected to be smaller. In this case the quantum efficiency is strongly affected by the transmittance of the external filter.

In the presented spectra, all features except for the low energy shoulder are reproduced by a simulation including general material properties of silicon, SiO_2, Si_3N_4 and aluminum. It can be expected that the redistribution function of eROSITA flight detectors is very similar to the one described in chapter 10. Small variations of layer thicknesses have only minor influence on the spectral redistribution function.

The low energy shoulder in X-ray spectra is caused by charge loss in the ICC layer (incomplete charge collection), modeled by a parameterized charge collection efficiency (CCE). The CCE function is influenced by the doping profile of the p^+-layer and interface properties of the Si-SiO_2 interface and hence sensitive to processing variations. Conclusively, it can be expected that the CCE model parameters show small variations between different detectors.

The impact of the aluminum layer on the spectral redistribution function is limited to the presence of an aluminum fluorescence peak. The flat shelf is not significantly affected by electrons generated in the aluminum layer, as only a negligible amount of these electrons reaches the sensitive volume. It can be concluded that the eROSITA detectors without on-chip filter have the same spectral redistribution function as presented in this work, however without the aluminum fluorescence peak. An impact of the external filter on the spectral redistribution function is discussed in the following section.

During the mission time, the eROSITA PNCCDs will be subject to radiation damage caused by high energetic particles. These particles cause defects in the crystal, leading to a higher trap density in the silicon material. Experiments regarding radiation damage on the PNCCD performance show that the main influence on the detector response is caused by bulk damage leading to a higher charge transfer inefficiency (CTI) (Meidinger et al., 2011). The CTI is usually determined and corrected before and during the mission phase.

11.3. Comparison of on-chip and external filter

A blocking filter for X-ray detectors is necessary to suppress visible and UV radiation in astronomical observations. Such a filter can be realized as an absorbing foil or as a thin film deposited directly on the chip. The PNCCD analyzed in this work is equipped with an on-chip solution, a thin layer of aluminum directly on top of the detector entrance window. This filter is mechanically stable and does not bear the risk of rupture during satellite launch.
For the seven flight cameras for the eROSITA mission, detectors with and without on-chip filter have been produced. Chips without on-chip filter have to be equipped with an external blocking filter. In order to maximize the mechanical stability of external filters, the absorbing aluminum film is deposited on top of a polyimide carrier foil. The eROSITA external filter is made of a polyimide (PI) foil of 200 nm thickness with an aluminum layer of 100 nm on top. Polyimide consists of carbon, oxygen and nitrogen with relative volume fractions of approximately 76 %, 15 % and 9 % respectively (see for example Lin et al., 2002). Such a filter causes an additional absorption edge in the quantum efficiency at the carbon K-shell binding energy of about 290 eV.

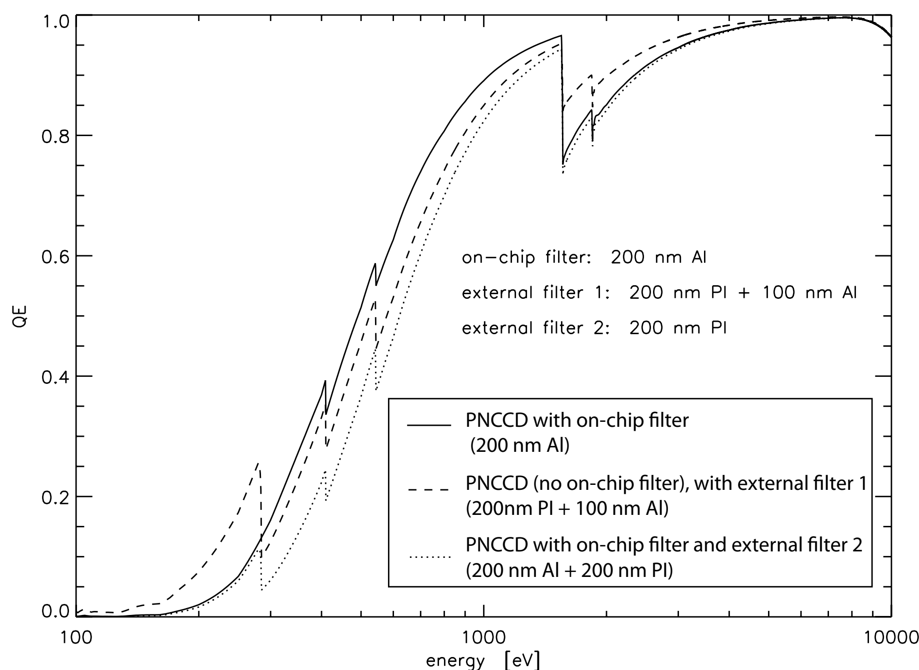

Figure 11.6.: Comparison of the quantum efficiency for eROSITA cameras using different blocking filters. The solid line shows the QE of a PNCCD with aluminum on-chip filter and no external filter. The dashed line refers to a detector without on-chip aluminum filter but using an external filter made of polyimide and aluminum. The dotted line combines the on-chip filter PNCCD with an external filter made only of polyimide.

The PNCCDs without on-chip filter exhibit the same entrance window as the one described in this work except for the aluminum layer. Figure 11.6 shows the calculated quantum efficiency curves for three possible configurations for eROSITA cameras. The solid line shows the quantum efficiency when using a detector with on-chip filter. The dashed line refers to a PNCCD without on-chip filter, but including an external filter made of PI and aluminum. Ad-

ditionally, the dotted line shows the quantum efficiency of a configuration using the aluminum on-chip filter and an external PI-filter. The last option bears the advantage that the EUV attenuation, decreasing strongly at the aluminum absorption edge, is enhanced by the Polyimide film. Furthermore, the PI filter in front of the PNCCD protects the detector from contamination. Outgasing of the instrument can lead to condensation of substances on the cold detector entrance window.

The attenuation of optical light and UV attenuation of the eROSITA on-chip filter have been measured as presented in chapter 7. These measurements revealed that the optical properties of thin metal layers can differ significantly from those of bulk material. A comparison to the blocking performance of an external filter is therefore not easily possible without experimental data. However, it can be expected that the EUV attenuation at energies below the aluminum L-edge is stronger when using an external filter due to the 200 nm thickness of the PI foil.
As described in chapter 7, the eROSITA on-chip filter exhibits microstructural inhomogeneities leading to pixel-wise variations of the attenuation coefficient. Such variations may be avoided when using an external filter due to the distance between filter and detector, leading to a smearing of bright spots.
On the contrary, the distance between external filter and PNCCD is disadvantageous for the filtering of events caused by cosmic particles. Such particles lead to the production of secondary electrons and photons in the absorbing material. When absorbed in the on-chip filter, primary and secondary particles deposit energy within the same or adjacent pixels. This leads to a track of signal pixels inside the detector. Such an event cluster is discarded by the analysis software because of exceeding the high energy threshold. Conclusively, most events caused by high energetic particles do not show in the final spectrum. Secondaries generated in the external filter however may hit the PNCCD in different, non-adjacent pixels. Such events, in particular those caused by electrons, can not be distinguished from X-ray photons, leading to an increased instrument background when using an external filter.

The measurements in this work revealed that the spectral redistribution function of both PNCCDs with and without on-chip filter is expected to be very similar. Furthermore the quantum efficiency as shown in fig. 11.6 shows only small deviations between the presented filter configurations. The model for the spectral redistribution function and quantum efficiency can be used to describe both configurations.

12. Summary

In the near future, the eROSITA space telescope will perform astronomical observations to study the geometry and dynamics of the Universe. The characterization and understanding of even small features of the detector response function are crucial to allow the correct and accurate scientific interpretation of measurement results during the mission time. Based on the successful devices applied for the XMM Newton telescope, the eROSITA PNCCDs are further optimized, including the development of an on-chip optical blocking filter. For such a detector it is essential to have detailed knowledge of the X-ray response function, including spectral performance, as well as of its reduced sensitivity to visible light and UV radiation. An experimental characterization of these properties was aimed in this thesis. In order to allow a physical interpretation of the results, a detailed study of the processes inside the PNCCD was targeted by means of Monte-Carlo simulations.

Over an extraordinary large photon energy range, from the optical to the soft X-ray regime, the attenuation properties of a PNCCD with on-chip filter have been measured. These measurements show that the on-chip filter attenuates visible light by a factor of more than 10^5. The optical properties of the aluminum filter turn out to be predominantly influenced by the morphology of the thin film structure and differ by orders of magnitude from bulk aluminum properties. An empiric model considering the thin film structure is applied to describe the attenuation properties of the on-chip filter. Measurements with photodiodes are presented, comparing improved entrance window configurations that have been developed at the MPI Semiconductor Laboratory.
The detector quantum efficiency for X-rays has been measured using two different experimental approaches in order to achieve most accurate results. One method derives the quantum efficiency from the responsivity of diodes and PNCCDs with the same entrance window, operated in integrating mode. The other method applies single photon counting techniques using a PNCCD in its standard operation mode. It is shown that the results from both measurements agree well. The measured quantum efficiency can be reproduced with calculations based on absorption coefficients given in literature. As this data is mostly given for condensed matter in atomic state, it can not describe the absorption edge fine structure. Measurements of this fine structure, characteristic for the materials comprised in the entrance window, are presented.
In addition to the quantum efficiency, the detector redistribution function for X-rays is characterized by measurements with monochromatic radiation in the photon energy range between 100 eV and 11 keV. The comparison of spectra close to the absorption edges allows to determine the origin of spectral features inside the detector. It turns out that the spectrum is mainly defined by the Si and SiO_2 properties, while outer layers of the entrance window have almost no impact on the spectrum.
The measurements are completed by a Monte-Carlo simulation of the X-ray spectral redistribution function. For this purpose, Geant4 based toolkits have been used and extended by a parameterized model for charge loss in the first hundred nanometers of silicon, the ICC layer. The simulation includes the complete chain of processes from photon absorption to charge

collection. The Monte-Carlo approach involves the simulation of each photon absorption process, allowing to reproduce well the statistics of signal charge collection and hence the energy resolution of the detector.
The analysis of the Geant4 simulation shows that the shape of the PNCCD background can be accurately reproduced, mainly by electron transport across the Si-SiO_2 interface of the entrance window. At the same time, shortcomings in a limited area of the Geant4 simulation, at low electron energies, are revealed.
Based on the interpretation of the simulation, an analytic model is presented that allows to estimate the relative amount of flat shelf events in a spectrum depending on the photon energy. Additional simplified analytic models for all relevant spectral features are reviewed.

In addition to detectors with on-chip filters, PNCCDs without aluminum filter have been manufactured at the MPI Semiconductor Laboratory. eROSITA cameras with such PNCCDs have to be equipped with external filters. The seven cameras of the eROSITA instrument can be chosen as a mixture of cameras with on-chip or external filter since both types show advantages. The analysis shows that the spectral redistribution function of PNCCDs without on-chip filter is very similar to the ones with filter. The quantum efficiency can furthermore be calculated with high accuracy. The expected performance of eROSITA flight detectors of both PNCCD types, assembled in the near future, is therefore well understood.
At last, an evaluation of the advantages and disadvantages of on-chip filters compared to external filters is given. The detector response is only moderately influenced by the choice of filter type, meaning that mechanical stability and associated risk of an external filter and the degree of contamination of an on-chip filter are more crucial aspects to be considered.

An in-depth understanding of X-ray spectra measured with a silicon detector has been achieved by a combination of different techniques, joining the benefits of experimental and theoretical approaches. This creates new opportunities for the scientific interpretation of high precision X-ray measurements.

Bibliography

Agostinelli, S., et al. (2003). GEANT4: A simulation toolkit. *Nucl. Instrum. Meth.*, *A506*, 250–303.

Allison, J., Amako, K., Apostolakis, J., et al. (2006). Geant4 developments and applications. *Nuclear Science, IEEE Transactions*, *53*(1), 270–278.

Andritschke, R., Hartner, G., Hartmann, R., Meidinger, N., & Strüder, L. (2008). Data analysis for characterizing PNCCDS. In *Nuclear Science Symposium Conference Record, IEEE*, (pp. 2166–2172).

Apostolakis, J., Giani, S., Maire, M., et al. (1999). Geant4 low energy electromagnetic model for electrons and photons. CERN open report 99-034.

Aspnes, D. (1982). Optical properties of thin films. *Thin Solid Films*, *89*(3), 249 – 262.

Bautz, M., Prigozhin, G., Pivovaroff, M., et al. (1999). X-ray CCD response functions, front to back. *Nuclear Instruments and Methods in Physics Research Section A*, *436*, 40–52.

Bautz, M. W., Pivovaroff, M. J., Baganoff, F., et al. (1998). X-ray CCD calibration for the AXAF CCD Imaging Spectrometer. In *Proc. SPIE*, vol. 3444, (pp. 210–224). SPIE.

Bergmann, L., & Schaefer, C. (2003). *Lehrbuch der Experimentalphysik: Optik*. De Gruyter.

Brandt, G., Eden, J., Fliegauf, R., et al. (2007). The Metrology Light Source - The new dedicated electron storage ring of PTB. *Nuclear Instruments and Methods in Physics Research Section B: Beam Interactions with Materials and Atoms*, *258*(2), 445–452.

Campbell, J. L., McDonald, L., Hopman, T., & Papp, T. (2001). Simulations of Si(Li) x-ray detector response. *X-Ray Spectrometry*, *30*(4), 230–241.

Cho, T., Yamaguchi, N., Kondoh, T., et al. (1988). Quantum efficiency of gold photocathodes and EXAFS in its secondary electron yield and in the detection currents of a microchannel plate and a silicon surface barrier detector. *Review of Scientific Instruments*, *59*(11), 2453 –2456.

Cullen, D. (2010). PREPRO 2010: 2010 ENDF/B Pre-processing Codes, IAEA-NDS-39, Rev.14. International Atomic Energy Agency, Vienna, Austria.

Cullen, D., Hubbell, J., & Kissel, L. (1997). EPDL97: The evaluated photo data library '97 version. Lawrence Livermore National Lab., United States.

Cullen, D. E., et al. (1989). Tables and graphs of photon interaction cross-sections from 10 eV to 100 GeV derived from the LLNL evaluated photon data library (EPDL). Part A: Z = 1 to 50. Lawrence Livermore National Laboratory. UCRL-50400-V.6-REV.4-PT.A.

Ebermayer, S., Andritschke, R., Elbs, J., et al. (2010). Quantum efficiency measurements of eROSITA pnCCDs. In *Proc. SPIE*, vol. 7742, (pp. 77420U–10).

Eggert, T. (2004). *Die Spektrale Antwort von Silizium-Röntgendetektoren*. Ph.D. thesis, Technische Universität München.

Elbs, J., Andritschke, R., Hälker, O., et al. (2010). Electronic test system for the eROSITA x-ray PNCCDs. In *Proc. SPIE*, vol. 7742.

Fischetti, M. V., Laux, S. E., & Crabbé, E. (1995). Understanding hot-electron transport in silicon devices: Is there a shortcut? *Journal of Applied Physics*, *78*, 1058–1087.

Fox, A. (2001). *Optical properties of solids*. Oxford University Press.

Fragstein, C. v., & Römer, H. (1958). Über die Anomalie der optischen Konstanten. *Zeitschrift für Physik A Hadrons and Nuclei*, *151*(1), 54–71.

Fraser, G., Abbey, A., Holland, A., et al. (1994). The X-ray energy response of silicon Part A. Theory. *Nuclear Instruments and Methods in Physics Research Section A: Accelerators, Spectrometers, Detectors and Associated Equipment*, *350*(1-2), 368–378.

Goto, S. (1993). Response functions of a Si(Li) detector for photon energies from 1 to 10 keV. *Nuclear Instruments and Methods in Physics Research Section A: Accelerators, Spectrometers, Detectors and Associated Equipment*, *333*(2-3), 452 – 457.

Granato, S., Andritschke, R., Elbs, J., et al. (2011). The spectral redistribution function of eROSITA PNCCDs. In *Nuclear Science Symposium and Medical Imaging Conference (NSS/MIC), 2011 IEEE*, (pp. 122 –128).

Gullikson, E. M. (2001a). Atomic scattering factors. In *X-Ray Data Booklet*, chap. 1.7. Berkeley University of California.

Gullikson, E. M. (2001b). Mass absorption coefficients. In *X-Ray Data Booklet*, chap. 1.6. Berkeley University of California.

Hartmann, R., Buttler, W., Gorke, H., et al. (2006). A high-speed pnCCD detector system for optical applications. *Nuclear Instruments and Methods in Physics Research Section A: Accelerators, Spectrometers, Detectors and Associated Equipment*, *568*(1), 118–123.

Hartmann, R., Hartner, G., Briel, U., et al. (1999). Quantum efficiency of the XMM pn-CCD camera. In *Proc. SPIE*, vol. 3765, (p. 703).

Hartmann, R., Stephan, K. H., & L., S. (2000). The quantum efficiency of pn-detectors from the near infrared to the soft X-ray region. *Nuclear Instruments and Methods in Physics Research Section A: Accelerators, Spectrometers, Detectors and Associated Equipment*, *439*(2-3), 216–220.

Hasinger, G. (2006). eROSITA, Vorschlag für ein Röntgenteleskop auf der russischen PlattformSpektr-RG. Max-Planck-Institut für extraterrestrische Physik.

Henke, B., Gullikson, E., & Davis, J. (1993). X-ray interactions: photoabsorption, scattering, transmission, and reflection at E= 50-30000 eV, Z= 1-92. *Atomic data and nuclear data tables*, *54*(2), 181–342.

Henke, B. L., Lee, P., Tanaka, T. J., Shimabukuro, R. L., & Fujikawa, B. K. (1982). Low-energy x-ray interaction coefficients: Photoabsorption, scattering, and reflection : E = 100-2000 eV Z = 1-94. *Atomic Data and Nuclear Data Tables*, *27*(1), 1–144.

Herrmann, S., Buttler, W., Hartmann, R., et al. (2008). CAMEX readout ASICs for pnCCDs. In *IEEE Nuclear Science Symposium Conference Record*.

Horowitz, P., & Hill, W. (1989). *The Art of Electronics*. New York, NY, USA: Cambridge University Press.

Ibach, H., & Lüth, H. (2003). *Solid-State Physics: An Introduction to Principles of Materials Science*. Advanced Texts in Physics. Springer.

Iskef, H., Cunningham, J. W., & Watt, D. E. (1983). Projected ranges and effective stopping powers of electrons with energy between 20 eV and 10 keV. *Physics in Medicine and Biology*, *28*(5), 535–545.

Jones, S. E., Bautz, M. W., Kissel, S. E., & Pivovaroff, M. (1996). Using tritium and x-ray tubes as x-ray calibration sources for the AXAF CCD Imaging Spectrometer. In O. H. Siegmund & M. A. Gummin (Ed.) *Society of Photo-Optical Instrumentation Engineers (SPIE) Conference Series*, vol. 2808 of *Presented at the Society of Photo-Optical Instrumentation Engineers (SPIE) Conference*, (pp. 158–169).

Jungemann, C., Keith, S., Bufler, F. M., & Meinerzhagen, B. (1996). Effects of band structure and phonon models on hot electron transport in silicon. *Electrical Engineering (Archiv fur Elektrotechnik)*, *79*(2), 99–101.

Kimmel, N. (2008). *Analysis of the charge collection process in solid state x-ray detectors*. Ph.D. thesis, Universität Siegen.

Kittel, C. (1995). *Introduction to Solid State Physics*. Springer Verlag.

Klein, C. A. (1968). Bandgap Dependence and Related Features of Radiation Ionization Energies in Semiconductors. *Journal of Applied Physics*, *39*(4), 2029 –2038.

Klein, R., & Ulm, G. (2005). Die Metrology Light Source. In *Sonderdruck aus PTB Mitteilungen 115*.

Knoll, G. (1989). *Radiation detection and measurement*. John Wiley & Sons New York.

Kopitzki, K. (1986). *Einführung in die Festkörperphysik*. Teubner Studienbücher.

Krumrey, M. (1998). Design of a four-crystal monochromator beamline for radiometry at BESSY II. *Journal of Synchrotron Radiation*, *5*, 6–9.

Krumrey, M., Tegeler, E., & Ulm, G. (1989). Complete characterization of a Si(Li) detector in the photon energy range 0.9-5 keV. In *Rev. Sci. Instrum.*, vol. 60, (pp. 2287–2290). TSUKABA (JAPAN): AIP.

Krumrey, M., & Ulm, G. (2001). High-accuracy detector calibration at the PTB four-crystal monochromator beamline. *Nuclear Instruments and Methods in Physics Research Section A: Accelerators, Spectrometers, Detectors and Associated Equipment*, *467-468*(Part 2), 1175–1178.

Lechner, P. (1998). *Zur Ionisationsstatistik in Silicium*. Ph.D. thesis, Technische Universität München.

Lifshin, E. (1999). *X-ray Characterization of Materials*. Wiley-VCH.

Lin, X., , Grove, D., et al. (2002). Morphological evolution and surface and interface structure of aluminum on polyimide. *Journal of Vacuum Science and Technology*, *B 20*, 766–775.

Lowe, B. G. (2000). An analytical description of low-energy X-ray spectra in Si(Li) and HPGe detectors. *Nuclear Instruments and Methods in Physics Research Section A: Accelerators, Spectrometers, Detectors and Associated Equipment*, *439*(2-3), 247–261.

Lutz, G. (1999). *Semiconductor Radiation Detectors*. Springer Verlag.

MacDonald, J. (1971). *Metal-Dielectric Multilayers*. Hilger Illustrated.

Madelung, O. (Ed.) (1996). *Semiconductors - Basic Data, 2nd revised Edition*. Springer.

Mayer-Kuckuk, T. (1997). *Atomphysik*. Teubner Verlag.

GEANT4 collaboration (2008). *GEANT4 Physics Reference Manual, Version 4-9-2*.

Meidinger, N., Andritschke, R., Elbs, J., et al. (2011). Status of the CCD camera for the eROSITA space telescope. In *Proc. SPIE*, vol. 8145.

Meidinger, N., Andritschke, R., Halker, O., et al. (2006a). Systematic testing and results of x-ray CCDs developed for eROSITA and other applications. In *Proc. SPIE*, vol. 6276, (pp. 627618–11). Orlando, FL, USA: SPIE.

Meidinger, N., Andritschke, R., Hälker, O., et al. (2006b). Next generation of pnCCDs for X-ray spectroscopy and imaging. *Nuclear Instruments and Methods in Physics Research Section A: Accelerators, Spectrometers, Detectors and Associated Equipment*, *568*(1), 141 – 148.

Nguyen, H. V., An, I., & Collins, R. W. (1993). Evolution of the optical functions of thin-film aluminum: A real-time spectroscopic ellipsometry study. *Phys. Rev. B*, *47*(7), 3947–3965.

Niklasson, G. A., Aspnes, D. E., & Craighead, H. G. (1986). Grain-size effects in the parallel-band absorption spectrum of aluminum. *Phys. Rev. B*, *33*(8), 5363–5367.

Owens, A., Bayliss, S. C., Fraser, G. W., & Gurman, S. J. (1997). On the relationship between total electron photoyield and X-ray absorption coefficient. *Nuclear Instruments and Methods in Physics Research Section A: Accelerators, Spectrometers, Detectors and Associated Equipment*, *385*(3), 556–558.

Owens, A., Fraser, G. W., & Gurman, S. J. (2002). Near K-edge linear attenuation coefficients for Si, SiO_2 and Si_3N_4. *Radiation Physics and Chemistry*, *65*(2), 109–121.

Palik, E. D. (1985). *Handbook of Optical Constants of Solids I*. Academic Press.

Parmigiani, F., Kay, E., Huang, T. C., et al. (1986). Optical and electrical properties of thin silver films grown under ion bombardment. *Phys. Rev. B*, *33*(2), 879–888.

Perkins, S., Cullen, D., & Seltzer, S. (1991a). Tables and graphs of electron-interaction cross sections from 10 eV to 100 GeV derived from the LLNL Evaluated Electron Data Library (EEDL), Z = 1–100. Lawrence Livermore National Laboratory.

Perkins, S. T., Chen, M. H., Cullen, D. E., & Hubbell, J. H. (1991b). Tables and graphs of atomic subshell and relaxation data derived from the LLNL Evaluated Atomic Data Library (EADL), Z=1–100. Lawrence Livermore National Laboratory.

Pia, M., Seo, H., Batic, M., et al. (2011). Evaluation of Atomic Electron Binding Energies for Monte Carlo Particle Transport. *Nuclear Science, IEEE Transactions on*, *58*(6), 3246 –3268.

Poindexter, E. H., & Caplan, P. J. (1983). Characterization of Si/SiO_2 interface defects by electron spin resonance. *Progress in Surface Science*, *14*(3), 201–294.

Popp, M. (2000). *Untersuchung und analytische Modellierung der Systemantwort von pn-CCD Detektoren.*. Ph.D. thesis, Ludwig-Maximilians-Universität München.

Predehl, P., Boehringer, H., Brunner, H., et al. (2010). eROSITA on SRG. *Society of PhotoOptical Instrumentation Engineers SPIE Conference Series*, *7732*(1), 6.

Prigozhin, G., Jones, S., Bautz, M., Ricker, G., & Kraft, S. (2000). The physics of the low-energy tail in the ACIS CCD: The spectral redistribution function. *Nuclear Instruments and Methods in Physics Research Section A: Accelerators, Spectrometers, Detectors and Associated Equipment*, *439*(2-3), 582–591.

Prigozhin, G. Y., Woo, J., Gregory, J. A., et al. (1998). X-ray absorption near edge structure in the quantum efficiency of X-ray charge-coupled devices. *Opt. Eng.*, *37*(10), 2848–2854.

Reed, S. J. B., & Ware, N. G. (1972). Escape peaks and internal fluorescence in X-ray spectra recorded with lithium drifted silicon detectors. *Journal of Physics E: Scientific Instruments*, *5*(6), 582.

Scholze, F., Beckhoff, B., Brandt, G., et al. (2003a). High-Accuracy EUV Metrology of PTB Using Synchrotron Radiation. *Proc. SPIE*, *4344*, 402–413.

Scholze, F., Henneken, H., Kuschnerus, P., et al. (2000). Determination of the electron-hole pair creation energy for semiconductors from the spectral responsivity of photodiodes. *Nuclear Instruments and Methods in Physics Research Section A: Accelerators, Spectrometers, Detectors and Associated Equipment*, *439*(2-3), 208–215.

Scholze, F., Tümmler, J., & Ulm, G. (2003b). High-accuracy radiometry in the EUV range at the PTB soft x-ray beamline. *Metrologia*, *40*, 224.

Scholze, F., & Ulm, G. (1994). Characterization of a windowless Si(Li) detector in the photon energy range 0.1-5 keV. *Nuclear Instruments and Methods in Physics Research Section A: Accelerators, Spectrometers, Detectors and Associated Equipment*, *339*(1-2), 49–54.

Schopper, H. (1954). Die optischen Eigenschaften und der Aufbau dünner Metallschichten. *Fortschritte der Physik*, *2*(6).

Schötzig, U. (2000). Half-life and X-ray emission probabilities of 55Fe. *Applied Radiation and Isotopes*, *53*(3), 469–472.

Schwinger, J. (1949). On the classical radiation of accelerated electrons. *Physical Reviews*, *75*.

Seo, H., Pia, M., Saracco, P., & Kim, C. H. (2011). Ionization cross sections for low energy electron transport. *Nuclear Science, IEEE Transactions on*, *58*(6), 3219 –3245.

Sevier, K. D. (1979). Atomic electron binding energies. *Atomic Data and Nuclear Data Tables*, *24*(4), 323–371.

Strüder, L., Briel, U., Dennerl, K., et al. (2001). The European Photon Imaging Camera on XMM-Newton: The pn-CCD camera. *A&A*, *365*(1), L18–L26.

Sze, S. (1981). *Physics of semiconductor devices*. Wiley.

Thornagel, R., Klein, R., & Ulm, G. (2001). The electron storage ring BESSY II as a primary source standard from the visible to the x-ray range. *Metrologia*, *38*(5), 385–389.

Weidenspointner, G., Andritschke, R., Aschauer, S., et al. (2011). Strategy for calibrating the non-linear gain of the DSSC detector for the European XFEL. In *Nuclear Science Symposium and Medical Imaging Conference (NSS/MIC), 2011 IEEE*, (pp. 468 –473).

Wiedemann, H. (2003). *Synchrotron radiation*. Advanced texts in physics. Springer.

Wikipedia (2011). Elektromagnetisches Spektrum — Wikipedia, The Free Encyclopedia. [Online; accessed 01-August-2011].

Wustefeld, G., Feikes, J., Holldack, K., & Kuske, P. (2004). Compressed Electron Bunches for THz-Generation - Operating BESSY II in a Dedicated Low Alpha Mode. In *Proceedings of EPAC*, (pp. 2290–2292).

Zoglauer, A., Andritschke, R., & Schopper, F. (2006). MEGAlib - The Medium Energy Gamma-ray Astronomy Library. *New Astronomy Reviews*, *50*(7-8), 629–632.

Zoglauer, A., Weidenspointner, G., Galloway, M., Boggs, S., & Wunderer, C. (2009). Cosima - The cosmic simulator of MEGAlib. In *Nuclear Science Symposium Conference Record (NSS/MIC), 2009 IEEE*, (pp. 2053 –2059).

List of Figures

1.1. The eROSITA instrument 1

2.1. Electronic states in atomic and crystalline silicon 6
2.2. Energy level diagrams for metals, semiconductors and insulators 7
2.3. First Brillouin zone of silicon and aluminum 8
2.4. Band structure of silicon and aluminum 9
2.5. Optical constants of silicon and aluminum 13
2.6. Interaction mechanisms of X-ray radiation with matter 16
2.7. Interaction cross sections for X-ray photons in silicon 17
2.8. Schematics of fluorescence photon and Auger electron emission 20
2.9. X-ray fluorescence notation 21
2.10. Interaction cross sections, range and energy loss of electrons in silicon 22
2.11. Scattering rates for electrons in silicon 23

3.1. Schematic of pn junction 26
3.2. Sidewards depletion of PNCCDs 28
3.3. Cross section of a PNCCD (1) 29
3.4. Cross section of a PNCCD (2) 29
3.5. PNCCD mounted on ceramic circuit board 30
3.6. Readout structure of PNCCD and CAMEX 31
3.7. eROSITA entrance window 33
3.8. Exemplary X-ray spectrum (1) 34
3.9. Exemplary X-ray spectrum (2) 35

4.1. Continuous spectrum at BESSY II 43
4.2. Diffraction pattern behind multiple slits 44

5.1. Mobile vacuum chamber 46
5.2. SX700 monochromator at BESSY II 48

5.3. KMC monochromator at BESSY II 48
5.4. Diode structure and measurement circuit 50
5.5. Diode mounting for attenuation measurements 51
5.6. Setup for attenuation measurements with diodes 51
5.7. Schematic of the attenuation measurement setup at RÖSTI 54
5.8. LED board for attenuation measurements at RÖSTI 54
5.9. Beam spot during QE measurement 56
5.10. Impact of photon flux on QE measurement in integrating mode 58

6.1. Impact of event threshold on 200 eV spectrum 63
6.2. Linearization of digitized output signal 65
6.3. Determination of peak position and width 67
6.4. Spatial distribution of the number of photon counts during QE measurement . . 68

7.1. Measured optical and UV attenuation of eROSITA PNCCDs 70
7.2. Homogeneity of attenuation factor 71
7.3. Deviation between thin film and bulk optical properties of on-chip blocking filter . 72
7.4. TEM image of the aluminum thin film 73
7.5. Attenuation factor versus thickness of on-chip aluminum layer of photodiodes . . 74
7.6. Pixel wise variations of the attenuation factor 76

8.1. Measured absorption edge fine structure in eROSITA QE 79
8.2. Measured and calculated X-ray QE 81
8.3. Result of QE measurement with continuous spectrum 83
8.4. Measurement of the quantum efficiency homogeneity 85

9.1. Schematic of the detector response simulation 88
9.2. Geant4 simulation geometry 89
9.3. Schematic of Geant4 interaction mechanisms 90

10.1. Measured spectra of eROSITA PNCCD 96
10.2. Measured spectra at the K-shell absorption edges 98
10.3. Comparison between measured and simulated spectra 100
10.4. Comparison between measured and simulated spectrum at low photon energy . 101
10.5. Measured and simulated energy resolution 103

10.6. Point of origin of flat shelf events 106

11.1. Schematic of the origin of spectral features 108
11.2. Maximum range of electrons after photoabsorption 110
11.3. Fraction of flat shelf events in normalized spectrum 111
11.4. Fraction of fluorescence and escape events in normalized spectrum 112
11.6. Comparison of the QE with on-chip and external filters 116

A.1. Absorption length in aluminum 130
A.2. Absorption length in silicon 130
A.3. Absorption length in SiO_2 131
A.4. Absorption length in Si_3N_4 131

List of Tables

2.1. Separation and terms of photon energy regimes 5
2.2. Atomic shells of silicon 6
2.3. Electron binding energies 19
2.4. Auger and fluorescence transition rates and energies 21

5.1. Overview on the measurements 45

6.2. Gain and noise values for spectral measurements 66

10.1. Measured and simulated energy resolution 102

B.1. Quantum efficiency measurement results 132
B.2. Attenuation measurement results 133
B.3. Parameterization of the spectral redistribution function 137

A. Absorption length in Al, Si, SiO_2 and Si_3N_4

The following graphs show the absorption length (see eq. 2.9) in aluminum, silicon, silicon dioxide and silicon nitride. It is calculated from optical constants for photon energies in the visible and UV regime, and from interaction cross sections or mass absorption coefficients in the X-ray regime as described in chapter 2.

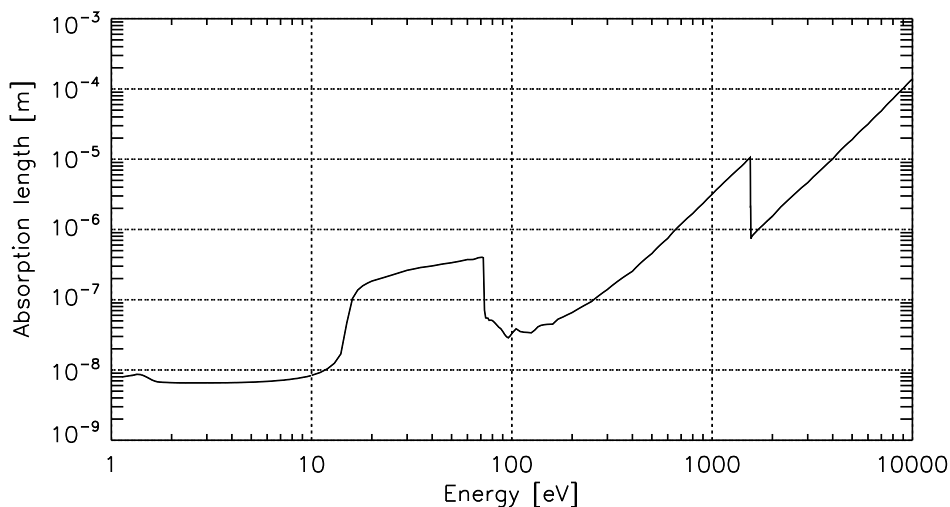

Figure A.1.: Absorption length (see eq. 2.8) in aluminum with a density ρ = 2.70 g/cm^3 *based on data from Henke et al. (1993), Palik (1985).*

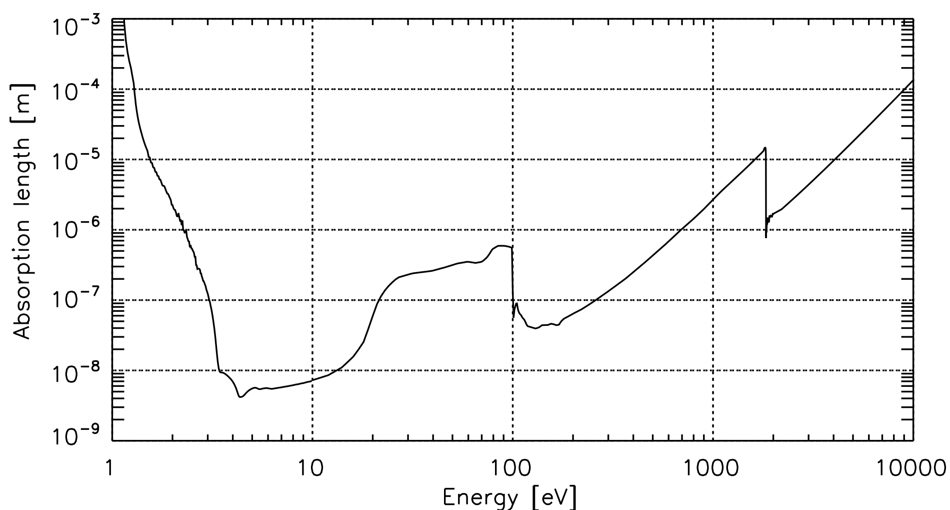

Figure A.2.: Absorption length (see eq. 2.8) in silicon with a density ρ = 2.33 g/cm^3 *based on data from Henke et al. (1993), Owens et al. (2002), Palik (1985).*

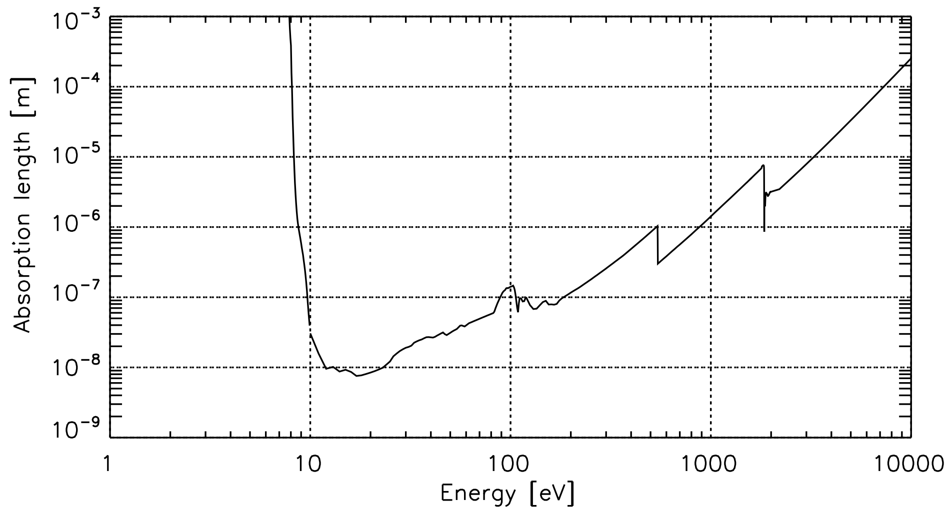

Figure A.3.: Absorption length (see eq. 2.8) in SiO_2 with a density $\rho = 2.20\,\mathrm{g/cm^3}$ based on data from Henke et al. (1993), Owens et al. (2002), Palik (1985).

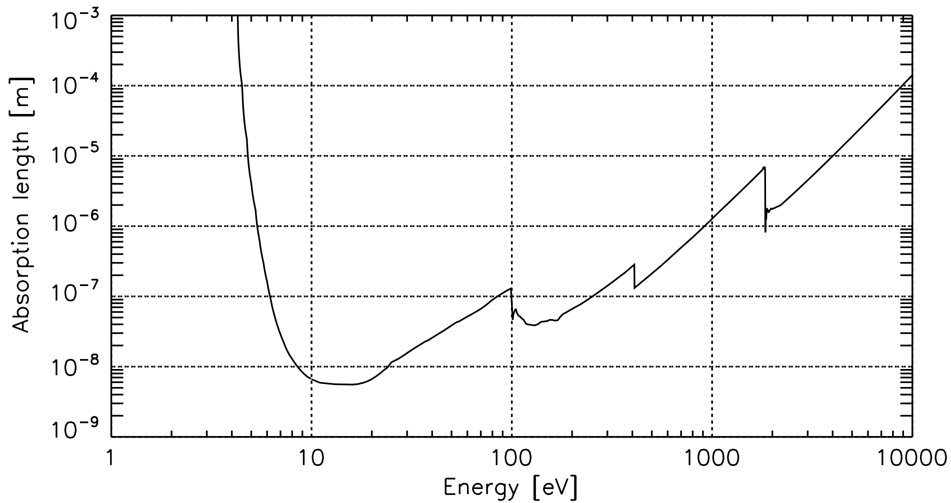

Figure A.4.: Absorption length (see eq. 2.8) in Si_3N_4 with a density $\rho = 3.44\,\mathrm{g/cm^3}$ based on data from Henke et al. (1993), Owens et al. (2002), Palik (1985).

B. Measurement data

B.1 Quantum efficiency and attenuation measurement data

B.1.1. Tabulated data

E [eV]	QE [%]	+/-ΔQE [%]	photons per frame [-]	I_{ref} [A]
200	2.0	0.1/-0.1	7.4×10^2	3.2×10^{-11}
250	8.3	0.1/-0.1	2.7×10^3	3.5×10^{-11}
280	13	0.2/-0.2	8.5×10^2	7.8×10^{-12}
320	21	0.3/-0.3	1.6×10^3	1.1×10^{-11}
380	36	1/-1	9.6×10^2	4.9×10^{-12}
398	40	2/-2	2.2×10^2	1.1×10^{-12}
404	31	1/-1	1.8×10^2	1.2×10^{-12}
410	35	1/-1	2.2×10^2	1.3×10^{-12}
480	53	2/-2	2.8×10^2	1.3×10^{-12}
534	60	2/-2	3.0×10^2	1.4×10^{-12}
538	48	2/-2	2.0×10^2	1.2×10^{-12}
560	55	2/-2	3.5×10^2	1.9×10^{-12}
600	65	2/-2	4.3×10^2	2.1×10^{-12}
800	83	7/-3	2.6×10^2	1.4×10^{-12}
1250	95	2/-2	1.3×10^3	9.9×10^{-12}
1540	93	3/-3	1.6×10^2	1.5×10^{-12}
1559	79	6/-6	1.2×10^2	1.4×10^{-12}
1564	64	5/-5	1.2×10^2	1.6×10^{-12}
1600	77	6/-6	1.3×10^2	1.6×10^{-12}
1800	86	2/-3	6.5×10^3	9.5×10^{-11}
1840	83	2/-2	6.8×10^3	1.2×10^{-10}
1849	74	2/-2	4.5×10^3	8.9×10^{-11}
1880	82	2/-2	5.3×10^3	9.7×10^{-11}
2500	93	1/-1	6.8×10^3	9.5×10^{-11}
3000	95	1/-1	6.0×10^3	9.8×10^{-11}
4000	97	2/-2	3.8×10^3	7.9×10^{-11}
7000	99	2/-2	2.5×10^3	9.1×10^{-11}
10 000	95	2/-2	1.6×10^3	8.8×10^{-11}
11 000	92	2/-2	1.5×10^3	9.3×10^{-11}

Table B.1.: Quantum efficiency measurement results with a PNCCD at the PTB experimental stations at BESSY II. See text for a description of the given values.

E [eV]	λ [nm]	χ [-]	+/-$\Delta\chi$ [-]	photons per frame [-]	P_{ref} [W]
1.88*	660	2×10^5	$+3 \times 10^5/-7 \times 10^4$	-	-
2.34**	530	2.5×10^5	$+4 \times 10^4/-1 \times 10^4$	-	-
2.64**	470	3.8×10^5	$+1.5 \times 10^5/-3.3 \times 10^5$	-	-
2.76	450	2.4×10^5	$+5.0 \times 10^3/-5.0 \times 10^3$	5.5×10^4	1.1×10^{-6}
2.89	429	3.3×10^5	$+8.0 \times 10^3/-7.0 \times 10^3$	4.4×10^4	1.3×10^{-6}
3.03	410	5.8×10^5	$+1.0 \times 10^4/-1.0 \times 10^4$	2.9×10^4	1.6×10^{-6}
3.10	400	7.7×10^5	$+2.0 \times 10^4/-2.0 \times 10^4$	2.3×10^4	1.7×10^{-6}
3.27	380	1.5×10^6	$+5.0 \times 10^4/-4.0 \times 10^4$	1.2×10^4	1.8×10^{-6}
3.35	370	2.1×10^6	$+7.0 \times 10^4/-7.0 \times 10^4$	8.6×10^3	1.8×10^{-6}
3.55	350	2.5×10^6	$+7.0 \times 10^4/-6.0 \times 10^4$	2.1×10^4	2.1×10^{-6}
3.76	330	2.8×10^6	$+7.0 \times 10^4/-7.0 \times 10^4$	1.8×10^4	2.1×10^{-6}
4.14	300	3.3×10^6	$+1.0 \times 10^5/-1.0 \times 10^5$	9.0×10^3	1.4×10^{-6}
4.77	260	4.3×10^6	$+1.0 \times 10^5/-1.0 \times 10^5$	8.7×10^3	2.0×10^{-6}
5.17	240	2.5×10^6	$+7.0 \times 10^4/-6.0 \times 10^4$	1.3×10^4	1.9×10^{-6}
5.64	220	2.4×10^6	$+6.0 \times 10^4/-6.0 \times 10^4$	1.2×10^4	1.8×10^{-6}
6.21	200	3.8×10^6	$+2.0 \times 10^5/-2.0 \times 10^5$	7.4×10^3	2.0×10^{-6}
7.30	170	1.3×10^7	$+1.0 \times 10^6/-1.0 \times 10^6$	8.4×10^2	9.1×10^{-7}
8.56	145	9.6×10^7	$+1.0 \times 10^8/-4.0 \times 10^6$	8.4×10^3	1.1×10^{-6}
9.19	135	2.7×10^8	$+2.0 \times 10^{10}/-2.0 \times 10^7$	1.1×10^3	7.6×10^{-7}
9.55	130	2.8×10^8	$+4.0 \times 10^9/-3.0 \times 10^7$	7.3×10^2	5.5×10^{-7}
16.6	75.0	3.4×10^5	$+2.0 \times 10^7/-3.0 \times 10^4$	6.3×10^2	5.5×10^{-9}
19.1	65.0	1.9×10^4	$+1.0 \times 10^5/-8.0 \times 10^2$	1.0×10^4	5.6×10^{-9}
22.6	55.0	1.9×10^3	$+2.0 \times 10^3/-1.0 \times 10^2$	1.3×10^3	1.7×10^{-9}
27.6	45.0	1.3×10^2	$+1.0 \times 10^1/-5.0$	2.1×10^4	2.2×10^{-9}
31.0	40.0	5.6×10^1	$+5.0/-3.0$	2.1×10^4	1.1×10^{-9}
E [eV]	λ [nm]	χ [-]	+/-$\Delta\chi$ [-]	photons per frame [-]	I_{ref} [A]
38.0	32.7	3.1×10^1	$+5.0 \times 10^{-1}/-5.0 \times 10^{-1}$	5.1×10^3	1.2×10^{-11}
50.0	24.8	1.1×10^1	$+2.0 \times 10^{-1}/-2.0 \times 10^{-1}$	1.0×10^4	1.4×10^{-11}
72.0	17.2	4.3	$+7.0 \times 10^{-2}/-6.0 \times 10^{-2}$	1.5×10^4	1.2×10^{-11}
73.0	17.0	2.4×10^1	$+4.0 \times 10^{-1}/-4.0 \times 10^{-1}$	4.1×10^3	1.9×10^{-11}
80.0	15.5	4.8×10^1	$+1.0/-1.0$	9.9×10^2	1.1×10^{-11}
85.0	14.6	2.0×10^2	$+3.0/-3.0$	1.3×10^3	6.7×10^{-11}
90.0	13.8	6.3×10^2	$+1.0 \times 10^1/-1.0 \times 10^1$	9.8×10^2	1.8×10^{-10}
95.0	13.1	2.5×10^3	$+4.0 \times 10^1/-4.0 \times 10^1$	1.1×10^3	8.8×10^{-10}

Table B.2.: Attenuation measurement results for an eROSITA type PNCCD. See text for a description of the given values. The dataset marked by (*) was measured with a photodiode of eROSITA entrance window and laser illumination. The datasets marked by (**) were measured with a PNCCD and illumination with LEDs. All other values were measured at the PTB experimental stations at BESSY II. At the MLS-UV beamline, the radiant power was given by the PTB. At the SX700 beamline, the reference photocurrent was given.

Table B.1 and table B.2 contain quantum efficiency and attenuation measurement data depending on the photon energy or wavelength, measured with CCD C12_10_52 (PNCCD with on-chip filter) as described in chapter 5. For the sake of simplicity, a reduced number of datasets is listed, as the original measurement data comprises more than 250 datasets.
Only the datasets marked by (**) were measured with CCD C12_08_52 and LED illumination, and the dataset marked by (*) with a photodiode and laser illumination.
Results of the quantum efficiency measurements are given in table B.1, the attenuation measurements are listed in table B.2. In order to give an idea of the measurement conditions for each dataset, the mean number of photons per frame measured with the PNCCD and the photocurrent I_{ref} of the PTB reference diode are given. At the MLS-UV beamline, the radiant power was determined directly by the PTB. Hence, for all datasets measured at the MLS-UV beamline, the radiant power P_{ref} is given instead of the reference photocurrent.
The measurement uncertainty is listed as absolute positive and negative deviation ΔQE, so that QE-ΔQE and QE+ΔQE serve as lower and upper limits. The same applies for the attenuation values χ. The given uncertainty was determined as described in the following section.

B.1.2. Measurement uncertainty

Whenever an error is expected to remain the same for multiple executions of the same experiment, it is regarded as systematic, otherwise statistical. Statistical error contributions are summed up quadratically, whereas systematic errors are summed up linearly. The final measurement error is calculated by the sum of systematic and statistical errors. Methods for the calculation of error propagation can for example be found in Knoll (1989).

The uncertainty of the quantum efficiency and attenuation measurements in integrating mode for each dataset is listed in table B.1 and table B.2. The possible error contributions of the quantum efficiency and attenuation measurements are:

- Reference measurement accuracy

  The reference diodes used by the PTB (Physikalisch Technische Bundesanstalt) are calibrated to an accuracy of 1 %. Hence, this value is perceived as a contribution to the systematic error. The statistical error caused during a photocurrent measurement with the reference diodes was determined depending to the measurement method at each beamline.
  For a reference diode measurement at the KMC beamline, the dark current was measured before and after the photon signal current. The deviation between initial and final dark current measurement is added as statistical error. At the SX700 and MLS-UV beamlines, no variation of the dark current was observed. However, for very low photocurrents the variation between several repetitions was observed. To account for this, an uncertainty of 30 fA is assumed in the error calculation of the photocurrent.
  A reference current measurement consisted of a repetition of current measurements. The statistical error of the mean photocurrent was derived from the standard deviation of all measurement values σ and the number of measurements n as

$$\epsilon_{\text{photo,ref}} = \frac{\sigma}{n} . \tag{B.1}$$

Datasets with reference currents lower than 1 pA were excluded from the evaluation, as they exhibit a larger uncertainty due to the small signal amplitude.

- PNCCD measurement accuracy

  All QE measurements with the PNCCD are evaluated by linearization of the measurement data and conversion of adu to eV using a constant amplification factor (see section 6.3). The estimated accuracy of this gain calibration is $\approx 2\,‰$. A common mode correction of the PNCCD frames is not performed. To account for the uncertainty of low signal measurements, the offset map drift in non-illuminated pixels was determined and added to the uncertainty of signal in illuminated pixels. This deviation was rather small compared to other error contributions.

- Stability of the radiation source

  At the SX700 monochromator, measurements at high photon energies above 1 keV had to be strongly attenuated by slits at the monochromator. The slit was almost completely closed, such that already thermal variations can cause a change in the slit opening. During a time span of more than a few minutes this can lead to a change in the photon flux. A systematic drift in the results of QE measurements was observed whenever the time difference between PNCCD and reference diode measurement was larger than 20 minutes. This applies to the measurement results around the aluminum K-edge, as several photon energies where first measured with the PNCCD and then the same photon energies were measured with the reference diode. For these data points, an inaccuracy of 4 % was estimated and added to the total error calculation.
  The ring current, which is used for normalization of the photon flux with time, was measured by the operating staff of the BESSY II and MLS storage rings. For typical values for the ring current in the range of 30 mA the uncertainty is on the order of 10^{-4}(Thornagel et al., 2001). This contribution can be neglected compared to other uncertainty contributions. For the measurements at MLS, the precision of the ring current measurement is also neglected, as other error contributions are dominant.

- Higher order radiation

  At the MLS-UV and SX700 experimental setups, higher order radiation with a photon energy twice as large as the nominal monochromator photon energy has to be taken into account. This radiation may influence or dominate the quantum efficiency measurement, whenever the PNCCD quantum efficiency is low for the nominal photon energy, but higher for photons with twice the energy. When denoting f as the fraction of higher order radiation, the measured PNCCD signal caused by the nominal photon energy and additional higher order radiation is

$$\nu_{\mathrm{e}} = \frac{\varphi E_{\mathrm{ph}}}{w} \left[QE(E_{\mathrm{ph}}) + 2f \cdot QE(2E_{\mathrm{ph}}) \right] \ . \tag{B.2}$$

  This can be derived from eq. 5.5, substituting the radiant power by the photon flux φ multiplied by the photon energy E_{ph}. The value of f varies with photon energy due to different monochromator settings and is given by the PTB as an upper limit in the range between 0.01 and 0.001. An upper limit for the uncertainty due to higher order radiation is then given by

$$\Delta QE = \frac{2f \cdot QE(2E_{\text{ph}})}{2f \cdot QE(2E_{\text{ph}}) + QE(E_{\text{ph}})} \quad \text{(B.3)}$$

The influence of higher order radiation on the measurement depends on f and the ratio of quantum efficiencies at both energies. It leads to an underestimation of the quantum efficiency. Analogously, this equation can be formulated for the attenuation, which is systematically overestimated through higher order radiation influence.
For the quantum efficiency measurement at 800 eV, the fraction of higher order light could be estimated from the monochromatic spectrum and amounts about 20 %. The quantum efficiency value at this single energy was therefore evaluated including the estimated second order radiation.

B.2 Measurement data of the spectral redistribution function

The following table shows parameterized properties of X-ray spectra measured with PNCCD C12_10_52 with eROSITA entrance window. The listed values were used for the evaluation of the quantum efficiency measurement with continuous synchrotron spectrum, as described in section 6.5. A graphical presentation of the peak width is shown in fig. 10.5, and of the parameters for the off-peak features in section 11.1.

photon energy	peak width	peak position	$k_{\text{Al, fluo}}$	$k_{\text{Si, esc}}$	$< \frac{dN}{d\epsilon} >_{\text{shelf}}$
eV	eV	eV			[eV^{-1}]
200	47	180	-		2.7×10^{-4}
250	51	230	-		1.4×10^{-4}
320	56	299	-		7.2×10^{-5}
396	57	379	-		4.2×10^{-5}
480	58	466	-		2.5×10^{-5}
533	58	519	-		2.1×10^{-5}
600	59	589	-		3.4×10^{-5}
800	61	788	-		1.7×10^{-5}
1250	69	1242	-		5.1×10^{-6}
1564	76	1555	-		3.6×10^{-6}
1825	79	1815	2.8×10^{-3}	-	2.3×10^{-6}
1848	83	1836	2.5×10^{-3}	2.0×10^{-2}	1.9×10^{-5}
3000	97	2994*	9.5×10^{-4}	1.2×10^{-2}	2.9×10^{-6}
4000	112	3996	2.7×10^{-4}	8.8×10^{-3}	1.7×10^{-6}
5500	128	5495	7.8×10^{-5}	4.7×10^{-3}	9.8×10^{-6}
7000	142	6992	3.4×10^{-5}	2.8×10^{-3}	6.1×10^{-7}
8500	157	8492		1.9×10^{-3}	3.8×10^{-7}
11000	175	10993*		9.6×10^{-4}	3.9×10^{-7}

Table B.3.: Parameterized characteristics of spectra measured with an eROSITA-type PNCCD. For a given photon energy the table lists the peak width (FWHM), peak position, relative fractions of aluminum fluorescence and silicon escape events and the relative position of the flat shelf in normalized spectra. A detailed description of these parameters is given in section 11.1. The photon energies marked by stars were used for gain calibration. The respective peak positions were defined by simulation results. The decreasing peak positions for decreasing photon energy are not caused by nonlinear amplification, but by partial charge loss in the entrance window and the impact of event detection thresholds during data analysis.

C. Deriving the analytic expression for the peak shape

In an analytic description of the spectrum, the shape of the main peak can be modeled using the last term of eq. 11.5. This term is derived from the absorption law and the charge collection efficiency as described in the following.

Following the same approach as Popp (2000), the number of events dN in a spectrum within an event energy range $d\varepsilon$ can be written as

$$\frac{dN}{d\varepsilon} = \frac{dN}{dz} \cdot \frac{dz}{d\varepsilon} \ . \tag{C.1}$$

The first factor, $\frac{dN}{dz}$, is the derivative of the number of absorbed photons $N(z)$ within a depth z in the sensitive volume. The number of absorbed photons can be derived from Beers Law (see eq. 2.8), leading to

$$N(z) = N_0(1 - \exp(-\alpha z)) \ , \tag{C.2}$$

with initial photon number N_0 and the absorption coefficient in silicon α.

The second factor in eq. C.1, $\frac{dz}{d\varepsilon}$, can be derived from the charge collection efficiency (CCE)

$$CCE(z) = 1 - \gamma \cdot exp\Big(-\frac{z}{\tau}\Big) \ , \tag{C.3}$$

as given in eq. 9.2, with free parameters γ and τ. A photon with energy E_{ph}, absorbed in the depth z, causes an event in the spectrum with a mean energy ε(z):

$$\varepsilon(z) = E_{\mathrm{ph}} \cdot \Big(1 - \gamma \exp(-\frac{z}{\tau})\Big) \ . \tag{C.4}$$

Events with a minimum energy $(1-\gamma) \cdot E_{\mathrm{ph}}$ are caused by absorption in a depth z = 0. For larger z, the event energy approaches the photon energy, as charge loss decreases with distance to the Si-SiO_2 interface.

In order to derive the term for $\frac{dz}{d\varepsilon}$, eq. C.4 is inverted and differentiated. Finally, z(ε) is inserted into the derivative of eq. C.2, leading to

$$\frac{dN}{d\varepsilon} = \frac{dN}{dz} \cdot \frac{dz}{d\varepsilon} = \frac{\tau\alpha N_0}{E_{\mathsf{ph}} - \varepsilon} \left[\frac{1}{\gamma}(1 - \frac{\varepsilon}{E_{\mathsf{ph}}}) \right]^{\tau\alpha} \quad . \tag{C.5}$$

This term, folded with a Gaussian function in order to account for statistical fluctuations, forms the shape of the main peak as described in section 11.1 and shown in fig. 11.5.

In order to normalize the modeled spectrum, eq. C.5 has to be integrated. For this purpose, the substitutions $A = \tau\alpha$, $B = (\gamma E_{\mathsf{ph}})^{-1}$ and $x = E_{\mathsf{ph}} - \varepsilon$ are performed. The resulting antiderivative is then

$$F(x) = N_0 (Bx)^A \; , \tag{C.6}$$

which can be used to normalize the spectrum.

D. Comments on the Geant4 simulation

The simulations of the spectral redistribution function shown in this work were performed with the Geant4 toolkit, version 4-9-2, using the 'Low Energy Electromagnetic Processes' models. The agreement between simulated and measured spectra is remarkably good, especially for photon energies above several keV. However, some limitations were revealed and are summarized shortly in the following.

In section 10.3 it was stated that the silicon escape and aluminum fluorescence peak in the simulations are slightly shifted compared to the peaks in the measured and calibrated spectra. As the fluorescence photon energy is a function of the electron binding energies in the respective material, these positions are determined by the binding energy data used in the Geant4 simulation. The binding energies used by Geant4 lead to fluorescence photon energies of $E_{\text{Al-K}\alpha}$ = 1469 eV and $E_{\text{Si-K}\alpha}$ = 1720 eV. More accurate binding energies of silicon and aluminum in their condensed state, as listed in table 2.3, give resulting fluorescence energies of $E_{\text{Al-K}\alpha}$ = 1485 eV and $E_{\text{Si-K}\alpha}$ = 1739 eV. Naturally, the shift in binding energy depending on the chemical composition of a material is not included in the simulation, as it is based on atomic data. Furthermore, a survey of Geant4 binding energy data by Pia et al. (2011) suggests improvements on the accuracy of binding energy data in Geant4. An improvement of the binding energy data in future Geant4 distributions can lead to a even better quality of simulated PNCCD spectra.
It is presented in section 10.3 that the simulated flat shelf is underestimated at event energies closely above zero and below the peak. It was seen that this part of the flat shelf is caused by electrons with low energies, in particular those generated very close to the Si-SiO_2 interface. In the applied Geant4 code, electron interactions are modeled by so-called condensed-random-walk algorithms. In such algorithms, the net angular and spatial displacement and energy loss of electrons as a result of multiple scattering processes are determined. The discrete nature of ionization processes is included by additional secondary electron emission. The emission of secondary electrons is limited by a user-defined secondary production threshold, which is set to 50 eV for the eROSITA response simulation. Although the adjustment of secondary production thresholds and the step size for electron simulation was extensively studied, the weakness in low energy electron simulation could not be mitigated. As stated in section 9.3, the accuracy of the data sources used in Geant4 declines strongly for low electron energies and could be one reason for the observed deviation. Recently, Seo et al. (2011) published a report on two models for the calculation of electron ionization cross sections, intended to extend and improve Geant4 simulation capabilities in the electron energy range below 1 keV. It is possible that the improvement of cross section data can solve the problem observed in this work. However, it might as well be that a condensed algorithm is not able to correctly reproduce electron interactions and transport in the thin layers of the entrance window. In this case, a detailed simulation including all collisions and interactions by an electron might be necessary. Of course, this approach is only possible with significantly higher computational power.

Acknowledgements

First and foremost I would like to express my gratitude to my advisor Prof. Dr. Lothar Strüder and my supervisor Dr. Norbert Meidinger, who provided me with guidance and support throughout my work at the MPI Semiconductor Laboratory. I am thankful for their continuous participation in my thesis and I greatly profited from their experience. I would also like to thank Prof. Dr. Ullrich Pietsch, for his interest and suggestions, and for being second advisor for this thesis.

In my daily work I have been fortunate to benefit from the expertise of many of my colleagues. I would like to thank Johannes Elbs for his help and ideas regarding PNCCD measurements and their interpretation. Many thanks to Robert Andritschke, who assisted me in questions regarding the data evaluation methods and made available his Standard Analysis Software. I am grateful to Georg Weidenspointner, for providing his valuable simulation tool and giving advice for questions regarding the simulation results. Thank you to Tanja Eraerds, my current office mate, for critical proofreading and encouragement during the final phase of the thesis. Many thanks to all of the mentioned and even more colleagues who helped me with proofreading this thesis. I am also grateful to all fellow students for the nice atmosphere, and for their interesting contributions during discussions in the student seminar.

I am indebted to the eROSITA team members for their involvement with the preparations and accomplishment of the measurements at the synchrotrons. The colleagues of the Physikalisch-Technische Bundesanstalt provided excellent measurement conditions at their beamlines at BESSY II and MLS. Thank you to Dieter Schlosser and Sebastian Ihle, who were themselves preparing synchrotron measurements and therefore provided support and helpful ideas.
Especially during the first phase of my work at the Semiconductor Laboratory, I benefited from advice and suggestions of many colleagues. To mention at least some, I would like to thank Florian Schopper and Klaus Heinzinger for their help and ideas during my first measurements characterizing the on-chip filter. Furthermore I wish to thank Robert Hartmann and Dr. Heike Soltau for their support. I also have to acknowledge all colleagues involved in the development and processing of the excellent detectors I worked with.

I am grateful to my family, for their understanding and support through the duration of my studies. Finally, I would like to thank my husband Luca, especially for his encouragement and tolerance of my moods during the final stage of my thesis.

Eidesstattliche Erklärung

Ich erkläre hiermit, dass ich die vorliegende Arbeit ohne unzulässige Hilfe Dritter und ohne Benutzung anderer, nicht angegebener Hilfsmittel angefertigt habe. Die aus anderen Quellen direkt oder indirekt übernommenen Daten und Konzepte sind unter Angabe der Quelle gekennzeichnet.
Die Arbeit wurde bisher werder im In- noch im Ausland in gleicher oder ähnlicher Form einer anderen Prüfungsbehörde vorgelegt.
Es wurden keine Dienste eines Promotionsvermittlungsinstituts oder einer ähnlichen Organisation in Anspruch genommen.